Fermilab

FERMILAB-THESIS-1996-18

A MEASUREMENT OF THE INCLUSIVE DRELL-YAN e^+e^- CROSS SECTION IN THE INVARIANT MASS RANGE OF 30-60 GEV/C^2 FROM $p\bar{p}$ COLLISIONS AT $\sqrt{S} = 1.8$ TEV

By

James Walter Thomas McKinley

A DISSERTATION

Submitted to
Michigan State University
in partial fulfillment of the requirements
for the Degree of

DOCTOR OF PHILOSOPHY

Department of Physics and Astronomy

1996

ABSTRACT

A MEASUREMENT OF THE INCLUSIVE DRELL-YAN e^+e^- CROSS SECTION IN THE INVARIANT MASS RANGE OF 30-60 GEV/C^2 FROM $p\bar{p}$ COLLISIONS AT $\sqrt{S} = 1.8$ TEV

By

James T. McKinley

We present a measurement of the inclusive Drell-Yan e^+e^- cross section measured using the DØ detector at Fermi National Accelerator Laboratory. 14.7 pb^{-1} of data were collected during the first data taking run of the DØ detector which was used to measure the invariant mass, photon rapidity, and photon transverse momentum distributions in the invariant mass range of 30-60 GeV/c^2. These distributions are compared to the resummed theoretical predictions.

For My Parents.

ACKNOWLEDGMENTS

I would first like to thank my thesis advisor Dr. James T. Linnemann for his guidance throughout my graduate career and especially during the analysis and preparation of this dissertation. I learned a great deal about computing and statistics as well as physics under his tutelage. Also his support of my research was invaluable in the current tight financial environment of governmentally funded physics research.

I would also like to thank Dr. C.-P. Yuan and Csaba Balàzs of Michigan State University for adding the photon couplings to their RESBOS Monte Carlo program. This made my analysis and comparison to the current theory much easier. I would also like to thank them for many valuable theoretical discussions and guidance during the preparation of this dissertation.

My DØ colleagues deserve my thanks as well, but are too numerous to list here. Some who deserve special thanks are: Mike Tartaglia for giving me guidance and training when I was first getting my feet wet in experimental high energy physics. Jan and Joan Guida and Dean Schamberger whose tireless efforts kept the DØ experiment running smoothly even during its first days online and who taught me a great deal about the technical aspects of DØ. Meena Narain, Ulrich Heintz, Eric Flattum and Ian Adam with whom I had many valuable discussions regarding electron identification in DØ. Scott Snyder for his vast computing knowledge, some of which he shared with me. Also Richard Genik III, for helping me keep my sense of humor as well as for some interesting physics conversations.

I am thankful to my girlfriend Rachel A. Postema for putting up with me during the final days of my dissertation work and for keeping my outlook bright.

Finally, I wish to thank my parents Jacqueline L. Curry and Michael J. Curry, whose unwavering support throughout my university career, as well as my whole life, allowed me to reach this goal.

Contents

LIST OF TABLES **viii**

LIST OF FIGURES **x**

1 Introduction **1**

2 Theory **3**

2.1 Introduction 3

2.2 Lowest Order Drell-Yan Process 7

2.3 Higher Order Drell-Yan Processes 15

2.4 Kinematics 23

2.4.1 Lowest Order Kinematics 24

2.4.2 Higher Order Kinematics 29

2.5 Summary 32

3 APPARATUS **35**

3.1 The Accelerator 35

3.2 The DØ Detector 40

3.2.1 Overview 40

3.2.2 The Central Detector (CD) 42

3.2.3 The Calorimeters 50

3.2.4 The Muon Detectors 59

3.2.5 The Trigger And Data Acquisition System 65

4 Data Sample And Event Selection **79**

4.1 Luminosity 79

4.2 Level 0 Trigger Selection Criteria 81

4.3 Level 1 Trigger Selection Criteria 82

4.4 Level 2 Trigger Selection Criteria 86

4.5 Offline Data Reconstruction 89
4.5.1 Energy Reconstruction 90
4.5.2 Track Reconstruction 90
4.5.3 Muon Reconstruction 91
4.5.4 Vertex Reconstruction 92
4.6 Offline Electron Identification 93
4.6.1 H-matrix 97
4.6.2 Isolation Fraction 103
4.6.3 Track Match Significance 107
4.6.4 dE/dx 117
4.7 Summary 119

5 Data Analysis **127**
5.1 Selected Data Sample 127
5.2 Background Estimation 127
5.2.1 Dijet Background Estimation Method 141
5.2.2 Z$\rightarrow \tau^+\tau^- \rightarrow e^+e^-$ Background Estimation Method 146
5.2.3 Background Subtraction 146
5.3 Online Efficiencies 149
5.4 Offline Efficiencies 155
5.5 Fiducial Acceptance, Kinematic Corrections And Unsmearing 157
5.6 Cross Section 167
5.7 Systematic Errors 170

6 Results And Comparison To Theory **177**
6.1 Statistical Compatibility Tests 177
6.1.1 Pearson χ^2 Test 178
6.1.2 Smirnov-Cramèr-Von Mises Test 179
6.2 Mass Distribution 180
6.3 Photon p_T Distribution 182
6.4 Photon Rapidity Distribution 192
6.5 Effect Of Parton Distributions 193
6.6 Conclusions 200
6.7 Possible Future Improvements 201

A The Level 2 Electromagnetic Filter **204**
A.1 Filter Scripts 205

A.2 The L2_EM Algorithm 207
A.2.1 Longitudinal Algorithm 208
A.2.2 Transverse Algorithm 209
A.2.3 Cone Algorithm 211
A.3 Energy And η Dependence Of Cuts 212
A.4 Cut Tuning 213
A.4.1 Tuning Of EC Shower Shape Cuts 214
A.4.2 Tuning Of CC Shower Shape Cuts 216
A.5 Internal Organization Of The L2_EM Filter 218
A.5.1 Correspondence Between RCP And Internal Variables 220
A.6 Calorimeter Geometry 222
A.7 L2_EM filter cut values 225

LIST OF REFERENCES **235**

List of Tables

2.1 Table of elementary particles. 3
2.2 Some symmetry operations and related conservation laws. 4
2.3 Definition of mathematical notation. 25

4.1 Table of electron selection cuts. 119
4.2 Table of single electron efficiency parameterizations. 120

5.1 Drell-Yan signal + background events per invariant mass bin. 128
5.2 Drell-Yan signal + background events per pair rapidity bin. 128
5.3 Drell-Yan signal + background events per pair p_T bin. 129
5.4 Dijet background events per invariant mass bin. 132
5.5 Dijet background events per pair rapidity bin. 132
5.6 Dijet background events per pair p_T bin. 134
5.7 Z$\rightarrow \tau^+\tau^- \rightarrow e^+e^-$ background events per invariant mass bin. 138
5.8 Z$\rightarrow \tau^+\tau^- \rightarrow e^+e^-$ background events per pair rapidity bin. 139
5.9 Z$\rightarrow \tau^+\tau^- \rightarrow e^+e^-$ background events per pair p_T bin. 139
5.10 Drell-Yan events per invariant mass bin. 147
5.11 Drell-Yan events per photon rapidity bin. 147
5.12 Drell-Yan events per photon p_T bin. 149
5.13 Efficiency corrections for Drell-Yan e^+e^- events per invariant mass bin. 157
5.14 Efficiency corrections for Drell-Yan e^+e^- events per photon rapidity bin. 157
5.15 Efficiency corrections for Drell-Yan e^+e^- events per photon p_T bin. . . 162
5.16 Total Efficiency, Kinematic, Fiducial Acceptance and Smearing correction for Drell-Yan e^+e^- events per invariant mass bin. 167
5.17 Total Efficiency, Kinematic, Fiducial Acceptance and Smearing correction for Drell-Yan e^+e^- events per photon rapidity bin. 168
5.18 Total Efficiency, Kinematic, Fiducial Acceptance and Smearing correction for Drell-Yan e^+e^- events per photon p_T bin. 168
5.19 Integrated Drell-Yan cross section per invariant mass bin. 170
5.20 Integrated Drell-Yan cross section per photon rapidity bin. 171

5.21 Integrated Drell-Yan cross section per photon p_T bin. 171

6.1 Cumulative distribution functions from the $d\sigma/dm$ distribution used in the Smirnov-Cramèr-Von Mises test. 181

6.2 Goodness-of-fit test results from comparing the experimental $d\sigma/dm$ distribution to the RESBOS and ISAJET Monte Carlo distributions. . 182

6.3 Smirnov-Cramèr-Von Mises test on the $d\sigma/dm$ distribution combined with a χ^2 test on the integrated cross section (normalization). 182

6.4 Cumulative distribution functions from the $d\sigma/dp_T$ distribution used in the Smirnov-Cramèr-Von Mises test. 187

6.5 Goodness-of-fit test results from comparing the experimental $d\sigma/dp_T$ distribution to the RESBOS and ISAJET Monte Carlo distributions. . 188

6.6 Smirnov-Cramèr-Von Mises test on the $d\sigma/dp_T$ distribution combined with a χ^2 test on the integrated cross section (normalization). 188

6.7 Cumulative distribution functions from the $d\sigma/dy$ distribution used in the Smirnov-Cramèr-Von Mises test. 192

6.8 Goodness-of-fit test results from comparing the experimental $d\sigma/dy$ distribution to the RESBOS and ISAJET Monte Carlo distributions. . 193

6.9 Smirnov-Cramèr-Von Mises test on the $d\sigma/dy$ distribution combined with a χ^2 test on the integrated cross section (normalization). 193

6.10 Difference in integrated cross sections due to input parton distribution functions. 196

6.11 Goodness-of-fit test results from comparing the experimental $d\sigma/dp_T$ distribution to the RESBOS Monte Carlo distributions using the CTEQ3M and MRSD0′ input parton distribution functions. 198

6.12 Integrated cross section summary. 200

List of Figures

2.1 Lowest order Drell-Yan Feynman diagram. 8
2.2 Drell-Yan $O(\alpha_s)$ correction Feynman diagrams. 16
2.3 Drell-Yan $O(\alpha_s^2)$ correction Feynman diagrams. 16
2.4 Drell-Yan virtual correction Feynman diagrams. 16
2.5 Resummed Drell-Yan $d\sigma/dm$. 22
2.6 Resummed Drell-Yan $d\sigma/dp_T$. 22
2.7 Resummed Drell-Yan $d\sigma/dy$. 23
2.8 The Collins-Soper O' reference frame. 24
2.9 Gluon Bremsstrahlung 29
2.10 Comparison of RESBOS and ISAJET p_T spectra. 34

3.1 The Fermilab Tevatron Collider. 36
3.2 An isometric cut-away view of the DØ detector. 41
3.3 An overview of the DØ calorimeters 51
3.4 The pseudo-projective geometry of the DØ calorimeter towers. 53
3.5 A calorimeter unit cell. 55
3.6 A schematic of the DØ Data Acquisition System 72
3.7 A schematic diagram of a Level 2 node 74

4.1 The Level 1 trigger efficiency vs. input E_T 85
4.2 The Level 2 trigger efficiency vs. input E_T 88
4.3 PELC/PPHO efficiency vs. E_T, E, and IETA. 96
4.4 H-matrix χ^2 for electrons. 98
4.5 H-matrix χ^2 for background. 98
4.6 CC H-matrix $\chi^2 < 100$ Efficiency vs. input |IETA|. 101
4.7 EC H-matrix $\chi^2 < 100$ Efficiency vs. input |IETA|. 102
4.8 Isolation fraction for electrons. 103
4.9 Isolation fraction for background. 104
4.10 CC Isolation fraction $ISO < 0.15$ Efficiency vs. input |IETA|. 105

4.11 EC Isolation fraction $ISO < 0.15$ Efficiency vs. input |IETA|. 106
4.12 Track match significance for electrons. 108
4.13 Track match significance for background. 108
4.14 Central calorimeter $\sigma_{\delta z}$ vs. input energy and IETA 113
4.15 Central calorimeter $\sigma_{R\delta\phi}$ vs. input energy and IETA. 114
4.16 End calorimeter $\sigma_{\delta z}$ vs. input energy and IETA. 115
4.17 End calorimeter $\sigma_{R\delta\phi}$ vs. input energy and IETA. 116
4.18 dE/dx for electrons and background. 118
4.19 Level 1 and Level 2 electron efficiency vs. input E_T after calorimeter based offline cuts. 121
4.20 CC H-matrix $\chi^2 < 100$ + isolation fraction $ISO < 0.15$ efficiency vs. input |IETA|. 123
4.21 EC H-matrix $\chi^2 < 100$ + isolation fraction $ISO < 0.15$ efficiency vs. input |IETA|. 124
4.22 Track match significance + dE/dx cut Efficiency vs. input |IETA|. . . 126

5.1 Drell-Yan + background events vs. invariant mass. 129
5.2 Drell-Yan + background events vs. pair rapidity. 130
5.3 Drell-Yan + background events vs. pair p_T. 130
5.4 Dijet background events vs. Drell-Yan signal + background events. . 133
5.5 Direct photon background events vs. Drell-Yan signal + background events. 136
5.6 W + jet background events vs. Drell-Yan signal + background events. 137
5.7 Z$\rightarrow \tau^+\tau^- \rightarrow e^+e^-$ background events vs. Drell-Yan signal + background events. 140
5.8 CC PELC rejection vs. cluster E_T, IETA. 144
5.9 EC PELC rejection vs. cluster E_T, |IETA|. 145
5.10 Drell-Yan (signal + background) - (dijet + Z$\rightarrow \tau^+\tau^- \rightarrow e^+e^-$) background events. 148
5.11 Level 1 EM $E_T > 7.0$ GeV efficiency for Drell-Yan e^+e^- events after offline cuts. 153
5.12 Level 2 EM $E_T > 10.0$ GeV + Level 2 ISO < 0.15 efficiency for Drell-Yan e^+e^- events after offline cuts. 154
5.13 PPHO efficiency for Drell-Yan e^+e^- events. 158
5.14 PELC/PPHO efficiency for Drell-Yan e^+e^- events. 159
5.15 H-matrix $\chi^2 < 100$ + ISO < 0.15 efficiency for Drell-Yan e^+e^- events. 160
5.16 Track match significance + dE/dx cuts efficiency for Drell-Yan e^+e^- events. 161

5.17 Comparison of two smearing correction methods for Drell-Yan e^+e^- events. 165
5.18 Kinematic, Fiducial Acceptance and Smearing correction for Drell-Yan e^+e^- events. 166
5.19 Total Efficiency, Kinematic, Fiducial Acceptance and Smearing correction for Drell-Yan e^+e^- events. 169
5.20 Drell-Yan e^+e^- differential cross section $d\sigma/dm$ vs. invariant mass. . 172
5.21 Drell-Yan e^+e^- differential cross section $d\sigma/dy$ vs. photon rapidity. . 173
5.22 Drell-Yan e^+e^- differential cross section $d\sigma/dp_T$ vs. photon p_T. 174

6.1 Drell-Yan e^+e^- differential cross section $d\sigma/dm$ vs. invariant mass compared to the RESBOS Monte Carlo. 183
6.2 Drell-Yan e^+e^- differential cross section $d\sigma/dm$ vs. invariant mass compared to the ISAJET Monte Carlo. 184
6.3 Drell-Yan e^+e^- differential cross section $m^3d^2\sigma/dmdy|_{y=0}$ vs. invariant mass compared to theory. 185
6.4 Drell-Yan e^+e^- differential cross section $d\sigma/dm$ vs. invariant mass compared to the CDF 1988-1989 cross section. 186
6.5 Drell-Yan e^+e- differential cross section $d\sigma/dp_T$ vs. photon p_T compared to the RESBOS Monte Carlo. 189
6.6 Drell-Yan e^+e- differential cross section $d\sigma/dp_T$ vs. photon p_T compared to the ISAJET Monte Carlo. 190
6.7 Drell-Yan e^+e- differential cross section $d\sigma/dp_T$ vs. photon p_T compared to the RESBOS and ISAJET Monte Carlos plotted on a linear scale. 191
6.8 Drell-Yan e^+e- differential cross section $d\sigma/dy$ vs. photon rapidity compared to the RESBOS Monte Carlo. 194
6.9 Drell-Yan e^+e- differential cross section $d\sigma/dy$ vs. photon rapidity compared to the ISAJET Monte Carlo. 195
6.10 Drell-Yan e^+e- differential cross section differences between using the MRSD0′ and CTEQ3M parton distributions as input to the RESBOS Monte Carlo. 198
6.11 Drell-Yan e^+e- differential cross section differences between the ISAJET(CTEQ2L) and RESBOS(CTEQ3M) Monte Carlos. 199

Chapter 1

Introduction

The subject of this dissertation is the measurement of the inclusive e^+e^- (Drell-Yan) cross section in $p\bar{p}$ collisions at $\sqrt{s} = 1.8$ TeV. I have measured the virtual photon mass, rapidity, and transverse momentum (Q_T) spectra using data from the DØ detector collected during DØś first collider data run.

The DØ experiment was originally proposed in 1983. The name is derived from the Tevatron Collider's D0 interaction region at the Fermi National Accelerator Laboratory (FNAL or Fermilab) in Batavia, Illinois in which the detector resides. Installation was completed in early 1992. The first collisions occurred in the DØ detector on May 12, 1992. Several test beam runs were also conducted using the FNAL fixed target facilities during the fabrication and assembly of DØ to study its various components. This thesis will focus on the 14.7 pb^{-1} of data taken during DØś first run which occurred during the 14 month period between May, 1992 and July, 1993 which is also known as run 1A.

The Drell-Yan lepton pair production mechanism was first described by Sidney D. Drell and Tung-Mow Yan in their paper titled "Massive Lepton-Pair Production in Hadron-Hadron Collisions at High Energies" [1]. This model is often called the "naive" Drell-Yan model since it does not take into account the transverse momentum

of the incoming hadrons and thus predicts a zero transverse momentum for the virtual photon.

The Drell-Yan process, though rare in proton-antiproton interactions, has the virtue of being unaffected by complex final state interactions and is directly comparable to theoretical calculations in a way that few processes involving the strong nuclear force are. It serves as an important test-bed for perturbative QCD (Quantum Chromodynamics) calculations.

Much theoretical work has been done to describe this process more accurately within the framework of the Standard Model and take into account higher order (QCD) corrections to the basic Drell-Yan model. Recent work by C.-P. Yuan and G. A. Ladinsky of Michigan State University, in which the non-perturbative functions in the Collins-Soper-Sterman resummation formalism were studied using fixed-target and collider Drell-Yan data, resulted in parameterizations which yield better agreement with with CDF (Collider Detector at Fermilab) Z boson data than previously found in the literature.

CDF has recently (Jan. 1994) published their Drell-Yan cross section for the rapidity range $|y| < 1.0$ from 4.13 pb^{-1} of data collected in the 1989 collider run at Fermilab. I take advantage of the DØ detector's large rapidity coverage to measure the Drell-Yan cross section in the rapidity range $|y| < 2.5$. I also compare measurements of the DØ Drell-Yan mass, rapidity, and Q_T spectra to that predicted by the resummed cross section.

Chapter 2

Theory

2.1 Introduction

The Standard Model (SM) of elementary particles describes the interactions between the three basic types of elementary particles which are leptons, quarks, and mediators (force carrying particles). There are six types each of leptons and quarks which are further grouped in pairs into three generations. Table 2.1 shows the currently known leptons and quarks grouped by generation and "flavor".

All these elementary particles have corresponding anti-particles as well, for a total of 12 leptons. In addition, quarks come in three "colors" for a total of $12 \times 3 = 36$ quarks. All quarks and leptons are fermions with spin $\frac{1}{2}$.

The force carrying particles are the photon (γ), W^+, W^-, and Z vector bosons and the gluon (g) which all have spin 1. The photon mediates the electromagnetic force, the W and Z bosons mediate the weak nuclear force, and the gluon carries the strong

Table 2.1: Table of elementary particles.

generation	I	II	III
quarks	u d	c s	t b
leptons	e ν_e	μ ν_μ	τ ν_τ

Table 2.2: Some symmetry operations and related conservation laws.

symmetry		conservation law
time translation	$\leftrightarrow$	energy conservation
space translation	$\leftrightarrow$	momentum conservation
rotation	$\leftrightarrow$	angular momentum conservation
gauge transformation	$\leftrightarrow$	charge conservation

nuclear force. There are eight different types of gluons which, when combined with the vector bosons, give a total of 12 force carrying particles in the Standard Model (SM). In addition, the Glashow-Weinberg-Salaam model requires the existence of at least one Higgs boson whose coupling strength to the other particles brings about the difference in their masses.

The Standard Model is based on the symmetries that exist in nature. Noether's Theorem states that symmetries imply conservation laws and vice versa. For example, Table 2.2 lists some symmetries in nature and the physical conservation laws associated with them.

The definition of a symmetry is an operation that can be performed (at least conceptually) on a system that leaves it invariant. The systematic mathematical study of symmetries is called group theory. The defining properties of a group are exactly the set of symmetry operations on a system that must hold true, namely

- *Closure.* If R_i and R_j are members of the set, then the product $R_iR_j = R_k$ must also be a member of the set.
- *Identity.* A member I of the set must exist such that $IR_i = R_iI = R_i$.
- *Inverse.* Every member of the set R_i must have an inverse R_i^{-1} such that $R_iR_i^{-1} = I$.
- *Associativity.* $R_i(R_jR_k) = (R_iR_j)R_k$.

The most often used groups in elementary particle physics are unitary groups $U(\mathrm{n})$. Unitary groups are groups whose members have the property $R^{-1} = R^{\dagger}$. A unitary group with determinant 1 is called a special unitary group or $SU(\mathrm{n})$. A unitary group with only real elements is known as an orthogonal group $O(\mathrm{n})$. Finally, a unitary group with only real elements that has determinant 1 is called special orthogonal or $SO(\mathrm{n})$.

The SM is composed of three groups which describe the internal symmetries of the theory, namely hypercharge, weak isospin, and color. The hypercharge symmetry is represented by the group $U(1)$, weak isospin by $SU(2)_L$ (where the subscript L denotes that only left-handed particles obey this symmetry), and color by $SU(3)$. Thus, the standard model is represented by $SU(3) \otimes SU(2)_L \otimes U(1)$. The number of gauge bosons that mediate the forces in the SM is equal to the number of generators in the symmetry group that represents the force. The $U(1)$ group has one generator so the electromagnetic force has one gauge boson, the photon. The $SU(2)$ group has $2 \otimes 2 = 2^2 - 1 = 3$ gauge bosons which are the W^+, W^-, and Z^0 bosons. Finally, the $SU(3)$ group has $3 \otimes 3 = 3^2 - 1 = 8$ gauge bosons which are the gluons.

The internal symmetries of the SM refer to the behavior of the SM Lagrangian under $U(1)$, $SU(2)_L$, and $SU(3)$ gauge transformations; the SM Lagrangian is left unchanged under these transformations. An Abelian gauge theory is one in which the fields which represent the gauge bosons commute. In Non-Abelian gauge theories the gauge fields do not commute. Thus, gauge fields do not directly interact with each other in Abelian gauge theories and do directly interact with one another in Non-Abelian theories. Quantum Electrodynamics (QED) which describes electromagnetic interactions is an Abelian gauge theory and photons do not directly interact with themselves. Quantum Chromodynamics (QCD) on the other hand, is a non-Abelian theory and gluons do directly interact with each other. A simple description of this is

that photons are uncharged so they cannot couple to each other, whereas gluons carry color charge so they can and do couple to one another.

This difference in the behavior of the gauge boson force mediators is the major difference between QED and QCD. In QED, an electric charge polarizes the vacuum due to the virtual electron-positron pairs which surround it. The charge density is higher near the charge and results in an effective coupling constant α_E given by

$$\alpha_E = \frac{\alpha(\mu)}{1 - (\frac{\alpha(\mu)}{3\pi}) \ln(\frac{Q^2}{\mu^2})}$$

where Q is related to the energy of the probe and μ is a lower cutoff energy.

In QCD, a quark is surrounded by not only virtual quark-antiquark pairs, but by virtual gluon pairs as well. The virtual gluon pairs decrease the effective strong coupling constant near the quarks, whereas the quark-antiquark pairs increase the effective coupling. The gluon pairs' effect dominates and α_s is decreased near the quarks. The strong coupling constant has the form

$$\alpha_s(Q) = \frac{12\pi}{(33 - 2n_f) \ln(\frac{Q^2}{\Lambda^2})}$$

where n_f is the number of quark flavors and Λ is the QCD scaling parameter. At lower Q^2 values, the strong coupling becomes large which explains why colored particles are confined in color neutral combinations. As Q^2 becomes large, α_s approaches zero. This is known as asymptotic freedom. This is the reason that perturbative methods can be used for high momentum transfer QCD calculations (known as "pQCD"). Unfortunately the other side of the coin is that for "soft" processes, perturbative methods break down, and little is known about "non-perturbative" QCD. At this time the most

productive method for studying non-perturbative QCD is "lattice gauge theory" where the goal is to make progress in finding solutions by working with a minimum distance scale so the theory is cut off in momentum transfer and then introducing a variety of techniques such as statistical mechanics for handling complicated systems. Non-perturbative QCD calculations are still very much "work-in-progress". Consequently, when describing the hadronic collisions which inevitably involve these non-perturbative interactions, one must rely on measured and parameterized parton momentum distributions for the initial state hadrons and fragmentation functions which describe how the final state partons evolve into hadron jets. The technique of separating the "hard-scattering" from the "soft" processes is called factorization. It is not obvious that this approach is valid, however John Collins, Davison Soper, and George Sterman [4] have shown that factorization is valid to all orders in Drell-Yan cross sections for leading twist.

2.2 Lowest Order Drell-Yan Process

To calculate the cross section for the lowest order Drell-Yan interaction we first calculate the hard scattering cross section. The Feynman diagram of the lowest order Drell-Yan interaction is shown in Figure 2.1.

The hard scattering cross section is defined in terms of the matrix element for the process of interest

$\frac{d\hat{\sigma}_{DY}}{d\cos\theta} = \frac{1}{32\pi\hat{s}}\overline{|\mathcal{M}|}^2(q\overline{q} \to \gamma^* \to \ell\overline{\ell})$

Using the Feynman Rules we can write down the matrix element for this process

$-i\mathcal{M} = \overline{u}(p_3)(ig_2\sin(\theta_W)\gamma^\mu)v(p_4)(\frac{ig_{\mu\nu}}{q^2})\overline{v}(p_2)(-ie_f g_2\sin(\theta_W)\gamma^\nu)u(p_1)$

where e_f is the quark charge fraction e_q/e. A bit of simplification yields

$\mathcal{M} = \frac{ie_f g_2^2\sin^2(\theta_W)}{q^2}[\overline{u}(p_3)\gamma^\mu v(p_4)][\overline{v}(p_2)\gamma_\mu u(p_1)]$

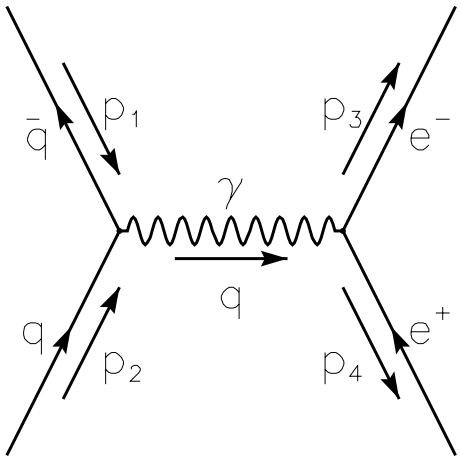

Figure 2.1: The Lowest order Drell-Yan Feynman diagram.

Now, we wish to find the Hermitian conjugate of the matrix element. First we note that

$\gamma^{\mu\dagger} = \gamma^0\gamma^\mu\gamma^0$

$\overline{u} = u^\dagger\gamma^0$

$\overline{v} = v^\dagger\gamma^0$

$(\gamma^0)^2 = 1$

so the hermitian conjugate of the matrix element is

$\mathcal{M}^\dagger = \frac{-ie_f g_2^2 \sin^2(\theta_W)}{q^2}[\overline{v}(p_4)\gamma^\mu u(p_3)][\overline{u}(p_1)\gamma_\mu v(p_2)]$

Thus we have

$|\mathcal{M}|^2 = \mathcal{M}^\dagger\mathcal{M} = \frac{e_f g_2^2 \sin^2(\theta_W)}{q^4}[\overline{v}(p_4)\gamma^\alpha u(p_3)\overline{u}(p_3)\gamma^\beta v(p_4)][\overline{u}(p_1)\gamma_\alpha v(p_2)\overline{v}(p_2)\gamma_\beta u(p_1)]$

Since the initial spins and colors of the incoming quarks are unknown, we must average over these quantities and then sum over the final spins of the leptons which gives

$$\overline{|\mathcal{M}|}^2 = \left(\frac{1}{3}\right)_{q \text{ colors}} \cdot \left(\frac{1}{3}\right)_{\overline{q} \text{ colors}} \cdot \left(\frac{1}{2}\right)_{q \text{ spin}} \cdot \left(\frac{1}{2}\right)_{\overline{q} \text{ spin}} \cdot \sum_{\text{colors}} \sum_{\text{spins}} |\mathcal{M}|^2$$

$$\overline{|\mathcal{M}|}^2 = \frac{1}{36} \cdot \frac{e_f g_2^2 \sin^2(\theta_W)}{q^4} \cdot \sum_{i=\text{colors}} \sum_{abcd=\text{spins}} \gamma^{\alpha}_{ab} \gamma^{\beta}_{cd} \gamma_{\alpha ab} \gamma_{\beta cd} \cdot$$

$$\overline{v}_a(p_4) v_d(p_4) u_b(p_3) \overline{u}_c(p_3) \overline{u}_a(p_1) u_d(p_1) v_b(p_2) \overline{v}_c(p_2) \cdot \lambda^i \lambda_i$$

The sum over colors gives

$$\overline{|\mathcal{M}|}^2 = \frac{1}{12} \cdot \frac{e_f g_2^2 \sin^2(\theta_W)}{q^4} \cdot \sum_{abcd=\text{spins}} \gamma^{\alpha}_{ab} \gamma^{\beta}_{cd} \gamma_{\alpha ab} \gamma_{\beta cd} \cdot$$

$$\overline{v}_a(p_4) v_d(p_4) u_b(p_3) \overline{u}_c(p_3) \overline{u}_a(p_1) u_d(p_1) v_b(p_2) \overline{v}_c(p_2)$$

From the Dirac equation we have

$\sum \overline{u} u = \not{p} + m$ and $\sum \overline{v} v = \not{p} + m$

which yields

$$\begin{aligned}
\overline{|\mathcal{M}|}^2 &= \frac{1}{12} \sum_{abcd} \frac{e_f^2 g_2^4 \sin^4(\theta_W)}{q^4} \cdot \\
&\quad [(\not{p}_4 - m_\ell)_{ad} (\not{p}_3 - m_\ell)_{bc} (\not{p}_2 - m_q)_{ad} (\not{p}_1 - m_q)_{bc} \gamma^{\alpha}_{ab} \gamma^{\beta}_{cd} \gamma_{\alpha ab} \gamma_{\beta bc}] \\
&= \left(\frac{1}{12}\right) \left(\frac{e_f^2 g_2^4 \sin^4(\theta_W)}{q^4}\right) \cdot \\
&\quad \mathrm{Tr}[(\not{p}_4 - m_\ell) \gamma^\alpha (\not{p}_3 - m_\ell) \gamma^\beta] \cdot \mathrm{Tr}[(\not{p}_2 - m_q) \gamma_\alpha (\not{p}_1 - m_q) \gamma_\beta]
\end{aligned}$$

The Q scale we are interested in is 30-60 GeV, which is orders of magnitude greater that the lepton and quark masses (we are well above the bottom quark mass and well

below the top quark mass) so we set the m_q and m_ℓ in the above equation to zero which gives

$\overline{|\mathcal{M}|}^2 = \left(\frac{1}{12}\right)\left(\frac{e_f^2 g_2^4 \sin^4(\theta_W)}{q^4}\right)\mathrm{Tr}[\not{p}_4\gamma^\mu \ \not{p}_3\gamma^\nu]\mathrm{Tr}[\not{p}_1\gamma_\mu \ \not{p}_2\gamma_\nu]$

Now we need to evaluate the above traces which can be readily accomplished using the following three identities

$\mathrm{Tr}[\not{p}_i\gamma^\mu \ \not{p}_j\gamma^\nu] = p_{i\alpha}p_{j\beta}\mathrm{Tr}[\gamma^\alpha\gamma^\mu\gamma^\beta\gamma^\nu]$

$\mathrm{Tr}[\gamma^\alpha\gamma^\mu\gamma^\beta\gamma^\nu] = 4[g^{\alpha\mu}g^{\beta\nu} - g^{\alpha\beta}g^{\mu\nu} + g^{\alpha\nu}g^{\beta\mu}]$

$g^{\mu\nu}g_{\mu\nu} = 4$

so the product of the two traces is

$$\begin{aligned}
\mathrm{Tr}[\not{p}_4\gamma^\mu \ \not{p}_3\gamma^\nu]\mathrm{Tr}[\not{p}_1\gamma_\mu \ \not{p}_2\gamma_\nu] &= 16p_{4\alpha}p_{3\beta}p_1^\gamma p_2^\delta \cdot \\
&\quad [g^{\alpha\mu}g^{\beta\nu}g_{\gamma\mu}g_{\delta\nu} - g^{\alpha\mu}g^{\beta\nu}g_{\gamma\delta}g_{\mu\nu} + g^{\alpha\mu}g^{\beta\nu}g_{\gamma\nu}g_{\delta\mu} - \\
&\quad g^{\alpha\beta}g^{\mu\nu}g_{\gamma\mu}g_{\delta\nu} + g^{\alpha\beta}g^{\mu\nu}g_{\gamma\delta}g_{\mu\nu} - g^{\alpha\beta}g^{\mu\nu}g_{\gamma\nu}g_{\delta\mu} + \\
&\quad g^{\alpha\nu}g^{\beta\mu}g_{\gamma\mu}g_{\delta\nu} - g^{\alpha\nu}g^{\beta\mu}g_{\gamma\delta}g_{\mu\nu} + g^{\alpha\nu}g^{\beta\mu}g_{\gamma\nu}g_{\delta\mu}] \\
&= 16[(p_4\cdot p_1)(p_3\cdot p_2) - (p_4\cdot p_3)(p_1\cdot p_2) + \\
&\quad (p_4\cdot p_2)(p_1\cdot p_3) - (p_4\cdot p_3)(p_1\cdot p_2) + \\
&\quad 4(p_4\cdot p_3)(p_1\cdot p_2) - (p_4\cdot p_3)(p_1\cdot p_2) + \\
&\quad (p_4\cdot p_2)(p_1\cdot p_3) - (p_4\cdot p_3)(p_1\cdot p_2) + \\
&\quad (p_4\cdot p_1)(p_3\cdot p_2)]
\end{aligned}$$

So we have

$\mathrm{Tr}[\not{p}_4\gamma^\mu \ \not{p}_3\gamma^\nu]\mathrm{Tr}[\not{p}_1\gamma_\mu \ \not{p}_2\gamma_\nu] = 32[(p_4\cdot p_1)(p_3\cdot p_2) + (p_4\cdot p_2)(p_1\cdot p_3)]$

Which finally gives us

$\overline{|\mathcal{M}|}^2 = \left(\frac{8}{3}\right)\left(\frac{e_f^2 g_2^4 \sin^4(\theta_W)}{q^4}\right)[(p_4\cdot p_1)(p_3\cdot p_2) + (p_4\cdot p_2)(p_1\cdot p_3)]$

We are now in a position to use what we know about the kinematics of the interaction, namely that the momentum and energy are conserved in the process. In the

rest frame of the vector boson

$$p_1 = \begin{pmatrix} E \\ 0 \\ 0 \\ E \end{pmatrix}, \qquad p_2 = \begin{pmatrix} E \\ 0 \\ 0 \\ -E \end{pmatrix}, \qquad p_3 = \begin{pmatrix} E \\ E\sin(\theta) \\ 0 \\ E\cos(\theta) \end{pmatrix}, \qquad p_4 = \begin{pmatrix} E \\ -E\sin(\theta) \\ 0 \\ -E\cos(\theta) \end{pmatrix}$$

where θ is the angle between the leptons and the beam axis in the cm frame and $E = \sqrt{\hat{s}}/2$ where $\hat{s}$ is the cm energy of the quark-antiquark interaction. Using these definitions we have

$(p_4 \cdot p_1) = (p_3 \cdot p_2) = E^2(1 - \cos(\theta))$

$(p_4 \cdot p_2) = (p_1 \cdot p_3) = E^2(1 + \cos(\theta))$

so

$(p_4 \cdot p_1)(p_3 \cdot p_2) = E^4(1 - 2\cos(\theta) + \cos^2(\theta))$

$(p_4 \cdot p_2)(p_1 \cdot p_3) = E^4(1 + 2\cos(\theta) + \cos^2(\theta))$

and

$(p_4 \cdot p_1)(p_3 \cdot p_2) + (p_4 \cdot p_2)(p_1 \cdot p_3) = 2E^4(1 + \cos^2(\theta))$

hence

$\overline{|\mathcal{M}|}^2 = \left(\frac{16}{9}\right)\left(\frac{E^4 e_f^2 g_2^4 \sin^4(\theta_W)}{q^4}\right)(1 + \cos^2(\theta))$

Now that we have evaluated the summed and averaged square of the matrix element, we can write down the lowest order Drell-Yan hard scattering cross section

$$\begin{aligned} \frac{d\hat{\sigma}(q\overline{q} \to \gamma^* \to \ell\overline{\ell})}{d\cos(\theta)} &= \left(\frac{1}{32\pi\hat{s}}\right)\overline{|\mathcal{M}|}^2 \\ &= \left(\frac{1}{6\pi}\right)\left(\frac{E^4}{q^4\hat{s}}\right)(e_f^2 g_2^4 \sin^4(\theta_W))(1 + \cos^2(\theta)) \end{aligned}$$

To put this in more familiar notation we note that

$g_2 \sin(\theta_W) = e$

$\alpha^2 = \frac{e^4}{16\pi^2} \approx \frac{1}{137}$

$q^4 = 16E^4$

which upon substitution gives

$$\frac{d\hat{\sigma}(q\overline{q} \to \gamma^* \to \ell\overline{\ell})}{d\cos(\theta)} = \left(\frac{e_f^2}{3}\right)\left(\frac{\pi\alpha^2}{2\hat{s}}\right)(1+\cos^2\theta)$$

Integration over $\theta = 0$ to π gives the familiar $\sigma_0(q\overline{q} \to \gamma^* \to \ell\overline{\ell})$ total hard scattering amplitude

$$\int_0^\pi d\cos\theta(1+\cos^2\theta) = \int_{-1}^1 dx(1+x^2) = \frac{8}{3}$$

$$\hat{\sigma}_0(q\overline{q} \to \gamma^* \to \ell\overline{\ell}) = \frac{4\pi\alpha^2 e_f^2}{9\hat{s}}$$

This is the hard scattering cross section for a specific quark flavor in the cm frame of the interacting partons (the virtual photon rest frame) where $\hat{s}$ is the cm energy squared of the partons. The cross section for proton-antiproton scattering is the sum over all flavors, which requires knowledge of the incoming hadron types as well as the longitudinal momentum distributions $f_a(x_a)$ and $f_b(x_b)$ of the interacting partons where x_a and x_b are the usual longitudinal momentum fractions of the interacting partons relative to the momenta of the their parent hadrons.

The Factorization Theorem states that

$$\frac{d\sigma}{dQ^2 dy dQ_T^2} = \frac{4\pi^2\alpha^2}{9Q^2 S}\sum_{ab}\int_{x_A}^1 \frac{d\xi_A}{\xi_A}\int_{x_B}^1 \frac{d\xi_B}{\xi_B}$$
$$\times f_{a/A}(\xi_A;\mu)T_{ab}(Q_T, Q, x_A/\xi_A, x_B/\xi_B; g(\mu), \mu)f_{b/B}(\xi_B;\mu)$$

where T_{ab} is the infra-red safe perturbative hard-scattering cross section

$$T_{ab}(Q_T, Q, x_A/\xi_A, x_B/\xi_B; g(\mu), \mu) = \sum_{N=0}^{\infty} \left[\frac{\alpha_s(\mu)}{\pi}\right]^N \times T_{ab}^{(N)}(Q_T, Q, x_A/\xi_A, x_B/\xi_B; \mu)$$

and $f_{a/A}(\xi_A, \mu)$, $f_{b/B}(\xi_B, \mu)$ are the parton distribution functions for partons of type a,b in hadrons of type A,B

$$f_{a/A}(\xi_A, \mu) = \delta_{aA}\delta(1-\xi_A) + \sum_{n=1}^{\infty} \left(\frac{\alpha_s}{\pi}\right)^n f_{a/A}^{(n)}$$

This states that the parton remains itself in the absence of interactions. The variable μ here is the factorization scale, which is arbitrary and determines the energy at which the parton distributions are evaluated. It is typically chosen to be $\mu = Q$. Factorization allows one to use perturbation theory to calculate the hard scattering cross section and remove the divergences which are then absorbed into the parton distributions. The parton distributions are non-perturbative quantities, but are *universal*; they are the same in deep inelastic scattering (DIS) as they are in Drell-Yan. Consequently, one can measure the parton distributions in DIS, and then apply the results to make predictions about Drell-Yan.

A heuristic argument for the idea of a parton density was given by Feynman [11] [12]. If we consider electron-proton scattering (DIS) where the proton is assumed to be made up of constituent partons, the partons interact with one another, and exist in purely virtual states. A typical state has a lifetime τ in this frame. In the rest frame of the electron, τ is dilated to $\tau(E_p/m_p)$, while the proton radius r_p

is Lorentz-contracted to $r_p(m_p/E_p)$. Thus, during the short time it takes for the proton to pass over the electron in this frame, the partons appear to be stationary, because their self-interactions act on dilated time scales that are much longer than the time for the electron-parton collision. Since parton-parton interactions and electron-parton scattering take place on such different time scales, they cannot interfere in a quantum mechanical sense. Consequently, the quantum mechanical amplitudes for the distributions of partons exhibit incoherence relative to the electron-parton cross section, as if they were classical quantities. Thus it makes sense to talk about the probability of finding a parton with a given momentum in a proton and to treat it separately from the hard scattering. This probability is the parton density f.

Given the parton distribution functions, the differential cross section $\frac{d\sigma(p\overline{p}\to\gamma^*\to\ell\overline{\ell})}{dMdx_F}$ can be written as

$$\frac{d^2\sigma}{dMdx_F} = \frac{8\pi\alpha^2}{9M^3(x_a+x_b)}\sum_f^{flavor} e_f^2[f_f^a(x_a)f_{\overline{f}}^b(x_b)+f_{\overline{f}}^a(x_a)f_f^b(x_b)]$$

This is the naive Drell-Yan result. In terms of the Q and rapidity of the vector boson ($x_a=\sqrt{\tau}e^{y_{\gamma^*}}$) the total cross section can be written as

$$\begin{aligned}\sigma(p\overline{p}\to\gamma^*\to\ell\overline{\ell}) &= \sum_f^{flavor}\int_0^1\int_0^1 dx_a dx_b f_a(x_a)f_b(x_b)\int_0^\pi \frac{d\sigma(q\overline{q}\to\gamma^*\to\ell\overline{\ell})}{d\cos\theta} \\ &= \sum_f^{flavor}\int_0^1\int_{-\infty}^{\infty} d\tau dy_{\gamma^*} f_a(\sqrt{\tau}e^{y_{\gamma^*}})f_b(\sqrt{\tau}e^{-y_{\gamma^*}})\cdot \\ &\quad \int_0^\pi \frac{d\hat{\sigma}(q\overline{q}\to\gamma^*\to\ell\overline{\ell})}{d\cos\theta}d\cos\theta\end{aligned}$$

where $\tau=\hat{s}/S$, S is the center of mass energy squared of the colliding proton-antiproton beams and y_{γ^*} is the rapidity of the virtual photon. Thus, the

differential cross section relative to the lepton angular distribution in the cm frame and $\tau = \hat{s}/S = Q^2/S = M^2/S$ is

$$\frac{d\sigma(p\overline{p} \to \gamma^* \to \ell\overline{\ell})}{d\cos\theta d\tau} = \sum_f^{flavor} \int_{-\infty}^{\infty} dy_{\gamma^*} f_a(\sqrt{\tau}e^{y_{\gamma^*}}) f_b(\sqrt{\tau}e^{-y_{\gamma^*}}) \frac{d\hat{\sigma}(q\overline{q} \to \gamma^* \to \ell\overline{\ell})}{d\cos\theta}$$

In the naive Drell-Yan model, the Q_T of the virtual photon is identically zero. Examination of experimental Drell-Yan data however, clearly shows that this is not the case in nature. Also, the overall event rate predicted by the lowest order calculation is too low by roughly a factor of two when compared to the measured cross section (the so-called "K" factor). This large difference is due to the absence of the higher order Drell-Yan processes which contain large logarithmic terms in (Q^2/Λ^2). Consequently, one must go beyond leading order for an accurate comparison of theory and experiment.

2.3 Higher Order Drell-Yan Processes

The calculation of higher order Drell-Yan interactions is significantly more complicated than the lowest order calculation. One complication is that we now have a multi-body final state instead of a two-body final state. This complication is overcome in the next-to-leading order (NLO) calculation by splitting the calculation into two two-body pieces: one calculates the process $q + \overline{q} \to \gamma^* + g$ for example, and then calculates the decay of the virtual photon into a lepton pair. Another problem is that the perturbative NLO result (and higher orders) is singular as $Q_T \to 0$ since it contains both infra-red (i.e. very soft gluon radiation) and collinear (i.e. gluon radiation along the quark direction) divergences.

The infra-red and collinear singularities can be removed by the dimensional regularization technique [3] combined with factorization. Dimensional regularization

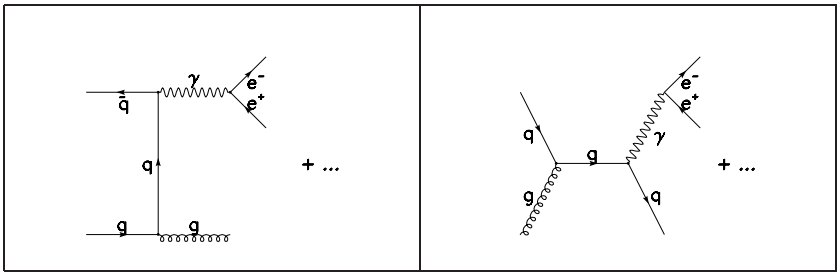

Figure 2.2: Drell-Yan $O(\alpha_s)$ correction Feynman diagrams.

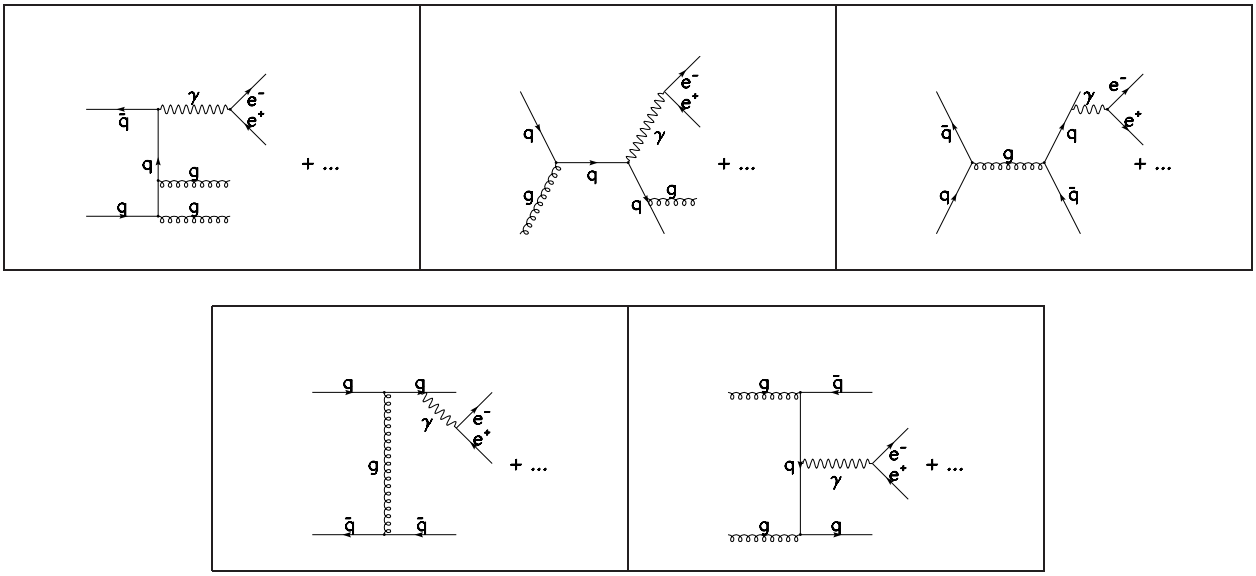

Figure 2.3: Drell-Yan $O(\alpha_s^2)$ correction Feynman diagrams.

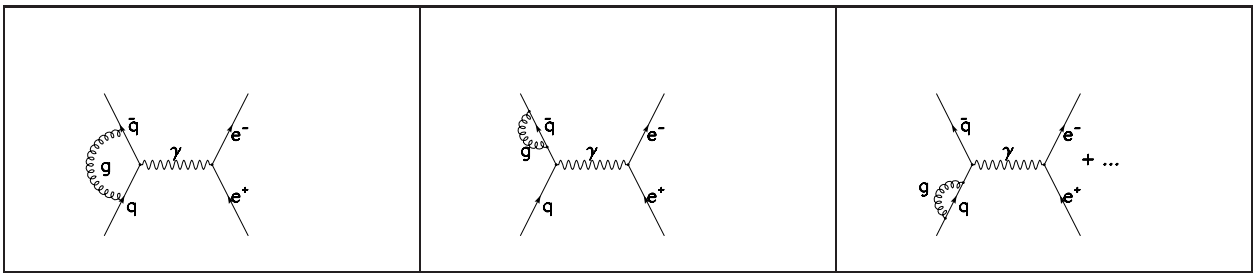

Figure 2.4: Drell-Yan virtual correction Feynman diagrams.

removes the divergence of an integral by allowing one to evaluate the integral in n dimensional space and then analytically continue back to the desired dimensionality. This technique respects gauge invariance and Lorentz invariance provided the integrand is well defined in n dimensions. When calculating cross sections, one prefers to do the calculation as generally as possible. For example, it is desirable to generalize Drell-Yan to the general vector boson cross section since the differences in the cross section for different vector boson types are due mainly to the differences in the γ, Z, and $W^{\pm}$ couplings. Unfortunately, the W coupling contains γ_5 which is ill defined in n dimensions. However, a canonical γ_5 prescription exists that allows one to calculate the anti-symmetrical part of the matrix element in n dimensional space-time [5] [6] [7]. Thus it is possible to perform the general vector boson calculation as desired.

The transverse momentum Q_T distribution of the vector boson cannot be described by the NLO calculation in the low Q_T region. This is because the convergence of the perturbative expansion of the Drell-Yan cross section

$$\frac{d\sigma}{dQ_T^2} = \alpha_V \alpha_s (u_1 + \alpha_s u_2 + \alpha_s^2 u_3 + \alpha_s^3 u_4 + \cdots)$$

deteriorates as $Q_T \to 0$. At first order in α_s the final state gluon or quark balances the Q_T of the vector boson. At second order, an additional jet may be produced and the interference of the one-loop corrections with the first order diagrams appears. It is this interference which, when evaluated at all orders, prevents the divergence of the cross section and yields a physical result. The dominant contributions to the perturbative expansion at low Q_T have the form

$$\frac{d\sigma}{dQ_T^2} \approx \frac{\alpha_s \alpha_V}{Q_T^2} \ln\left(\frac{Q^2}{Q_T^2}\right) \left[v_1 + v_2 \alpha_s \ln^2\left(\frac{Q^2}{Q_T^2}\right) + v_3 \alpha_s \ln^4\left(\frac{Q^2}{Q_T^2}\right) + \cdots \right]$$

where Q^2 is the square of the vector boson mass. This is known as the leading-logarithm approximation to $\frac{d\sigma}{dQ_T^2}$. The convergence of this series is governed by $\alpha_s \ln^2(Q^2/Q_T^2)$ instead of α_s. Thus at low Q_T, $\alpha_s \ln^2(Q^2/Q_T^2)$ will be large even if α_s is small. The logarithms in the above expression result from the infra-red and collinear singularities inherent in each addition of either a real or virtual gluon to the diagrams at each successive order. Both singularities are logarithmic and are effectively cut off by the total Q_T. In addition, the overall factor of $\ln(Q^2/Q_T^2)$ produces a singularity at $Q_T = 0$. This divergence is formally canceled by a negative delta function at the origin. However, one can produce an arbitrarily large cross section by performing an arbitrarily small cut on Q_T. This unphysical result is due to the finite order of the conventional perturbative expansion. At first, it may seem that this would preclude the possibility of performing the calculation to any order, since any order would require the calculation to all orders! However, this is not the case. The coefficients v_i in the leading-log approximation are not independent and may all be expressed in terms of v_1. The summation of this series removes the divergence as $Q_T \to 0$. This prescription is called "resummation", and allows one to perform the calculation to arbitrary order.

The Collins-Soper resummation formalism [8] [9], basically consists of separating the hard-gluon emission and soft-gluon emission pieces of the cross section and "resumming" the soft non-perturbative pieces to all orders in α_s while only calculating the perturbative hard piece to a given order n. The resummation is facilitated by the realization that the soft pieces of the cross section all have a similar α_s and Q^2 dependence which is raised to higher powers at each order. Thus, the sum of the soft pieces can be represented by an exponential function whose argument is called the Sudakov form factor $S(b, Q)$. Here b is the "impact parameter" which is the Fourier transform of the Q_T of the interaction. Thus we see that this problem has two scales, namely Q_T

and Q. Only the result of this calculation will be presented here; the details may be found in the above references. The fully differential inclusive cross section for vector boson production and decay to lepton pairs in hadron-hadron collisions was recently published by C. Balázs, J. Qiu, and C.-P. Yuan [10]. The kinematics of the vector boson V can be expressed in terms of its mass Q, rapidity y, transverse momentum Q_T, and azimuthal angle ϕ_V. The kinematics of the leptons from the vector boson decay can be described in terms of the polar angle θ and azimuthal angle ϕ in the Collins-Soper frame [2]. The resummed fully differential cross section is then given in terms of these quantities by

$$\left(\frac{d\sigma(A+B\to V(\to \ell\overline{\ell'})+X)}{dQ^2dydQ_T^2d\phi_V d\cos\theta d\phi}\right)_{res} = \frac{1}{96\pi^2 S}\frac{Q^2}{(Q^2-M_V^2)^2+M_V^2,\ {}^2_V}$$
$$\times\{\frac{1}{2\pi^2}\int d^2b e^{iq_T\cdot b}\sum_{j,k}\tilde{W}_{jk}(b_*,Q,x_A,x_B,\theta,\phi)F_{jk}^{NP}(b,Q,x_A,x_B)$$
$$+Y(Q_T,Q,x_A,x_B,\theta,\phi)\}$$

where $\tilde{W}_{jk}$ is

$$\tilde{W}_{jk}(b,Q,x_A,x_B,\theta,\phi) = \exp\{-S(b,Q)\}|V_{jk}^2|$$
$$\times\{[(C_{ja}\otimes f_{a/A})(x_A)(C_{\overline{k}b}\otimes f_{b/B})(x_B)+(C_{\overline{k}a}\otimes f_{a/A})(x_A)(C_{jb}\otimes f_{b/B})(x_B)]$$
$$\times(g_L^2+g_R^2)(f_L^2+f_R^2)(1+\cos^2\theta)$$
$$+[(C_{ja}\otimes f_{a/A})(x_A)(C_{\overline{k}b}\otimes f_{b/B})(x_B)-(C_{\overline{k}a}\otimes f_{a/A})(x_A)(C_{jb}\otimes f_{b/B})(x_B)]$$
$$\times(g_L^2-g_R^2)(f_L^2-f_R^2)(2\cos\theta)\}$$

and $\otimes$ denotes the convolution defined by

$$(C_{ja} \otimes f_{a/A})(x_A) \quad = \quad \int_{x_A}^{1} \frac{d\xi_A}{\xi_A} f_{a/A}(\xi_A, \mu) C_{ja}\left(\frac{x_A}{\xi_A}, b, \mu\right)$$

The matrix V_{jk} is the Cabbibo-Kobayashi-Masakawa matrix in the case of $V = \mathrm{W}^{\pm}$ or the identity matrix in the case of $V = \mathrm{Z}, \gamma$ where j represents quark flavors and $\overline{k}$ represents antiquark flavors. Summation over the dummy indices a and b which represent quarks, antiquarks, or gluons is implied in the above expressions. The Sudakov form factor $S(b, Q)$ is given by

$$S(b, Q) \quad = \quad \int_{b_0^2/b^2}^{Q^2} \frac{d\overline{\mu}^2}{\overline{\mu}^2} \left[\ln\left(\frac{Q^2}{\overline{\mu}^2}\right) A(\alpha_s(\overline{\mu})) + B(\alpha_s(\overline{\mu})) \right]$$

The A and B functions and the Wilson coefficients $C_{ja,\overline{k}b,\overline{k}a,jb}$ are given in [9]. After fixing the arbitrary renormalization constants $C_1 = b_0 = 2e^{-\gamma_E}$ (γ_E is the Euler constant) and $C_2 = 1$, $A^{(1)}$, $B^{(1)}$, $A^{(2)}$ and $B^{(2)}$ may be obtained from Eqs. (3.19) to (3.22) in [9]. If the renormalization scale μ is chosen such that $\mu b = C_3 = 2e^{-\gamma_E}$, the Wilson coefficients $C_{ja}^{(1)}$ from [9] eqs. (3.23) to (3.26) for the parity-conserving part of the resummed result are greatly simplified, and are given by

$$C_{jk}^{(1)} = \delta_{jk} \left\{ \frac{2}{3}(1-z) + \frac{1}{3}(\pi^2 - 8)\delta(1-z) \right\} \text{ and } C_{jg}^{(1)} = \frac{1}{2} z(1-z)$$

In addition, the same Wilson coefficients $C_{ja}^{(1)}$ are found to apply to the parity-violating part of the resummed result as well [10].

The integration limits on the impact parameter b are from 0 to ∞ in the expression for the differential cross section. However, for $b \geq b_{max}$ (where $b_{max} = 0.5$ GeV^{-1}

here), the QCD coupling becomes so large that perturbation theory can no longer be used. Therefore the non-perturbative function F^{NP} is necessary and has the form

$$F_{jk}^{NP}(b, Q, Q_0, x_A, x_B) = \exp\left[-ln\left(\frac{Q^2}{Q_0^2}\right)h_1(b) - h_{j/A}(x_A, b) - h_{\overline{k}/B}(x_B, b)\right]$$

where h_1, $h_{j/A}$, and $h_{\overline{k}/B}$ cannot be calculated perturbatively and so must be measured empirically and fit. Also, $\tilde{W}$ is evaluated at b_* where

$$b_* = \frac{b}{\sqrt{1 + (b/b_{max})^2}}$$

so that b_* never exceeds b_{max}.

The Y-term in the differential cross section is given by

$$Y(Q_T, Q, x_A, x_B, \theta, \phi) = \int_{x_A}^{1} \frac{d\xi_A}{\xi_a} \int_{x_B}^{1} \frac{d\xi_B}{\xi_B} \sum_{N=0}^{\infty} \left[\frac{\alpha_s(Q)}{\pi}\right]^N f_{a/A}(\xi_A; Q) R_{ab}^{(N)}(Q_T, Q, z_A, z_B, \theta, \phi) f_{b/B}(\xi_B; Q)$$

where the functions $R_{ab}^{(N)}$ are less singular than $\frac{1}{Q_T^2}\times$ (logs or 1) as $Q_T \to 0$. Figures 2.5, 2.6, 2.7 show the resummed virtual photon cross section vs. mass, transverse momentum, and rapidity.

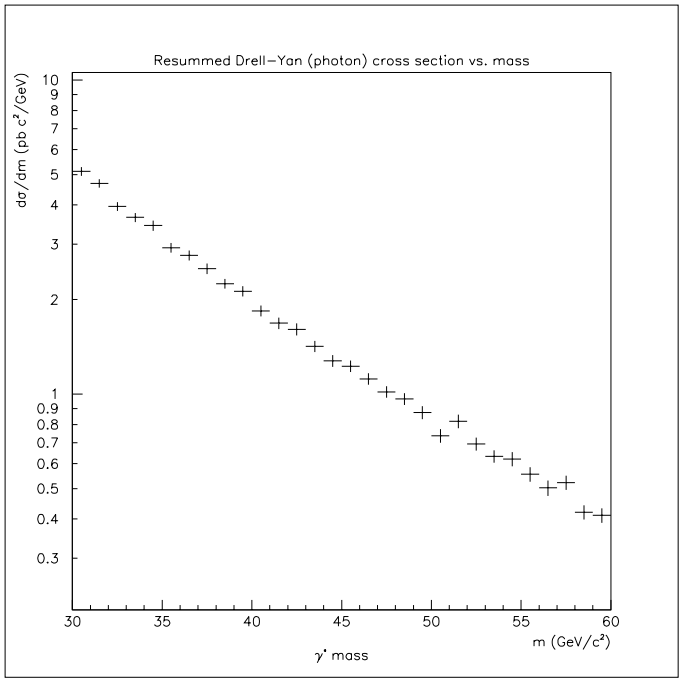

Figure 2.5: Resummed Drell-Yan $d\sigma/dm$.

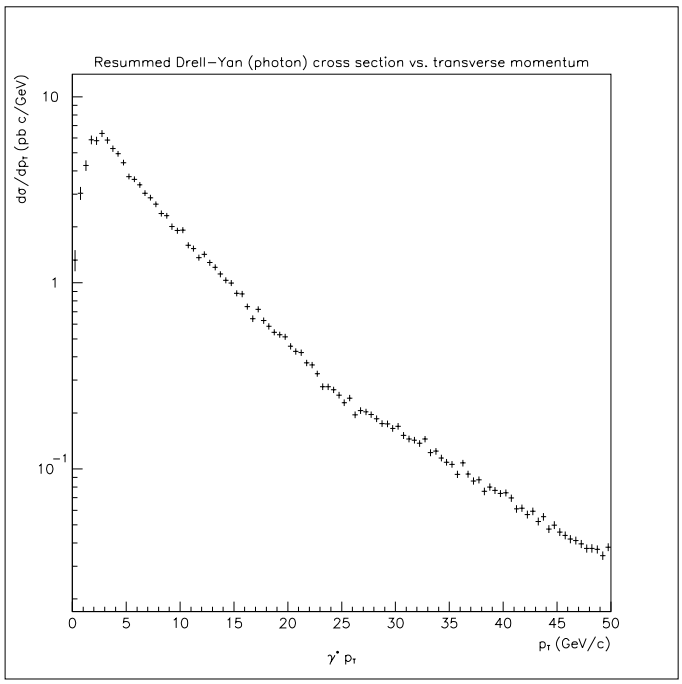

Figure 2.6: Resummed Drell-Yan $d\sigma/dp_T$.

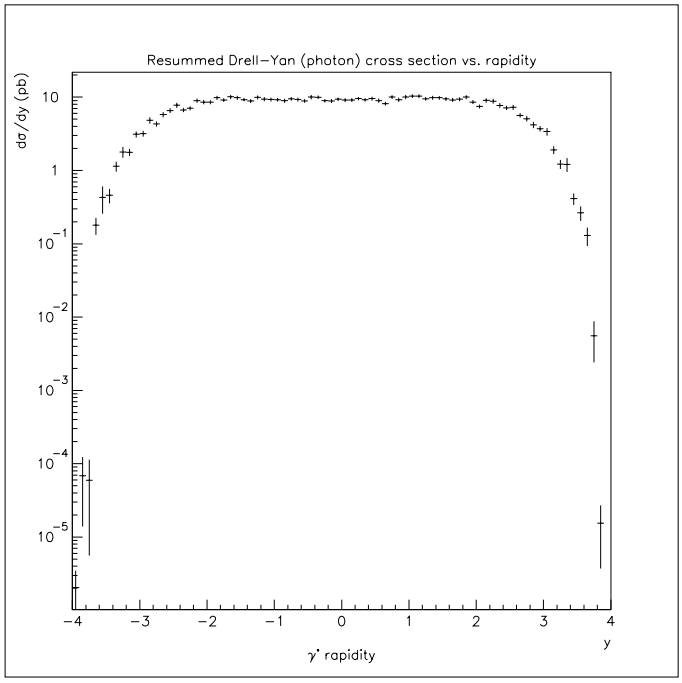

Figure 2.7: Resummed Drell-Yan $d\sigma/dy$.

2.4 Kinematics

The Collins-Soper O' reference frame [2] is the dilepton (virtual boson) rest frame defined as follows: In general, the parton momenta $\vec{k}_a$ and $\vec{k}_b$ are not collinear, hence the z'-axis is chosen such that it bisects the angle θ_{ab} between $\vec{k}_a$ and $-\vec{k}_b$. The polar angle θ is the angle between the lepton momentum $\vec{\ell}'$ and the z'-axis. The azimuthal angle ϕ is measured relative to the transverse unit vector $\hat{q}_T$ that lies in the $(\vec{k}_a, \vec{k}_b)$ plane and is anti-parallel to the direction of $(\vec{k}_a + \vec{k}_b)_T$. Consequently, $\vec{\ell}' \cdot \hat{q}_T = \ell' \sin\theta \cos\phi$. Since the x and y axes are not specified, this notation is covariant under rotations in the O' frame. An illustration of this reference frame is shown in Figure 2.8.

Note that the definition of the z'-axis is somewhat arbitrary. Its orientation is chosen by assuming that on the average, the incoming partons have equal transverse momenta, which should be roughly correct when many events are averaged. However,

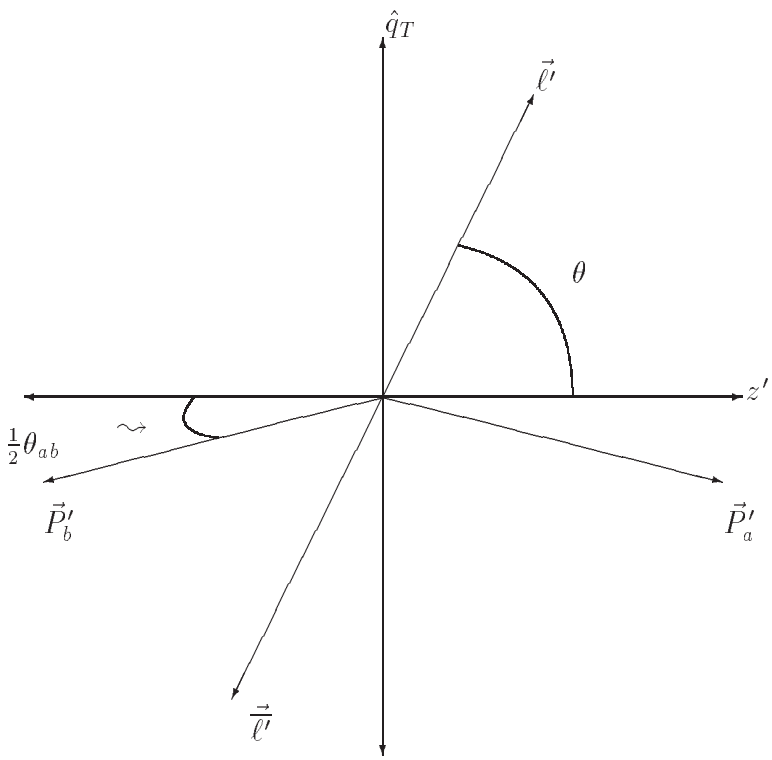

Figure 2.8: The Collins-Soper O' reference frame.

since the transverse momentum of the incoming partons is unknown, this reference frame does not coincide with the center of momentum reference frame of the partons on an event-by-event basis. The notation used here follows the notation used in [2] and is shown in Table 2.3.

2.4.1 Lowest Order Kinematics

The kinematics of the lowest order Drell-Yan process are very straight-forward to calculate. In this "naive" Drell-Yan model, the transverse momenta of the incoming partons is zero, and thus the Lorentz transformation between the lab and center of momentum frames is well defined and is along the $z = z'$ axis. Thus the O' frame does coincide with the cm frame of the partons in this special case. The parton longitudinal momentum fractions are defined as

Table 2.3: Definition of mathematical notation.

Notation	
lab	Center of momentum frame of P_a^μ and P_b^μ
O'	Collins-Soper Frame
P_a^μ	proton beam 4-momentum in lab frame
$P_a^{\mu\prime}$	proton beam 4-momentum in O' frame
P_b^μ	antiproton beam 4-momentum in lab frame
$P_b^{\mu\prime}$	antiproton beam 4-momentum in O' frame
k_a^μ	parton from hadron a 4-momentum in lab frame
$k_a^{\mu\prime}$	parton from hadron a 4-momentum in O' frame
k_b^μ	parton from hadron b 4-momentum in lab frame
$k_b^{\mu\prime}$	parton from hadron b 4-momentum in O' frame
ℓ^μ	lepton 4-momentum in lab frame
$\ell^{\mu\prime}$	lepton 4-momentum in O' frame
$\overline{\ell^\mu}$	antilepton 4-momentum in lab frame
$\overline{\ell^\mu}'$	antilepton 4-momentum in O' frame
$q^\mu = (q^0, Q_T, 0, q^3)$	γ^* 4-momentum in lab frame
$q^{\mu\prime} = (m, 0, 0, 0)$	γ^* 4-momentum in O' frame
$\sqrt{S}$	center of mass energy of beams in lab frame
m	mass of γ^*
v_T	transverse component of vector $\vec{v}$
v_z	longitudinal component of vector $\vec{v}$
θ	angle between $\vec{l}'$ relative to z' axis in O' frame
θ_{ab}	angle between $\vec{P}_a'$ and $\vec{P}_b'$ in O' frame
x_a	fraction of proton momentum carried by interacting parton
x_b	fraction of antiproton momentum carried by interacting parton
τ	unit-less "mass fraction" parameter

$x_a = \frac{k_a^3}{P_a^3}$

$x_b = \frac{k_b^3}{P_b^3}$

and it can be shown that

$m^2 = x_a x_b S$

$\tau = \frac{m^2}{S} = x_a x_b$

$q^3 = \frac{\sqrt{S}(x_a - x_b)}{2} = p_{cm} =$ z boost from O' to lab

$q^0 = \frac{\sqrt{S}(x_a + x_b)}{2} =$ energy of vector boson in lab

$\beta_{cm} = \frac{(x_a - x_b)}{(x_a + x_b)} = \frac{\vec{q}}{q^0}$

$\gamma_{cm} = \frac{(x_a + x_b)}{2\sqrt{x_a x_b}}$

Using the above values for γ_{cm} and β_{cm} we can write down the Lorentz transformations between the lab and O' frames.

$$\Lambda_{lab \to O'} = \begin{pmatrix} \gamma_{cm} & 0 & 0 & -\gamma_{cm}\beta_{cm} \\ 0 & 1 & 0 & 0 \\ 0 & 0 & 1 & 0 \\ -\gamma_{cm}\beta_{cm} & 0 & 0 & \gamma_{cm} \end{pmatrix}$$

$$\Lambda_{O' \to lab} = \begin{pmatrix} \gamma_{cm} & 0 & 0 & \gamma_{cm}\beta_{cm} \\ 0 & 1 & 0 & 0 \\ 0 & 0 & 1 & 0 \\ \gamma_{cm}\beta_{cm} & 0 & 0 & \gamma_{cm} \end{pmatrix}$$

We can also write down the 4-vectors of the vector boson in the lab and O' frames

$$q^\mu = \begin{pmatrix} q^0 \\ 0 \\ 0 \\ q^3 \end{pmatrix}, \qquad q^{\mu\prime} = \begin{pmatrix} m \\ 0 \\ 0 \\ 0 \end{pmatrix}$$

and using energy and momentum conservation, we know that

$\ell_T{}' = -\overline{\ell_T}'$

$\ell^{3\prime} = -\overline{\ell^3}'$

$\ell^{0\prime} = \overline{\ell^0}'$

By definition,

$q^{0\prime} = m = Q$

so

$\ell^{0\prime} = \overline{\ell^0}' = \frac{m}{2} = \frac{1}{2}\sqrt{Sx_a x_b}$

If we assume that the leptons are massless (this is certainly a valid approximation for electrons at FNAL) then

$(\ell^{0\prime})^2 = (\ell_T{}')^2 + (\ell^{3\prime})^2$

$\frac{m^2}{4} = (\ell_T{}')^2 + (\ell^{3\prime})^2$

$\tan(\theta) = \frac{\ell_T{}'}{\ell^{3\prime}} = \frac{\overline{\ell_T}'}{\overline{\ell^3}'}$

so

$(\ell^{3\prime})^2 \tan^2(\theta) = \frac{m^2}{4} - (\ell^{3\prime})^2$

which gives

$(\ell^{3\prime})^2 = \frac{m^2}{4(1+\tan^2(\theta))}$ $(\ell_T{}')^2 = \frac{m^2 \tan^2(\theta)}{4(1+\tan^2(\theta))}$

so we have

$\ell^{3\prime} = -\overline{\ell^3}' = \frac{m\cos(\theta)}{2}$

$\ell_T{}' = -\overline{\ell_T}' = \frac{m\sin(\theta)}{2}$

putting m in terms of x_a, x_b and S yields

$\ell^{3\prime} = -\overline{\ell^3}' = \frac{1}{2}\sqrt{Sx_a x_b}\cos(\theta)$

$\ell_T{}' = -\overline{\ell_T}' = \frac{1}{2}\sqrt{Sx_a x_b}\sin(\theta)$

Since $Q_T = 0$ for the lowest order Drell-Yan process, the lepton angular distribution has no ϕ dependence (the distribution is flat in ϕ). Consequently, we may arbitrarily choose $\phi = 0$ since the Lorentz transformation between lab and O' frames leaves ϕ invariant. Thus, using this choice of ϕ, the lepton 4-vectors in the O' frame are

$$\ell^{\mu\prime} = \frac{1}{2}\sqrt{Sx_a x_b}\begin{pmatrix} 1 \\ \sin(\theta) \\ 0 \\ \cos(\theta) \end{pmatrix}$$

$\overline{\ell^{\mu}}' = g^{\mu}_{\nu}\ell^{\mu\prime}$

where g^{μ}_{ν} is the Bjorken-Drell metric.

Given the above lepton 4-vectors in the O' frame and the Lorentz transformation from the O' frame to the lab frame we can also write down the lepton 4-vectors in the lab frame in terms of the O' frame variables, namely

$$\ell^{\mu} = \frac{\sqrt{S}}{4}\begin{pmatrix} (x_a + x_b) + (x_a - x_b)\cos(\theta) \\ 2\sqrt{x_a x_b}\sin(\theta) \\ 0 \\ (x_a - x_b) + (x_a + x_b)\cos(\theta) \end{pmatrix}$$

$$\overline{\ell^{\mu}} = \frac{\sqrt{S}}{4}\begin{pmatrix} (x_a + x_b) - (x_a - x_b)\cos(\theta) \\ -2\sqrt{x_a x_b}\sin(\theta) \\ 0 \\ (x_a - x_b) - (x_a + x_b)\cos(\theta) \end{pmatrix}$$

Other useful kinematic quantities include the lepton rapidities y_{ℓ}, $y_{\overline{\ell}}$ and vector boson rapidity y_{γ^*} in the lab frame. The rapidity of a particle is defined as

$y = \frac{1}{2}\ln(\frac{E+p_z}{E-p_z})$

Since we now know the lepton and vector boson 4-vectors we can immediately write down their rapidities

$y_{\gamma^*} = \frac{1}{2}\ln(\frac{x_a}{x_b})$

$y_{\ell} = y_{\gamma^*} + \frac{1}{2}\ln(\frac{1+\cos(\theta)}{1-\cos(\theta)})$

$y_{\overline{\ell}} = y_{\gamma^*} + \frac{1}{2}\ln(\frac{1-\cos(\theta)}{1+\cos(\theta)})$

Given the above rapidities we see that we can neatly write the vector boson rapidity in terms of the lepton rapidities

$y_{\gamma^*} = \frac{1}{2}(y_{\ell} + y_{\overline{\ell}})$

In addition, it is evident from the above that the angle θ in the O' frame may be conveniently expressed in terms of the difference of the lepton rapidities $\Delta y_{\ell\overline{\ell}} = y_{\ell} - y_{\overline{\ell}}$

$\cos(\theta) = \tanh(\Delta y_{\ell\overline{\ell}})$

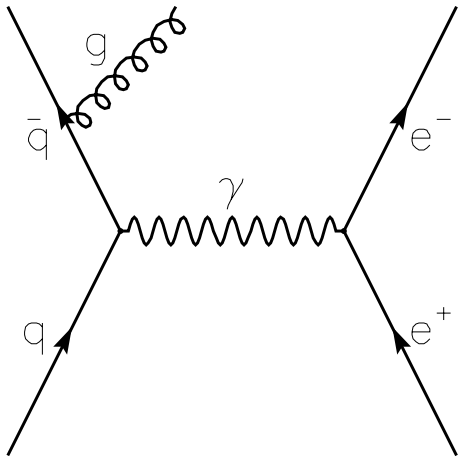

Figure 2.9: Gluon Bremsstrahlung

Finally, we wish to write the parton momentum fractions x_a and x_b in terms of the lepton momenta in the lab frame. This can be readily accomplished using the various kinematic quantities given in the above discussion

$x_a = \frac{1}{\sqrt{S}}(\ell^0 + \overline{\ell^0} + \ell^3 + \overline{\ell^3})$

$x_b = \frac{1}{\sqrt{S}}(\ell^0 + \overline{\ell^0} - \ell^3 - \overline{\ell^3})$

we can also put x_a and x_b in terms of the vector boson momenta

$x_a = \frac{2}{\sqrt{S}}(q^0 + q^3)$

$x_b = \frac{2}{\sqrt{S}}(q^0 - q^3)$

Similarly, the angle θ may be expressed in terms of the lepton momenta

$\cos(\theta) = \frac{\ell^0 - \overline{\ell^0}}{\ell^3 + \overline{\ell^3}}$

2.4.2 Higher Order Kinematics

The process shown in Figure 2.9 is an example of a higher order Drell-Yan process.

One would like to be able to calculate the initial x_a and x_b of the incoming quarks as was done for the lowest order Drell-Yan process, but this requires knowledge of the energy carried off by the gluon. Before the gluon bremsstrahlung the quark and antiquark momenta are

$$k_b^\mu = \begin{pmatrix} \frac{x_a\sqrt{S}}{2} \\ 0 \\ 0 \\ \frac{x_a\sqrt{S}}{2} \end{pmatrix}, \qquad k_b^\mu = \begin{pmatrix} \frac{x_b\sqrt{S}}{2} \\ 0 \\ 0 \\ -\frac{x_b\sqrt{S}}{2} \end{pmatrix}$$

The quarks are assumed to have no intrinsic k_T here. After the gluon bremsstrahlung, we can write the fraction of the proton momentum carried away by the gluon as

$x_g = \frac{|\vec{p_{gluon}}|}{|\vec{P_A}|+|\vec{P_B}|} = \frac{E_{gluon}}{\sqrt{S}}$

Since we assume here that the gluon is the sole source of the quark and antiquark transverse momentum and that the quarks are massless and on shell, then if we choose the $\hat{Q}_T$ axis along the x axis ($\phi = 0$) the quark momenta are given by

$$\tilde{k_a^\mu} = \begin{pmatrix} \frac{1}{2}(x_a - x_g)\sqrt{S} \\ \frac{1}{2}Q_T \\ 0 \\ \frac{1}{2}\sqrt{(x_a - x_g)^2 S - Q_T^2} \end{pmatrix}, \qquad \tilde{k_b^\mu} = \begin{pmatrix} \frac{1}{2}(x_b - x_g)\sqrt{S} \\ \frac{1}{2}Q_T \\ 0 \\ -\frac{1}{2}\sqrt{(x_b - x_g)^2 S - Q_T^2} \end{pmatrix}$$

where we have followed the Collins-Soper prescription of dividing the Q_T equally among the quark and antiquark. The momentum of the vector boson is then

$$q^\mu = \begin{pmatrix} \frac{1}{2}(x_a + x_b - 2x_g)\sqrt{S} \\ Q_T \\ 0 \\ \frac{1}{2}\sqrt{(x_a - x_g)^2 - Q_T^2} - \frac{1}{2}\sqrt{(x_b - x_g)^2 - Q_T^2} \end{pmatrix}$$

and the mass of the vector boson is given by

$$\begin{aligned} m^2 &= \frac{1}{4}(x_g^2 - x_a x_g - x_b x_g - x_a x_b)S - \frac{1}{2}Q_T^2 + \\ &\quad \frac{1}{2}\sqrt{(x_a - x_g)^2(x_b - x_g)^2 S^2 + Q_T^4 - ((x_a - x_g)^2 + (x_b - x_g)^2)Q_T^2 S} \end{aligned}$$

The above parameterization in terms of x_g is fairly general although it was derived from the specific case of a single gluon bremsstrahlung. If we instead define x_g as the fraction of energy radiated prior to the quark-antiquark annihilation, the above equations still hold true. In principle one can use the above quantities to solve for x_a and x_b provided one knows x_g. Unfortunately, it is very difficult to measure the energy of the initial state radiation since it is often small and the radiated particles escape down the beam pipe. Also, the above does not take into account any intrinsic transverse momentum of the quark or antiquark or final state interactions.

The kinematics of the vector boson and its subsequent decay into lepton pairs are predicted by the resummed cross section given in Section 2.3 and are calculated in [10]. They are given in the lab frame by

$$\ell^\mu = \frac{Q}{2}\left(\frac{q^\mu}{Q} + X^\mu \sin\theta\cos\phi + Y^\mu \sin\theta\sin\phi + Z^\mu\cos\theta\right)$$

where

$$\begin{aligned}
q^\mu &= (M_T\cosh y, Q_T\cos\phi, Q_T\sin\phi, M_T\sinh y) \\
X^\mu &= -\frac{Q}{Q_T M_T}\left(q_+ n^\nu + q_- \overline{n}^\nu - \frac{M_T^2}{Q^2}q^\mu\right) \\
Y^\mu &= \epsilon^{\mu\nu\alpha\beta}\frac{q_\nu}{Q}Z_\alpha X_\beta \\
Z^\mu &= \frac{1}{M_T}(q_+ n^\nu - q_- \overline{n}^\nu)
\end{aligned}$$

and $q_\pm = \frac{1}{\sqrt{2}}(q^0 \pm q^3)$, $M_T = \sqrt{Q^2 + Q_T^2}$, $n^\nu = \frac{1}{\sqrt{2}}(1,0,0,1)$, and $\overline{n}^\nu = \frac{1}{\sqrt{2}}(1,0,0,-1)$.

2.5 Summary

Annihilating quarks radiate gluons just as electrically charged particles radiate photons when accelerated. Gluon radiation increases as the time $(1/Q)$ available for the annihilation decreases. Consequently, since gluons carry away transverse momentum, the width of the Q_T distribution of the vector boson must increase. Hence, for an accurate comparison of theory and experiment for the Q_T distribution of the Drell-Yan interaction it is necessary to take into account the effect of multiple soft-gluon emission on the Q_T distribution. The resummation prescription provides a theoretical means to this end.

The resummation calculation is necessary to properly describe the low Q_T regime of the Drell-Yan process. At high Q_T, the standard perturbation method is adequate. An overlap region exists however, where it is necessary to match the low Q_T and high Q_T results. The energy boundaries of this overlap region depend on the Q of the interaction. One could arbitrarily choose some Q_T cut in this region and use one result above and the other below the cut, but the resulting relative error in this method is formally $O(\alpha^2 \ln^4(1/\alpha_s^2))$. By properly matching the resummation calculation with the conventional perturbative result however, the relative error can be reduced to $O(\alpha_s^2)$ [13].

The theoretical techniques required to perform the resummation calculation are fairly complex, but are available in the literature. Fortunately for experimentalists wishing to test the theory, C.-P. Yuan and C. Balázs have recently written a Monte Carlo event generator called RESBOS [15] which includes the resummation calculation. This makes comparison between theory and experiment significantly easier since it allows one to easily make the cuts required by experimental analysis on the theoretical results.

Since the RESBOS Monte Carlo program has only recently been available, other Monte Carlo event generators were also used for various aspects of this analysis. The ISAJET [14] event generator was used extensively. ISAJET includes the NLO perturbative calculation but produces the low Q_T portion of the distribution in a more empirical manner. The basic method is to calculate the hard scattering and then "evolve backwards" by radiating quarks and gluons and adjusting the momenta of the initial state particles up to some cutoff supplied by the user. The choice of this cutoff makes a noticeable effect on the Drell-Yan Q_T distribution. A comparison between the RESBOS resummed Q_T distribution and the ISAJET result is shown in 2.10. The Q_T distributions from RESBOS and ISAJET are clearly different, however the integrated cross sections from both Monte Carlos agree to within a few percent. The parton distributions used in the RESBOS MC are the CTEQ3M distributions; for ISAJET, the CTEQ2L distributions were used (the CTEQ3 parton distributions are not yet available in ISAJET). However, the parton distribution differences are not the source of the large differences between the Q_T spectra of these two Monte Carlos, rather it is the empirical manner in which ISAJET generates the Q_T distribution. It may be possible to tune the ISAJET parameters which control the Q_T distribution to reproduce the RESBOS result, but this has not been done. Thus it is preferable to use the RESBOS Monte Carlo where possible since it uses the full resummation formalism to produce the Q_T distribution.

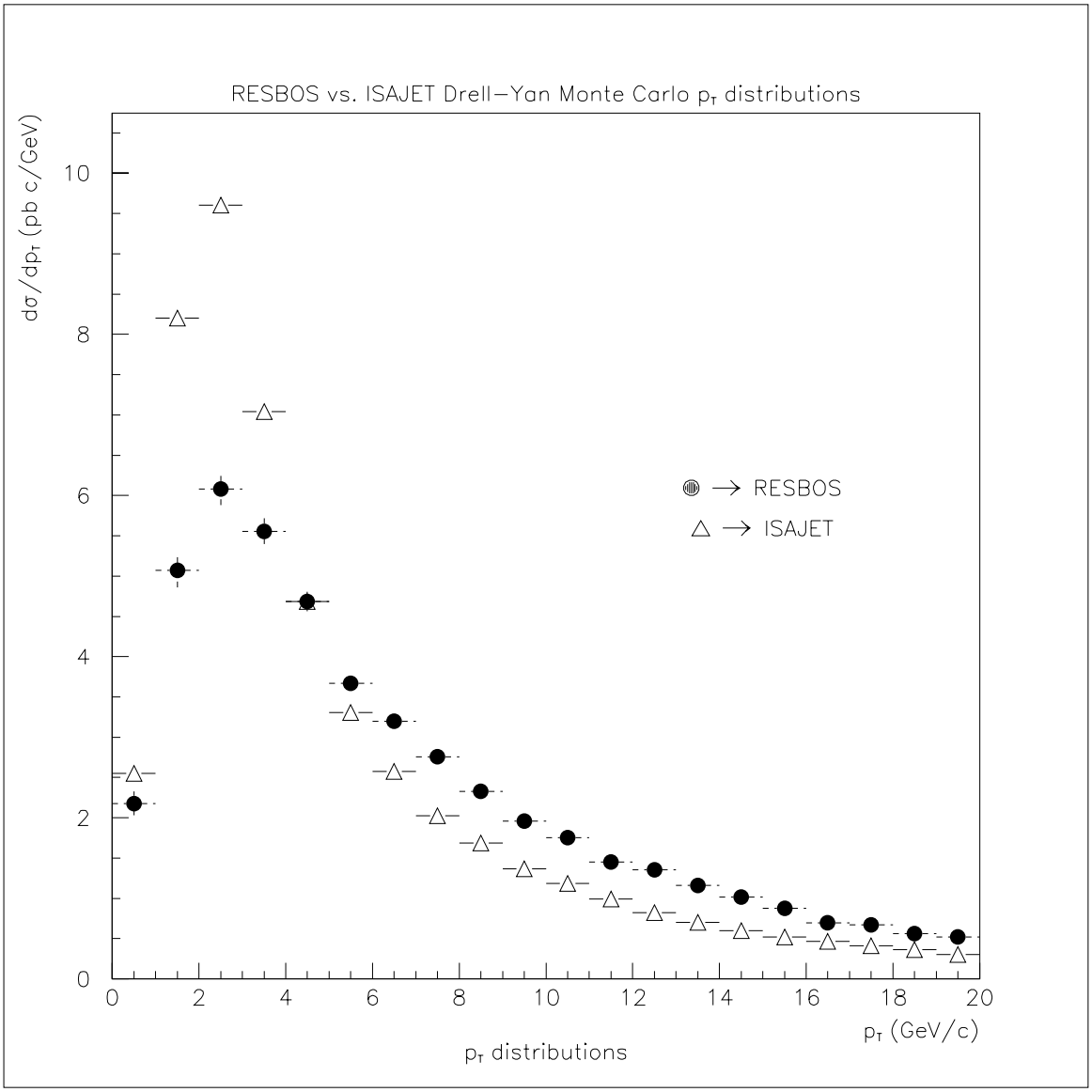

Figure 2.10: Comparison of RESBOS and ISAJET p_T spectra.

Chapter 3

APPARATUS

3.1 The Accelerator

The accelerator facility at Fermi National Accelerator Laboratory is currently the highest energy accelerator in the world, capable of colliding protons (p's) on anti-protons ($\bar{p}$'s) with a center of mass energy ($\sqrt{s}$) of 1.8 trillion electron volts (1.8 TeV). It is comprised of several stages:

- The Cockcroft-Walton.
- The Linac.
- The Booster.
- The Main Ring.
- The Tevatron.
- The Antiproton Storage Ring.

The accelerator is capable of operating in two modes, fixed target mode and collider mode. DØ has used both modes: fixed target mode for test beam studies of our detector components in the NWA (Neutrino West A) experimental hall and collider

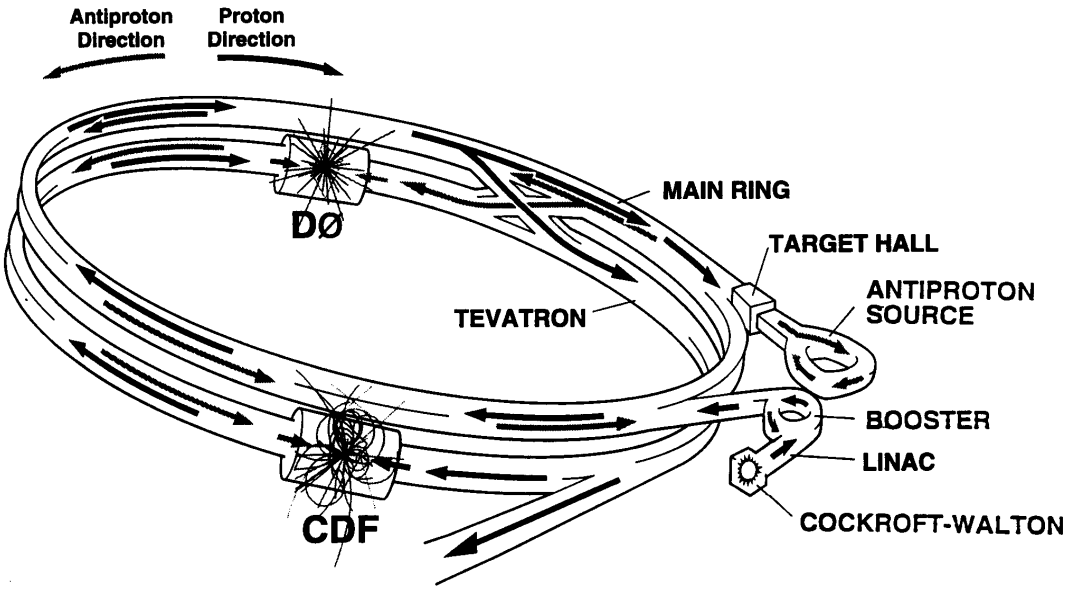

Figure 3.1: The Fermilab Tevatron Collider.

mode for actual physics data taking. A schematic of the accelerator systems can be seen in Figure 3.1.

The operation of the accelerator in fixed target mode is as follows. Electrons are added to hydrogen atoms to make negative hydrogen ions and accelerated to an energy of 750 thousand electron volts (750 keV) in the Cockcroft-Walton accelerator.

The negatively charged hydrogen ions are then injected into a 500 foot long linear accelerator called the Linac. Here an alternating electric field is applied to nine drift tubes which are spaced further and further apart as the ions travel down the Linac. The fields are varied such that the ions are hidden in the drift tubes when the field is in a direction that would slow them down and emerge into the gaps between the tubes when the field is in the proper direction to accelerate them. The Linac accelerates the ions to an energy of 400 million electron volts (400 MeV). After leaving the Linac the hydrogen ions pass through a carbon foil which strips off the electrons leaving a bare positively charged proton.

The 400 MeV protons are then injected into the Booster. The Booster is a rapidly cycling synchrotron 500 feet in diameter. In it, the protons are accelerated by electric fields many times while being forced to travel in a circular path by a magnetic field. The magnetic field is ramped up to maintain the protons' orbit within the Booster since as the protons gain energy from the electric fields they require a stronger magnetic field keep them contained in the Booster. The protons travel around the Booster approximately 20,000 times which accelerates them to an energy of 8 billion electron volts (8 GeV). The Booster typically cycles twelve times in rapid succession injecting twelve bunches of protons into the Main Ring for the next stage of acceleration.

The Main Ring, like the Booster, is also a synchrotron, but is approximately 4 miles in circumference. A ten foot diameter tunnel buried 20 feet below the Illinois prairie west of Chicago houses the 1,000 conventional copper coil dipole magnets that make up the Main Ring. The p's travel through the main ring and are accelerated by radio frequency cavities (RF cavities) as the magnetic fields are ramped up to maintain the orbit. The RF cavities contain RF electromagnetic (EM) fields which are synchronized such that when the proton bunch enters a cavity, the EM pulse builds up behind it and the protons "surf" on the EM wave. The Main Ring accelerates the protons to 150 GeV.

The 150 GeV protons are then extracted from the Main Ring and injected into the Tevatron. The Tevatron is housed in the same underground tunnel that holds the Main Ring and is the same diameter, but it is made up of 1,000 superconducting dipoles. The Tevatron resides directly underneath the Main Ring and gets its name from its ability to accelerate protons to nearly 1 TeV. There are also quadrupole magnets in the Tevatron and Main Ring which focus the beam to maintain the protons bunches' transverse dimensions. The superconducting magnets must be cooled to about -450 F in order to operate, which requires a vast cryogenic system. If a superconducting

magnet drops out of the superconducting phase while in operation, the large currents necessary to create the 2 Tesla fields that steer the proton bunches around the ring create an immense amount of heat. Dumping all this heat into liquid helium causes it to immediately turn to gas which must be vented. This is known as a quench, and makes a very loud *whoosh* if one is standing near one of the vents when it occurs. Thankfully it does not occur very often. Under normal operation the protons are accelerated to 900 GeV in the Tevatron.

The Tevatron is the last stage of acceleration for the protons. During fixed target operation the 900 GeV protons are extracted from the Tevatron via a switch-yard that steers the bunches down the various experimental beam-lines. These beam-lines contain additional transfer apparatus such as dipoles and quadrupoles, as well as other elements such as targets and mass selectors, to create secondary and even tertiary beams of electrons, pions, muons, neutrinos, etc... which the experimentalists use to perform various physics experiments or for calibration and testing purposes.

Collider mode operation at Fermilab is the same as fixed target mode up to the Tevatron stage. Running in collider mode requires a source of antiprotons which are created by extracting 120 GeV protons from the Main Ring and slamming them into a target to create antiprotons in the same fashion that other desired particles are created in the experimental beam-lines in fixed target mode. The antiprotons produced are then collected and injected into the Debuncher ring where they are reduced in size by a method known as stochastic cooling. The antiprotons are then transferred to the Accumulator for storage. The combination of Debuncher and Accumulator make up the Antiproton Storage Rings. Accumulating the antiprotons is known as "stacking" and when the antiproton stack is large enough, six bunches of antiprotons are accelerated via the Main Ring and Tevatron to 900 GeV. The protons and antiprotons circulate in opposite directions in the Main Ring and Tevatron due to their opposite charges.

The antiproton injection phase of colliding mode operation is the most critical since it takes many hours to accumulate the antiprotons and if they are lost much time and money is wasted. Approximately 10^7 $\bar{p}$'s can be produced from each batch of 1.8×10^{12} p's.

In collider mode operation, six bunches of protons and anti-protons circulate around the ring simultaneously. The particle bunches are focused into head-on collisions at interaction regions which are surrounded by detectors that measure properties of the particles produced in the collisions. One advantage of a collider is that much higher center of momentum energies are obtainable than in a fixed target accelerator. At the Tevatron, each particle beam (proton and antiproton) is a 900 GeV beam, giving a center of mass energy of $\sqrt{s} = 1.8$ TeV. If instead, a 900 GeV $\bar{p}$ beam were incident on a fixed p target, the center of mass energy would be only 42 GeV. Thus the energy available for producing new particles in fixed target mode is much lower than in collider mode.

Another advantage of a $p\bar{p}$ collider is that if the p and $\bar{p}$ bunches can be kept separated, the same accelerator can be used to accelerate both types of particles simultaneously, thus avoiding the need for a separate accelerator for each type of particle. This method reduces the overall cost of construction and operation of the collider and is in fact what is used at Fermilab.

The the number of interactions of a given type that can be produced in a given time is directly proportional to the luminosity of an accelerator, where the constant of proportionality is the cross section of the given interaction.

$N_i = \sigma_i \int L dt$

Thus for a fixed length data run, the luminosity of the accelerator determines how many reactions of a given type will occur since the cross section for the reactions is

fixed by nature (and is often what is to be determined). The instantaneous luminosity of a $p\bar{p}$ collider is given by the formula

$$L = fn\frac{N_p N_{\bar{p}}}{A}$$

where f is the revolution frequency, n is the number of proton (antiproton) bunches in the collider, A is the cross-sectional area of the beams, N_p is the number of protons per bunch and $N_{\bar{p}}$ is the number of antiprotons per bunch. The Fermilab Accelerator Division is responsible for the optimization of these variables in order to provide the highest possible luminosity. The instantaneous luminosity record for run 1A was $L \approx 1 \times 10^{31}\text{cm}^{-2}s^{-1}$.

There are four interaction regions available: B0, C0, D0, and E0, two of which are currently in use. B0 is home to CDF (Collider Detector Facility at Fermilab) and D0 is home to the DØ Detector.

3.2 The DØ Detector

3.2.1 Overview

The DØ detector [16] is a general purpose detector. The design goals were to provide excellent calorimetric energy and position resolution, good electron and muon identification, good measurement of parton jets, and good missing E_T and scalar E_T measurement. The primary physics goals of the DØ experiment are to study high mass states and high p_T phenomena. The design of the experiment was based on the fact that new phenomena usually have relatively large branching ratios into leptons whereas the background processes do not. Also parton jets are generally of greater interest in studying the underlying physics processes than are the individual hadrons of which they are comprised. A cut-away isometric view of the DØ detector is shown in Figure 3.2.

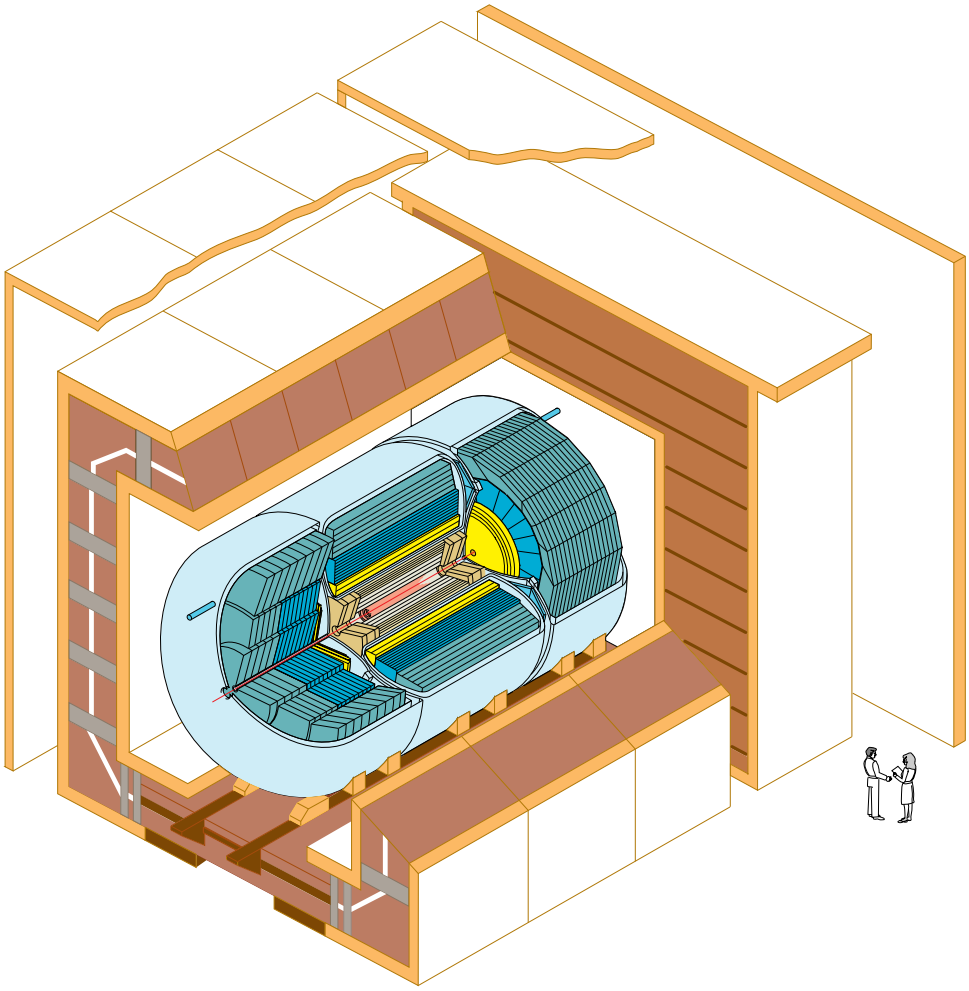

Figure 3.2: An isometric cut-away view of the DØ detector.

The DØ detector consists of three major detector components:

- A highly hermetic, finely segmented calorimeter constructed of depleted uranium and liquid argon with unit gain, which is thick and radiation hard.
- A compact tracking system which has fairly good spatial resolution and no central magnetic field.
- Muon detectors surrounding a thick magnetized iron toroid which allow adequate momentum measurement while minimizing backgrounds from hadron punch-through.

In addition, a programmable, high performance triggering and data acquisition system provides a means of reducing the overall event rate by selecting the most interesting events; detecting beam crossings and monitoring the luminosity at D0; and providing facilities for writing the selected event data to magnetic tape.

The DØ coordinate system is a right-handed coordinate system with the positive z-axis pointing the proton direction and the positive y-axis pointing upward (away from the center of the earth). The angles ϕ and θ are the azimuthal and polar angles respectively with $\theta = 0$ along the proton direction. The cylindrical r-coordinate is the perpendicular distance from the z-axis (beams). The pseudo-rapidity, $\eta = -ln(\tan(\theta/2))$, is approximately equal to the rapidity $y = \frac{1}{2}ln((E+p_z)/(E-p_z))$, in the limit $(m/E) \rightarrow 0$.

3.2.2 The Central Detector (CD)

The DØ central detector is made up of the tracking detectors and the transition radiation detector. The separate detectors are, moving radially outward: (i) the vertex tracking chamber (VTX), (ii) the transition radiation detector (TRD), (iii) the central

drift chamber (CDC), and (iv) two forward drift chambers (FDC) which cap the CD on either end.

The VTX, TRD, and CDC detectors cover the large angle region of roughly $-1.2 \leq \eta \leq 1.2$, and are oriented parallel to the beam-line. The FDCs are oriented perpendicular to the beam. The volume of the CD suite of detectors is bounded by $r = 78$ cm and $z = \pm 135$ cm and is surrounded by the calorimeters. The transition between the VTX-TRD-CDC cylinder and the FDC detectors is matched to the transition between the central and end cap calorimeters. The FDC detectors cover the small angle regions of approximately $1.5 \leq |\eta| \leq 2.5$.

Due to the absence of a central magnetic field in DØ , the primary design goals for the CD were resolution of closely spaced tracks, high tracking finding efficiency, and good ionization energy measurement to allow differentiation between single charged particles and photon conversions. The purpose of the TRD was to allow further discrimination between charged hadrons and electrons.

The size of the CD drift cells were chosen so that the drift time matched the Tevatron bunch crossing time interval of 3.5 μs. A flash analog-to-digital conversion (FADC) system is used for signal digitization with a charge sampling time interval of $\sim$ 10 ns. This provides for good two track resolving power and gives an effective detector segmentation of 100-350 μm. The vertex z position is measured in DØ using a combination of methods in the CD detectors. These include charge division in the VTX, helical cathode pads in the TRD, and delay lines in the CDC and FDC.

The Vertex Drift Chambers (VTX)

The innermost tracking detector in DØ is the vertex chamber [18, 20]. The inner radius is 3.7 cm and the outer radius is 16.2 cm. It is comprised of three concentric, mechanically independent cell layers made of carbon fiber tubes. Eight sense wires

measure the $r - \phi$ coordinate in each cell. The innermost cell layer consists of 16 cells and the outer two layers are made up of 32 cells each. The carbon fiber tubes whose volumes define the gas volumes have 1 mil thick Al traces on a multi-layer epoxy/Kapton laminate on their surfaces (carbon fiber tube at ground) which provide coarse field shaping for the cells. A coat of resistive epoxy covering the traces prevents charge buildup. The cells are defined by grid of field shaping wires held at ground on either side of the sense wires and which line up with the coarse field shaping traces. Together with the field shaping wires, planes of cathode wires provide a uniform drift field region.

Left-right ambiguities were resolved by staggering adjacent wires by $\pm$ 100 μm in each cell. The three radially adjacent cells are offset in ϕ to help in pattern recognition and calibration.

The sense wires are made of 25 μm NiCoTin [21] at 80 g tension and are read out at both ends to measure the z coordinate of a hit via charge division. The resistivity of the sense wires is 1.8 kΩ/m. The grid and cathode wires are made of 152 μm gold-plated aluminum at a tension of 360 g. A more detailed description of the electrostatic properties of the VTX may be found in [17].

To obtain good spatial resolution and track pair resolving power, the gas mixture chosen for the VTX was 95% CO_2 plus 5% ethane at 1 atm with a small admixture of H_2O. The average drift velocity under normal DØ operating conditions ($< E > \approx$ 1 kV/cm) is about 7.3 μm/ns. Gas gain at the sense wires is about 4×10^4. An addition of 0.5% H_2O to the gas helps stabilize VTX operation in a high radiation environment.

The Transition Radiation Detector (TRD)

Highly relativistic particles ($\gamma > 10^3$) produce X-ray transition radiation when crossing boundaries between materials with differing dielectric constants [22]. The amount of energy produced by these particles depends on the Lorentz γ which provides a means to discriminate between electrons and other heavier charged particles such as pions.

The DØ TRD is made up of three separate units, each containing a radiator and a detection chamber. The radiator section of each unit is composed of 393 layers of 18 μm thick polypropylene foil in a volume filled with nitrogen gas. The mean distance between the foil layers is 150 μm with a variation of about 150 μm. The gaps between foil layers are produced by a pattern embossed on the foil. The foil is wrapped around a cylindrical support to produce the gaps. The energy spectrum of the X-rays produced is determined by the thickness of the radiator foil and the gaps. The DØ TRD X-rays have a distribution which is peaked at 8 keV with most X-rays having an energy less than 30 keV [23].

The transition radiation X-rays are detected in a two-stage time-expansion radial-drift proportional wire chamber (PWC) located behind each radiator unit. The X-rays typically convert in the first stage of the PWC and the charge drifts radially outward to the sense wires where amplification occurs. The radiator stack and PWC sections of each TRD unit are separated by a pair of 23 μm mylar windows separated by a distance of 2 mm. The outer mylar window is aluminized and serves as a high voltage cathode for the conversion stage of the PWC. Dry CO_2 gas flows between the mylar windows to prevent the nitrogen gas in the radiator stack from leaking into the PWC and contaminating the 91% Xe, 7% CH_4, and 2% C_2H_4 gas mixture circulating therein. The cylindrical shape of the mylar windows is maintained by a small pressure

difference between the radiator, gap, and detector volumes.

In addition to the charge produced by the transition radiation, all charged particles which pass through the conversion and amplification gaps produce ionization. The charge clusters produced arrive at the sense wires over the full 0.6 μs drift interval. Thus, both the magnitude of charge produced and the arrival time of the charge are useful in differentiating between electrons and charged hadrons.

The outer support cylinder for each TRD unit is a 1.1 cm thick plastic honeycomb covered by fiberglass skins. Kevlar end rings support the cathode structures. The radiator stack is enclosed by a carbon-fiber tube with end flanges made of Rohacell with carbon-fiber skins.

The 15 mm conversion stage and 8 mm amplification stage of the PWC section of each TRD unit are separated by a cathode grid of 70 μm gold-plated tungsten wires. The outer cathode of the amplification stage of each PWC section are constructed of helical copper strips deposited on Kapton foil. The amplification stage anodes of each PWC section are 30 μm gold-plated tungsten wires separated by 100 μm gold-plated beryllium/copper potential wires. Each TRD unit has 256 anode readout channels and 256 helical cathode strips with pitch angles between 24 and 46 degrees.

The Central Drift Chamber (CDC)

Beyond the TRD are the four cylindrical, concentric layers of the CDC [19]. The CDC provides coverage for large angle tracks. The CDC is a cylindrical annulus 184 cm in length with inner and outer radii of 49.5 and 74.5 cm respectively. The CDC is made up of four concentric rings of 32 azimuthal cells each. The high voltage for each cell is individually instrumented to allow it to be turned off remotely.

Each CDC cell contains 7 sense wires made of 30 μm gold-plated tungsten which

are read out at one end and two delay lines which are read out on both ends. The delay lines are situated one on either side of the sense wires. The sense wires are staggered in ϕ by ± 200 μm to remove left-right ambiguities. Radially alternate cells are offset by one-half cell to further aid in pattern recognition. The maximum drift distance is about 7 cm. The delay lines consist of a wire coil wound around a carbon fiber epoxy core. The delay line propagation velocity is about 2.35 mm/ns with a delay to rise time ratio of about 32:1. A pair of potential wires is situated between each anode sense wire with an additional grounded potential wire between the outermost sense wires and the other sense wires to minimize the signal induced on the delay lines by the inner sense wires. The z-coordinate of a hit is determined via the delay lines by measuring the arrival time of the pulse at each end of the delay line. The current is monitored on the grounded potential wires to generate a voltage trip if abnormal conditions arise.

The CDC is constructed of 32 identical modules. Each module is made of 4 Rohacell "shelves" covered with epoxy-coated Kevlar cloth and wrapped with two layers of 50 μm Kapton tape. Each shelf contains grooves at the sense wire locations to accommodate a Teflon tube containing a delay line. Field shaping is accomplished by resistive strips screen-printed onto the cathode surfaces. The gas mixture used in the CDC is 92.5% Ar, 4% CH_4, 3% CO_2, and 0.5% H_2O. The CDC is stable for collected charges on the anode wires of up to 0.35 C/m. The drift velocity in the CDC is about 34 μm/ns for a drift field of 620 V/m in the region where dv_{drift}/dE is negative. The voltage on the inner sense wires is 1.45 kV. The outer sense wire voltage is raised to 1.58 kV to induce larger delay line signals. The gas gain for the inner sense wires is 2×10^4 while the outer sense wire gas gain is 6×10^4.

A single layer scintillating fiber detector was installed between the CDC and the central calorimeter which covers about 1/32 of the full azimuth. The 128 individual

1 mm diameter fibers are aligned parallel to the beam and are read out with a multi-anode photomultiplier tube. This detector is used in conjunction with the CDC drift time to better understand the drift time vs. distance relationship and to quickly determine the CDC calibration constants if the operating conditions are changed.

The Forward Drift Chambers (FDC)

The two FDCs [19] cap the concentric VTX-TRD-CDC cylinders on either end and provide detection of small angle tracks. The FDCs' inner radius is $r \leq 61$ cm which is somewhat larger than that of the VTX chamber to allow passage of cables from the large angle tracking detectors.

Each FDC detector is composed of three separate modules: A Φ module to measure the ϕ coordinate sandwiched between two Θ modules (which are rotated relative to each other by 45 degrees in ϕ) to measure the θ coordinate. The Φ module is constructed of 36 sectors which contain 16 anode wires each along the z-coordinate. Each Θ module consists of 4 mechanically separate quadrants each containing 6 rectangular cells at increasing radii which contain 8 anode wires along the z-coordinate. The sense wires of the three inner cells are at one edge of the cell so that the ionization electrons drift in a single direction to remove left-right ambiguity. Each Θ cell contains one delay line which is identical to the CDC delay lines to measure the orthogonal coordinate. The adjacent anode wires in both the Θ and Φ chambers are staggered by ± 200 μm to resolve ambiguities.

The Φ chamber electrostatic properties are formed by a single grounded guard wire between anodes. The cell walls are covered with 25 μm aluminum strips on 125 μm G-10 to provide field shaping. The front and back surfaces are Kevlar-coated Nomex honeycomb with copper traces on Kapton. The electrostatics of the Θ modules are formed from two grounded guard wires between adjacent anodes as in the CDC. The

front and back surfaces are Kevlar-coated Rohacell with copper traces on Kapton for field shaping. The side walls are 200 μm aluminum foil on Nonex honeycomb. The FDCs employ the same gas as that used in the CDC and have similar gas gain and drift fields. The maximum drift time at the full radius of the Φ chamber is 1.5 μs.

The Central Detector Electronics

The readout electronics are almost identical for all CD devices. They consist of three signal processing stages: the preamplifiers, the shapers, and the flash ADC digitizers.

The preamplifiers for the sense wires, TRD cathode strips, and CDC/FDC delay lines are based on the Fujitsu MB43458 quad common base amplifier [24]. The CD requires 6080 readout channels. The preamplifier gain is 0.3 mV/fC. Rise and fall times are 5 and 34 ns respectively. Input noise is 2300 electrons for a detector input capacitance of 10 pF. Calibration is accomplished via test pulse charge injection into the preamplifier inputs.

The preamplifier output signals travel over 15 m coaxial cables to the shaping circuits [25]. The shaper consists of a video amplifier, a two-zero three-pole shaping circuit, and a cable driver.

The shaper output signals travel over 45 m coaxial cables to the FADC digitizers. Gain corrections and voltage offsets occur in an analog buffer amplifier circuit [26]. The dynamic range is increased by using one of two different gains depending upon the amplitude of the signal which results in an expansion of the dynamic range by about a factor of 3. This improves the dE/dx measurement quite a bit. The gain corrected signals then enter the FADC section which is based on SONY CX20116 8-bit FADC which operates at 106 MHz. The digitized data are then stored in a FIFO until a pass/fail decision is made by the Level 1 and Level 1.5 trigger.

Due to the long drift times relative to the FADC sampling rate and the high Level 1 output bandwidth, zero suppression of the CD signals is required in order not to exceed the capabilities of the data paths. Zero suppression is accomplished in the last digitization stage via an ASIC designed at FNAL [27] and manufactured by Intel, Inc. The zero suppression circuit examines the sequence of digitized charges and adjacent FADC bucket charge differences. Operating at 26.5 MHz on 4 byte words, it is able to process the data in real time. Digitized data are saved between leading and trailing signal edges where leading and trailing edges are defined by one of several algorithms based on digitized charges or charge differences over threshold [28].

3.2.3 The Calorimeters

The DØ calorimeters are the most important DØ detector component for electron, positron and photon detection. In addition to providing the only energy measurement of electrons and positrons (since DØ has no central magnetic field), they also provide the majority of the quantities used in electron and photon identification. They also are important for energy measurement and identification of jets and muons and for measuring the scalar E_T and missing E_T. E_T is the transverse energy of a cluster defined as $E_T = \sqrt{E_x^2 + E_y^2}$ where E_x and E_y are gotten by multiplying the cluster energy by the direction cosines of the cluster position with the x and y-axes respectively.

The DØ calorimeters use liquid argon (LAr) as the active medium to sample the ionization produced by electromagnetic and hadronic showers. LAr was chosen for its unit gain (low electro-negativity), simplicity of calibration, radiation hardness, and flexibility in segmenting the calorimeter. The downsides to using LAr are a complicated cryogenic system, uninstrumented regions due to the bulk of the cryostats, and inability to access the calorimeter modules during operation. The calorimeter layout can be seen in Figure 3.3.

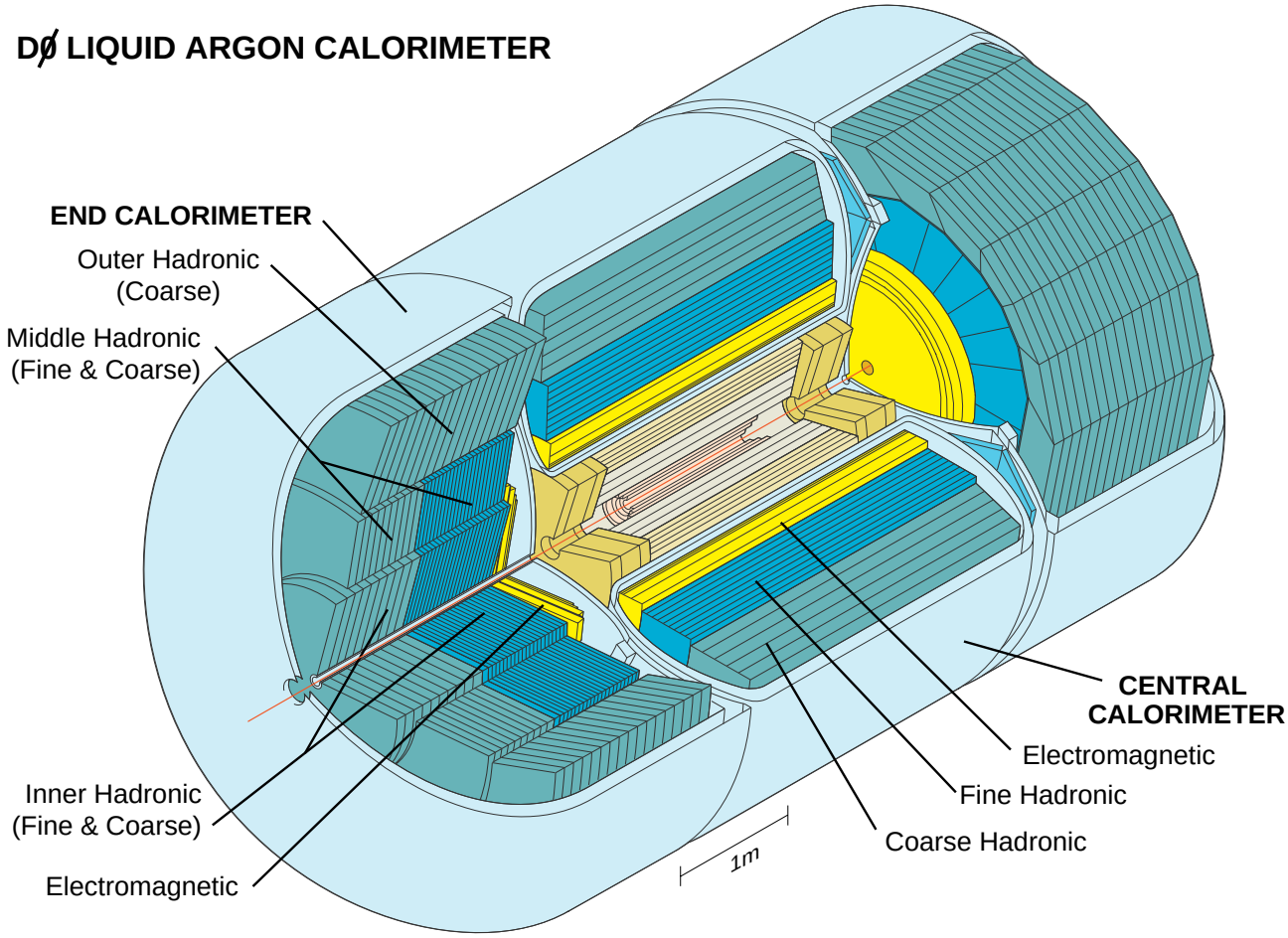

Figure 3.3: The DØ calorimeters. The various parts of the calorimeters are labeled on the figure.

The three DØ calorimeters, North End Calorimeter (ECN), Central Calorimeter (CC), and South End Calorimeter (ECS), each reside in separate cryostats in order to provide access to the central detectors which they surround. The rapidity coverage is roughly $-1.0 \leq \eta \leq 1.0$ for the CC. The end calorimeters (EC) extend the coverage to $|\eta| \approx 4.0$. The gaps between the EC and CC are roughly perpendicular to the beam which reduces the missing E_T degradation relative to having the ECs nested within the CC shell with gaps parallel to the beams. The DØ calorimeters are pseudo-projective; the separate modules are arranged in order to simulate a projective geometry as shown in Figure 3.4. The centers of the cells at increasing depth lie on rays projecting from the center of the interaction region, but cell boundaries are perpendicular to the absorber plates.

The Tevatron beam pipe passes through the EC cryostats at the center. The main ring beam pipe passes through all three cryostats near the outer radius. Bellows are used to accommodate the thermal and differential pressure motion of the cryostats to which they are welded.

The CC and EC each contain three different types of modules: the electromagnetic (EM), fine hadronic, and coarse hadronic arranged as shown in Figure 3.3. The EM sections use nearly pure depleted uranium [29] absorber plates, the CCEM plates are 3 mm thick and the ECEM plates are 4 mm thick. The fine hadronic sections use uranium(98%)-niobium(2%) alloy [29] absorber plates with a thickness of 6 mm. The coarse hadronic absorber plates are 46.5 mm thick and are made of copper in the CC and stainless steel in the EC. Electrical connections to the absorber plates were made by percussive welding of thick niobium wires to the edges of the plates.

The EM sections of the CC and EC are made of four depth layers. The first two layers (EM1 and EM2) help differentiate between neutral pions (which usually decay

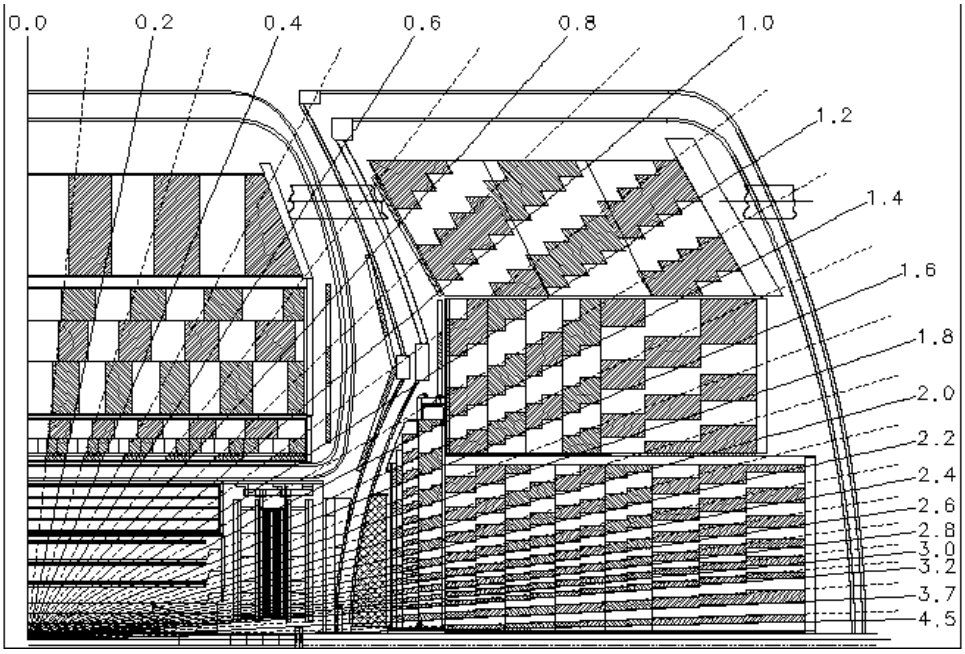

Figure 3.4: A side view of the DØ calorimeter towers showing the pseudo-projective geometry.

into two photons) and single photons due to the greater conversion probability of the pair of photons. The region of EM shower maximum is covered by the third (EM3) layer, which has finer transverse readout segmentation than the other EM layers. The fourth EM layer (EM4) completes the EM section. The fine hadronic modules are ganged into three or four layers and the coarse hadronic modules are ganged into one or three layers. The depth of the EM plus hadronic layers is 7.2 nuclear absorption lengths (λ_A) at $\eta = 0$ in the CC and 10.3 λ_A at the smallest angles in the EC.

The transverse size of the readout cells was chosen to be comparable to the size of EM showers. The typical transverse size of the EM and hadronic cells is $\Delta\eta = 0.1$ and $\Delta\phi = 2\pi/64 \approx 0.1$. The EM3 layer's segmentation is twice as fine ($\Delta\eta = 0.05$ and $\Delta\phi = 2\pi/128 \approx 0.05$) to improve the measurement of the EM shower centroid. Inter-module gangings are made prior to signal digitization in the front end electronics to join segments of cells which cross the CC and EC boundaries.

The calorimeter signal boards (excluding the ECEM and small angle EC hadronic) were constructed by laminating two 0.5 mm G-10 [30] sheets together. One of the G-10 sheets is copper clad with the segmented readout pattern milled into it. The other plain G-10 sheet covers the copper readout pattern. The outer surfaces of the G-10 laminate were coated with high resistivity carbon loaded epoxy [31]. Several signal boards at approximately the same η and ϕ are ganged together in depth to form a readout cell. Differences in the signal ganging cause the readout cells to vary from module to module. The signal board ganging connections are made using insulation displacement connectors and solid wires which has been very reliable.

The signal boards for the ECEM and two smallest angle EC hadronic modules were made from multi-layer printed circuit boards. The outer surfaces of these signal boards were coated with the same epoxy as the other signal boards. The segmentation is produced by etched patterns on the interior surfaces. Signal traces on another interior surface bring the signals to the outer edges of the boards. The signal and trace layers are connected by plated-through holes. These signal boards are ganged together in depth via solder-tail header connectors and Kapton printed circuit lines.

The electric field in a typical calorimeter cell is created by grounding the absorber plate and connecting the resistive coat of the signal board to a positive high voltage of 2-2.5 kV. The electron drift time across the 2.3 mm gap is approximately 450 ns. The gap thickness is chosen to be large enough to measure minimum ionizing particles. A schematic of a typical calorimeter unit cell is shown in Figure 3.5

The Central Calorimeter (CC)

The central calorimeter is comprised of three concentric cylindrical shells. The inner shell is the EM section which is made up of 32 separate modules. The middle shell is the fine hadronic (FH) section which contains 16 separate modules. The outer shell

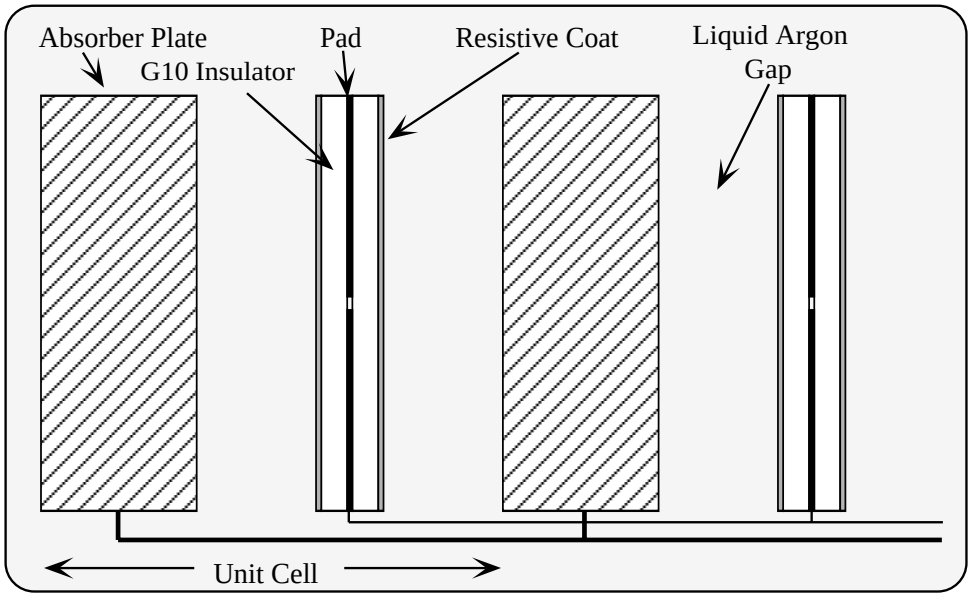

Figure 3.5: Calorimeter unit cell schematic.

is the coarse hadronic (CH) also made up of 16 modules. The three shells are rotated relative to one another so that particles encounter no more than one intermodule ϕ gap. The CC modules are made by loosely stacking alternating absorber plates and readout boards in a stainless steel box structure. Delrin spacers pass through holes in the readout boards and extend 2.3 mm on one side and 1.5 mm on the other side. Adjacent spacers have opposite long and short sides to provide room for the signal boards to flex.

The CCEM calorimeter is longitudinally segmented into four layers by ganging the readout signals. The first two layers (EM1 and EM2) are each 2 X_0 thick. The third CCEM layer (EM3) is 6.8 X_0. The fourth CCEM layer (EM4) is 9.8 X_0. The CCFH is longitudinally segmented into three layers (FH1, FH2, FH3) of thickness 1.3, 1.0, and 0.9 λ_A. The CCCH modules comprise a single longitudinal segment of thickness 3.2 λ_A. The total weight of the CC modules and their support structure is 305 metric tons with an additional weight of LAr of 26 metric tons.

The End Calorimeters

The two end calorimeters (ECN and ECS) each contain four types of modules. The ECs each contain one EM module and one inner hadronic (IH) module to avoid the gaps that would be produced by multiple modules. The absorber plates and readout boards for these modules form disks with no azimuthal gaps. The ECEM is longitudinally segmented into four layers of thickness 0.3, 2.6, 7.9, and 9.3 X_0 (EM1, EM2, EM3, EM4). The cryostat wall increases the thickness of EM1 to about 2 X_0. The alternating absorber plates and readout boards are stacked on either side of a stainless steel support whose thickness in radiation lengths is equivalent to a uranium plate. Tie rods and spacers position the plates and readout boards. The ECIH module is longitudinally segmented into four fine hadronic sections each 1.1 λ_A thick built of uranium absorber plates and one coarse hadronic section 4.1 λ_A thick made of stainless steel absorber plates. The construction of the ECIH is similar to the ECEM.

Outside the ECEM and ECIH modules are concentric rings of the middle hadronic (MH) and outer hadronic (OH) modules. The MH and OH modules are offset relative to each other to prevent particles from penetrating through the azimuthal gaps between adjacent modules. The ECMH modules are longitudinally segmented into four fine hadronic sections and one coarse hadronic section. The fine hadronic sections use uranium absorber plates and are each 0.9 λ_A thick. The coarse hadronic section is 4.4 λ_A thick and has absorber plates made of stainless steel. The ECOH modules use stainless steel absorber plates which are at an angle of about 60 degrees relative to the beam. The total weight of the EC calorimeter is approximately 238 metric tons.

The Intercryostat Detectors And Massless Gaps

In the transition region between the central and end calorimeters (roughly $0.8 \leq |\eta| \leq 1.4$) there exists a large amount of uninstrumented material in the form of cryostat walls and support structures. In an attempt to measure the energy deposited in this region a pair of scintillation counter arrays called the intercryostat detector (ICD) was installed on the front surface of the ECs. Each ICD is made up of 384 scintillator tiles of size $\delta\eta = \delta\phi = 0.1$. Inside the CC and EC cryostats, additional single cell structures called massless gaps were installed. One ring with standard segmentation was mounted on the CCFH end plates and additional rings were mounted on the front plates of the ECMH and ECOH. These two detectors provide a fair approximation of the standard DØ sampling of hadronic showers. The ICD readout uses 1.3 cm diameter phototubes [32] which were extensively tested to prevent failures.

Calorimeter Electronics

Calorimeter signals are read out via insulated 30 Ω coaxial Tefzel [33] cables connected to multi-layer printed circuit feed-through boards which pass through four cryostat feed-through ports located above the liquid argon level. The eight 27-layer T-shaped feed-through boards reorder the signals from the module oriented inputs to an output η-ϕ ordering to facilitate easier analysis. The feed-through board outputs travel over short cables to charge-sensitive hybrid preamplifiers [34]-[37] mounted on the outer cryostat surfaces. A single 2SK147 Toshiba j-FET with g_M $0.05\Omega^{-1}$ is used at each preamplifier input. Two different preamplifiers are used with equivalent full scale outputs of 100 and 200 GeV to provide full dynamic range response. The gain variation among the preamps is about 0.5%.

The preamplifier output signals travel over 30 m twisted pair cables to baseline

subtracter (BLS) shaping and sample-and-hold hybrid circuits. The input signals are integrated ($RC = 433$ ns) and differentiated ($RC = 33$ μs). Readout cells which cross the CC-EC boundary are merged at the BLS input. A trigger pickoff at the BLS input extracts a portion of the signal with a rise time of about 100 ns which is added into trigger towers of $\Delta\eta = \Delta\phi = 0.2$ for use in event selection.

The calorimeter signals are sampled just before a bunch crossing and 2.2 μs after. The difference between the two samples is proportional to the collected charge. Two storage capacitors for each channel provide analog double buffering. To prevent event pile-up, fast baseline restoration occurs within a few μs.

The BLS output is amplified by 1 or 8 (depending upon the signal size) to reduce the dynamic range required in the ADCs. A bit records which gain was used. A specific gain may be chosen for calibration purposes. The BLS outputs are multiplexed 16-fold onto the crate backplane and travel over 50 m twisted pair cables in serial time slices to the 24-channel 12-bit ADCs [34]-[37] in the moving counting house (MCH). The ADCs combined with the variable gain ($\times 1$ or $\times 8$) provide a dynamic range of 2^{15}. Each time slice of each channel is digitized in about 10 μs yielding a total digitization time of 160 μs for 384 signals. The gain parameters are set so that an energy deposition of about 3.75 MeV corresponds to at least one count. A minimum ionizing particle deposits between 8 (EM1) and 90 (FH1) MeV including noise. An adjustable threshold allows channels with (signal-pedestal) below the threshold to be suppressed from the readout buffer (zero suppression).

Both single-channel random noise (electronic noise and uranium radioactivity) and multi-channel coherent noise have been measured. The single-channel noise can be represented by $2000 + 3000 \times C(\text{nF})$ electrons. For N channels (N large), the total random noise varies as $\sqrt{N}$. The total coherent noise varies as N. The point at which

the coherent noise becomes larger than the random noise is on the order of 5000 channels.

Calibration of the DØ calorimeter electronics is accomplished by a precision pulser [38] which injects charge into the front ends of the preamplifiers via a large resistor. A pulse distribution system delivers equal pulses to each input. A programmable attenuator allows calibration over the full dynamic range. Precision and stability of the calibration system have been measured to be better than 0.25%.

3.2.4 The Muon Detectors

The DØ muon detection system consists of five iron toroidal magnets surrounded by proportional drift tubes (PDTs) to measure the direction of muon tracks (and thus their momentum) down to an angle of 3 degrees from the beam. Since most hadronic particles comprising parton jets are stopped inside the calorimeter, it is possible to detect muons within the jets much more easily than electrons in jets. The magnetic field direction produced in the toroids is approximately along the ϕ-coordinate which results in the muon tracks bending roughly in the r-z plane. Given the width of the interaction region at D0 ($\sigma_z \approx 30$ cm), it is necessary to measure the muon track direction both before and after the bend. The entrance point of the muon track into the toroid is determined by a closely spaced set of measurements before the toroid and the track direction after leaving the toroid is gotten by a set of measurements separated by 1-3 m. The direction of the track before the toroid is determined by combining the primary event vertex, the track measured by the central detector and the first muon chamber track vector (before the toroid) . Muon energy deposition can also be seen in the calorimeter. From the incident and exit tracks on either side of the toroid, the bend angle may be found and used to calculate the momentum. Multiple Coulomb scattering in the toroid limits the relative momentum resolution to greater

than 18%. A measurement of the sign of the muon is possible for $P_T \leq 200$ GeV/c at $\eta = 0$ and $P_T \leq 30$ at $|\eta| = 3.3$ with 99

The central toroid (CF) spans the region $|\eta| \leq 1$ and the two end toroids (EF) cover the region $1 < |\eta| \leq 2.5$. The two small angle muon system (SAMUS) toroids fit within the central hole of the EF toroids and cover the region $2.5 < |\eta| \leq 3.6$. The layout of the muon system can be seen in Figure 3.2. The muon system toroids are very thick and thus provide a very clean environment (at least from particles originating from the interaction, cosmic rays and beam loss must be removed by other means) for muon identification. The muon system is fairly hermetic apart from the gaps caused by the CF-EF transition, various support structures, and detector access requirements. The minimum muon momentum necessary to pass through the toroids varies from about 3.5 GeV at $\eta = 0$ to around 5 GeV at smaller angles. The wide angle muon system (WAMUS) detects all muon tracks which pass through the CF toroids and most of those which pass through the EF toroids. The WAMUS system contains 164 PDTs of varying sizes. The PDT wires are oriented along the direction of the magnetic field to accurately measure the bend coordinate. The SAMUS system contains three stations with three planes per station on each end.

The CF toroid is a 109 cm thick square annulus centered on the beam pipe and weighs 1973 metric tons. Twenty coils of ten turns each carry currents of 2500 A and produce internal magnetic fields of 1.9 T. The two EF toroids are positioned at $447 \leq |z| \leq 600$ cm and are centered on the beams. The main ring beam pipe passes through a 25 cm hole in the EFs. Eight coils of eight turns each carry 2500 A and produce an internal field of about 2 T. Each EF toroid weighs 800 metric tons. Inside the inner hole of each EF toroid is a SAMUS toroid. The SAMUS toroids each weigh 32 metric tons and are centered on the beams. Two coils of 25 turns each carry currents of 1000 A producing a field around 2 T.

WAMUS

The wide angle muon system [39] PDTs are arrayed in three layers called A,B, and C layers that surround the toroids. The A layer is just before the toroid and the B and C layers are after the toroid and are separated by 1-3 m to provide a long track lever arm after the magnet. The A layer contains four planes of PDTs and the B and C layers are comprised of three PDT planes each. All WAMUS PDT cells are the same. The differences between chambers are depth in number of cells (3 or 4), width in number of cells (14 to 24), and length (191 to 579 cm).

The WAMUS PDT cells are built from aluminum extrusions which are cut to length and pressed together and then sealed with epoxy. The extrusions are shaped such that adjacent planes are offset to remove left-right ambiguities. The cathode pads are made from copper clad Glasteel[1] [40] sheets which have a repeating diamond shaped pattern milled into them using a computer controlled router and are then cut into strips to form the individual cathode pads. The cathode strips are inserted into channels in the top and bottom of the unit cells. The cathode pad surfaces facing the active portion of the cell are covered with 50 μm Kapton tape to ensure electrical isolation from the extrusion. A 50 μm gold plated tungsten anode wire is strung through the center of the cell and is held at 300 g tension by a plug mounted in the aluminum cap extrusion which seals the ends of the cells. The maximum drift distance is 5 cm. The wire sag over 610 cm is 0.6 mm. The aluminum extrusions which form the cells are grounded with the cathode pads held at +2.3 kV and the anode wires held at +4.56 kV.

The coordinate along the wire direction (ξ) is measured by the cathode pad signals and timing information from the anode wires. Adjacent cell anode wires are jumpered

[1] This material outgasses and deposits on the wires which reduces the efficiency

at one end and the signals for the pair are read out at the other end. A rough measurement of ξ can be made by measuring the time difference at the ends of the paired wire. Two hits per wire pair are accommodated to allow for δ rays. This method produces a ξ measurement with a precision of 10 to 20 cm along the wire. A finer ξ measurement is made using the cathode pad signals. The upper and lower cathode strips are made from two independent electrodes which form the inner and outer parts of a repeating diamond pattern. The repeat distance of the diamond pattern is 61 cm. The two inner parts of the diamond pattern (top and bottom) in a given cell are added and read out independently of the sum of the two outer parts of the diamond pattern. Calculation of the sum and difference of the inner and outer signals provides a measurement of ξ modulo the approximately 30 cm half-wavelength of the diamond pattern. The correct cathode pad solution is determined by the Δt measurement. The cathode diamond pattern is offset by about 1/6 of the repeat length between adjacent planes of PDTs to reduce the ambiguities near the extrema of the diamond pattern. The overall ξ resolution for a given chamber is ± 3 mm.

The WAMUS PDT chambers use a gas mixture of 90% Ar, 5% CF_4, and 5% CO_2. The drift velocity is on the order of 6.5 cm/μs but varies across the cells with changing E [41]. Tests of this gas mixture show a nearly linear time to distance relationship. Typical leak rates of WAMUS chambers are about 0.005 cubic feet per hour.

SAMUS

The three small angle muon system stations at either end of the DØ detector are called A, B and C stations. The A station precedes the SAMUS toroid and the B and C stations lie between the SAMUS toroid and the low-beta quadrupole magnet for the D0 insertion. The SAMUS stations are perpendicular to the beams and cover an area of 312×312 cm^2. Each SAMUS station consists of three doublets of 29 mm internal

diameter cylindrical PDT chambers [42]. The orientation of the doublets are along the x, y, and u coordinates (the u coordinate is at an angle of 45 degrees with respect to the x coordinate). The PDTs that make up the doublets form a close packed array with adjacent tubes offset by one-half a tube diameter.

The SAMUS PDTs are made from 3 cm diameter stainless steel tubes with individual end plugs which allow for the gas and electrical connections. A 50 μm gold plated tungsten anode wire at 208 g tension runs through the center of the tube. The wire sag over 3.1 m is 0.24 mm. The gas mixture used is 90% CF_4 and 10% CH_4. The drift velocity is 9.7 cm/μs with a time to distance relationship that is approximately linear. The position resolution for the small angle system is about 300 μm [43].

Muon System Electronics

The DØ muon system is spread over a large area and consequently the readout electronics for the PDTs are mounted on the chambers. Signal shaping, time to distance conversion, hit latching, monitoring, and signal multiplexing for efficient signal transport are all performed locally. Only the digitization and triggering electronics are located in the moving counting house (MCH). The electronics boards for each WAMUS chamber are located in an enclosure mounted on the side of the chamber body. The individual boards are: fast signal shaping "motherboards" for each six cells of each chamber plane, one hardware-status "monitor" board, and one multiplexing and signal driver "corner-board".

The motherboard contains a set of hybrid circuits which perform signal shaping and time-information encoding. The cathode pad signal sums are brought to a hybrid circuit charge-sensitive preamplifier (CSP) which is very similar to the calorimeter preamplifiers. The CSP output enters a baseline subtracter (BLS) circuit (similar to the calorimeter BLS) which performs pre- and post-sampling of the signal and stores

the difference output on one of two output capacitors. Signals from the jumpered anode wire pairs are amplified and discriminated in a pair of hybrid circuits (2WAD). The 2WAD outputs enter two hybrid time-to-voltage and two time-difference to voltage hybrid circuits which provide time information and time difference for up to two hits per wire pair. The final circuit on the motherboard is a pad latch which latches hits on the cathode pads based on information in the pad BLS hybrids.

The corner-board collects the information from the motherboards, multiplexes the pad latch information and sends it across long cables to the MCH. The latch bits are also ORed on the corner-board to provide information on muon activity and majority logic indicating 1, 2, 3, or 4 hits in the chamber. The motherboard analog signals from the pad BLSs and the time and time-difference hybrids is multiplexed and sent in 96 time slices to digitizers in the MCH. The corner boards also contain circuitry for the addition of a cosmic ray veto scintillator array mounted on the outer surface of the detector. Finally, the corner-boards contain pulsers for front end electronics calibration.

Information from the monitor board on each chamber passes over a token ring network to the general detector monitoring system. This board monitors the temperature, currents, voltages, and gas flow in each chamber. The monitor board is also used to set pad latch thresholds and pulser amplitudes.

The SAMUS front end electronics consist of a card containing an amplifier, discriminator, time-to-voltage converter, and a latch for each PDT. A SAMUS control board supervises the multiplexing of these signals which are sent to the MCH. The SAMUS monitor boards are the same as the WAMUS boards. The latched SAMUS hits are used to form the SAMUS triggers.

Muon chamber cathode pad signals and voltage encoded time information are

digitized in the MCH using 12-bit ADCs which are similar to the calorimeter ADCs. The muon system contains a total of 50,920 analog elements.

3.2.5 The Trigger And Data Acquisition System

The DØ trigger and data acquisition system is used to select interesting physics events and events used for calibration purposes. The DØ trigger consists of four main decision levels of increasing sophistication in event selection. The Level 0 trigger is an array of scintillators mounted on the surface of each end calorimeter and is used to signal an inelastic collision in D0. At a luminosity of 5×10^{30} cm^{-2}s^{-1}, the Level 0 rate is about 150 kHz. The Level 1 trigger is a programmable architecture which uses information from the various DØ detector components to select events. Level 1 trigger decisions can be made in the 3.5 μs time interval between bunch crossings incurring no deadtime. Level 1.5 triggers require more time. The Level 1 trigger output rate is on the order of 200 Hz. The level 1.5 trigger further reduces the Level 1 output rate to about 100 Hz. The events which pass the Level 1 (and possibly Level 1.5) trigger are transported via the DØ data acquisition system to a farm of 48 DEC VAXstation 4000/60 and 4000/90 microcomputers known as the Level 2 system. Level 2 assembles the raw event data and runs a combination of sophisticated filters to perform further event selection. The Level 2 output rate is about 2 Hz which coincides with the speed events can be written to the host computer system.

The Level 0 Trigger

The Level 0 (L0) trigger is used to signal the occurrence of an inelastic collision at D0 and to monitor the luminosity at D0. It consists of two hodoscopes built of scintillation counters which are mounted on the outer surface of each end calorimeter. Two planes of scintillators are rotated 90 degrees with respect to one another to form

a checkerboard pattern in each hodoscope. The hodoscopes provide partial coverage for the pseudo-rapidity range $1.9 < |\eta| < 4.3$ and almost full coverage for the range $2.3 < |\eta| < 3.9$. The η coverage is governed by the requirement that a coincidence of both L0 detectors be $\geq 99\%$ efficient for detection of non-diffractive inelastic collisions.

Each hodoscope contains 20 short (7×7 cm^2 squares) read out by a photomultiplier tube (PMT) at one end and 8 long (7×65 cm^2 rectangles) read out at both ends. To provide good timing, 1.6 cm thick Bicron BC-408 PVT scintillators and Phillips XP-2282 photomultiplier tubes are used. Optical fibers distribute UV laser pulses to each PMT for monitoring and calibration purposes.

The Level 0 trigger is also used to provide a fast determination of the event vertex for use in the Level 1 and Level 2 triggers. Because the vertex distribution is so large at the Tevatron ($\sigma_z = 30cm$) it is necessary to measure it to provide more accurate E_T values for use in the Level 1 and Level 2 triggers. A "fast" L0 vertex with a resolution of 15 cm is computed within the time limit imposed by the Level 1 trigger and a "slow" L0 vertex with a resolution of 3.5 cm is provided to the Level 2 system. The L0 vertex z-coordinate is determined by the arrival time difference between particles which hit opposite hodoscopes. The Level 0 detectors also provide information about multiple interactions in a single bunch crossing which has an appreciable probability at higher luminosities. If a multiple interaction occurs, the L0 time difference is ambiguous and a flag is set to identify such events to subsequent trigger levels.

The L0 PMT signals are amplified and split into two readout paths. Along one path, an analog sum of the small counter signals for each hodoscope is computed and a fast vertex position measurement for Level 1 E_T corrections is made using a GaAs-based digital TDC [44]. A $|z_{vtx}| < 100$ cm cut is made to discriminate between beam-beam interactions and beam-halo or beam-gas interactions. The other readout

path digitizes the time and integrated charge for each counter. A more accurate slower determination of the event vertex is computed by applying full calibration and charge slewing corrections to this data and using the mean time for each hodoscope to find the vertex position. The rms deviation in the time difference is also computed and used to flag multiple interactions. All L0 computations are done in hardware.

The Tevatron luminosity is found by measuring the non-diffractive inelastic collision rate. These events are selected by requiring a L0 coincidence and that $|z_{vtx}| < 100$ cm. Scalars are used to count live crossings, coincidences which satisfy the vertex cut, and single hits in groups of counters both with and without valid coincidences. These scalars allow the luminosity to be measured independently for each beam bunch and provide feedback to the accelerator operators.

The Level 1 And Level 1.5 Trigger

During Run 1A, the Tevatron was operated with six bunches of protons and antiprotons which results in a time interval of about 3.5 μs between bunch crossings. Trigger decisions which can be made within this time interval incur no deadtime. The hardware calorimeter trigger satisfies this requirement, as does part of the muon trigger, however the remaining muon trigger requires several bunch crossings to complete and is logically incorporated as a veto on event transmission. The various Level 1 (L1) trigger components are managed by the L1 framework, which also controls the interface to subsequent trigger levels. The L1 framework collects digital information from each L1 specific trigger device and decides whether to pass the event on to the next trigger level. It also coordinates vetoes which inhibit triggers, provides prescaling for each trigger (if needed), correlates the trigger and readout functions, manages communication with the front end electronics and trigger control computer (TCC), and provides several scalars which allow measurement of trigger rates and deadtimes.

Trigger selection is performed using a two dimensional AND-OR network. The 256 latched bits called AND-OR input terms form one set of inputs and contain specific pieces of detector information (e.g., 2 EM clusters with $E_T > 10$ GeV). The 32 orthogonal AND-OR lines are the outputs from the AND-OR network and correspond to 32 specific Level 1 triggers. The firing of one or more specific L1 triggers results in a readout request by the data acquisition system, provided there are no front end busy restrictions or other vetoes. If a Level 1.5 confirmation is required for a specific Level 1 trigger, the L1 framework forms the L1.5 decision and passes the result to the data acquisition system. In addition, the L1 framework builds a block of information called the trigger block that contains a summary of all the conditions which led to a positive L1 decision (and L1.5 confirmation if required). The L1 trigger data block is passed on to the data logging stream to allow subsequent processors to recompute the input information and confirm the L1 decision.

The trigger control computer (TCC) provides for convenient interaction with the L1 trigger system. Configurations for active specific triggers are downloaded to the TCC from the host computer. The large tables of information necessary for programming and verification of the hardware memories in specific L1 triggers are downloaded and stored on the TCC's local disk. The TCC provides access to scalers and registers to allow trigger system programming, diagnostics and monitoring. The TCC software is based on the DEC VAXELN multi-tasking real-time operating system. The TCC software uses a low-level hardware database which contains aliases and descriptions of specific hardware components for easy reference, and a high-level object oriented database for defining and recording trigger configurations. Trigger configurations are continuously monitored for validity and an alarm is set in the general DØ alarm system if a configuration becomes invalid.

The Level 1 system can trigger on energy deposited in the calorimeter and on

tracks in the muon detector. Only the calorimeter trigger was used to collect the data for this thesis so only the calorimeter trigger is described here. For a description of the muon trigger see [16].

The Level 1 calorimeter trigger uses the trigger pickoffs from the calorimeter BLSs which are summed into trigger towers of size $\Delta\eta = \Delta\phi = 0.2$ out to $|\eta| = 4.0$. Separate trigger inputs exist for the EM and FH sections of the calorimeter. The summed energy (input voltage) in the trigger towers is converted to E_T by weighting it using a $\sin\theta$ lookup table that assumes an interaction vertex of $z = 0$. The E_T signal in each trigger tower is then digitized in a fast 8-bit FADC (20 ns from input to output) and clocked into latches allowing pipeline synchronization of all calorimeter information. The latches can also be supplied with test signals for diagnostic study of all subsequent trigger functions.

The 8-bit FADC information provides part of the address for several lookup memories. An additional 3 bits from the L0 trigger provides a rough measure of the interaction vertex z-coordinate. The lookup memories provide EM and FH transverse energies for each trigger tower above a fixed cut (based on electronics noise and physics considerations) which are corrected for the vertex position (if known). The sum of the EM and FH E_T for each trigger tower is formed and stored in a 9-bit register for use in future, more powerful hardware triggers. The lookup memories also provide the EM and FH E_T for each trigger tower without the cut and vertex correction. The global sums of the six energy variables returned from the lookup memories (EM, FH, and total transverse energy, corrected and uncorrected) are computed for all trigger towers by pipelined adder trees. The adder trees are arranged such that geographically contiguous regions are kept together thus allowing intermediate sums over large areas (bigger trigger towers) to be used if so desired.

The missing E_T for the event is computed from the x- and y-components of the global E_T. The corrected and uncorrected global total E_T are formed from the corrected and uncorrected EM and FH E_T. These seven energy variables (corrected and uncorrected EM, FH, and total E_T and missing E_T) are compared to up to 32 programmable thresholds and the results of the comparisons are provided as AND-OR input terms to the Level 1 framework. In addition, the EM E_T for each trigger tower is compared to four different programmable reference values. A bit is set for each EM reference value that is exceeded by each trigger tower's EM E_T provided that the FH E_T for the trigger tower does not exceed a corresponding hadronic reference value (hadronic veto). The total E_T is also compared to four different reference values for each trigger tower producing an additional four bits for each trigger tower. These 12 individual reference values are separately programmable for each trigger tower. The global count of the number of trigger towers whose E_T exceeds their reference values is computed by summation over all trigger towers in the pipelined counter trees for each of the four EM E_T and total E_T reference value sets. The global counts for each reference set are then compared to up to 32 programmable count thresholds and the results of the comparisons are provided to the Level 1 framework as input AND-OR terms.

The Data Acquisition System

The DØ data acquisition system and Level 2 trigger hardware are tightly coupled together and must be described simultaneously. The data acquisition system and Level 2 trigger hardware [45]-[50] is based on a farm of 48 parallel nodes connected to the detector electronics and triggered by a set of eight 32-bit wide high-speed data cables. The nodes consist of a DEC VAXstation 4000/60 or 4000/90 running the DEC VAXELN realtime operating system connected via a VME bus adaptor to multi-port

memory (for receiving data), and an output memory board. The Level 2 system (L2) collects data from all relevant detector elements and trigger blocks for events which pass the Level 1 triggers. Various software algorithms (L2 filters) are then applied to the events to reduce the L2 input rate from 100 Hz to an output rate of around 2 Hz sent to the host computer system for storage. The data for each event that passes the L1 trigger is sent over parallel data cables to a non-busy node selected to receive the event. The node puts the event data into a final format and runs a combination of L2 filter algorithms on the event. A block diagram of the Level 2 system is shown in Figure 3.6.

Approximately 80 VME crates hold the calorimeter and muon chamber ADCs and the FADCs for the central detector components. Fully digitized data appears in the output buffers of these VME crates about 1 ms after a L1 or L1.5 trigger. The L0 and L1 trigger hardware also produce data blocks containing information about the trigger decision. Each VME crate contains a 512 kB memory module with two data buffers. Each VME buffer driver board [50] (VBD) uses list processors to control data transfer from locations in the VME crate onto an output data cable highway. Internal crate transfer bandwidth is about 30 MB/s. The VBD outputs for each sector of the detector are sequentially connected to a high speed data cable. The data cables consist of 32 twisted pair lines for data and 13 twisted pair lines for parity and control. The data cables, clocked at 100 ns intervals, transfer data at 40 MB/s/cable. Eight data cables correspond to the eight detector sections (VTX,TRD,CDC,FDC, north and south halves of the calorimeter, L1 trigger, and L0 trigger). Readout control and arbitration for the VBDs is performed using a token passing scheme. Upon receipt of a token the external port processor of the VBD compares the token bits with the crate buffers; if they match, the VBD transfers pending buffers to the data cable. The tokens circulate at a clock rate of 1 MHz.

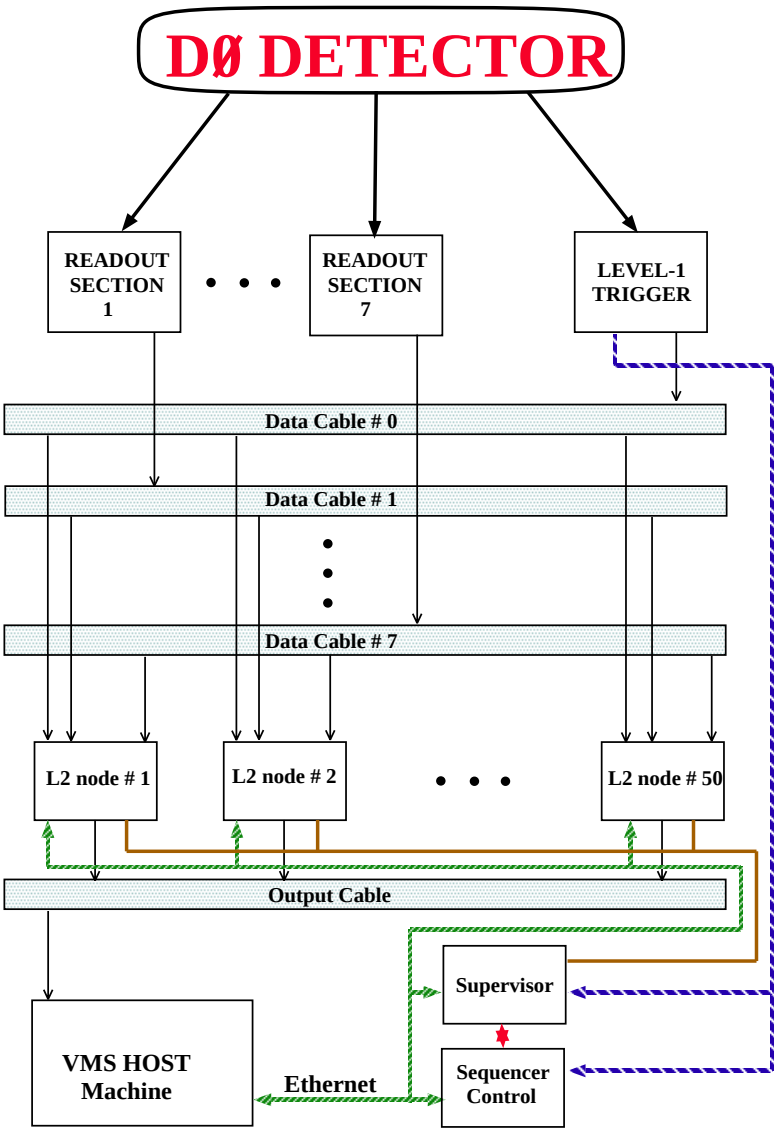

Figure 3.6: A schematic of the DØ Data Acquisition System.

A Level 2 supervisor processor controls the realtime operation of the data acquisition system. A sequencer processor controls data transfer over the data cables via a set of sequencer control boards (one for each data cable). When a valid hardware trigger occurs, the Level 1 system sends an interrupt to the supervisor containing the 32-bit pattern of specific triggers that fired, as well as a 16-bit event number. When the supervisor receives a Level 1 trigger it assigns a Level 2 node for that event and interrupts the sequencer. The sequencer creates readout tokens for the list of crates necessary for the specific trigger pattern, tokens include the low-order bits of the event number to ensure readout integrity. Token circulation and data readout are managed in parallel by the separate sequencer control boards on each data cable. Any combination of data cables, and thus any combination of detector elements, may be readout, providing for flexible debugging and calibration.

The eight data cables are connected to all 48 L2 nodes. The L2 nodes are located in a fixed counting area in the DØ hall, while the VME crates and L1 trigger hardware are located in the MCH. To connect these two separate counting areas, the data cables pass through an optical isolator circuit which decouples the electrical grounds of the detector and the fixed counting areas. Each L2 node contains multi-port memory modules which receive the data from the data cables, a VAXstation 4000/60 or 4000/90 processor, a VBD for buffering data that is sent to the host. An integral part of the L2 nodes is the multi-port memory [51] (MPM) which is accessed by the data cables, and the output VBD. Each L2 node contains four MPMs which each contain two channels of 2 MB multi-ported memory to provide inputs for the eight data cables which pass through each node. The total input rate for each L2 node is 320 MB/s. The MPMs appear as contiguous I/O space memory to the CPU. The incoming data is directly mapped into a single raw data ZEBRA tree structure based on the CERN ZEBRA memory management package, which is used extensively in DØ. No copy operations

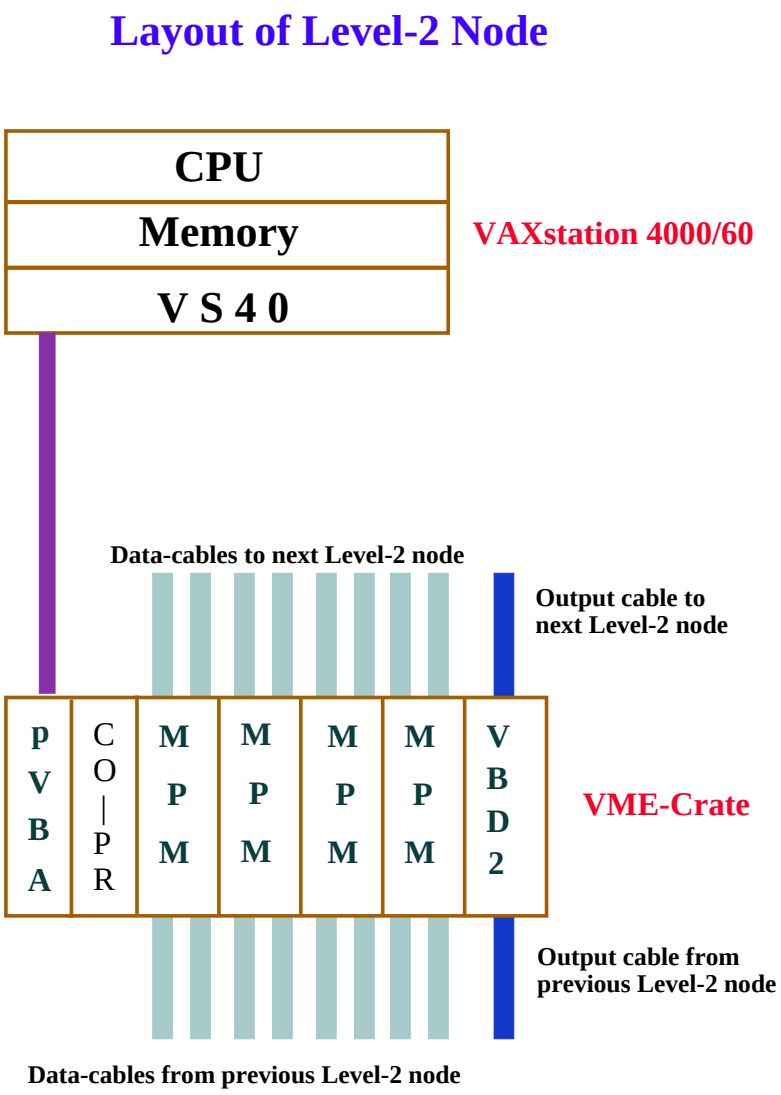

Figure 3.7: A schematic diagram of a Level 2 node and associated VME electronics.

are required on the data in the L2 nodes and no subsequent reformatting of the raw data is necessary offline. A schematic diagram of a L2 node can be seen in Figure 3.7.

It is possible to steer specific event types to specific L2 nodes for calibration purposes. Under normal run conditions an identical copy of the Level 2 software is downloaded to most L2 nodes, with possibly a few nodes running different code for testing purposes. High level languages are used for Level 2 software development (FORTRAN, C, EPASCAL) and the code is downloaded via Ethernet to the nodes.

A special surveyor node monitors the data flow and the processor, supervisor, and sequencer nodes. The surveyor collects statistical and diagnostic information which is used for realtime monitor displays and alarms.

When an event passes the Level 2 trigger, Level 2 analysis information and the raw data passes directly from the MPMs through a VBD to the host computer system for logging and further analysis. Readout from Level 2 to the host is handled similarly to the VME readout into Level 2. A sanitizer node circulates a token to the L2 output VBD which dumps its data on the output data cable where it is passed to an MPM module in a crate connected to the host system via a VME/XMI bus adaptor.

The Level 2 Filter

The filtering performed in the Level 2 nodes reduces the input rate of 100 Hz to about 2 Hz to allow it to be logged for offline analysis. Studies have shown [52] that to keep the Level 2 deadtime below 2%, the average processing time should be $\leq 70\%$ of the average time between events sent to a given L2 node (about 350 ms). The current average processing time is about 200 ms/event, which is well within this limit. The filtering performed in a L2 node is done by a series of filter tools. These tools each have a specific job to perform, such as identifying a specific particle type (i.e. electron or muon) above a given E_T threshold or identifying a particular event characteristic (i.e. more than 10 GeV of missing E_T in the event). Tools exist for jets, electrons, muons, scalar E_T, and missing E_T. Other tools are used to identify specific noise or background conditions. A Level 2 filter is built of these tools by constructing a filter "script" which defines which tools are to be used, what parameters the tools should be given (i.e. E_T thresholds, isolation cone sizes, etc...) and in what order the tools should be run. Each filter script is controlled by one of the 32 Level 1 specific triggers, and more than one filter script can depend on a given L1 trigger. The total number

of Level 2 filter bits is 128.

The L2 tools are generally developed offline under the VMS operating system and are tested using Monte Carlo, Test Beam and real DØ detector data. A new L2 tool is added to the Level 2 system using a program called L2STATE [53]. The L2STATE output consists of FORTRAN files that call the tools, configuration files which specify the arrangements of the L2 (and L1) filter tools, the specific input parameters used by the tools and lists of the resources required by the tools. A program called COOR which runs on the host system, assembles the L2STATE output and coordinates the downloading of code, configuration files, and resource lists to the lower-level hardware.

The L2 filter tools are generally written in FORTRAN. The operating system run by the L2 nodes is the VAXELN realtime operating system which imposes certain constraints on the Level 2 code. Standard FORTRAN-77 code will run under VAXELN but I/O operations and system service calls must be specially handled. The VAXELN operating system does not support virtual memory so all Level 2 code must fit in the available 8 MB of RAM on each node.

An offline simulation of the Level 1 and Level 2 systems that runs under the VMS operating system was written to allow study of trigger rates, timing, efficiencies and the like. A pair of linked utilities called L1SIM and L2SIM provide the simulation functions. L1SIM and L2SIM can be run on simulated detector data by processing Monte Carlo events with the DØGEANT detector simulator based on the CERN GEANT package to produce the simulated raw detector data. L1SIM and L2SIM may also be run on real DØ data either reusing the existing L1 trigger bits or producing them from the raw data. These simulations are used to optimize the Level 1 trigger configurations and the Level 2 filter scripts within the overall constraints of the rates and rejection factors. L1SIM and L2SIM use the actual online trigger configuration

files which guarantees that online and offline configurations are identical.

The Host

The DØ online host system consists of a VAX 6620, VAX 6410, and VAX 8810 mainframe computers, a set of shared disks connected by the high speed DEC CI cluster protocol, and 12 VAXstations of varying CPU power connected by an Ethernet/FDDI network. The Level 2 output cable is connected to the 6620, which is the primary data collection computer. The events are logged to a staging disk; a subset of the data is used by the workstations for monitoring purposes. Events can be recorded at about three 500 kB events per second. The 6410 spools the events from the staging disk onto 8 mm tapes and is responsible for various downloading operations. The 8810 performs hardware monitoring and also participates in downloading.

The host cluster serves as the primary human interface to the detector systems. It is responsible for high level control of the data-taking system, downloading of all settable parameters, hardware monitoring control, data recording, and displaying detector data. These data include $p\bar{p}$ interactions, calibration data, alarms and monitoring information.

The various computer processes necessary for the operation of DØ are distributed across the cluster. These processes communicate via a package called inter-task communication (ITC) developed by DØ. ITC works between processes on a single node or between processes running on separate nodes of the cluster. Data is made available to monitoring, display or calibration processes running on the cluster by a DØ extension of the global shared common (GSC) system developed by the Fermilab Computing Division. Events are put into GSC by a sub-process of the DØ data logger process which receives events from the Level 2 system. Events are selected from the extended GSC by client processes based on L2 filter bits.

Event monitoring and display is accomplished by a program framework called EXAMINE. The utilities within EXAMINE allow users to peruse current trigger lists, inform users of begin and end run conditions, display tracks and energies in the various detectors, and make plots of various interesting quantities. There is typically an EXAMINE running for each major detector subsystem as well as global analysis and display versions for normal data-taking runs.

The COOR program handles the overall coordination of data taking and runs as a detached server. Clients connect to COOR to request specific detector configurations or operational changes. COOR maintains connections to various subsystems which it sends download and control messages. COOR communicates with parts of the Level 1 and Level 1.5 trigger, the data acquisition and filtering parts of the Level 2 system, the front end digitizing electronics, pulsers, timing and gating logic, and the data logging system. These messages travel over networks using several protocols, including Ethernet, FDDI, and IBM token ring.

Chapter 4

Data Sample And Event Selection

4.1 Luminosity

The luminosity at DØ is measured using the Level 0 (L0) hardware described in Chapter 3. Beam crossings occur in DØ every 3.5 μs and the L0 trigger indicates which of these contain non-diffractive inelastic collisions and monitors the instantaneous luminosity of the collider. The instantaneous luminosity $\mathcal{L}$ is measured using

$$\mathcal{L}_{meas} = \frac{R_{L0}}{\sigma_{L0}}$$

where σ_{L0} is the cross section subtended by the L0 detectors. The counting rate is measured for each of the six bunch crossings.

This is strictly true only if the instantaneous luminosity is low enough that the counting rate corresponds to the interaction rate. As the luminosity increases there is the possibility for having multiple interactions in a single crossing. For this case, the counting rate is less than the interaction rate since multiple interactions get counted only once.

The multiple interaction correction is calculated using Poisson statistics.

The average number of interactions per crossing, $\bar{n}$, is given by:

$$\bar{n} = \mathcal{L}\ \tau\ \sigma_{LO}$$

where τ is the crossing time ($\tau = 3.5\ \mu$s). The multiple interaction correction factor is then:

$$\frac{\mathcal{L}}{\mathcal{L}_{\text{meas}}} = \frac{\bar{n}}{1 - e^{-\bar{n}}} = \frac{-\ln(1 - \mathcal{L}_{\text{meas}}\ \tau\ \sigma_{LO})}{\mathcal{L}_{\text{meas}}\ \tau\ \sigma_{LO}}$$

The luminosity had previously been calculated using the visible cross section (luminosity monitor constant) for the L0 trigger, $\sigma_{LO} = 48.2$ mb, based on the world average $p\bar{p}$ inelastic cross sections at $\sqrt{s} = 1.8$ TeV. Recent studies using the MBR and DTUJET Monte Carlo event generators and unbiased DØ data samples have resulted in a more precise determination of the DØ luminosity monitor constant. The result, $\sigma_{LO} = 46.7 \pm 2.5$ mb, lowers the central value of the luminosity constant by 3.1% and reduces the error from 12% to 5.4% [54].

In order to produce a cross section it is necessary to measure the total integrated luminosity L for the trigger used to collect one's data sample. The number of events N one should expect to collect for a given cross section σ is then given by

$$N = \sigma L$$

where the integrated luminosity is defined in terms of the instantaneous luminosity as

$$L = \int \mathcal{L} dt$$

The integration limits range over the total time during which collisions were occurring and the trigger was live. The integrated luminosity for the combination of Level 1 and Level 2 triggers used to collect the data sample for this analysis was 14.7 ± 0.8 pb^{-1}.

4.2 Level 0 Trigger Selection Criteria

The Level 0 system is designed to detect inelastic scattering events and to provide a fast measurement of the z position of the event vertex. It consists of two separate detectors located at each end of the central detector between the FDC and the EC. Each detector consists of two layers of rectangular scintillator panels which are read out with photomultiplier tubes. A description of the L0 hardware can be found in Chapter 3.

An inelastic collision typically produces quite a bit of activity in the far forward regions (from the spectator quarks); thus, one looks for a coincidence between the signals from the two scintillator arrays to indicate an inelastic collision in the DØ detector. The L0 trigger is >99% efficient for non-diffractive inelastic collisions. By comparing the arrival times of the signals from the two arrays, the approximate position of the interaction vertex may be found. A fast vertex determination with a resolution ± 15 cm is available within 800 ns after the collision. A more accurate determination with a resolution of ± 3.5 cm is available within 2.1 μs. The vertex position is available as several Level 1 trigger terms; it can also be used in Level 2 processing. The Level 0 system can also identify events which are likely to contain multiple interactions.

4.3 Level 1 Trigger Selection Criteria

The Level 1 trigger used in this analysis is based mainly on the DØ Level 1 calorimeter trigger. The other trigger terms used are the L0_FASTZ_GOOD and MRBS_LOSS terms described below. A description of the Level 1 (L1) calorimeter trigger hardware can be found in Chapter 3.

A passing L0_FASTZ_GOOD trigger term indicates 1) that an inelastic collision has occurred in the DØ detector and 2) that the fast vertex z position is within ± 97 cm of the nominal vertex position.

Since the Main Ring passes through the DØ detector, losses from the Main Ring will show up in the detector and must be rejected. The largest losses occur when beam is injected to the Main Ring every 2.4 s, and again 0.3 s later when the beam passes through transition. Transition is the point in the acceleration cycle at which the energy of the particles is sufficient to require a change between a non-relativistic model and a highly relativistic model for the behavior of the particles; the energy at which it occurs depends both on the mass of the particles being accelerated and the size of the accelerator ring.

When a bunch of non-relativistic particles are traveling in a circular orbit the particles with a larger than average momentum will also have a larger than average velocity and will pull ahead of the rest of the bunch. In order to keep the bunch from blowing up longitudinally, the particles near the front of the bunch must be decelerated relative to the mean momentum of the bunch, and those near the tail must be accelerated relative to the mean momentum of the bunch. Highly relativistic particles, however, must be treated differently. In this energy region, the velocity of a particle is nearly c and constant regardless of its momentum, however, the path length is not constant. A particle with larger than average momentum will have a larger

than average bending radius and will thus fall behind the rest of the bunch. So in this situation, one must accelerate the head of the bunch more than the tail. Properly rearranging the accelerating fields when passing through transition is difficult, and accelerators often produce extra losses at that point.

These losses are dealt with by vetoing on the MRBS_LOSS trigger term. This term is asserted as a possible veto during a 0.4 s window starting at injection, continuing through transition, and allowing time for the calorimeter and muon high voltage to recover from the large losses. This results in a dead time of about $0.4/2.4 \approx 17\%$.

The granularity of the L1 calorimeter trigger is $\Delta\eta = \Delta\phi = 0.2$ out to $|\eta| = 4.0$. The energy deposited in the calorimeter layers is summed into EM, hadronic, and EM+hadronic towers according to DØś pseudo-projective geometry and converted to E_T using $\sin\theta$ lookup tables as described in Chapter 3. The L1 trigger used in this analysis required 2 EM towers with $E_T > 7.0$ GeV and was known by the mnemonic EM_2_MED.

Ideally, a single EM tower trigger would have been better suited for a highly efficient L1 Drell-Yan trigger due to the electron energy asymmetry from the z boost caused by $x_a \neq x_b$. Unfortunately, the L1 to L2 event rate for such a trigger would much too high unless the E_T threshold was raised to values unsuitable for lower mass Drell-Yan kinematics. In addition, since L1 only has four available EM thresholds, they must be shared among all physics triggers, so compromise is necessary. Consequently, it was not possible to trigger on tower energy instead of E_T (thus allowing a sharp mass turn-on) nor to lower the L1 E_T threshold for the EM_2_MED trigger and cut harder in L2, since all users of this L1 trigger would have to agree to the change. For these reasons, the trigger used in this analysis was also used for the DØ Z boson analysis, and the thresholds were set to provide a very efficient L1 and L2 Z trigger

while still maintaining a low event rate. The efficiency of this trigger for Drell-Yan events is lower due to the difference between Drell-Yan and Z kinematics, especially for low mass Drell-Yan events.

The L1 efficiency turn-on is slower than one might naively expect since no clustering is being performed in L1. Since L1 has fixed towers of size $\Delta\eta = \Delta\phi = 0.2$, an electron may impact near the boundary of two towers (or even 4 towers in the worst case) sharing its energy between them. The result of this is that the L1 calorimeter trigger is not 100% efficient until the electron E_T is four times the threshold value! However, it is about 99% efficient at two times the L1 threshold value. A plot of the L1 efficiency turn-on for a 7 GeV L1 E_T threshold vs. the offline E_T of the cluster is shown in Figure 4.1. The offline E_T threshold was raised to 11.0 GeV to avoid the large uncertainty at $E_T = 10.0$ GeV. The efficiency of the EM_2_MED trigger is then the product of the efficiencies for the E_T of each EM cluster. A description of the Monte Carlo data used to measure this efficiency may be found in section 4.6.1.

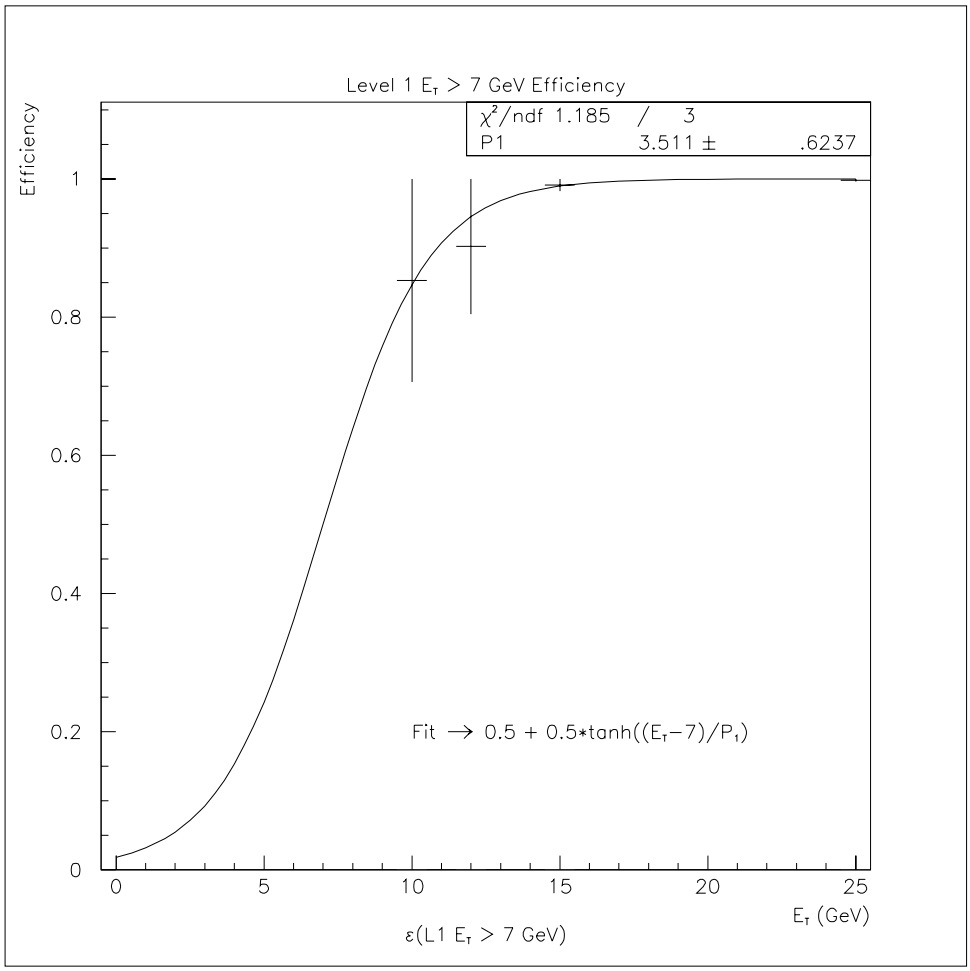

Figure 4.1: The Level 1 trigger efficiency vs. input E_T

4.4 Level 2 Trigger Selection Criteria

Events passing the EM_2_MED L1 trigger are passed on to the Level 2 system for further processing. The data used in this analysis were required to pass the ELE_2_HIGH filter script. A detailed description of the algorithm used by the L2_EM filter tool to select good electron candidates is given in Appendix A of this dissertation. The reader should refer to Appendix A for a description of the selection cuts referred to below.

The L2_EM filter algorithm uses the full segmentation of the DØ calorimeter to identify candidate electron showers. The trigger towers which fired the L1 EM_2_MED trigger are used as seeds for a simple clustering algorithm in the L2_EM filter. The highest E_T EM3 cells in the passing L1 trigger towers are found and the cells contained in a $\Delta\eta \times \Delta\phi = 0.3 \times 0.3$ square in each EM layer and the first FH layer around the EM3 seed cells are used to construct the majority of the L2_EM shower shape selection variables.

The L2_EM filter algorithm is based mainly on whether the EM+FH1 candidate cluster shapes are consistent with the shape of a typical electron shower in the DØ calorimeter. L2_EM uses the cluster cell E_T to form various shower shape variables which are compared to values determined from real electrons in the DØ test beam.

The cell E_T is used instead of cell energy for the shower shape variables because the Level 2 unpacking algorithm provides cell E_T for fast cluster E_T calculation. Since the $\sin\theta$ variation over a typical EM cluster is small and the majority of the L2_EM cut variables are ratios, the effect of using cell E_T instead of cell E is negligible.

The first L2_EM cut performed on candidate electrons from L1 is a cluster EM E_T cut. The sum of the E_T in the 4 EM calorimeter floors is corrected for the event vertex (Level 0 slow vertex z, resolution of ± 3.5 cm) and for energy leakage outside of the 3X3 readout tower cluster and compared to etmin_cc or etmin_ec depending upon

the cluster location within the DØ calorimeter.

Candidates which pass the E_T cut can then be subjected to longitudinal and transverse shower shape cuts. It was determined early in Run 1A that an acceptable event rate could be achieved with an E_T cut of 10 GeV on both electron candidates without using these cuts. The increase in the efficiency of the ELE_2_HIGH filter by not using these cuts was deemed preferable to a lower L1/L2 E_T threshold in combination with them for Z→ee events, thus they were not used in this analysis either. These cuts are however used for single electron triggers and provide an additional rejection of approximately a factor of three. A track match cut may also be performed after the shower shape cuts, but again it was not needed.

The final cut performed by L2_EM is an E_T isolation cut. The difference of the sum of the E_T in a $R = \sqrt{\eta^2 + \phi^2} = 0.4$ radius cone of readout towers and the cluster E_T ($R = 0.15$) is calculated and divided by the cluster E_T to form an isolation fraction. The electron candidate fails if its isolation fraction is greater than 0.15.

The ELE_2_HIGH filter required two electron candidates to pass E_T and isolation fraction cuts. The Level 2 efficiency vs. E_T for single electrons are in shown Figure 4.2. The offline E_T threshold was raised to 11.0 GeV to avoid the large uncertainty at $E_T = 10.0$ GeV. This plot was produced by overlapping single electron Monte Carlo events (plate level DØGEANT) with real DØ minimum bias events to simulate the electronic and uranium noise and underlying event activity in a typical DØ EM event and then running them through the Level 1 and Level 2 simulators. A description of the Monte Carlo data used to measure this efficiency may be found in section 4.6.1.

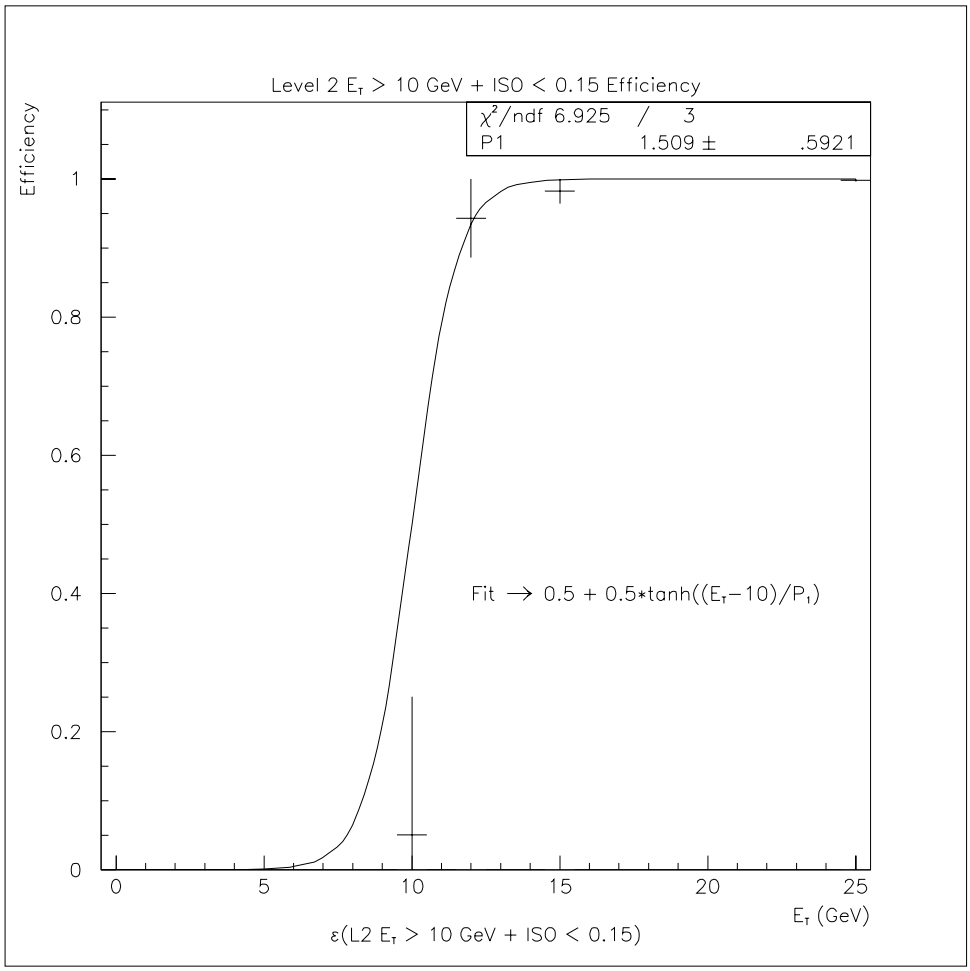

Figure 4.2: The Level 2 trigger efficiency vs. input E_T

4.5 Offline Data Reconstruction

The raw event data from the DØ detector is in the form of digitized counts of charge deposited in a calorimeter cell, counts per time bin for a tracking chamber wire etc. These quantities must be converted into meaningful data such as EM cluster energy or E_T, track position, and event vertex position to facilitate physics analysis. This conversion process is called "reconstruction", and is performed by a program known as DØRECO. DØRECO reads in all the calibration data and conversion constants for all the DØ sub-detectors and applies this data to all the measured quantities for an event to produce kinematic and particle selection variables. Event reconstruction can be divided into three main stages:

Hit Finding the raw detector data is unpacked and converted into *hits*, which consist of energy deposits in calorimeter cells, pulses on tracking chamber wires etc.

Clustering and Tracking hits whose spatial separation is small are combined to form *clusters* in the calorimeter or *tracks* in the tracking chambers.

Particle Identification calorimeter energy clusters and tracking chamber tracks as well as other information are combined to identify the sources of the tracks and clusters as electron, photon, jet, or muon candidates. The criteria used to identify the particle candidates are quite loose at this stage to guarantee high particle acceptance so as not to lose any candidates. In addition, DØRECO computes many selection variables to be used in further analysis, where much tighter selection cuts are generally used to construct a final data sample for a given analysis.

4.5.1 Energy Reconstruction

Calorimeter hit finding basically consists of converting the charge deposited in a calorimeter cell to energy in GeV. The conversion factors are determined primarily from test beam measurements where the calorimeter response to an incident particle of known energy and position is found. The conversion factors, known as "sampling fractions", are then used to reconstruct the unknown energies of particles in DØ. Additional cell-by-cell corrections are made for variations in electronics gain and pedestals. These corrections are periodically measured during times in which there are no collisions and are stored in a database which is accessed by DØRECO during reconstruction. However, due to various differences between the fixed target test beam setup and the collider installation of the DØ detector, this calibration is slightly low and must be corrected. Fortunately, the mass of the Z boson has been measured very precisely at LEP [56], and so serves as an additional calibration point. The measured electron energies are scaled up so that the Z boson peak in the e^+e^- mass distribution matches the LEP measurement. This correction is about 5% in the CC, and 1-2% in the EC.

After finding the calorimeter cell energies in GeV, cells with the same η and ϕ coordinates are summed together for the EM and hadronic layers of the calorimeter to form readout "towers". These towers are then used in subsequent clustering algorithms which attempt to reconstruct the total energy or E_T of the incident particles.

4.5.2 Track Reconstruction

Hit finding in the DØ tracking chambers is begun by unpacking the digitized charge deposition versus time. Individual pulses are identified by looking for leading and trailing edges of pulses. Each pulse is integrated to find the total deposited charge.

This integrated charge is then used to compute the energy deposition per unit g/cm^2 traveled through the tracking chamber, known as dE/dx. The arrival time of the pulse at the front end electronics is used to find the position of the pulse. The time required for the ionization created by the particle traversal to drift to the sense wire measures the radial distance of the hit from the sense wire, and the arrival time of the pulse on the delay line gives its location along the sense wire. Due to left/right ambiguities, there may be two possibilities for the location of a hit which are both used as input to the tracking phase. The staggering of the sense wires usually guarantees that only the correct solutions will yield a good track.

In central detector tracking, the object is to identify groups of hits which lie along a straight line. Tracking is first done for each individual layer of the detector to produce track segments. The track segments are then matched between the layers of each detector to form tracks. Finally, these tracks are matched between the vertex chamber, TRD, and outer tracking chambers (CDC and FDC).

4.5.3 Muon Reconstruction

A similar procedure is used to find muon tracks in the DØ muon detector. However, due to differences in geometry and electronics, the details are quite different. A basic description of DØ muon momentum measurement is as follows: A muon track is found in the central detectors as described above and is then matched to a track in the A layer of the muon detector. This gives the track direction before the toroidal magnet. A track in the muon detector B and C layers is then found, and the angle between this track and the track from the central detector and muon A layer is computed. This angle in combination with the value of the magnetic field in the toroid is then used to compute the muon momentum.

4.5.4 Vertex Reconstruction

In order to compute the transverse energy or momentum of a particle it is necessary to measure the origin of the particle in the lab frame which is known as the event "vertex".

The x and y positions of the vertex are well known due to the fact that the cross-section of the beam is made very small in these dimensions in order to maximize the luminosity. The typical cross-section of the beam was about 50 μm and is positioned about 3-4 mm from the center of the detector with a drift of less than 50 μm over the length of a data run. Thus, the (x, y) position of the vertex can be taken as a constant, and for many purposes can be set to (0,0) (the geometrical center of the detector).

The z-coordinate of the vertex, however, is less well constrained. Each bunch of particles in the Tevatron has some extent along the beam direction, and the resulting width of the vertex z-coordinate distribution in the detector is about 30 cm. Thus, it is necessary to measure the z-position of the vertex for each event individually. This is done using tracks found in the CDC. The vertex finding method is as follows:

- Project the tracks found in the CDC back towards the center of the detector.
- For each track, calculate the impact parameter (the minimum distance between the track and the z-axis of the detector). Discard all tracks with an impact parameter larger than a given cutoff. (This eliminates low-momentum tracks which have undergone a large amount of multiple scattering.)
- Project each track into the (r, z) plane, and compute the intersection with the z-axis. Plot the z-positions of the intersections.
- Fit a Gaussian around the peak of the resulting distribution. The mean is the estimate of the z-position of the vertex. The tails of the distribution are also

searched for any secondary peaks.

The resulting resolution for the vertex z-coordinate is about 1-2 cm. Multiple vertices can typically be separated if they are at least 7 cm apart.

4.6 Offline Electron Identification

A standard DØ electron candidate, called a PELC, is constructed in the following manner:

- Candidate electron clusters are formed from calorimeter towers using a "nearest neighbor" algorithm [55]. Towers adjacent to the highest E_T tower are added to the cluster if they are above a given E_T threshold, and the cluster size is not too large.
- A PELC must have at least 90% of its energy in the EM calorimeter, and at least 40% of its energy must be contained in a single tower.
- Using the finer resolution cells in the EM3 layer, the cluster centroid is found by computing the log-weighted weighted sum of the cell positions

$$\vec{r}_{centroid} = \frac{\sum_i w_i \vec{r}_i}{\sum_i w_i}$$

where the weights w_i are given by

$$w_i = \max\left(0, w_0 + \ln\left(\frac{E_i}{\sum_j E_j}\right)\right)$$

The parameter w_0 is chosen to minimize the centroid uncertainty and the sums

are over all EM3 cells in the cluster. The resulting position resolution is about 1.5-4 mm.

- The reconstruction program then searches for a central detector track pointing from the event vertex to the calorimeter cluster within a "road" of $\Delta\eta = \Delta\phi = \pm 0.1$. If such a track is found, the cluster is identified as an electron candidate "PELC"; otherwise, it becomes a photon candidate "PPHO".

The above electron candidate (PELC) criteria are intentionally very loose so as not to lose any real electrons. Hence, the PELC sample is generally intended to be used as starting sample for electron final states and therefore to undergo further selection cuts for a given analysis. The starting data sample used for this analysis consisted of events containing 2 PELC objects with $E_T > 10$ GeV that passed the L1 EM_2_MED trigger and L2 ELE_2_HIGH filter. The additional cuts performed to select the final data sample are described below. The PELC criteria are a superset of the PPHO criteria since it is simply an additional requirement of a track within a $\Delta\eta = \Delta\phi = \pm 0.1$ road of PPHO candidate. Although the PPHO and PELC requirements are intended to be loose, and thus very efficient for real electrons, they are not 100% efficient and so the efficiency of these cuts on real electrons must be measured. Since the PELC criteria are a superset of the PPHO criteria, we may measure PPHO efficiency and then measure the PELC/PPHO efficiency (add the track requirement to a set of PPHOs).

To measure the PPHO efficiency we generate single Monte Carlo electrons and then measure the number of these Monte Carlo electrons that are reconstructed as PPHOs by the DØRECO reconstruction program. The Monte Carlo electrons are described in more detail in the following section. There is little energy or IETA dependence in the PPHO efficiency so we simply take the average of the PPHO efficiency for 10, 15, 25 and 50 GeV electrons in the CC, and the average PPHO efficiency for 25, 50,

100 and 200 GeV electrons in the EC. The CC PPHO efficiency is 97.7% and the EC PPHO efficiency is 99.4%.

The tracking portion of the DØ detector simulation has been shown to exceed the actual performance of the DØ tracking chambers [58], consequently Monte Carlo electrons are not used to measure the PELC efficiency. Instead of measuring the PELC efficiency directly, we measure the PELC/PPHO efficiency, namely the additional efficiency loss incurred by the PELC track requirement. Since the energy dependence of the DØ tracking resolution is minimal above 10 GeV (see section 4.6.3), it is possible to use high energy electrons to measure the PELC/PPHO efficiency. Thus we use electrons from Z decays to measure this efficiency. We start with a sample of PELC-PELC, PELC-PPHO, PPHO-PPHO events and require that the E_T of each PELC or PPHO be greater than 11.0 GeV. We then require that the invariant mass of the PELC-PELC, PELC-PPHO, PPHO-PPHO pair be within a 80-100 GeV mass window. We then perform all of the electron identification (id) cuts listed in Table 4.1 on one PELC/PPHO object, and if it passes, we fill histograms of energy, E_T, and IETA of the other PELC/PPHO object. This process is done again, but with the further requirement that the other object be a PELC. We then switch which object has the electron id cuts made on it and which goes into the histograms and repeat the process to double our statistics. The electron id cuts and the mass cut provide a fairly background free sample of real electrons from Z decays, which allows us to measure the PELC/PPHO efficiency by simply dividing the set of histograms with the additional PELC requirement by the histograms without this requirement. Figure 4.3 shows the resulting PELC/PPHO efficiency. Since there is no obvious energy, E_T, or IETA dependence we fit a flat line to each of these distributions and take the average as the PELC/PPHO efficiency. The PELC/PPHO efficiency is 86.9%, which is then multiplied by the PPHO efficiency to give the total PELC efficiency for electrons.

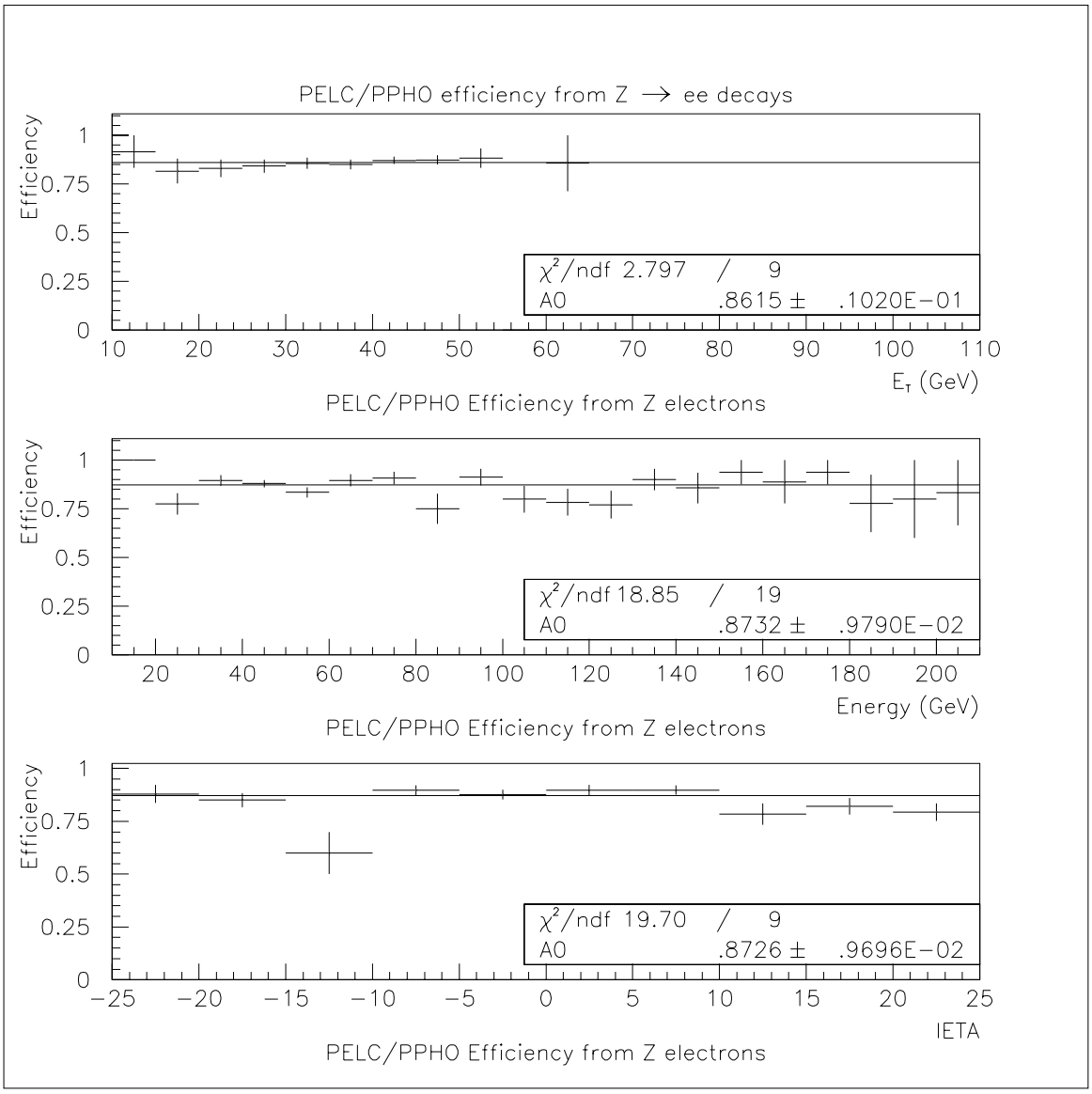

Figure 4.3: PELC/PPHO efficiency vs. E_T, E, and IETA.

4.6.1 H-matrix

The primary tool used for quantifying the information contained in the shape of the electromagnetic shower is the "H-matrix" χ^2 [57]. The H-matrix χ^2 does not follow a χ^2 distribution since the observables from which it is constructed are not Gaussian, but its definition is similar. Given a set of N observations of events of a given type, where each observation forms a vector of M variables $o^i = \{o^i_1, \cdots, o^i_M\}$, it is possible to form an estimate of the covariance matrix V

$$V = \frac{1}{N}\sum_{i=1}^{N}(o^i - \mu)^\top (o^i - \mu)$$

where μ is the mean of the N observations, namely, $\mu = \{\mu_1, \cdots, \mu_M\}$. The inverse of the covariance matrix is the "H-matrix"

$$H = V^{-1}$$

For any subsequent observation o' one can define a χ^2 that is a measure of how likely o' came from the same distribution as μ

$$\chi^2 = (o' - \mu)H(o' - \mu)^\top$$

Figures 4.4 and 4.5 show the H-matrix χ^2 distributions for electrons and background respectively.

A total of $M = 41$ variables were used in the construction of the H-matrix (41 degrees of freedom): the fraction of the total cluster energy contained in the EM1, EM2, and EM4 calorimeter layers (longitudinal shower shape), the fraction of the

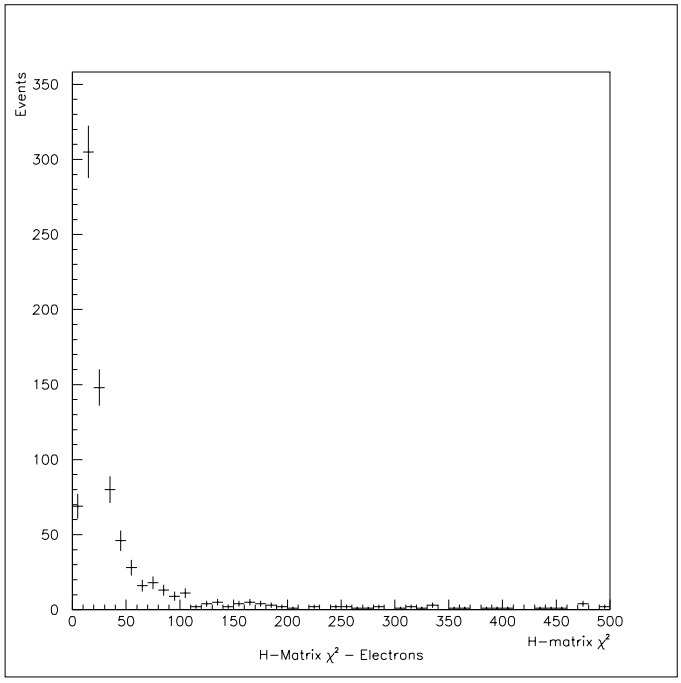

Figure 4.4: H-matrix χ^2 for electrons.

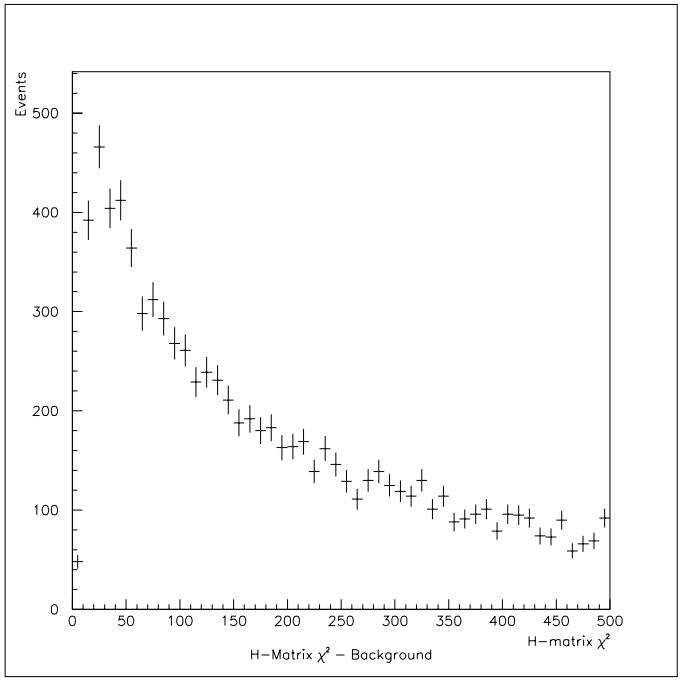

Figure 4.5: H-matrix χ^2 for background.

cluster energy contained in the 36 EM3 layer cells making up a 6×6 array around the highest E_T tower in the cluster (transverse shower shape), the logarithm of the cluster energy (to account for the energy dependence of the shower shape), and the z-position of the event vertex (to account for the change in the shower shape due to the impact angle of the track with calorimeter). A separate H-matrix is constructed for each ring in IPHI at each calorimeter |IETA| index.

In order to construct the H-matrix and the mean vector μ it is necessary to have a data sample which is believed to accurately represent properties of an electron interacting with the DØ detector over the full range of energies and angles. Due to lack of adequate test beam data (uniform illumination of each calorimeter IETA index at many energies) and the differences in the energy scale between the test beam and DØ described above, it was decided that Monte Carlo data would be used to tune the H-Matrix. A detailed representation of the DØ detector geometry was used in combination with the GEANT 3.14 Monte Carlo detector simulator from the CERN program library to simulate electron tracks passing through DØ. Ideally, one would construct an H-Matrix using input events which reflect the jet and underlying event activity as well as the kinematics of the physics signal one wished to extract. Unfortunately the amount computing time this would require is immense since propagating all the hadrons created in a typical $p\bar{p}$ event is *very* CPU intensive (not to mention the time required to perform the H-matrix construction for each analysis). Consequently, single electrons were used as the input to the DØGEANT simulation. One would expect then, that the H-Matrix would be less efficient at selecting real DØ electrons for a given χ^2 cut than it is at selecting single MC electrons.

In an attempt to simulate the effect of the actual DØ environment, single MC electrons were combined event by event with random minimum bias events taken at a luminosity of $2.5 \times 10^{30}\mathrm{cm}^{-2}\mathrm{s}^{-1}$. Minimum bias events taken at this luminosity were

chosen because the average instantaneous luminosity over all of Run 1A was around $2.5 - 3.0 \times 10^{30}\mathrm{cm}^{-2}\mathrm{s}^{-1}$. The difference in the efficiency measured without adding the minimum bias to the Monte Carlo electrons is on the order of 5%, so it is not a very large correction. The minimum bias events contain the effects of uranium noise and pile-up as well as some amount of hadronic activity that roughly approximates the underlying event activity in a typical DØ Drell-Yan event. The energy in the calorimeter cells of the single MC electron events is converted into equivalent ADC counts and added to the cell ADC counts from the raw minimum bias data before the zero suppression cut is performed. The events are then reconstructed as if the combined event originated in DØ. This data is then used to measure the efficiency of the H-matrix χ^2 cut. A plot of the efficiency of this cut versus input electron energy and calorimeter IETA is shown in Figures 4.6 and 4.7.

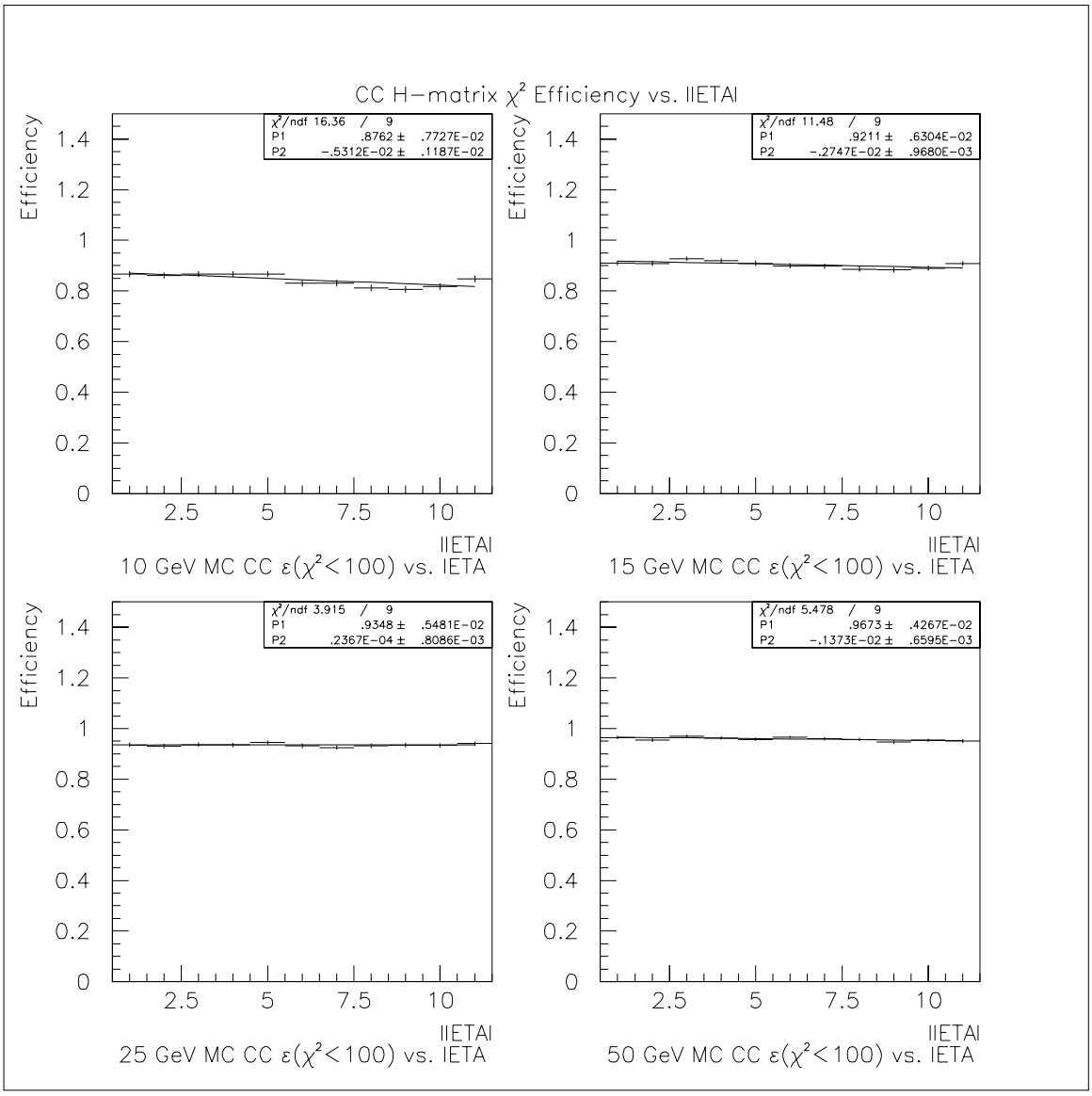

Figure 4.6: CC H-matrix $\chi^2 < 100$ Efficiency vs. input |IETA|.

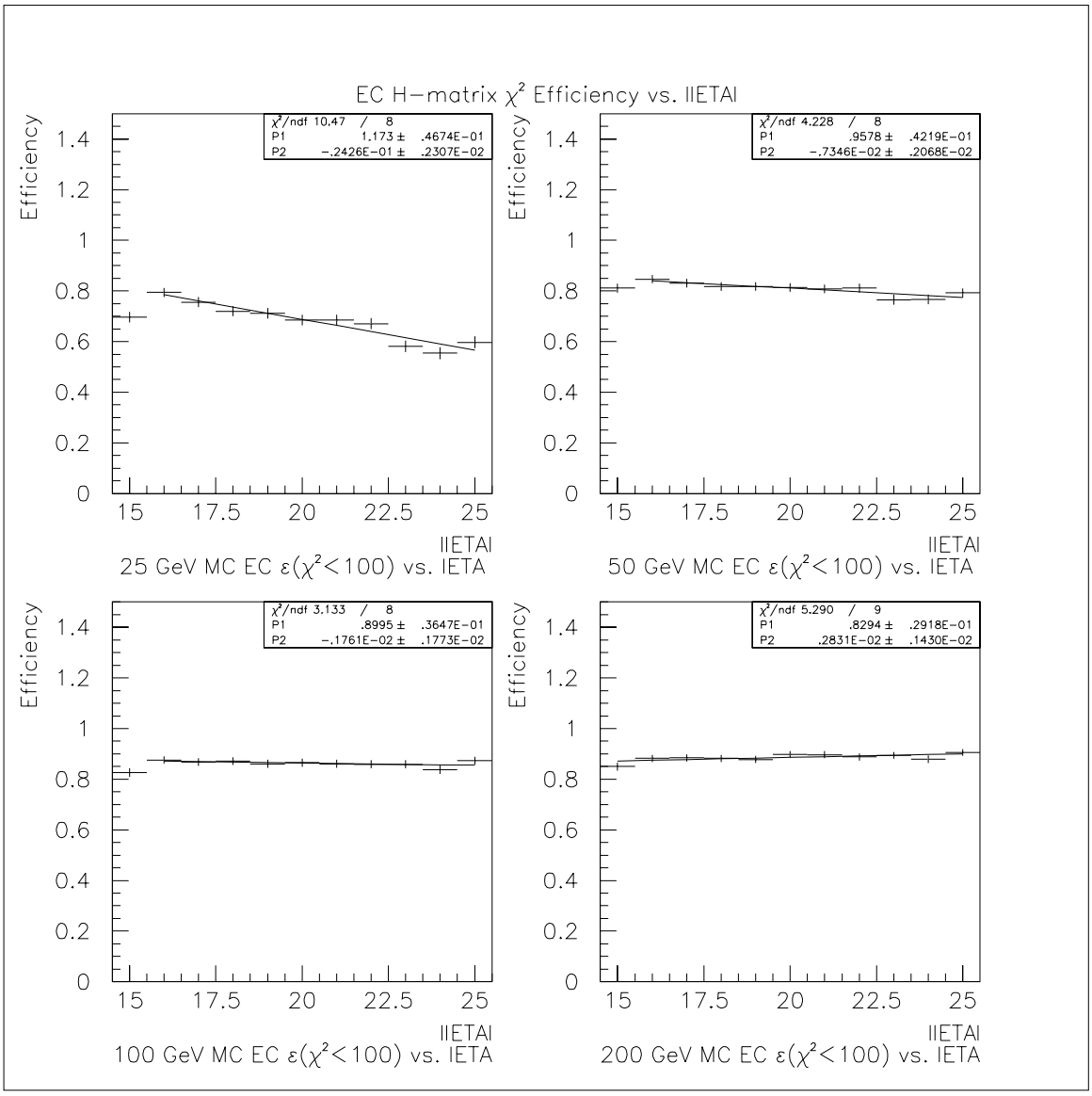

Figure 4.7: EC H-matrix $\chi^2 < 100$ Efficiency vs. input |IETA|.

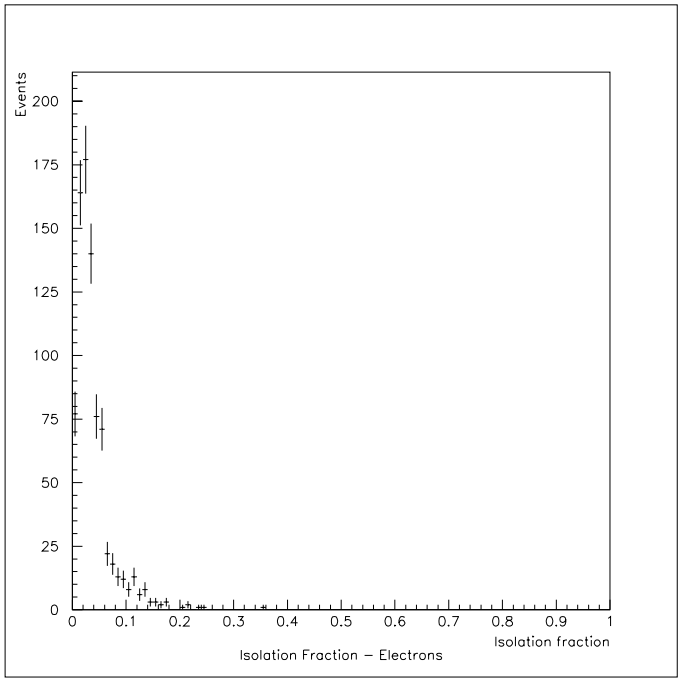

Figure 4.8: Isolation fraction for electrons.

4.6.2 Isolation Fraction

This variable is a measure of how isolated the PELC cluster is in the calorimeter. The definition of the isolation fraction is

$$ISO = \frac{E_{cone}^{Total} - E_{core}^{EM}}{E_{core}^{EM}}$$

where E_{cone}^{Total} is the total energy (sum of all calorimeter layers) contained in a cone of radius $\Delta R = \sqrt{\Delta\eta^2 + \Delta\phi^2} = 0.4$ and E_{core}^{EM} is the EM energy (sum of the four EM calorimeter layers) in a cone of radius $\Delta R = 0.2$. The electron candidate is required to have $ISO < 0.15$. The isolation fraction for electrons and background is shown in Figures 4.8 and 4.9 respectively.

Given the definition of this cut, one would expect that its efficiency increases with increasing electron energy. Since the amount of activity increases nearer the beam

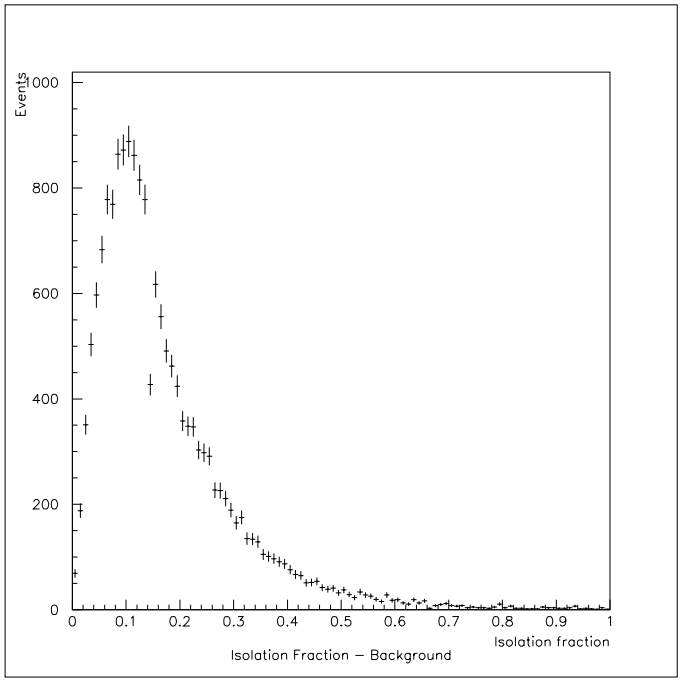

Figure 4.9: Isolation fraction for background.

pipe, one would also expect that the efficiency of this cut decreases as $|\eta|$ increases. The efficiency plots in Figures 4.10 and 4.11 bear out these expectations.

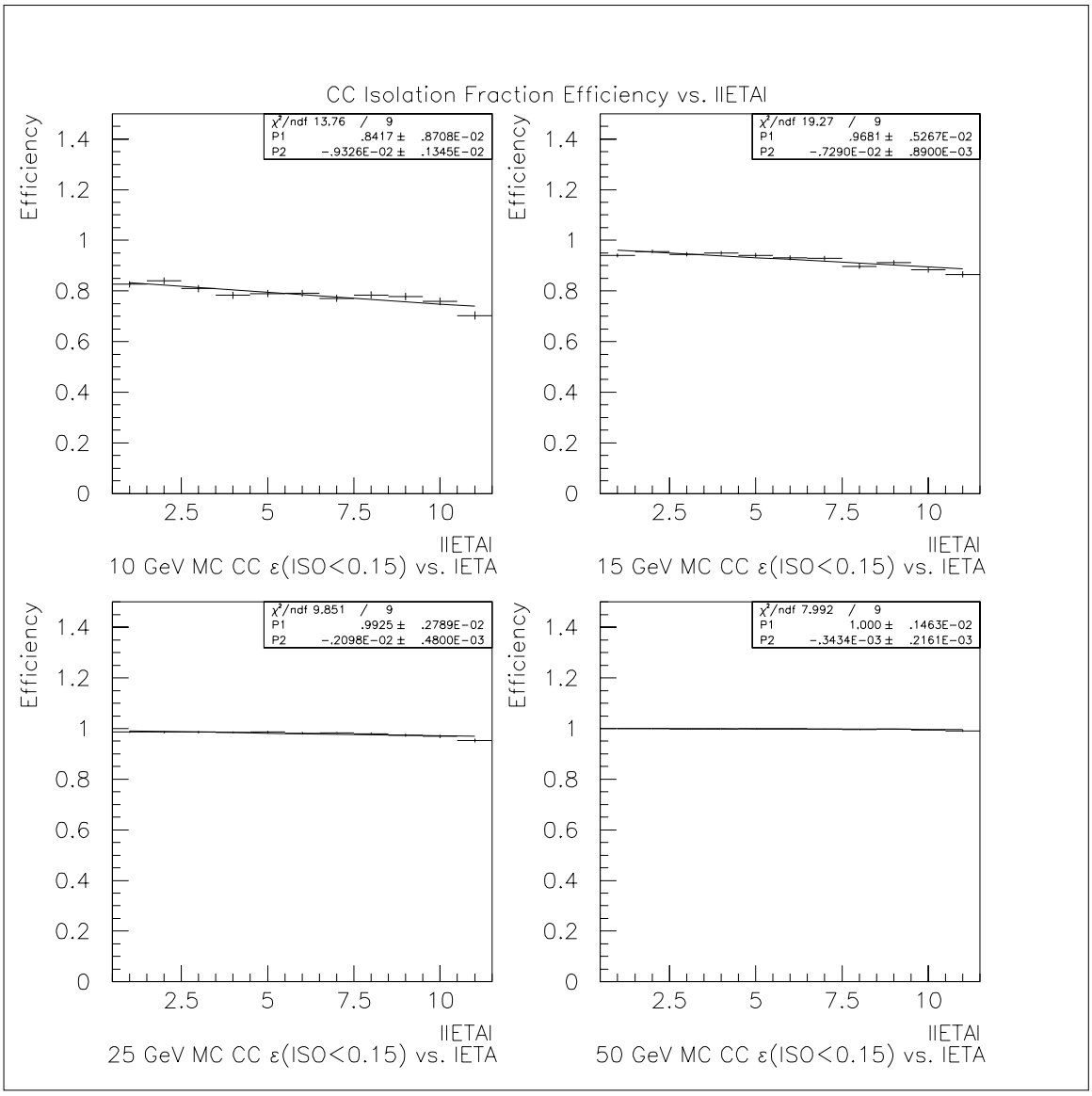

Figure 4.10: CC Isolation fraction $ISO < 0.15$ Efficiency vs. input |IETA|.

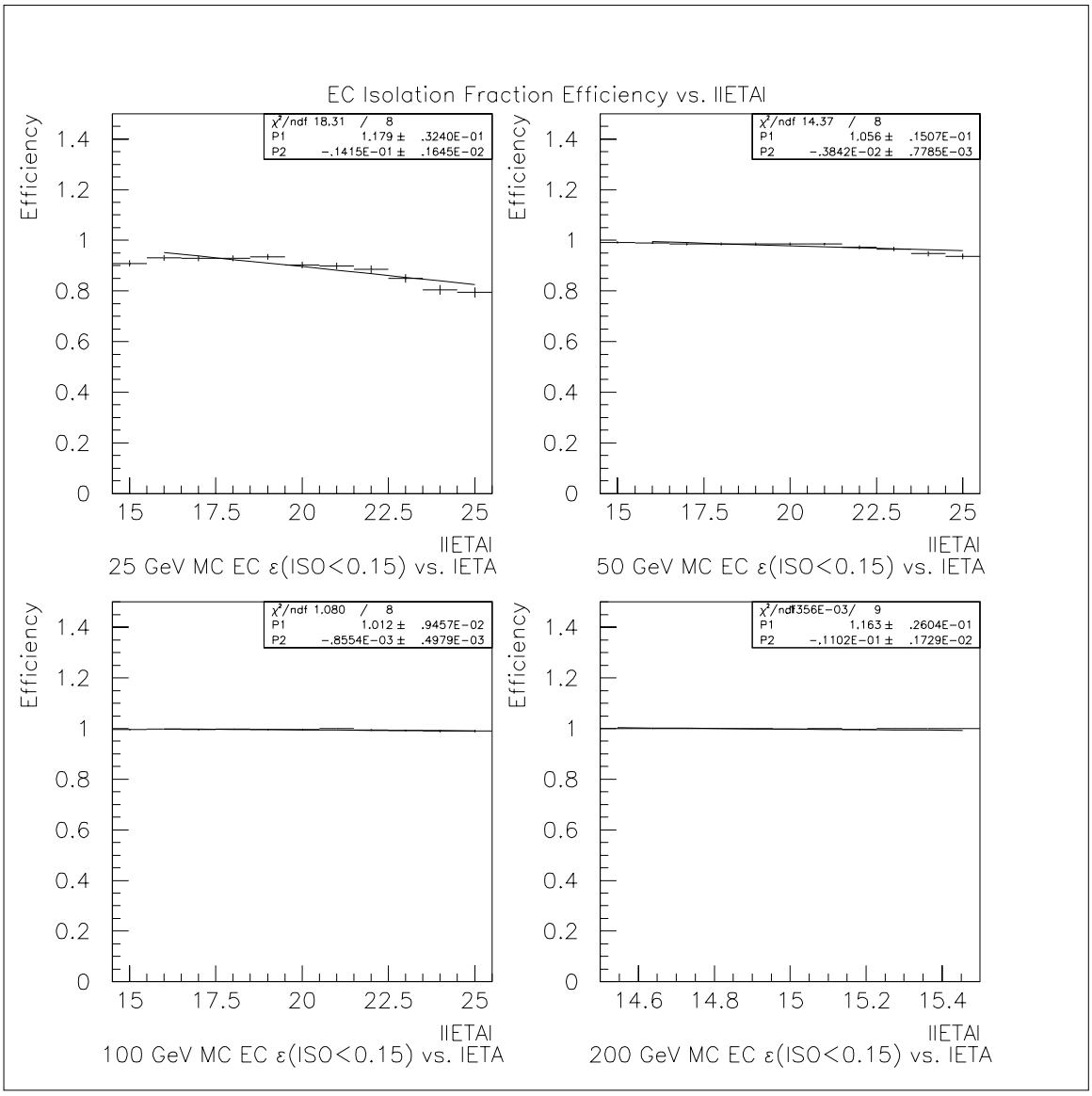

Figure 4.11: EC Isolation fraction $ISO < 0.15$ Efficiency vs. input |IETA|.

4.6.3 Track Match Significance

This variable is designed to reject EM objects which have no associated track. A large background to electrons in DØ are photons produced by π^0 and η decays. At Tevatron energies the pair of photons produced in these decays are generally not resolvable as separate photons and therefore the EM clusters produced look very much like electron clusters. However, since the photons are neutral, they do not produce tracks unless one of the photons converts prior to (or during) passage through the CD. Consequently this background may be rejected by requiring a CD track pointing to the EM cluster.

The track match significance is a χ^2 distributed variable defined as

$$\sigma_{trk-clus} = \sqrt{\left(\frac{R\delta\phi_{trk-clus}}{\sigma_{R\delta\phi_{trk-clus}}}\right)^2 + \left(\frac{\delta z_{trk-clus}}{\sigma_{\delta z_{trk-clus}}}\right)^2}$$

where $R\delta\phi_{trk-clus}$ is the transverse separation between the cluster centroid and the track position projected to the EM3 layer and similarly $\delta z_{trk-clus}$ is the z separation ($\delta z_{trk-clus}$ would be replaced by $\delta R_{trk-clus}$ in the EC). The $\sigma_{R\delta\phi_{trk-clus}}$ and $\sigma_{\delta z_{trk-clus}}$ are the position resolutions in $R\delta\phi$ and δz respectively. The position resolutions are made up of two components: the tracking resolution and the calorimeter position resolution

$$\begin{aligned}
\sigma_{R\delta\phi_{trk-clus}} &= \sqrt{\sigma^2_{R\delta\phi_{cal}} + \sigma^2_{R\delta\phi_{trk}}} \\
\sigma_{\delta z_{trk-clus}} &= \sqrt{\sigma^2_{z_{cal}} + \sigma^2_{z_{trk}}}
\end{aligned}$$

A plot of the track match significance for electrons and background is shown in Figures 4.12 and 4.13 respectively.

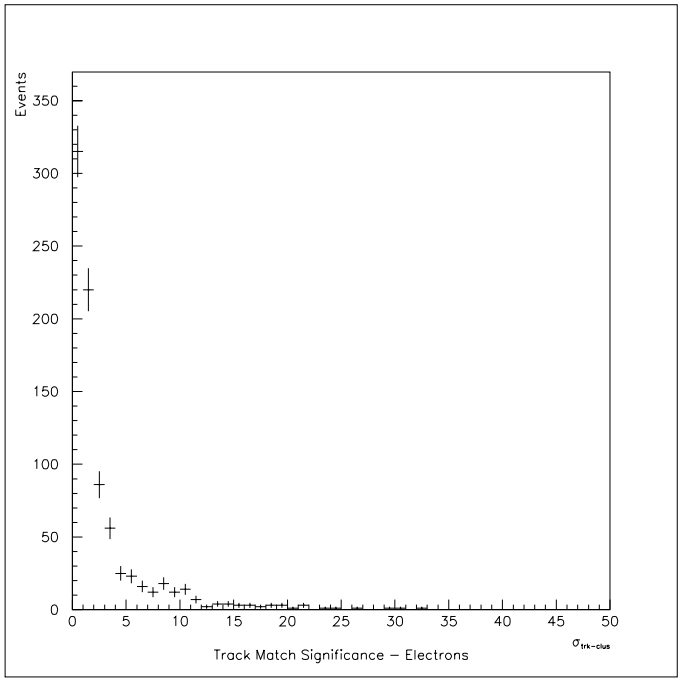

Figure 4.12: Track match significance for electrons.

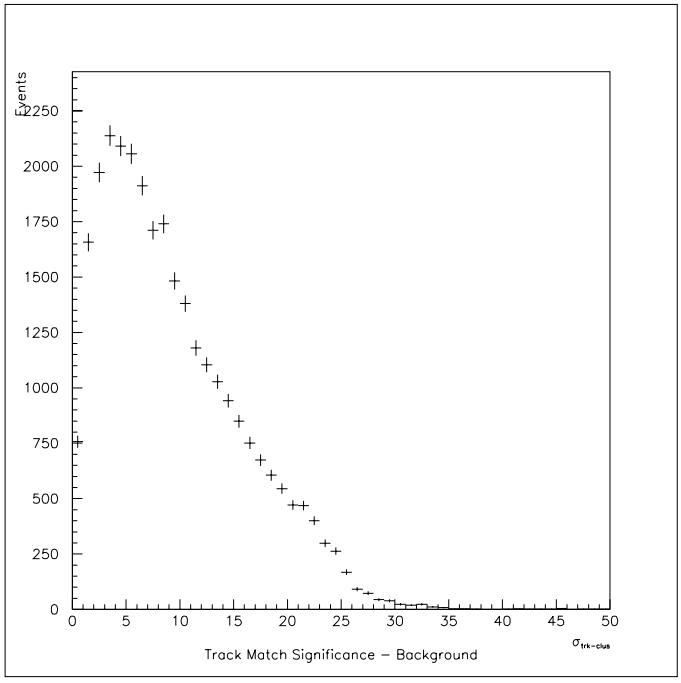

Figure 4.13: Track match significance for background.

The tracking resolution can be measured by projecting tracks back toward the beam and measuring the distance of closest approach between the reconstructed track and the beam to get the $\delta\phi$ resolution, and by measuring the z separation of the tracks to get the δz resolution [58]. This analysis was performed for the CDC but not for the FDC.

If d is the distance of closest approach between the reconstructed track and the beam, the width of the d distribution σ_d, is then related to $\sigma_{\phi_{trk}}$ by $\sigma_d = \sigma_{\phi_{trk}} R_{CDC}$ where R_{CDC} is the mean distance of the CDC sense wires from the beam. The measured σ_d was found to be 0.17 cm. The $\sigma_{R\delta\phi_{trk}}$ is then given by

$$\sigma_{R\delta\phi_{trk}} = (R_{EM3} - R_{CDC})\frac{\sigma_d}{R_{CDC}} = 0.082 \text{ cm}$$

where R_{EM3} is the distance from the beam to the EM3 layer (91.7 cm).

The measurement of $\sigma_{\delta z_{trk}}$ is somewhat more complicated since the vertex z position is not as well constrained as the (x, y) position, so a two track δz separation must be measured and the single track resolution subsequently extracted from it. A Gaussian fit to the distribution of the δz separation between two tracks projected back toward the event vertex gives a width of 4.5 cm [59]. Assuming the resolution of single tracks are independent and equal, the single track resolution $\sigma_{\delta z_{trk}}$, is then given by

$$\sigma_{\delta z_{trk}} = \frac{\sigma_{\delta z_{2tracks}} R_{CDC}}{(R_{EM3} - R_{CDC})\sqrt{2}} = 1.529 \text{ cm}$$

An alternative is to measure the total resolution $\sigma_{R\delta\phi_{trk-clus}}$ and $\sigma_{\delta z_{trk-clus}}$ instead of tracking and calorimeter position resolutions separately. This is done by simply measuring $R\delta\phi$ and δz for electrons from W boson decays (one can preferentially

select W electrons using a missing E_T cut) and fitting a Gaussian to the result. Unfortunately, this does not take into account any variation in the calorimeter or tracking position resolution with energy unless one bins the data in energy which was not done.

One does not expect much variation in the tracking resolution with energy for the following reasons: The multiple scattering formula for small angles is given by [60]

$$\theta_0 = \frac{13.6\text{MeV}}{\beta pc} z \sqrt{x/X_0}(1 + 0.038 \ln(x/X_0))$$

where $\theta_0 = \frac{\theta^{rms}_{space}}{\sqrt{2}}$. Thus we see that θ_0 is small for both 40 GeV (average W electron energy) and 10 GeV electrons by realizing that $\beta \approx 1$ and that although the magnitude of θ_0 differs by a factor of four, the value of θ_0 at 10 GeV is 0.025 degrees across the $x = 0.1X_0$ presented by the CD. This results in a mean deviation of only 0.013 cm between the positions at which the track impacts calorimeter with and without multiple scattering. Since all other factors which contribute to the tracking resolution are energy independent, and this deviation is a small fraction of the overall tracking resolution, the energy dependence of the tracking resolution may be ignored.

On the other hand, it has been shown that the calorimeter position resolution does vary significantly with energy [16] as well as position (IETA). The calorimeter position resolution was measured using single MC electrons combined with minimum bias data (to add noise and underlying event effects) by computing the difference between the reconstructed calorimeter position and the actual track direction from the MC. This was done for all IETAs at energies of 10, 15, 25 and 50 GeV in the CC and 25, 50, 100, and 200 GeV in the EC. The resulting distributions were then fit using a Gaussian to get the position resolution. The variation of $\sigma_{R\delta\phi_{cal}}$ and $\sigma_{z_{cal}}$ versus energy and IETA

are shown in Figures 4.14, 4.15, 4.16, and 4.17.

$\sigma_{z_{cal}}$ varies with both IETA and energy. The IETA dependence of $\sigma_{z_{cal}}$ was parameterized using $\sigma_{z_{cal}} = a+b(IETA)^4$, in the CC, and $\sigma_{z_{cal}} = a+b(IETA)+c(IETA)^2$, in the EC. The parameters from these fits were then fit versus energy using

$$\begin{aligned} a &= 1.813/\sqrt{E-4.5} + 2.620 \times 10^{-5} \cdot E^2 \\ b &= 9.608 \times 10^{-5} - 8.191 \times 10^{-7} \cdot E \end{aligned}$$

in the CC and

$$\begin{aligned} a &= 0.520 + 1.081 \left(\frac{1}{E-22.0}\right) \\ b &= -0.0314 - 0.0951 \left(\frac{1}{E-22.0}\right) \\ c &= 0.000517 + 0.00232 \left(\frac{1}{E-22.0}\right) \end{aligned}$$

to yield a 2 dimensional parameterization in energy and IETA for $\sigma_{z_{cal}}$.

$\sigma_{R\delta\phi_{cal}}$ does not vary with IETA in the CC, but does vary with energy in both CC and EC. Thus a constant was used to fit $\sigma_{R\delta\phi_{cal}}$ versus IETA in the CC; the EC IETA dependence was fit using the form $\sigma_{R\delta\phi_{cal}} = a + b(IETA) + c(IETA)^2$. The fit parameters were then fit versus energy using

$$a = 0.4073 - 0.00325E$$

in the CC, and

$$a = 0.186 + 0.922 \left(\frac{25.0}{E}\right)^{0.872}$$

$$b = -0.00446 - 0.0710 \left(\frac{25.0}{E}\right)^{0.825}$$

$$c = -0.0000605 + 0.00152 \left(\frac{25.0}{E}\right)^{0.792}$$

in the EC. Plots of the calorimeter position resolution are shown in Figures 4.14, 4.15, 4.16, and 4.17 with the energy and IETA parameterized fits (dashed), and the actual fit versus IETA (solid) superimposed.

In order to take into account the energy variation of the calorimeter position resolution in the track match significance, the parameterized calorimeter position resolution was combined in quadrature with the tracking resolution to give the overall track-to-cluster resolution. The tracking resolution was measured differently between the CDC and FDC. The CDC tracking resolution was measured as described above in this section. The FDC tracking resolution was gotten by subtracting the square of the measured 50 GeV calorimeter position resolution from the squared track-to-cluster resolution from W electrons and taking the square root. This FDC tracking resolution was then added in quadrature to the energy dependent EC calorimeter position resolution to yield an energy dependent track-to-cluster resolution for the EC-FDC track match significance.

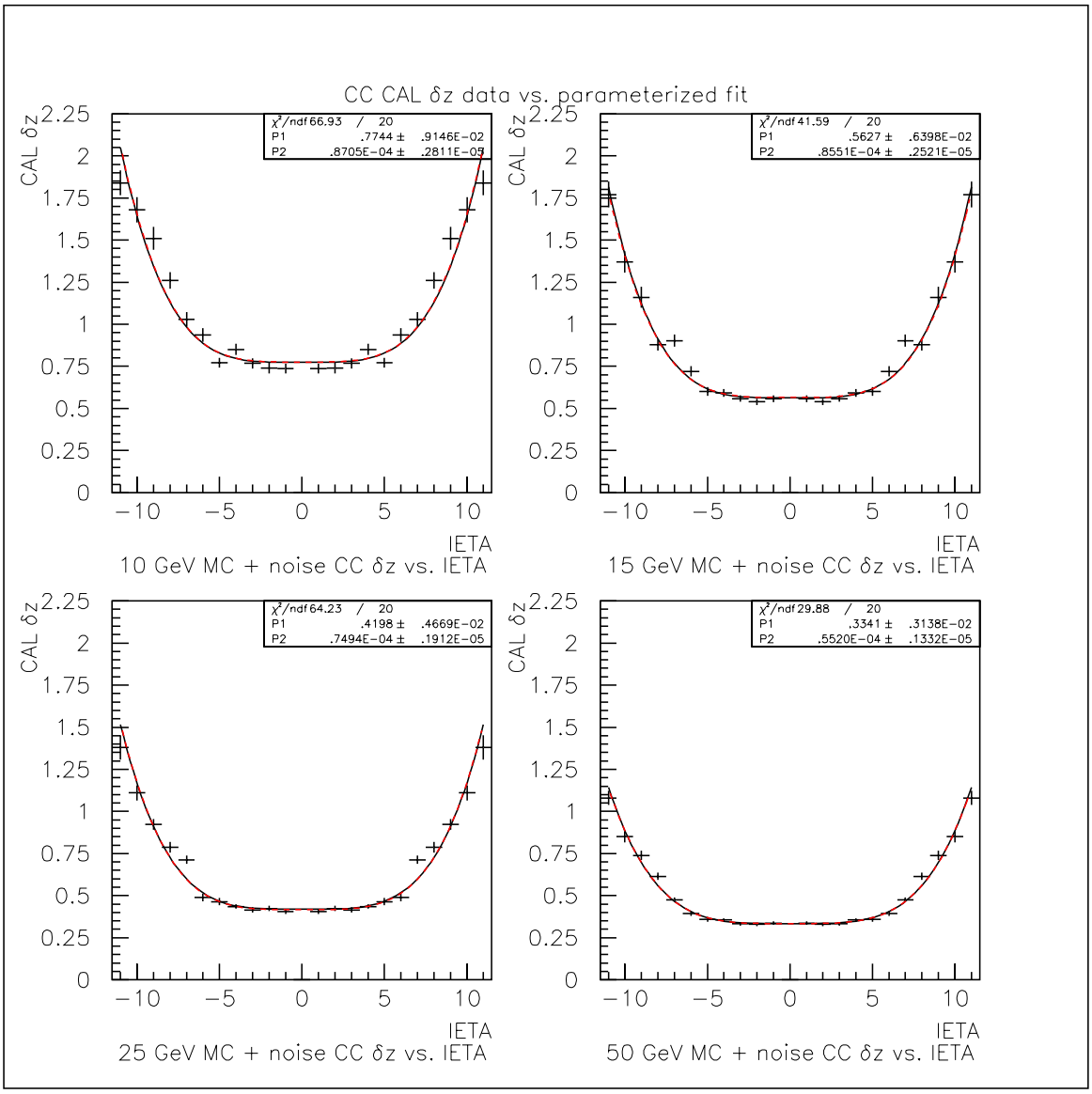

Figure 4.14: Central calorimeter $\sigma_{\delta z}$ vs. input energy and IETA. The solid curve is the fit vs. IETA; the dashed curve is the fit parameterized in energy and IETA.

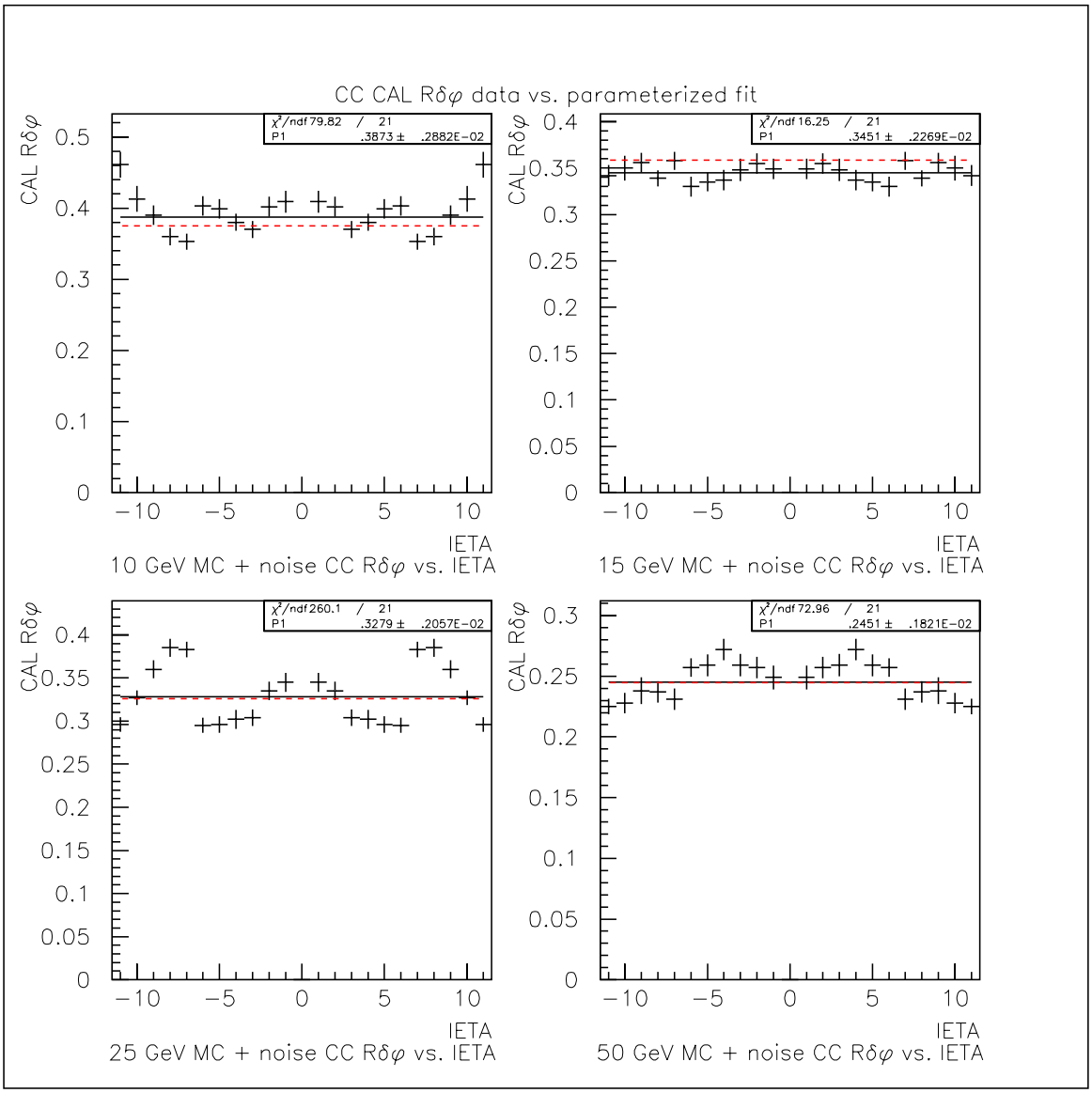

Figure 4.15: Central calorimeter $\sigma_{R\delta\phi}$ vs. input energy and IETA. The solid curve is the fit vs. IETA; the dashed curve is the fit parameterized in energy and IETA.

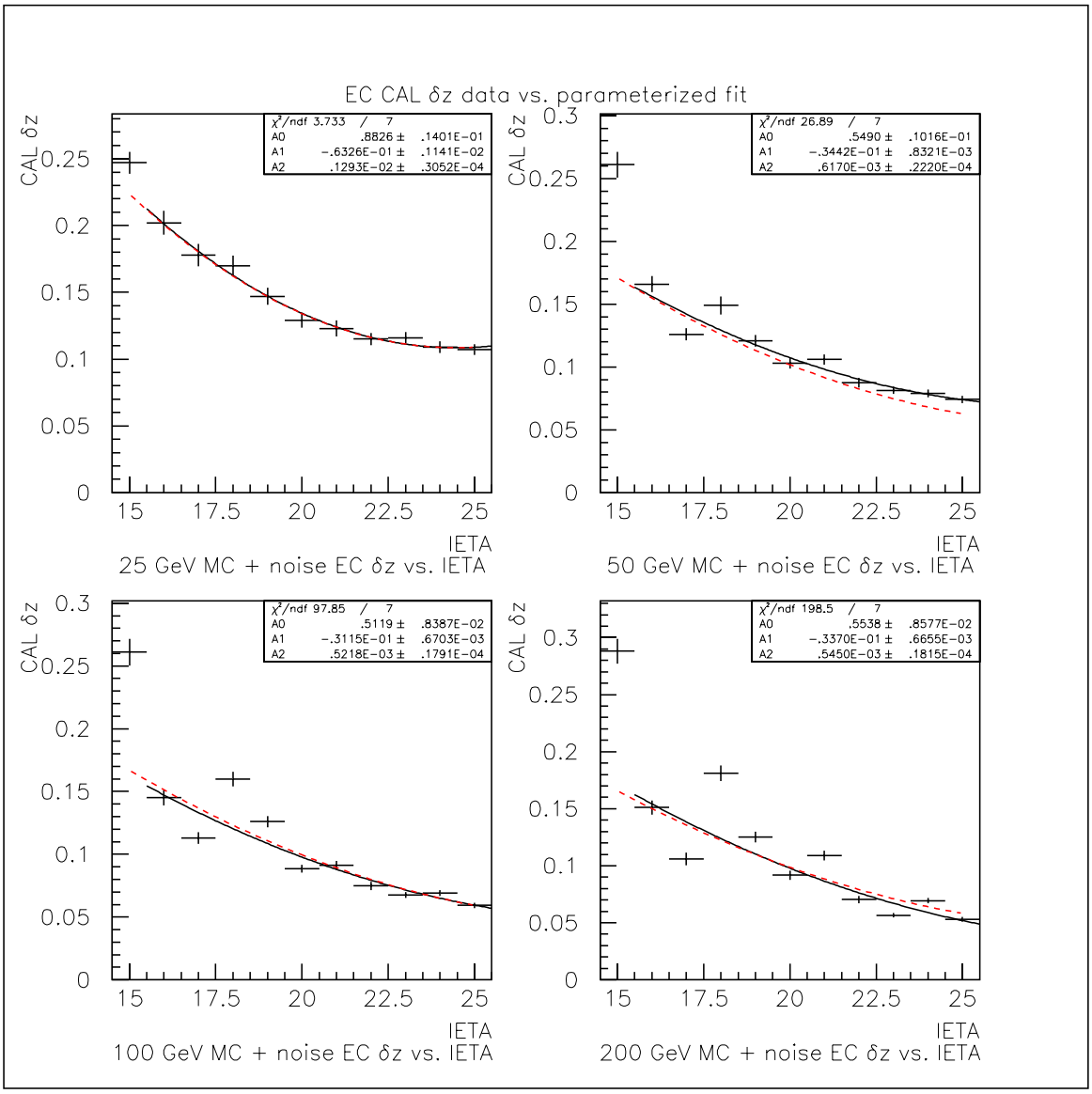

Figure 4.16: End calorimeter $\sigma_{\delta z}$ vs. input energy and IETA. The solid curve is the fit vs. IETA; the dashed curve is the fit parameterized in energy and IETA.

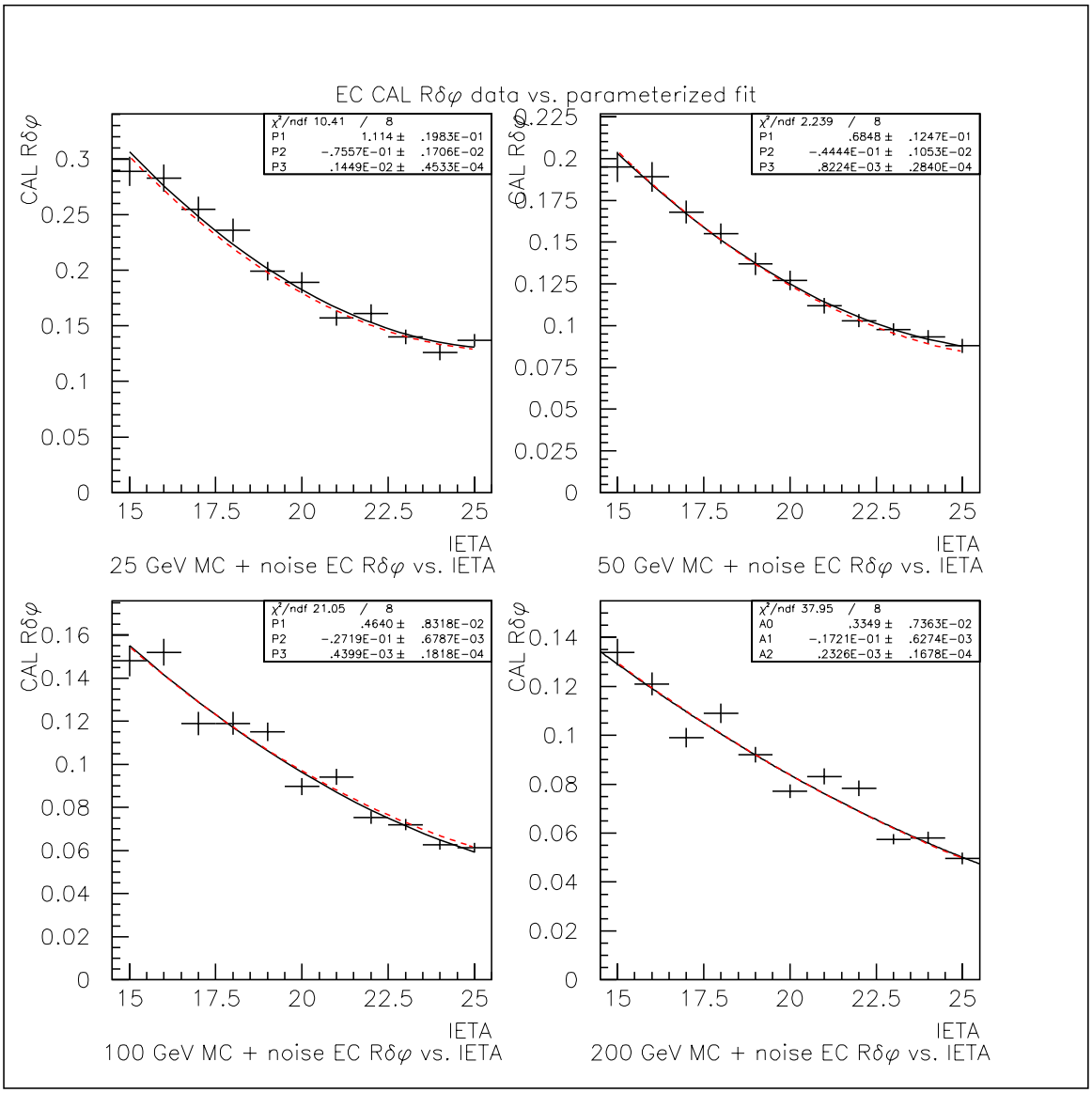

Figure 4.17: End calorimeter $\sigma_{R\delta\phi}$ vs. input energy and IETA. The solid curve is the fit vs. IETA; the dashed curve is the fit parameterized in energy and IETA.

4.6.4 dE/dx

Since DØ has no central magnetic field, e^+e^- pairs resulting from photon conversions do not diverge very far from each other, and are often reconstructed as a single track. However, the energy deposition per unit g/cm^2 in the tracking chambers will be twice that of a single electron (which is called one "MIP", for "minimum ionizing particle"). Thus, the background due to conversions can be reduced by cutting out the region around 2 MIPs. For tracks in the CDC, the excluded region is $1.6 < dE/dx < 3.0$ and for tracks in the FDC, it is $1.5 < dE/dx < 2.6$. The plots below show the ionization for electrons and background.

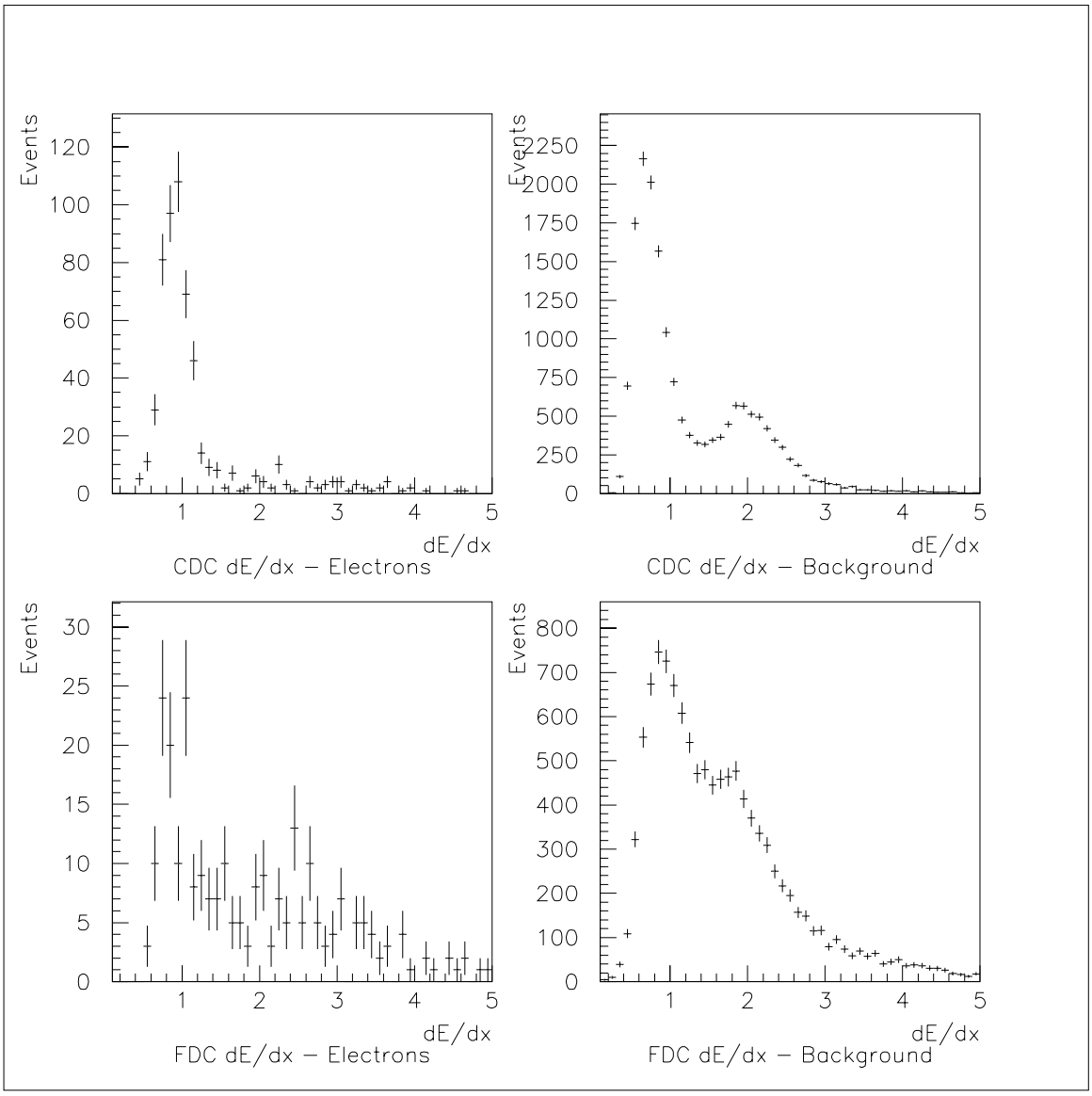

Figure 4.18: dE/dx for electrons and background.

Table 4.1: Table of electron selection cuts.

Cut Variable	Cut
Level 1 E_T	$E_T > 7$ GeV
Level 2 E_T	$E_T > 10$ GeV
Level 2 isolation fraction	$ISO < 0.15$
Online fiducial cut	$\lvert\text{IETA}\rvert \leq 12$ or $14 \leq \lvert\text{IETA}\rvert \leq 32$
EM energy fraction	$f_{EM} > 0.9$
Single tower energy	$E_{hot} > 0.4 \times E_{clus}$
Track in road	$\Delta\eta_{clus-trk} < 0.1$ and $\Delta\phi_{clus-trk} < 0.1$
Offline E_T	$E_T > 11$ GeV
Offline fiducial cut	$\lvert\text{IETA}\rvert \leq 11$ or $16 \leq \lvert\text{IETA}\rvert \leq 25$
H-matrix χ^2	$\chi^2 < 100.0$
Isolation fraction	$ISO < 0.15$
Track match significance	$\sigma_{trk} < 10.0$
CDC dE/dx ($\lvert\text{IETA}\rvert \leq 11$)	$dE/dx < 1.6$ or $dE/dx > 3.0$
FDC dE/dx ($16 \leq \lvert\text{IETA}\rvert \leq 25$)	$dE/dx < 1.5$ or $dE/dx > 2.6$

4.7 Summary

A summary table of all the cuts used to select the data sample for this analysis is given in Table 4.1. An event was required to contain 2 electron candidates which passed these cuts to be included in the data sample. Table 4.2 summarizes the single electron efficiency parameterizations for all efficiency corrections made on the data in the following chapters.

The Level 1 and Level 2 trigger efficiency curves shown in 4.1 and 4.2 had no additional cuts made on the input Monte Carlo electrons. Since the cuts made in the Level 1 and Level 2 triggers are correlated with the calorimeter based offline electron id cuts, it is necessary to make these cuts on the Monte Carlo electrons in order to be able to simply multiply the resulting Level 1 and Level 2 efficiencies with the efficiencies of the offline cuts when making the overall electron efficiency corrections to the data. Figure 4.19 shows the Level 1 and Level 2 electron efficiency after making the E_T, H-matrix, and isolation fraction cuts given in Table 4.1.

Table 4.2: Table of single electron efficiency parameterizations.

Cut Variable	Efficiency Parameterization
Level 1 E_T	$\epsilon = \frac{1}{2} + \frac{1}{2}\tanh\left(\frac{(E_T-7)}{w}\right)$ $w = 3.255 \pm 0.927$
Level 2 $E_T + ISO$	$\epsilon = \frac{1}{2} + \frac{1}{2}\tanh\left(\frac{(E_T-10)}{w}\right)$ $w = 0.701 \pm 0.072$
PPHO Efficiency	$\epsilon_{CC} = 0.977$ $\epsilon_{EC} = 0.994$
PELC/PPHO Efficiency	$\epsilon = 0.869$
CC H-matrix $\chi^2 + ISO$	$\epsilon = a + b \times \lvert\text{IETA}\rvert$ $a_{(10\leq E\leq 50)} = \left(\frac{1}{E-5.5}\right)^{(0.944\pm 0.016)}$ $a_{(E>50)} = 0.972$ $b_{(10\leq E\leq 25)} = (-0.017 \pm 0.002) + (0.0006 \pm 0.0001)E$ $b_{(E>25)} = -0.0017$
EC H-matrix $\chi^2 + ISO$	$\epsilon = a + b \times \lvert\text{IETA}\rvert$ $a_{(25\leq E\leq 200)} = (0.582 \pm 0.055) + \left(\frac{(0.930\pm 0.139)}{(E-20)^{\frac{1}{4}}}\right)$ $a_{(E>200)} = 0.85$ $b_{(25\leq E\leq 200)} = (0.024 \pm 0.003) + \left(\frac{(-0.076\pm 0.007)}{(E-20)^{\frac{1}{4}}}\right)$ $b_{(E>200)} = 0.0028$
$\sigma_{trk} + dE/dx$	$\epsilon = a + b \times (\text{IETA})^2$ $a = 0.934 \pm 0.010$ $b = -0.00047 \pm 0.00006$

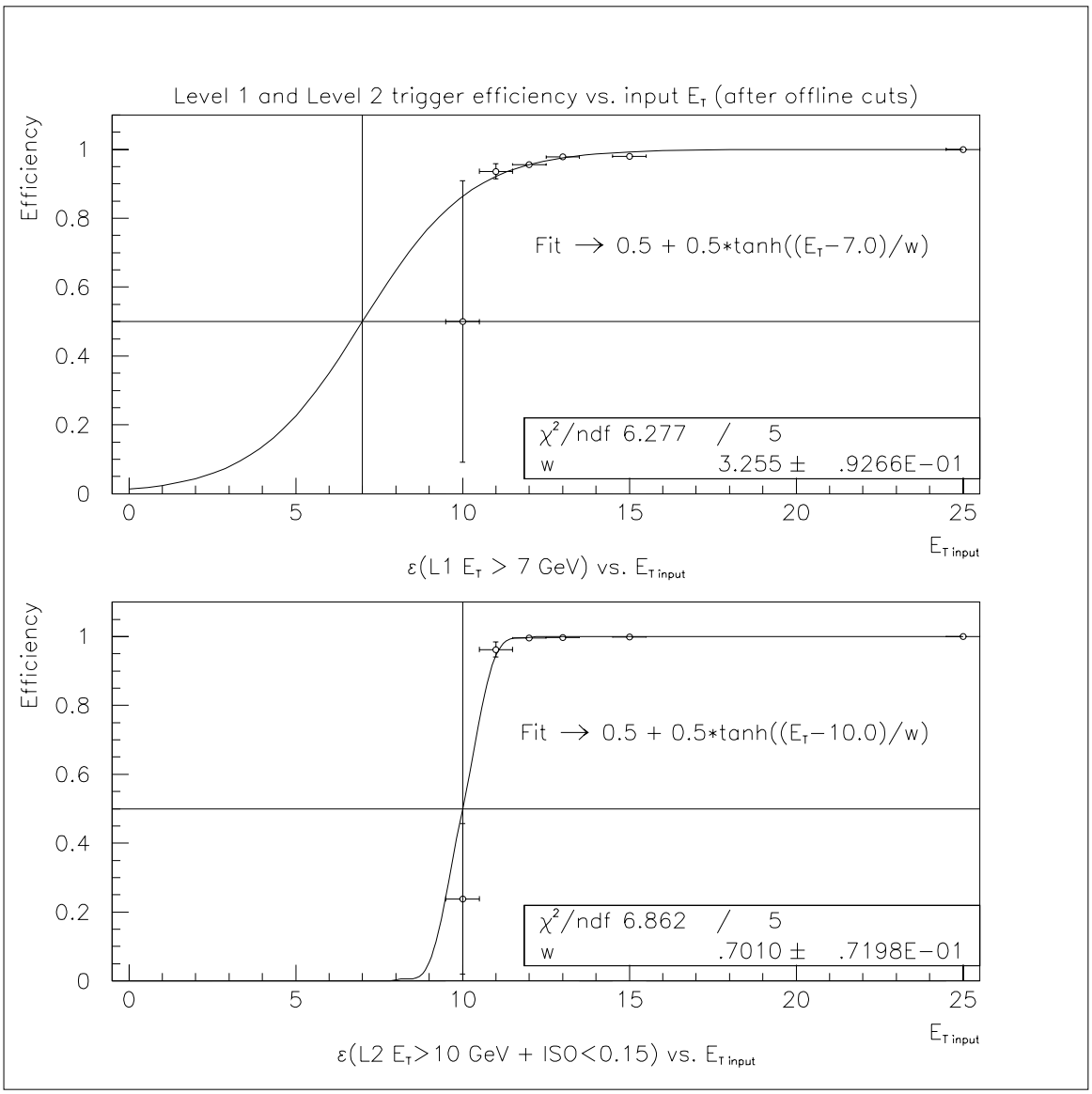

Figure 4.19: Level 1 and Level 2 electron efficiency vs. input E_T after calorimeter based offline cuts.

Figures 4.6, 4.7, 4.10, and 4.11 show the individual H-matrix χ^2 and isolation fraction cut efficiencies for electrons. These cuts are not completely independent however, since they are both based on calorimeter shower shape information. Consequently, it is necessary to measure the efficiency of requiring an electron to pass *both* cuts in combination. Figures 4.20 and 4.21 show the overall electron efficiency for both cuts.

Similarly, the track match significance and dE/dx cuts are both based on tracking information, and so the electron efficiency of these cuts should be measured in combination. The plate level DØGEANT detector simulation of the DØ calorimeters accurately reproduces electron showers as they appear in the central and end cap calorimeters, but the tracking hit resolution produced by the DØGEANT simulation is too small compared to the actual DØ tracking resolution [58]. Thus, using MC data to measure the efficiency of these cuts would yield a higher than actual efficiency for the track match significance cut. Fortunately, the tracking resolution is energy independent (see section 4.6.3), so it is possible to use real DØ electrons from Z$\rightarrow$ e^+e^- events to measure the efficiency of these cuts provided one uses an energy dependent track-to-cluster resolution to account for the variation of the calorimeter position resolution.

In order to measure the tracking cut efficiencies, one must first select a sample of di-electron events from Z boson decays. This can be accomplished using the same starting data sample (2 PELCs with $E_T > 10$ GeV which pass the Level 2 ELE_2_HIGH filter) used for the Drell-Yan analysis. The Z electron sample is then collected as follows: One PELC is required to pass all the cuts described in Table 4.1. The other PELC is then required to pass all the cuts described in Table 4.1 except the track match significance and dE/dx cuts. The invariant mass of the pair is then required to be within a 80-100 GeV mass window. This is sufficient to provide a relatively background-free di-electron sample which is used as the denominator of the tracking cut efficiency distribution.

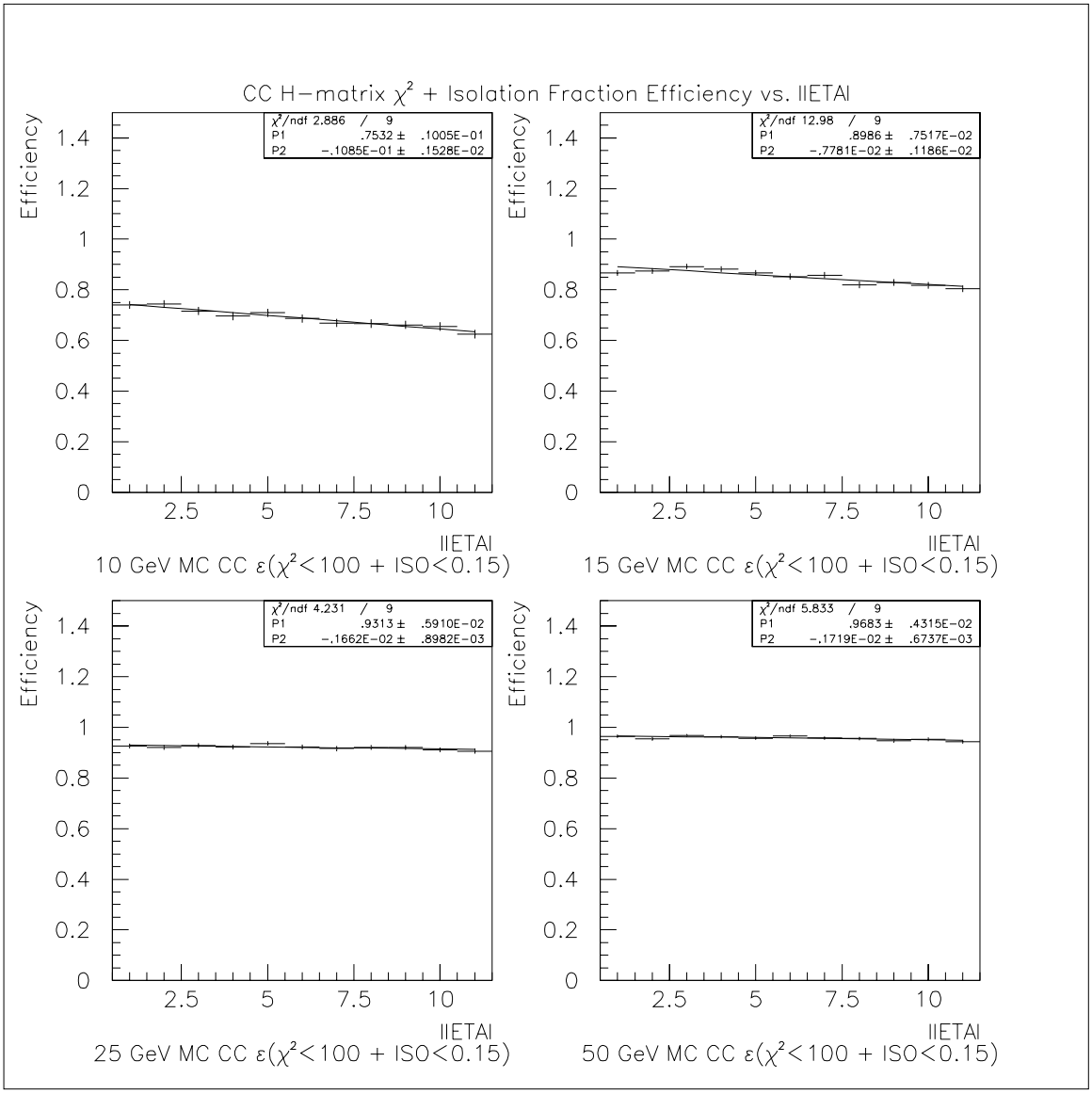

Figure 4.20: CC H-matrix $\chi^2 < 100$ + isolation fraction $ISO < 0.15$ efficiency vs. input |IETA|.

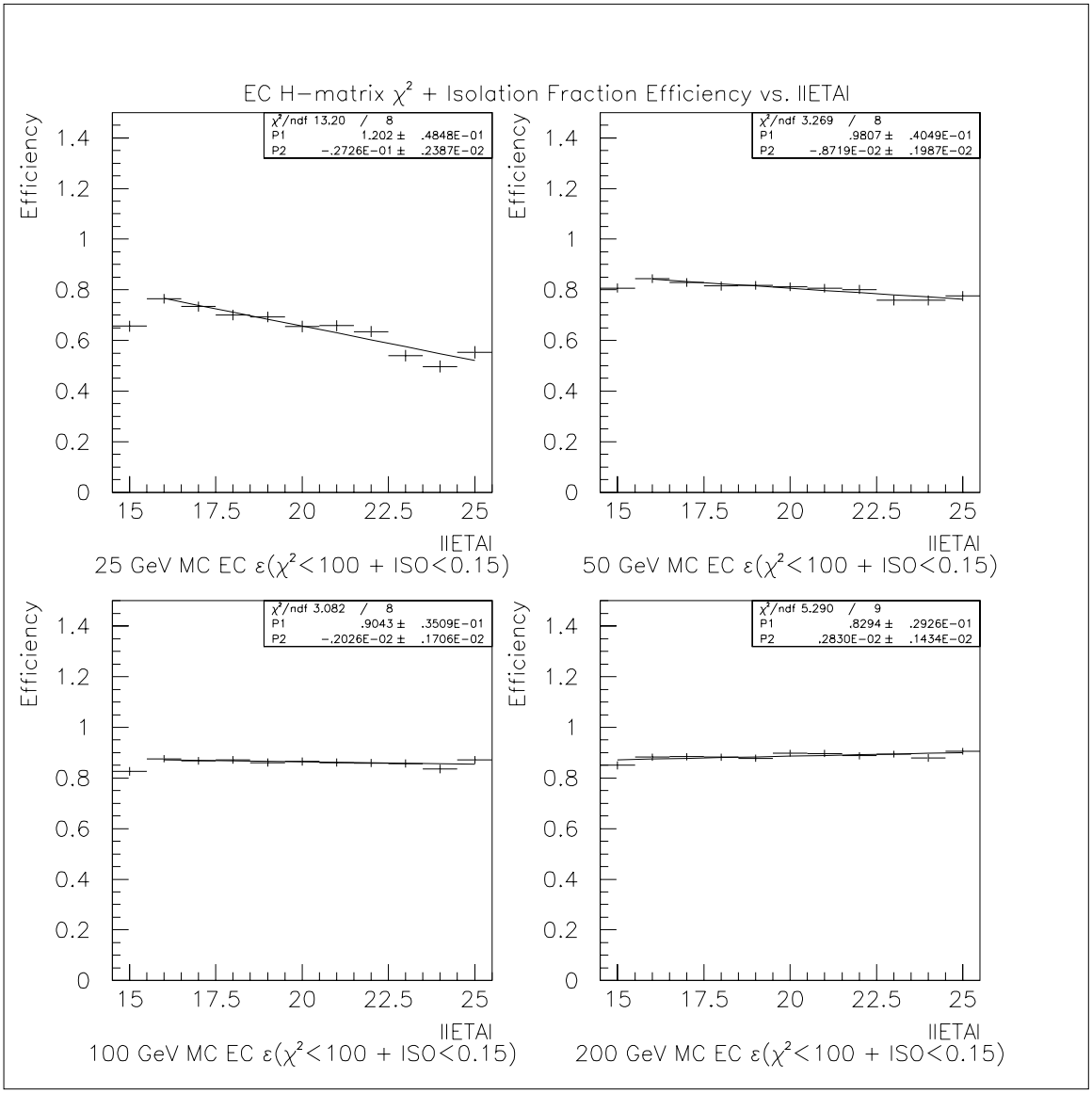

Figure 4.21: EC H-matrix $\chi^2 < 100$ + isolation fraction $ISO < 0.15$ efficiency vs. input |IETA|.

The tracking cuts are then applied to the second PELC to form the numerator of the tracking cut efficiency distribution and the ratio of numerator to denominator is computed to yield the tracking cut efficiency. Since the properties of the Z electrons should be independent, one can double one's statistics by switching PELCs (PELC 1 $\longleftrightarrow$ PELC 2) and repeating this procedure. The tracking cut efficiency versus IETA is shown in Figure 4.22 along with a quadratic fit of the form $\epsilon = p_1 + p_2 \times \mathrm{IETA}^2$.

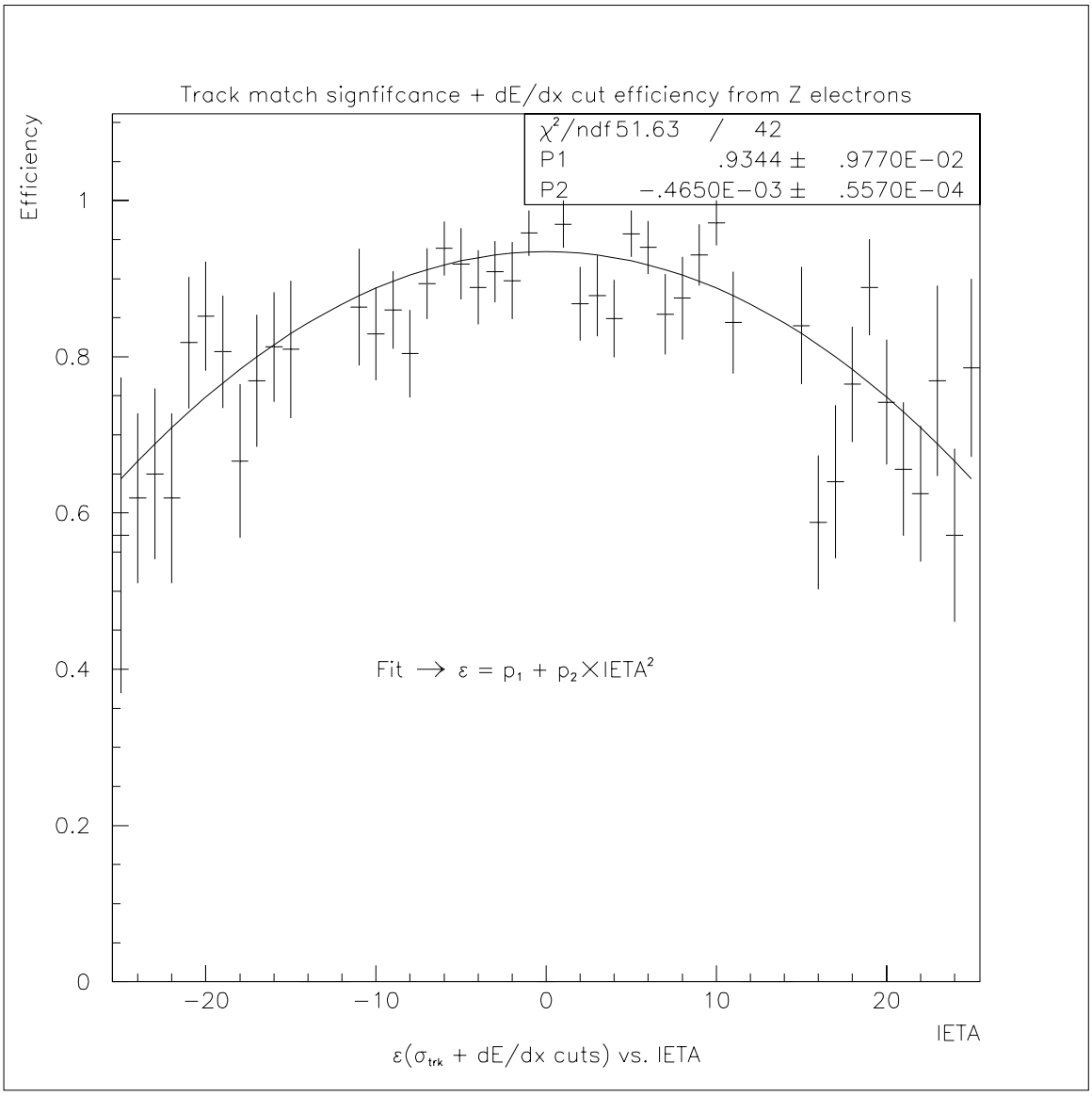

Figure 4.22: Track match significance + dE/dx cut efficiency vs. input |IETA|.

Chapter 5

Data Analysis

5.1 Selected Data Sample

The initial data sample for this analysis consisted of events which passed the ELE_2_HIGH trigger/filter combination outlined in Chapter 4. These events were further required to contain two PELC objects (see Chapter 4) with $E_T > 10.0$ GeV. This sample contained 18,749 events. The offline electron identification cuts were then applied to both PELC objects in each event in this data sample and the invariant mass of the PELC-PELC pair was required to be between 30 and 60 GeV/c^2. This selection criteria yielded a signal + background sample of 143 events. Figures 5.1, 5.2, 5.3 show the resulting signal + background distributions vs. invariant mass, pair rapidity, and pair p_T. Tables 5.1, 5.2, 5.3 show the number of signal + background events per pair mass, rapidity, and p_T bin respectively.

5.2 Background Estimation

There are several sources of background contamination in the Drell-Yan e^+e^- signal sample. They are:

- Dijet events in which the jets were mis-identified as electrons.

Table 5.1: Drell-Yan signal + background events per invariant mass bin.

Mass Bin (GeV/c^2)	Events	Error
30.0 - 35.0	37.00	± 6.08
35.0 - 40.0	33.00	± 5.75
40.0 - 45.0	23.00	± 4.80
45.0 - 50.0	21.00	± 4.58
50.0 - 55.0	16.00	± 4.00
55.0 - 60.0	13.00	± 3.61
Total	143.00	± 11.96

Table 5.2: Drell-Yan signal + background events per pair rapidity bin.

Rapidity Bin	Events	Error
-2.5 - -2.0	4.00	± 2.00
-2.0 - -1.5	8.00	± 2.83
-1.5 - -1.0	13.00	± 3.61
-1.0 - -0.5	21.00	± 4.58
-0.5 - 0.0	16.00	± 4.00
0.0 - 0.5	21.00	± 4.58
0.5 - 1.0	21.00	± 4.58
1.0 - 1.5	20.00	± 4.47
1.5 - 2.0	13.00	± 3.61
2.0 - 2.5	6.00	± 2.50
Total	143.00	± 11.96

Table 5.3: Drell-Yan signal + background events per pair p_T bin.

p_T Bin (GeV/c)	Events	Error
0.0 - 1.0	4.00	± 2.00
1.0 - 2.0	14.00	± 3.74
2.0 - 3.0	15.00	± 3.87
3.0 - 4.0	15.00	± 3.87
4.0 - 5.0	12.00	± 3.46
5.0 - 6.0	9.00	± 3.00
6.0 - 8.0	14.00	± 3.74
8.0 - 10.0	13.00	± 3.61
10.0 - 12.0	12.00	± 3.46
12.0 - 16.0	12.00	± 3.46
16.0 - 24.0	12.00	± 3.46
24.0 - 32.0	5.00	± 2.24
32.0 - 40.0	2.00	± 1.41
40.0 - 50.0	3.00	± 1.73
Total	142.00	± 11.92

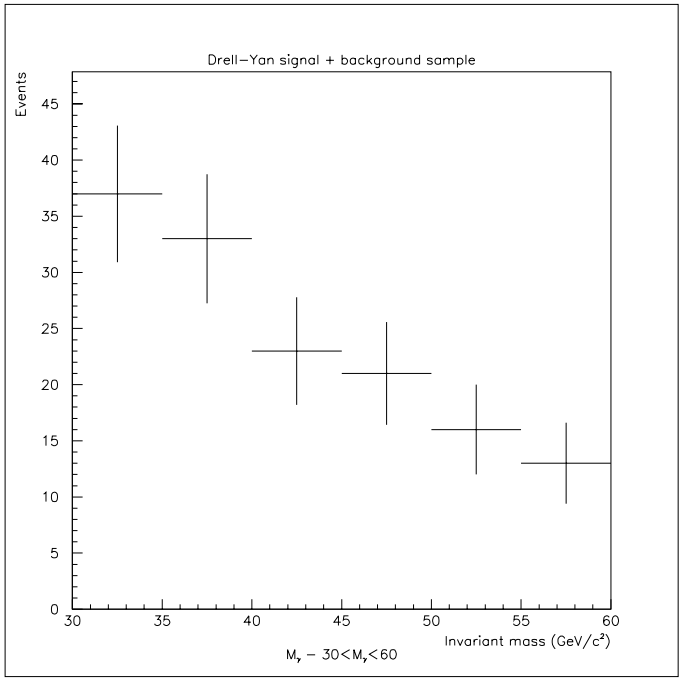

Figure 5.1: Drell-Yan + background events vs. invariant mass.

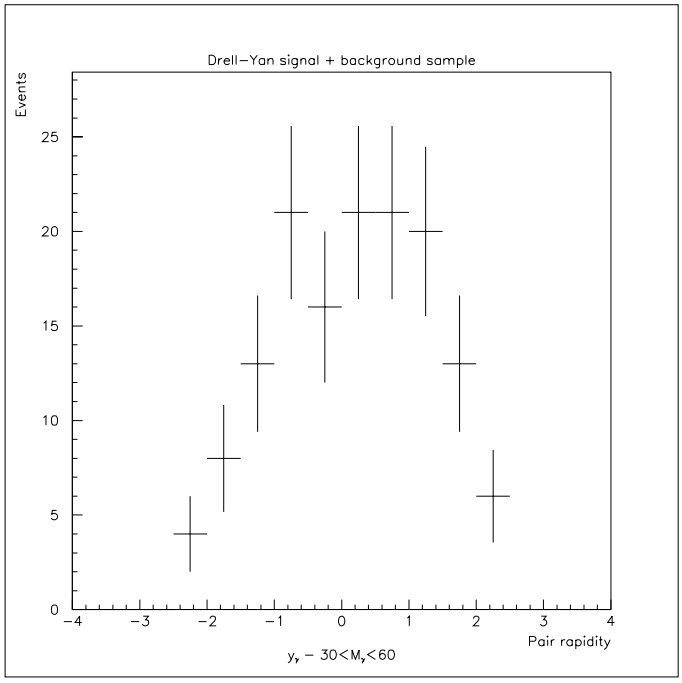

Figure 5.2: Drell-Yan + background events vs. pair rapidity.

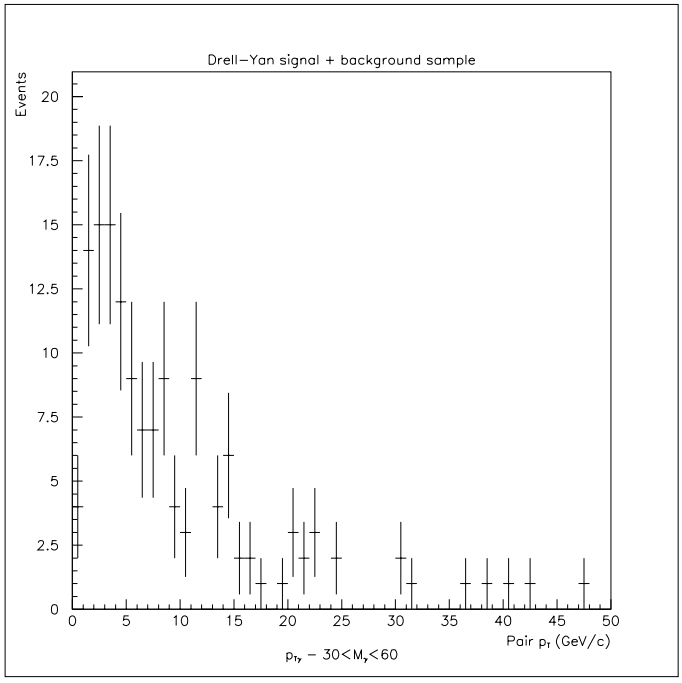

Figure 5.3: Drell-Yan + background events vs. pair p_T.

- Direct photon events in which the photon and associated jet are mis-identified as electrons.
- W$\rightarrow e\nu$ + jets events in which a jet is mis-identified as an electron.
- Z$\rightarrow \tau^+\tau^- \rightarrow e^+e^-$ events.

The largest background contribution comes from particle jets which pass the electron identification cuts described in Table 4.1. The probability that a jet "fakes" an electron in DØ is on the order 1×10^{-4}, and since we require two electrons in an event, the probability that a dijet event fakes a Drell-Yan event is the square of the probability that a single jet produces a fake electron. Although the probability that a dijet event fakes a Drell-Yan event is very small, the dijet cross section is several orders of magnitude larger than the Drell-Yan e^+e^- cross section and thus the dijet background is a significant background. Figure 5.4 shows the dijet background events relative to the Drell-Yan signal + background events. This background is 30-40% of the total Drell-Yan signal + background sample. The method used to estimate this background is described in the next section. Tables 5.4, 5.5, 5.6 show the number of dijet background events per bin in pair mass, rapidity, and p_T respectively. The reason that the integrated dijet background is smaller in the rapidity, and p_T distributions compared to the mass distribution (45.16, 45.17, vs. 45.61 events) is that all distributions have the $30 < M < 60$ GeV/c^2 requirement made on them, but the rapidity and p_T distributions also have the further constraint of the histogram bounds and we do not include overflow and underflow bins in the integral. The reason the error on the integrated dijet background p_T distribution is smaller than the error on the mass and rapidity distributions is due to a smaller systematic variation in the p_T distribution when the rejection fit parameters are varied.

Table 5.4: Dijet background events per invariant mass bin.

Mass Bin (GeV/c^2)	Events	Error
30.0 - 35.0	10.85	± 0.70
35.0 - 40.0	9.21	± 0.58
40.0 - 45.0	8.04	± 0.51
45.0 - 50.0	6.73	± 0.44
50.0 - 55.0	5.78	± 0.38
55.0 - 60.0	5.00	± 0.34
Total	45.61	± 1.24

Table 5.5: Dijet background events per pair rapidity bin.

Rapidity Bin	Events	Error
-2.5 - -2.0	2.77	± 0.35
-2.0 - -1.5	4.81	± 0.38
-1.5 - -1.0	4.87	± 0.33
-1.0 - -0.5	4.11	± 0.30
-0.5 - 0.0	3.46	± 0.29
0.0 - 0.5	3.86	± 0.33
0.5 - 1.0	4.66	± 0.34
1.0 - 1.5	6.51	± 0.42
1.5 - 2.0	5.99	± 0.43
2.0 - 2.5	4.14	± 0.47
Total	45.16	± 1.16

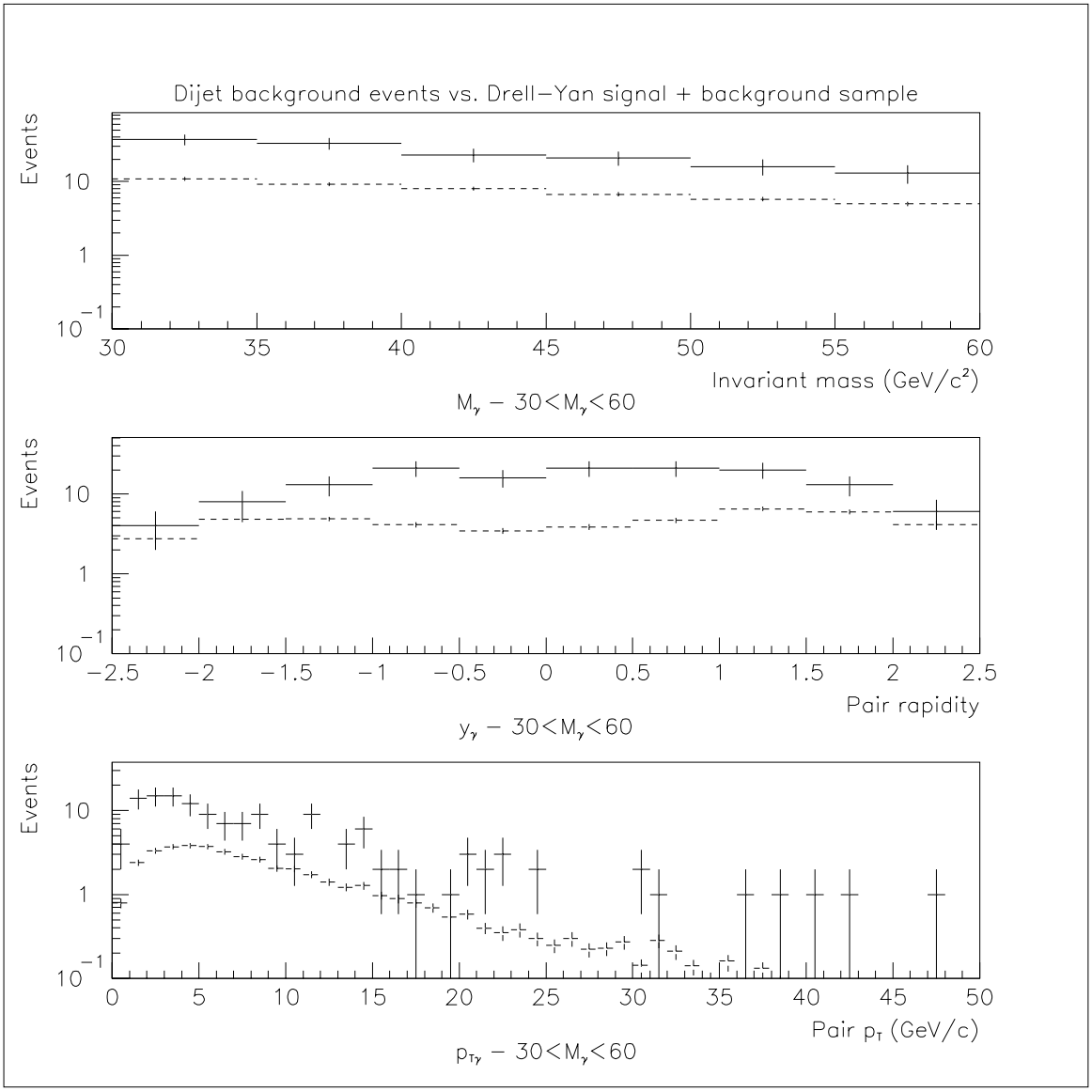

Figure 5.4: Dijet background events (dashed) vs. Drell-Yan signal + background events (solid).

Table 5.6: Dijet background events per pair p_T bin.

p_T Bin (GeV/c)	Events	Error
0.0 - 1.0	0.79	$\pm$ 0.10
1.0 - 2.0	2.39	$\pm$ 0.20
2.0 - 3.0	3.31	$\pm$ 0.26
3.0 - 4.0	3.70	$\pm$ 0.28
4.0 - 5.0	3.83	$\pm$ 0.29
5.0 - 6.0	3.73	$\pm$ 0.28
6.0 - 8.0	6.05	$\pm$ 0.33
8.0 - 10.0	4.65	$\pm$ 0.27
10.0 - 12.0	3.74	$\pm$ 0.24
12.0 - 16.0	4.88	$\pm$ 0.26
16.0 - 24.0	4.62	$\pm$ 0.23
24.0 - 32.0	1.99	$\pm$ 0.14
32.0 - 40.0	0.98	$\pm$ 0.10
40.0 - 50.0	0.50	$\pm$ 0.07
Total	45.17	$\pm$ 0.86

The direct photon background to Drell-Yan arises from a charged particle closely following the photon trajectory so that a track points to the EM cluster produced by the photon. The probability of such an overlap between the photon and a charged particle is about 12% [61] in the central region and around 40% in the forward regions. The jet which balances the photon p_T must also fake an electron for the event to fake a Drell-Yan event. While the direct photon cross section is larger than the Drell-Yan cross section, it is not large enough to produce a large background contribution since the probability that the event fakes a Drell-Yan event is on the order of 1×10^{-5}. Figure 5.5 shows an estimate of the direct photon background events relative to the Drell-Yan signal + background event sample. The reason the background looks higher relative to the mass distribution than the p_T or rapidity distributions in these plots is due to the coarser binning in the mass plot (events vs. events/bin width). This background estimate was produced using the ISAJET Monte Carlo to calculate the direct photon cross section and event kinematics. The Monte-Carlo events were then weighted by

the probability that a jet fakes an electron in DØ [62] times the probability that the photon has an associated track times the product of the electron id cut efficiencies for the photon. This background is on the order of a percent, which is much smaller than the error on this cross section measurement, so this background is ignored.

W + jets events may contribute background to Drell-Yan e^+e^- production if the W decays to $e + \nu$ and one of the jets fakes an electron. However, the W + jets cross section is rather small as is the probability that a jet will fake an electron. Consequently, the W + jets contribution to the Drell-Yan e^+e^- background is very small. Figure 5.6 shows the an estimate of the W + jets background events relative to the Drell-Yan signal + background sample. Again the apparent difference in the size of this background amongst the various plots is due to the binning. This background estimate was produced using the ISAJET Monte Carlo to calculate the W + jets cross section and event kinematics. The Monte-Carlo events were then weighted by the probability that a jet fakes an electron in DØ [62] times the product of the electron id cut efficiencies for the electron. This background is very small and thus is ignored in this analysis.

Any physics process other than Drell-Yan which produces a pair of real electrons (e^+e^-, e^-e^-, e^+e^+) will contribute to the background. For example, there is no way to experimentally differentiate between $\gamma^* \rightarrow e^+e^-$ and Z $\rightarrow e^+e^-$ since the final state is identical. Fortunately, the Z $\rightarrow e^+e^-$ cross section is small in the invariant mass region 30-60 GeV/c^2 of this analysis. However, in the invariant mass region of the Z resonance (around 91.17 GeV), the Z$\rightarrow \ell^+\ell^-$ production cross section is several orders of magnitude larger than the virtual photon cross section, and thus if a mechanism exists for an on-shell Z boson to produce a pair of electrons with an invariant mass in the 30-60 GeV/c^2 range, these events will contribute to the Drell-Yan background. It turns out that such a mechanism does exist, namely the decay chain

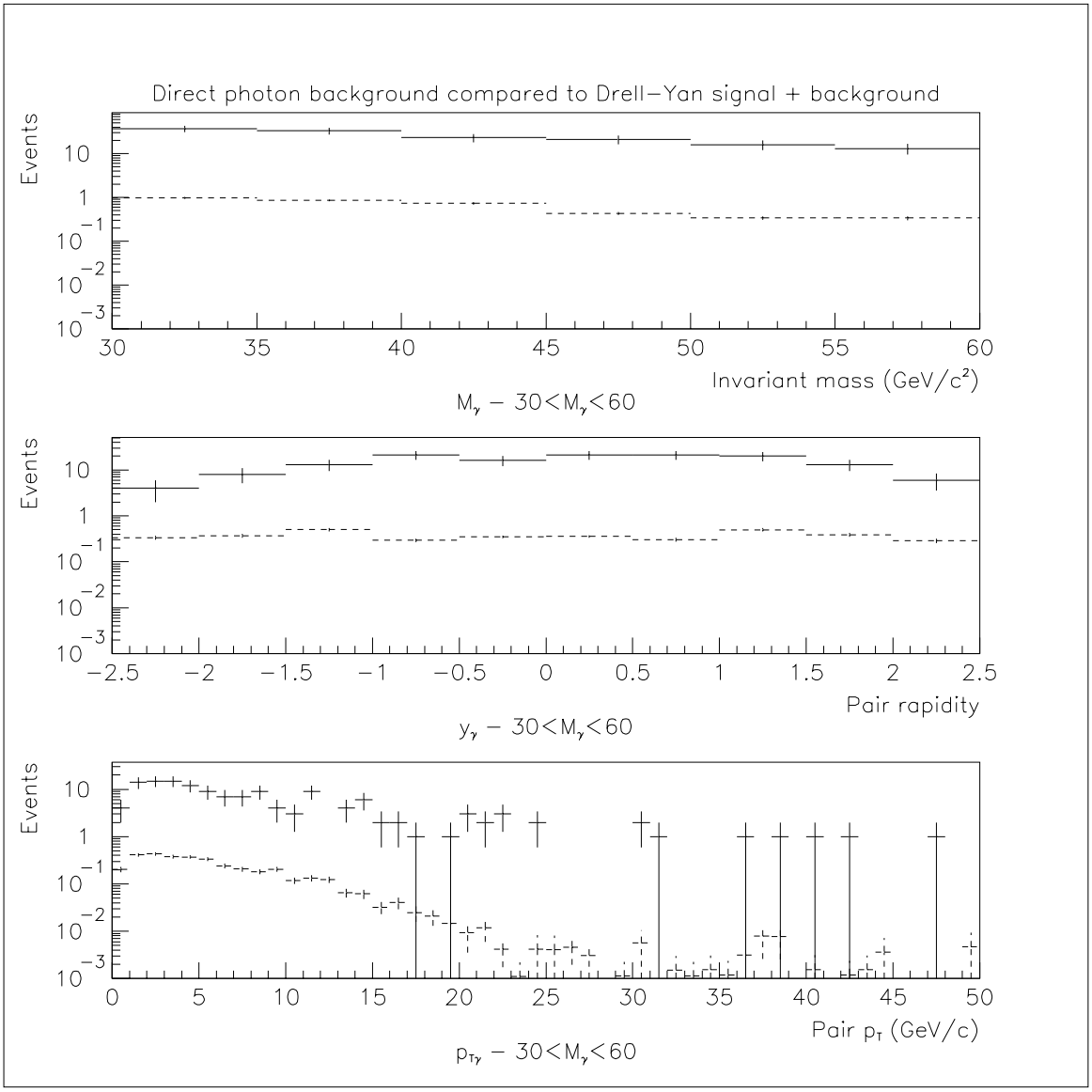

Figure 5.5: Direct photon background events (dashed) vs. Drell-Yan signal + background events (solid).

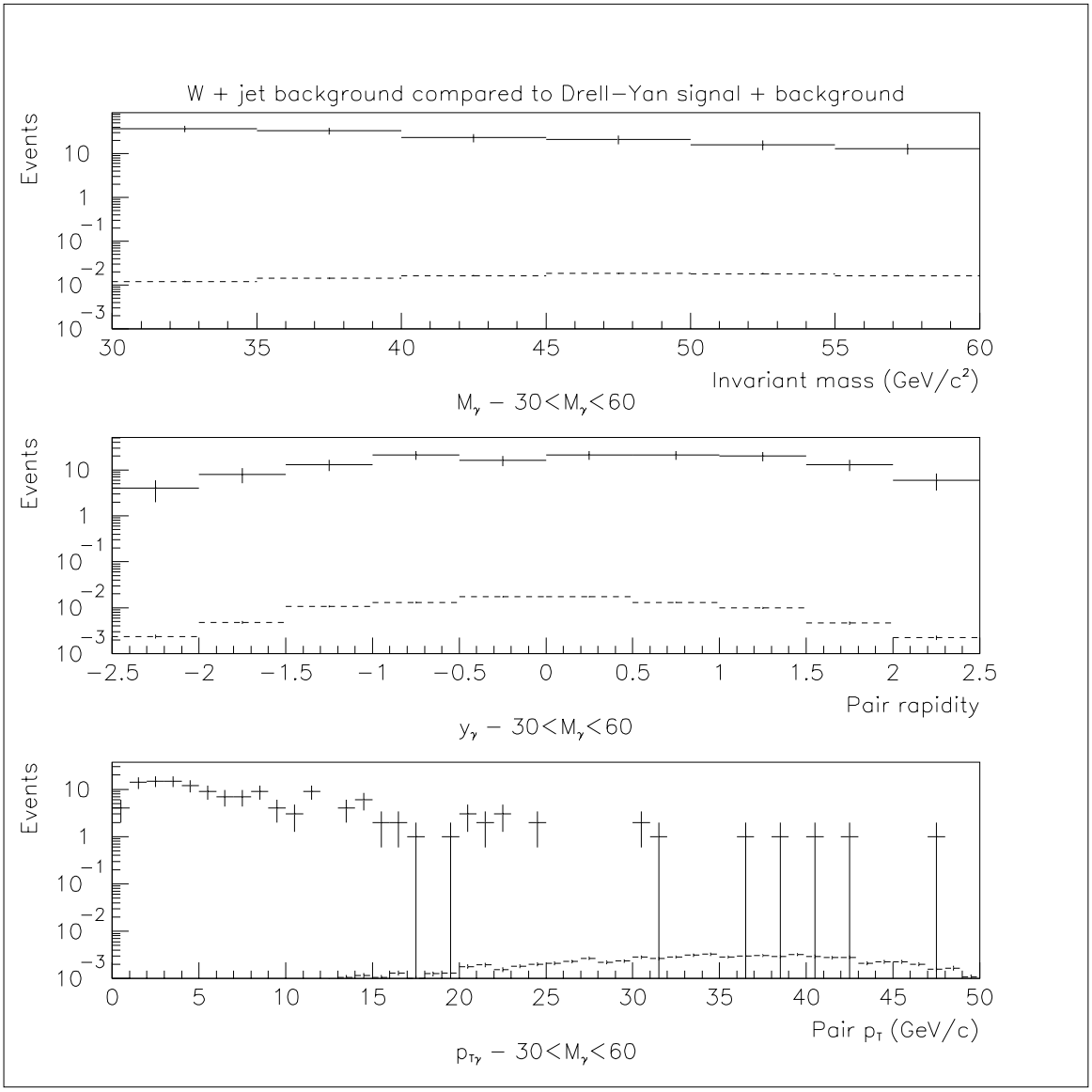

Figure 5.6: W + jet background events (dashed) vs. Drell-Yan signal + background events (solid).

Table 5.7: Z$\rightarrow \tau^+\tau^- \rightarrow e^+e^-$ background events per invariant mass bin.

Mass Bin (GeV/c^2)	Events	Error
30.0 - 35.0	0.64	$\pm$ 0.06
35.0 - 40.0	1.01	$\pm$ 0.08
40.0 - 45.0	1.17	$\pm$ 0.09
45.0 - 50.0	1.03	$\pm$ 0.08
50.0 - 55.0	0.89	$\pm$ 0.07
55.0 - 60.0	0.71	$\pm$ 0.07
Total	5.44	$\pm$ 0.182

Z$\rightarrow \tau^+\tau^- \rightarrow e^+\nu\nu e^-\nu\nu$. It is easy to see how this decay can produce an electron pair with an invariant mass in the 30-60 GeV/c^2 range using the following argument: if we assume that energy (mass) of the Z boson is divided equally between the τ^+ and τ^- , then each τ will have an energy of around 45 GeV. The τ leptons can then decay to an electron and two neutrinos, and if the τ energy is equally shared between the electron and neutrinos, the resulting electrons will each have an energy around 15 GeV, thus if the final state electrons are roughly back to back in the lab frame, the resulting invariant mass of the pair will be on the order of 30 GeV/c^2. Obviously this argument ignores the detailed kinematics of the decays, but it does illustrate how an on-shell Z boson can produce an electron pair in the 30-60 GeV/c^2 invariant mass region. The size of this background contribution is reduced by the branching ratio of $\tau \rightarrow e\nu\nu$ and the details of the kinematics, but the result is that this mechanism produces background that is as much as few percent of the Drell-Yan + background sample in the mass range of 30-60 GeV/c^2. Figure 5.7 shows the background events contribution from Z$\rightarrow \tau^+\tau^- \rightarrow e^+e^-$ events relative to the Drell-Yan signal + background sample. Once again, the apparent difference between the size of the background amongst the plots is due to the binning. Tables 5.7, 5.8, and 5.9 show the Z$\rightarrow \tau^+\tau^- \rightarrow e^+e^-$ background events in each pair mass, rapidity, and p_T bin respectively.

Table 5.8: Z$\rightarrow \tau^+\tau^- \rightarrow e^+e^-$ background events per pair rapidity bin.

Rapidity Bin	Events	Error
-2.5 - -2.0	0.05	± 0.01
-2.0 - -1.5	0.18	± 0.03
-1.5 - -1.0	0.39	± 0.04
-1.0 - -0.5	0.80	± 0.07
-0.5 - 0.0	1.30	± 0.09
0.0 - 0.5	1.28	± 0.09
0.5 - 1.0	0.77	± 0.07
1.0 - 1.5	0.42	± 0.05
1.5 - 2.0	0.21	± 0.03
2.0 - 2.5	0.05	± 0.01
Total	5.44	± 0.182

Table 5.9: Z$\rightarrow \tau^+\tau^- \rightarrow e^+e^-$ background events per pair p_T bin.

p_T Bin (GeV/c)	Events	Error
0.0 - 1.0	0.12	± 0.03
1.0 - 2.0	0.34	± 0.04
2.0 - 3.0	0.37	± 0.05
3.0 - 4.0	0.44	± 0.05
4.0 - 5.0	0.34	± 0.05
5.0 - 6.0	0.33	± 0.05
6.0 - 8.0	0.74	± 0.07
8.0 - 10.0	0.51	± 0.06
10.0 - 12.0	0.53	± 0.06
12.0 - 16.0	0.82	± 0.07
16.0 - 24.0	0.74	± 0.07
24.0 - 32.0	0.13	± 0.03
32.0 - 40.0	0.03	± 0.02
40.0 - 50.0	0.01	± 0.01
Total	5.43	± 0.182

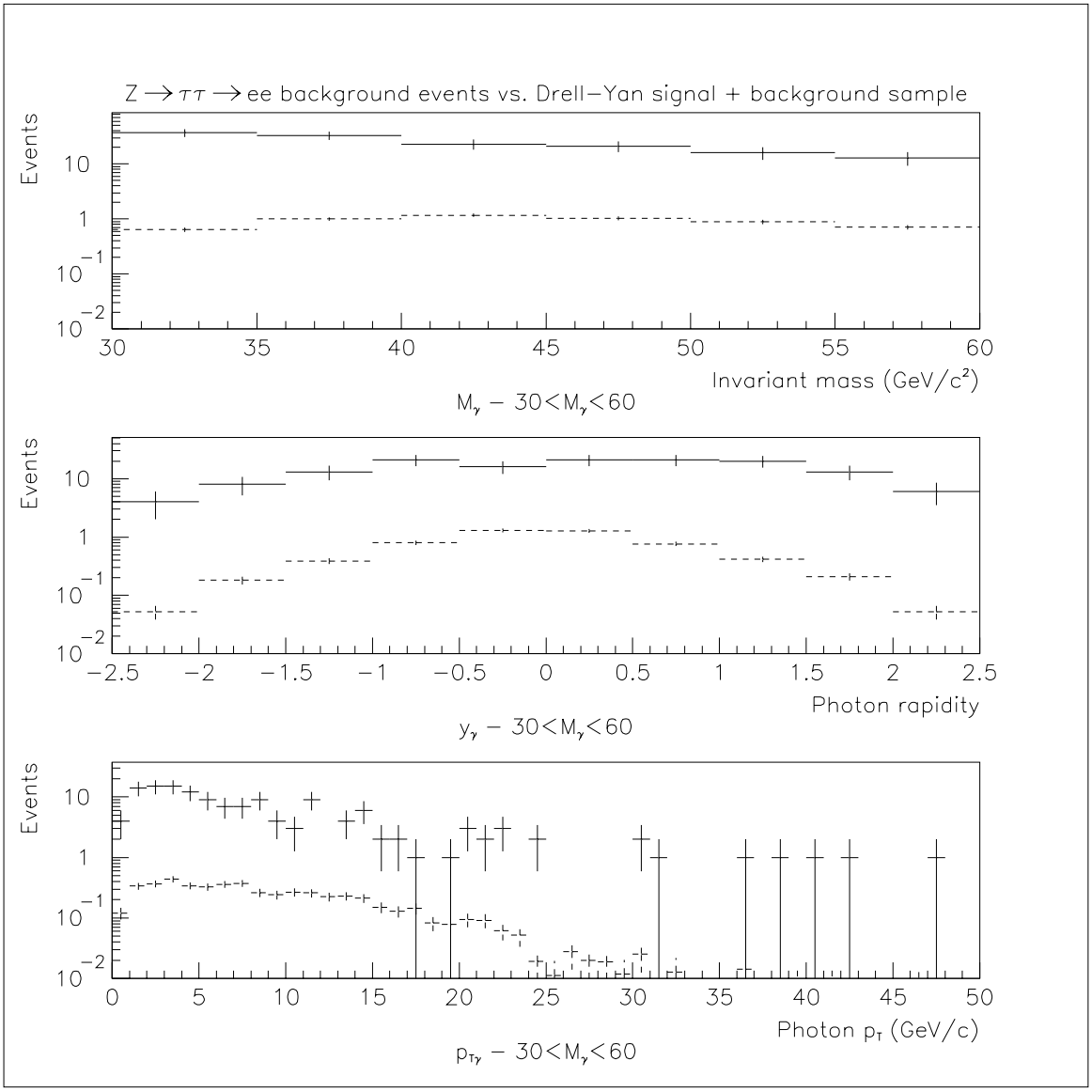

Figure 5.7: Z→ $\tau^+\tau^-$ → e^+e^- background events (dashed) vs. Drell-Yan signal + background events (solid).

5.2.1 Dijet Background Estimation Method

The probability that a jet is mis-identified as an electron in DØ has been studied extensively [63] [62]. However, due to the lack of a sufficiently large sample of dijet events, and the small probability that a jet fakes an electron, the error on the fake electron probability measured in these studies is large (as much as 50%). Consequently these probability estimates are not used to estimate the dijet background contribution to Drell-Yan. Rather, a less error prone method is used to estimate the dijet background.

Since the initial sample of events from which the Drell-Yan signal sample is selected is large and is almost entirely composed of dijet (or multijet) events, it is possible to use this sample to estimate the dijet background. We start by selecting a sub-sample of our initial data sample by requiring that the event contain 2 PELC objects each with $E_T > 11$ GeV, that are in the fiducial region $|\text{IETA}| < 11$ or $16 < |\text{IETA}| < 25$, with an invariant mass between 30 and 60 GeV/c^2. Since the dijet cross section is so large relative to any other cross section in this invariant mass range, the PELC-PELC sample is comprised almost entirely of dijet events which pass the (rather loose) PELC selection requirements. Two sets of histograms of PELC energy, E_T and IETA are then produced from this sample. One set of histograms contains entries of PELC objects with $|\text{IETA}| < 11$ (CC) and the other set contains entries of PELC objects with $16 < |\text{IETA}| < 25$ (EC). We fill these histograms with both PELC objects in the event in order to double our statistics, but a given PELC only gets entered into a single histogram. The data is split into two sets because the rejection of the offline electron id cuts is different in the CC and EC. Two more sets of histograms of the same quantities are then filled with PELC objects which pass the electron id cuts. Since we only make the additional electron id cuts on a single PELC in this case

(which then gets entered into a histogram if it passes), this sample is still mostly background. We then switch which PELC has the additional electron id cuts made on it (and consequently gets entered into a histogram if it passes) again to double our statistics and remain consistent with the histograms without the additional cuts.

Since these histograms contain Drell-Yan events we should subtract these signal events since we want to our PELC-PELC histograms to measure the rejection of our electron id cuts on jets which passed the PELC cuts. In order to do this, we use the RESBOS Monte Carlo to estimate the Drell-Yan cross section given our fiducial and kinematic cuts. We fill two sets of histograms (CC and EC again) of E_T, energy and IETA with both Drell-Yan Monte Carlo electrons if the event passes our kinematic and fiducial cuts, where each electron is weighted by the PELC efficiency given in Chapter 4 times our integrated luminosity and the Monte Carlo event weight. We then fill another two sets of histograms of E_T, energy and IETA of both electrons where each is additionally weighted by the product of the efficiencies of the all the electron id cuts to estimate the number of signal events in our dijet PELC-PELC histograms. We then subtract these signal estimates. Other real electron contamination in these background samples is ignored since it is very small relative to the mostly dijet PELC-PELC sample.

We then divide the resulting histograms of PELCs (which now have the Drell-Yan signal events subtracted out) that passed the additional cuts by the histograms without the additional cuts to produce plots of the rejection of these cuts vs. energy, E_T and IETA. These plots are then fit in order to parameterize the E, E_T or IETA dependence (if any) of the electron id cuts' rejection. This yields CC and EC single PELC $\rightarrow$ electron rejection in functional form. Figures 5.8 and 5.9 show the fitted rejection for CC and EC PELCs respectively. To aid the reader in understanding the foregoing description of the rejection estimation method, a "cartoon" of the rejection

in a given bin is

$$f(\text{PELC} \rightarrow \text{e}) = \frac{\text{e} - \text{DY}}{\text{PELC}}$$

Now that we have an estimate of the background rejection of the electron id cuts on a single PELC in our sample, we make yet another set of histograms of the variables we are interested in measuring (namely pair mass, rapidity, and p_T) using our initial PELC-PELC sample. Each event is required to pass our kinematic and fiducial cuts and is weighted by the product of the rejections we expect on each PELC based on each PELC's E_T or IETA which is input to our rejection fits (depending on whether it is in the CC or EC). These histograms then contain our bin-by-bin dijet background estimate which we will subtract from our signal sample. A cartoon of the dijet background in a given bin is

$$\hat{B}_{jj} \quad = \quad (\text{PELC-PELC}) \times f(\text{PELC}_1 \rightarrow \text{e}) \times f(\text{PELC}_2 \rightarrow \text{e})$$

In order to estimate the systematic error induced by using our rejection fits, this background estimate is then recomputed 100 times by varying the rejection fit parameters. The EC rejection fit is varied by varying the two fit parameters according to correlated Gaussians with mean zero and widths equal to the errors on the parameters from the fit. Correlated Gaussians are generated using the CERN program library routine CORGEN and are used because the fit parameters are very anti-correlated. The correlation is given by the covariance matrix from the fit. The CC rejection fit has only one parameter which is also varied by an independent Gaussian random number (gotten from the CERN program library routine RNORML) with mean zero and width equal to the standard deviation on this fit parameter. The standard deviation of these 100 background estimates is then computed bin-by-bin in an attempt

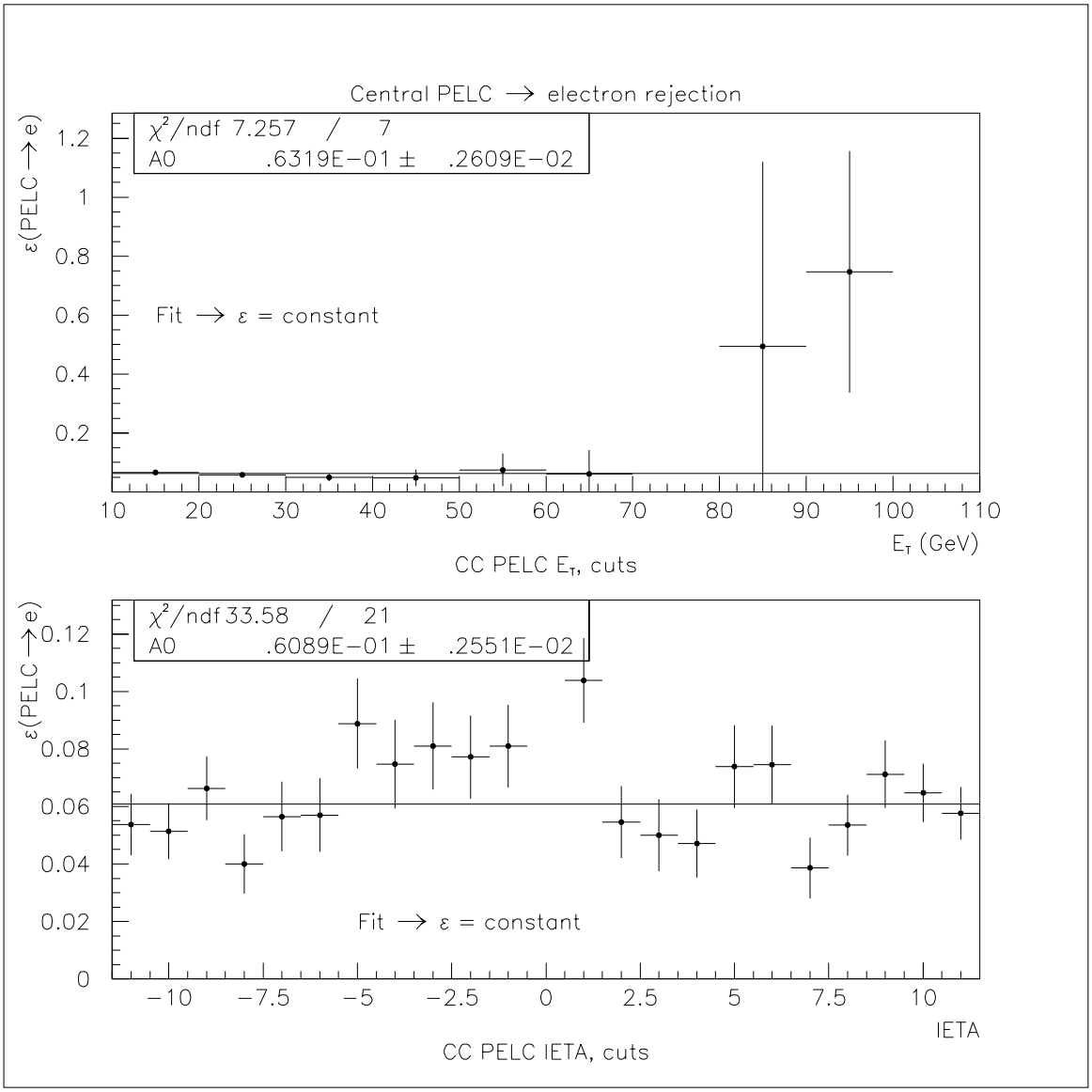

Figure 5.8: CC PELC rejection vs. cluster E_T, IETA.

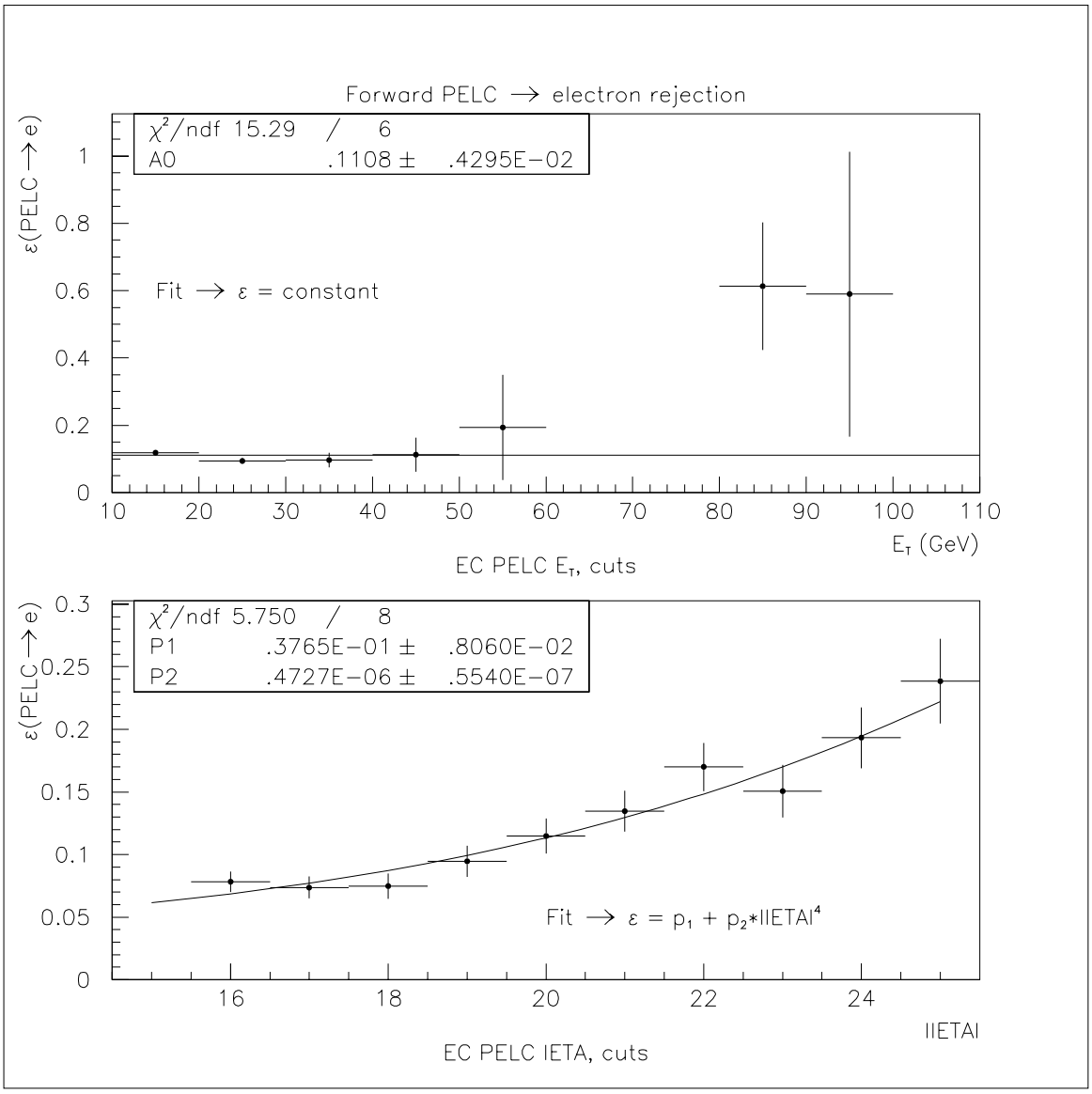

Figure 5.9: EC PELC rejection vs. cluster E_T, |IETA|.

to estimate the systematic error in this background measurement. The standard deviation of these measurements is then added in quadrature with the statistical error of the background computed using the central value of the fit parameters. The resulting dijet background estimate is shown in Figure 5.4. For further clarification on how this systematic error is computed see Section 5.3 (Online Efficiencies) where the Level 1 efficiency calculation is described. The systematic error estimation procedure is essentially the same, but the PELC-PELC event sample is used as the input rather than the RESBOS Drell-Yan Monte Carlo, and two rejection fits (CC and EC) are used for the background so more random numbers are required. Of course no systematic error due to Monte Carlo is performed here since no Monte Carlo events were used.

5.2.2 Z$\rightarrow \tau^+\tau^- \rightarrow e^+e^-$ Background Estimation Method

The Z$\rightarrow \tau^+\tau^- \rightarrow e^+e^-$ background is measured using the ISAJET Monte Carlo to generate the Z$\rightarrow \tau^+\tau^- \rightarrow e^+e^-$ cross section and kinematics. This cross section is then multiplied by the integrated luminosity for the ELE_2_HIGH trigger/filter combination and the online and offline electron id efficiencies computed using the electron kinematics of the Z$\rightarrow \tau^+\tau^- \rightarrow e^+e^-$ events. This yields an estimate of the number of background events in each mass, rapidity, or p_T bin of the data. The resulting background is shown in Figure 5.7.

5.2.3 Background Subtraction

The dijet and Z$\rightarrow \tau^+\tau^- \rightarrow e^+e^-$ background is subtracted bin-by-bin from the signal + background distributions. Figure 5.10 shows the Drell-Yan distribution after subtracting both the dijet background shown in Figure 5.4 and the Z$\rightarrow \tau^+\tau^- \rightarrow e^+e^-$ background shown in Figure 5.7 from the signal + background sample in Figures 5.1, 5.2, and 5.3. The number of events remaining per photon mass, rapidity, and p_T bin

Table 5.10: Drell-Yan events per invariant mass bin.

Mass Bin (GeV/c^2)	Events	Error
30.0 - 35.0	25.51	± 6.12
35.0 - 40.0	22.78	± 5.77
40.0 - 45.0	13.79	± 4.82
45.0 - 50.0	13.24	± 4.60
50.0 - 55.0	9.34	± 4.02
55.0 - 60.0	7.29	± 3.62
Total	91.95	± 12.02

Table 5.11: Drell-Yan events per photon rapidity bin.

Rapidity Bin	Events	Error
-2.5 - -2.0	1.18	± 2.03
-2.0 - -1.5	3.01	± 2.85
-1.5 - -1.0	7.74	± 3.62
-1.0 - -0.5	16.09	± 4.59
-0.5 - 0.0	11.24	± 4.01
0.0 - 0.5	15.86	± 4.60
0.5 - 1.0	15.57	± 4.60
1.0 - 1.5	13.07	± 4.49
1.5 - 2.0	6.80	± 3.63
2.0 - 2.5	1.81	± 2.49
Total	92.40	± 12.01

after background subtraction are given in Tables 5.10, 5.11, and 5.12 respectively. The difference in the event totals between the mass, rapidity, and p_T distributions are given by

$$
\begin{aligned}
d\sigma/dm \rightarrow 91.95 &= 143_{sig+bkg} - 45.61_{jj} - 5.44_{Z\rightarrow\tau\tau} \\
d\sigma/dy \rightarrow 92.40 &= 143_{sig+bkg} - 45.16_{jj} - 5.44_{Z\rightarrow\tau\tau} \\
d\sigma/dm \rightarrow 91.40 &= 142_{sig+bkg} - 45.17_{jj} - 5.43_{Z\rightarrow\tau\tau}
\end{aligned}
$$

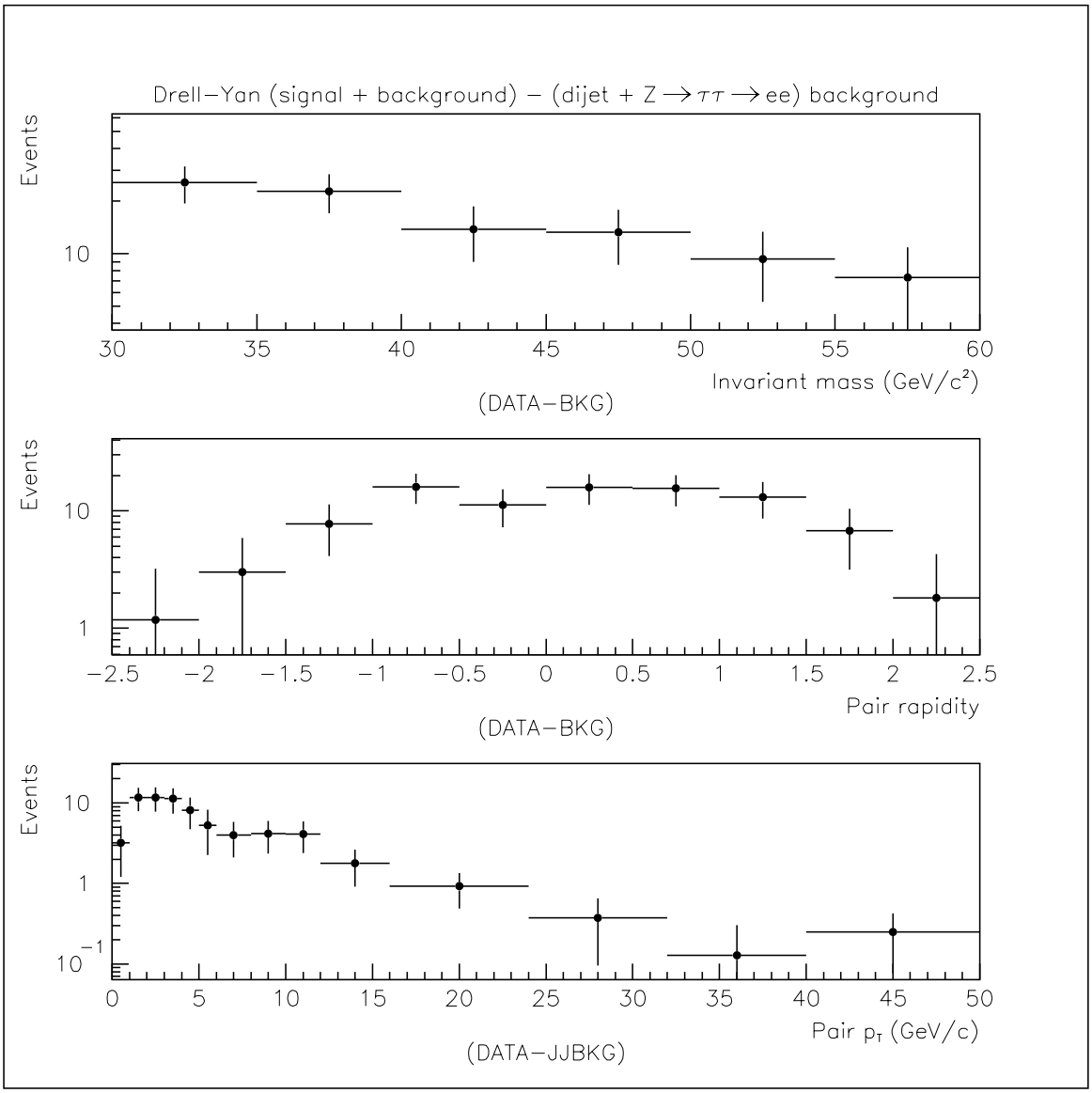

Figure 5.10: Drell-Yan (signal + background) - (dijet + Z$\rightarrow$ $\tau^+\tau^-$ $\rightarrow$ e^+e^-) background events.

Table 5.12: Drell-Yan events per photon p_T bin.

p_T Bin (GeV/c)	Events	Error
0.0 - 1.0	3.08	± 2.00
1.0 - 2.0	11.28	± 3.75
2.0 - 3.0	11.33	± 3.88
3.0 - 4.0	10.86	± 3.88
4.0 - 5.0	7.83	± 3.48
5.0 - 6.0	4.94	± 3.01
6.0 - 8.0	7.21	± 3.76
8.0 - 10.0	7.85	± 3.62
10.0 - 12.0	7.73	± 3.47
12.0 - 16.0	6.30	± 3.47
16.0 - 24.0	6.64	± 3.47
24.0 - 32.0	2.87	± 2.24
32.0 - 40.0	0.98	± 1.42
40.0 - 50.0	2.49	± 1.73
Total	91.40	± 11.95

5.3 Online Efficiencies

Figure 5.11 shows the Level 1 trigger efficiency vs. invariant mass, photon rapidity and photon p_T. These plots were generated using the Level 1 efficiency fit vs. electron E_T shown in 4.19. RESBOS Drell-Yan Monte Carlo events were used to provide the event kinematics which were input to the efficiency fit for each electron in each event. The event efficiency was then taken to be the product of the individual electron efficiencies. The general method for the efficiency in bin i is

$$\epsilon_i = \frac{1}{N_i}\sum_{j=1}^{N_i} \epsilon_{cut}(e_j^+) \times \epsilon_{cut}(e_j^-)$$

where N_i is the number of Monte Carlo events in bin i and $\epsilon_{cut}(e_j^{\pm})$ is the efficiency of the cut evaluated using the electron kinematics from the Monte Carlo. The various ϵ_{cut} functions are given in Table 4.2. Profile histograms were made of the invariant

mass, photon rapidity, and photon p_T using the event efficiency as the y-axis variable. A profile histogram is a histogram in which each bin contains the average of the y-values of the entries in that bin. These profile histograms contain the average bin-by-bin efficiency in mass, photon rapidity, and photon p_T.

The standard deviation of the mean in each bin gives the statistical variation of the efficiency estimate in each bin due to the variations of the electron kinematics within a mass, rapidity, or p_T bin. In order to estimate the systematic error associated with this efficiency measurement, these profile histograms were varied using two different methods which correspond to the systematic error induced by using the fit, and the systematic error induced by using the RESBOS Monte Carlo to furnish the electron kinematics.

To estimate the systematic error due to the fit, 100 sets of these profile histograms were generated by varying the fit parameter according to a Gaussian distribution with mean zero and width equal to the error on the fit parameter. The mean of each bin from each set of these 100 profile histograms were then used to fill another set of profile histograms of invariant mass, photon rapidity, and photon p_T. The bin-by-bin spread of these profile histograms gives an estimate of the bin-by-bin variation of the efficiency due to the variation of the Level 1 efficiency fit. The systematic efficiency variation in bin i due to the fit is given by

$$\mu_i \text{ fit} = \frac{1}{100}\sum_{k=1}^{100}\sum_{j=1}^{N_i} \epsilon_{cut}(e_i^+, p'_{1k}[, p'_{2k}, \ldots]) \times \epsilon_{cut}(e_i^-, p'_{1k}[, p'_{2k}, \ldots])$$

$$\sigma_i \text{ fit} = \frac{1}{100}\sum_{k=1}^{100}(e_{ik} - \mu_i)^2$$

where

N_i = Monte Carlo events

$\epsilon_{cut}(e^+, p'_1[, p'_2, \ldots]) =$ modified efficiency

$p'_{nk} = p_n + \sigma_n Z_{nk}$

σ_n = error on fit parameter p_n

Z_{nk} = random Gaussian

If there is more than one parameter in a fit, the Z_{nk} are correlated; the correlation is specified by the covariance matrix from the fit.

To measure the systematic effect of the particular Drell-Yan kinematics used, the profile histograms were filled using the ISAJET Monte Carlo to provide the kinematics of the events. A different set of parton distributions was used to generate the ISAJET events as well. The bin-by-bin difference between the RESBOS and ISAJET Monte Carlo generated histograms gives a bin-by-bin estimate of the systematic variation due to the input Monte Carlo

Systematic error from MC in bin $i \rightarrow \sigma_{i-MC} = |\mu_{i-RESBOS} - \mu_{i-ISAJET}|$

The plots shown in Figure 5.11 contain the average bin-by-bin event efficiency vs. mass, rapidity, or p_T using the central value of the Level 1 efficiency vs. electron E_T fit with kinematics provided by the RESBOS Monte Carlo. The error in each bin in each plot is the standard deviation of the bin mean added in quadrature with the spread induced by varying the fit and the variation produced by using the ISAJET Monte Carlo

$$\sigma_{i-total} = \sqrt{\sigma^2_{i-\mu} + \sigma^2_{i-fit} + \sigma^2_{i-MC}}$$

Figure 5.12 shows the Level 2 filter efficiency vs. invariant mass, photon rapidity and photon p_T. These plots were generated using the Level 2 efficiency fit vs. electron E_T shown in 4.19. The bin-by-bin mean efficiency and statistical + systematic error were produced in exactly the same fashion as for the Level 1 efficiency plots described above.

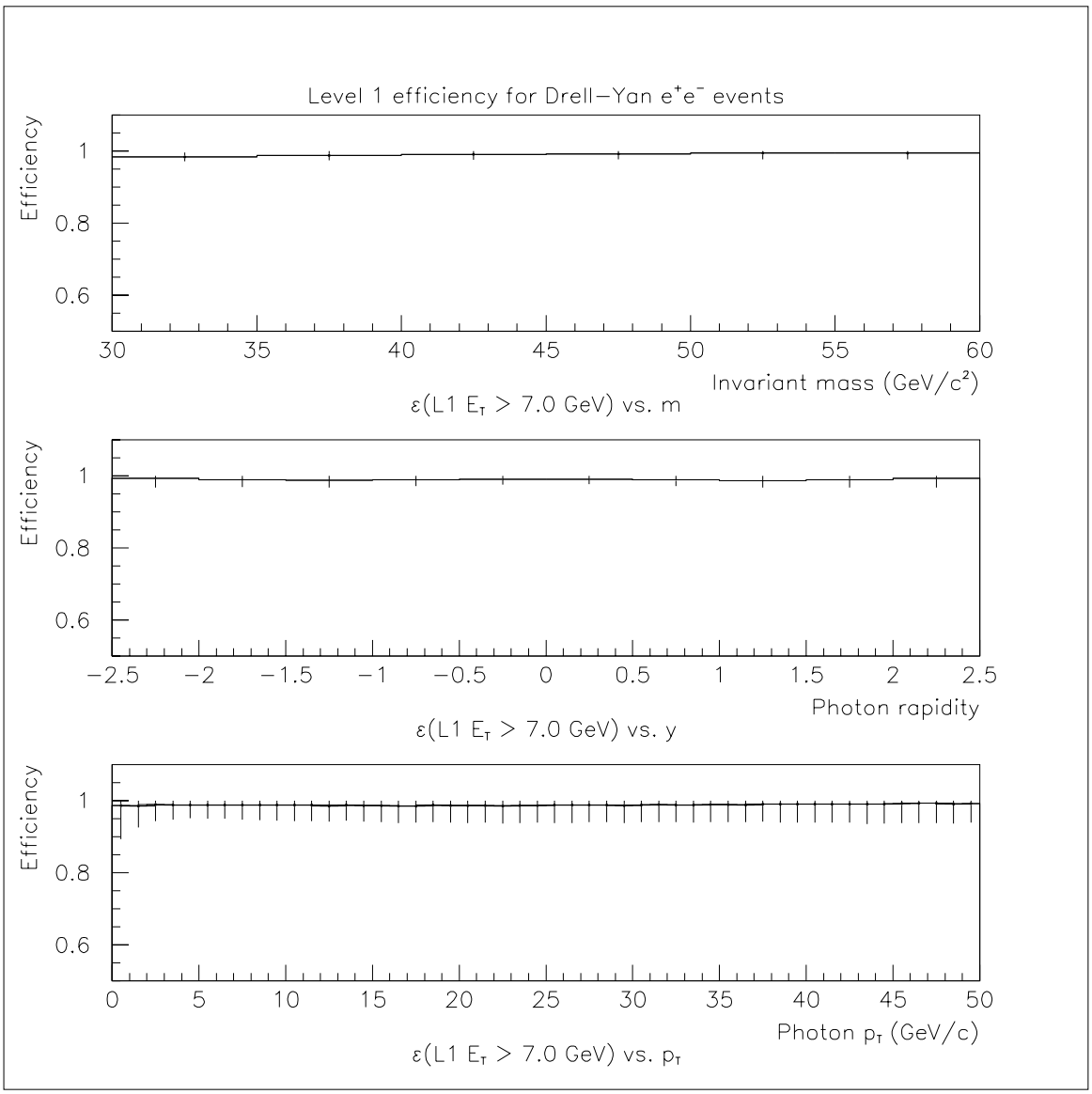

Figure 5.11: Level 1 EM $E_T > 7.0$ GeV efficiency for Drell-Yan e^+e^- events after offline cuts.

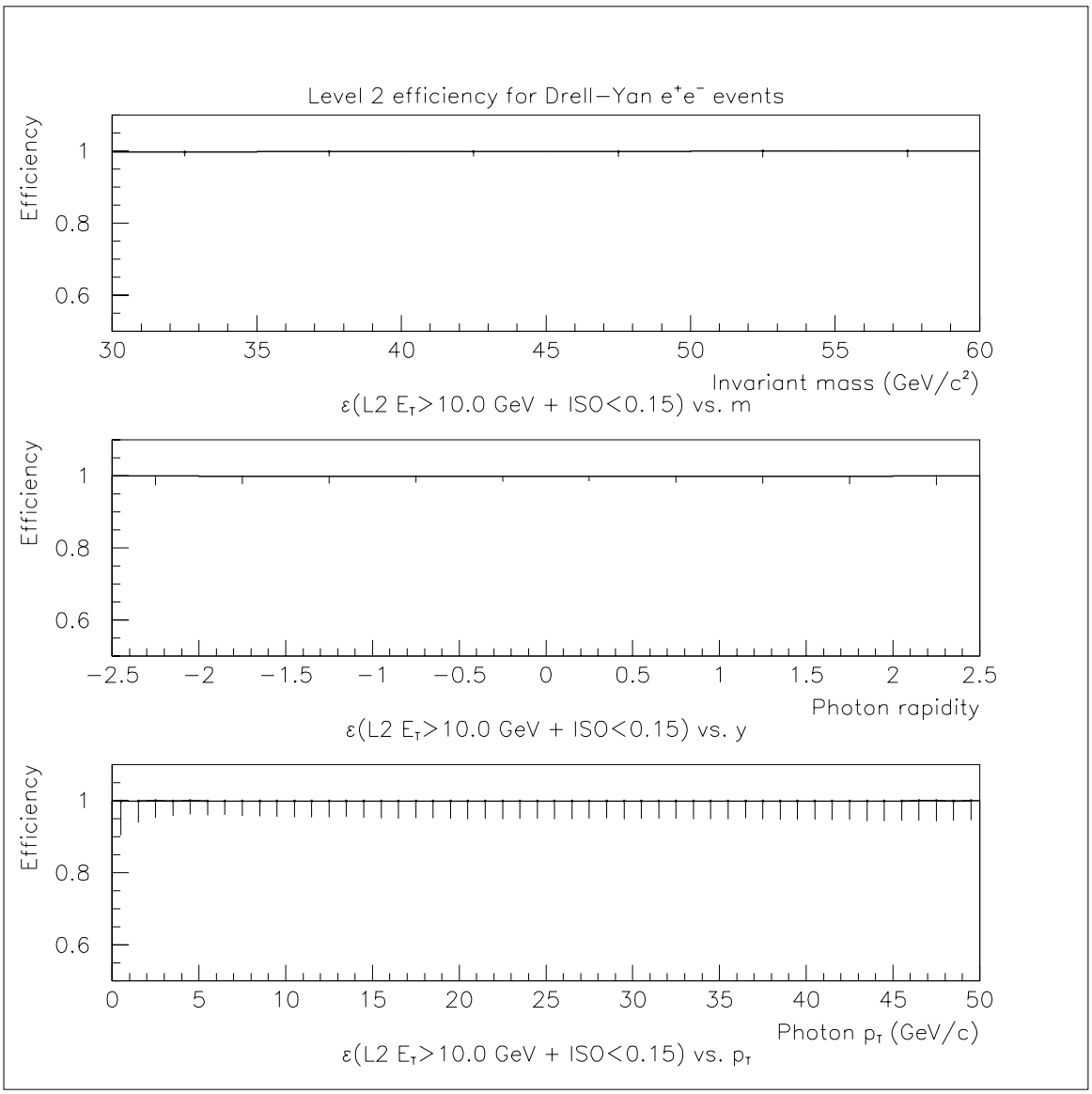

Figure 5.12: Level 2 EM $E_T > 10.0$ GeV + Level 2 ISO < 0.15 efficiency for Drell-Yan e^+e^- events after offline cuts.

5.4 Offline Efficiencies

The single electron offline electron identification cut efficiencies are given in Table 4.2 in Chapter 4 of this dissertation. These efficiencies were parameterized as functions of E_T or energy and/or IETA. In order to be able to make bin-by-bin efficiency corrections in invariant mass, photon rapidity, or photon p_T, we must determine the overall event efficiency for each cut on Drell-Yan e^+e^- events as we did for the online cut efficiencies. To do this, we again use the RESBOS Monte Carlo to provide the Drell-Yan electron kinematics which we input to our efficiency fits for each cut variable to calculate the efficiency for each electron. The event efficiency is then the product of the efficiencies for each electron

$$\epsilon_i = \frac{1}{N_i}\sum_{j=1}^{N_i} \epsilon_{cut}(e_j^+) \times \epsilon_{cut}(e_j^-)$$

where N_i is the number of Monte Carlo events in bin i and $\epsilon_{cut}(e_j^{\pm})$ is the efficiency of the cut evaluated using the electron kinematics from the Monte Carlo. The systematic efficiency variation in bin i due to the single electron efficiency fit is given by

$$\mu_i \text{ fit} = \frac{1}{100}\sum_{k=1}^{100}\sum_{j=1}^{N_i} \epsilon_{cut}(e_i^+, p'_{1k}[, p'_{2k}, \ldots]) \times \epsilon_{cut}(e_i^-, p'_{1k}[, p'_{2k}, \ldots])$$

$$\sigma_i \text{ fit} = \frac{1}{100}\sum_{k=1}^{100}(e_{ik} - \mu_i)^2$$

where

N_i = Monte Carlo events

$\epsilon_{cut}(e^+, p'_1[, p'_2, \ldots])$ = modified efficiency

$$p'_{nk} = p_n + \sigma_n Z_{nk}$$

$$\sigma_n = \text{error on fit parameter } p_n$$

$$Z_{nk} = \text{random Gaussian}$$

If there is more than one parameter in a fit, the Z_{nk} are correlated; the correlation is specified by the covariance matrix from the fit.

The systematic effect of the particular Drell-Yan kinematics used is again estimated using the ISAJET Monte Carlo to provide the kinematics of the events. The bin-by-bin difference between the RESBOS and ISAJET Monte Carlo generated histograms gives a bin-by-bin estimate of the systematic variation due to the input Monte Carlo

$$\text{Systematic error from MC in bin } i \rightarrow \sigma_{i-MC} = |\mu_{i-RESBOS} - \mu_{i-ISAJET}|$$

The total error in each bin in each plot is the standard deviation of the bin mean added in quadrature with the spread induced by varying the fit and the variation produced by using the ISAJET Monte Carlo

$$\sigma_{i-total} = \sqrt{\sigma^2_{i-\mu} + \sigma^2_{i-fit} + \sigma^2_{i-MC}}$$

Figure 5.13 shows the PPHO efficiency vs. invariant mass, photon rapidity, and photon p_T. Figure 5.14 shows the PELC/PPHO efficiency vs. the same variables. Figures 5.15 and 5.16 show the H-matrix χ^2 + Isolation fraction cuts and the track match significance + dE/dx cuts efficiencies vs. mass, rapidity, and p_T of the photon respectively. The only significant efficiency dependence appears in the efficiency vs.

Table 5.13: Efficiency corrections for Drell-Yan e^+e^- events per invariant mass bin.

Mass Bin	ϵ_{L1}	ϵ_{L1}	$\epsilon_{\chi^2_{HM}+ISO}$	ϵ_{PPHO}	$\epsilon_{PELC/PPHO}$	$\epsilon_{\sigma_{trk}+dE/dx}$	Total
30.0 - 35.0	0.984	0.998	0.788	0.966	0.743	0.741	0.412
35.0 - 40.0	0.987	0.998	0.796	0.965	0.743	0.741	0.417
40.0 - 45.0	0.990	0.999	0.803	0.966	0.743	0.735	0.419
45.0 - 50.0	0.992	0.999	0.812	0.966	0.743	0.740	0.427
50.0 - 55.0	0.994	0.999	0.820	0.966	0.743	0.734	0.430
55.0 - 60.0	0.995	0.999	0.829	0.966	0.743	0.736	0.435

Table 5.14: Efficiency corrections for Drell-Yan e^+e^- events per photon rapidity bin.

Rapidity Bin	ϵ_{L1}	ϵ_{L1}	$\epsilon_{\chi^2_{HM}+ISO}$	ϵ_{PPHO}	$\epsilon_{PELC/PPHO}$	$\epsilon_{\sigma_{trk}+dE/dx}$	Total
-2.5 - -2.0	0.993	0.999	0.741	0.988	0.743	0.509	0.275
-2.0 - -1.5	0.989	0.999	0.746	0.980	0.743	0.613	0.330
-1.5 - -1.0	0.987	0.998	0.770	0.970	0.743	0.696	0.381
-1.0 - -0.5	0.989	0.999	0.834	0.958	0.743	0.802	0.470
-0.5 - 0.0	0.991	0.999	0.852	0.955	0.743	0.849	0.508
0.0 - 0.5	0.991	0.999	0.851	0.955	0.743	0.849	0.508
0.5 - 1.0	0.988	0.998	0.836	0.958	0.743	0.804	0.472
1.0 - 1.5	0.986	0.998	0.766	0.971	0.743	0.693	0.377
1.5 - 2.0	0.989	0.999	0.746	0.980	0.743	0.613	0.329
2.0 - 2.5	0.993	0.999	0.742	0.988	0.743	0.509	0.275

photon rapidity plots. This dependence is due to the difference in the efficiencies between the forward and central regions of the detector.

5.5 Fiducial Acceptance, Kinematic Corrections And Unsmearing

The stipulations imposed by the online trigger/filter bandwidth combined with the fact that the DØ detector serves many physics analyses, required that the trigger for this analysis trigger on cluster E_T with a higher threshold than was desired. One consequence of this fact was that the data does not have a sharp mass turn-on. Also the DØ detector contains gaps at $|\text{IETA}| = 13$ where there is no EM calorimeter, as well as regions at which only some EM signals are present ($|\text{IETA}| = 12, 14$). In addition,

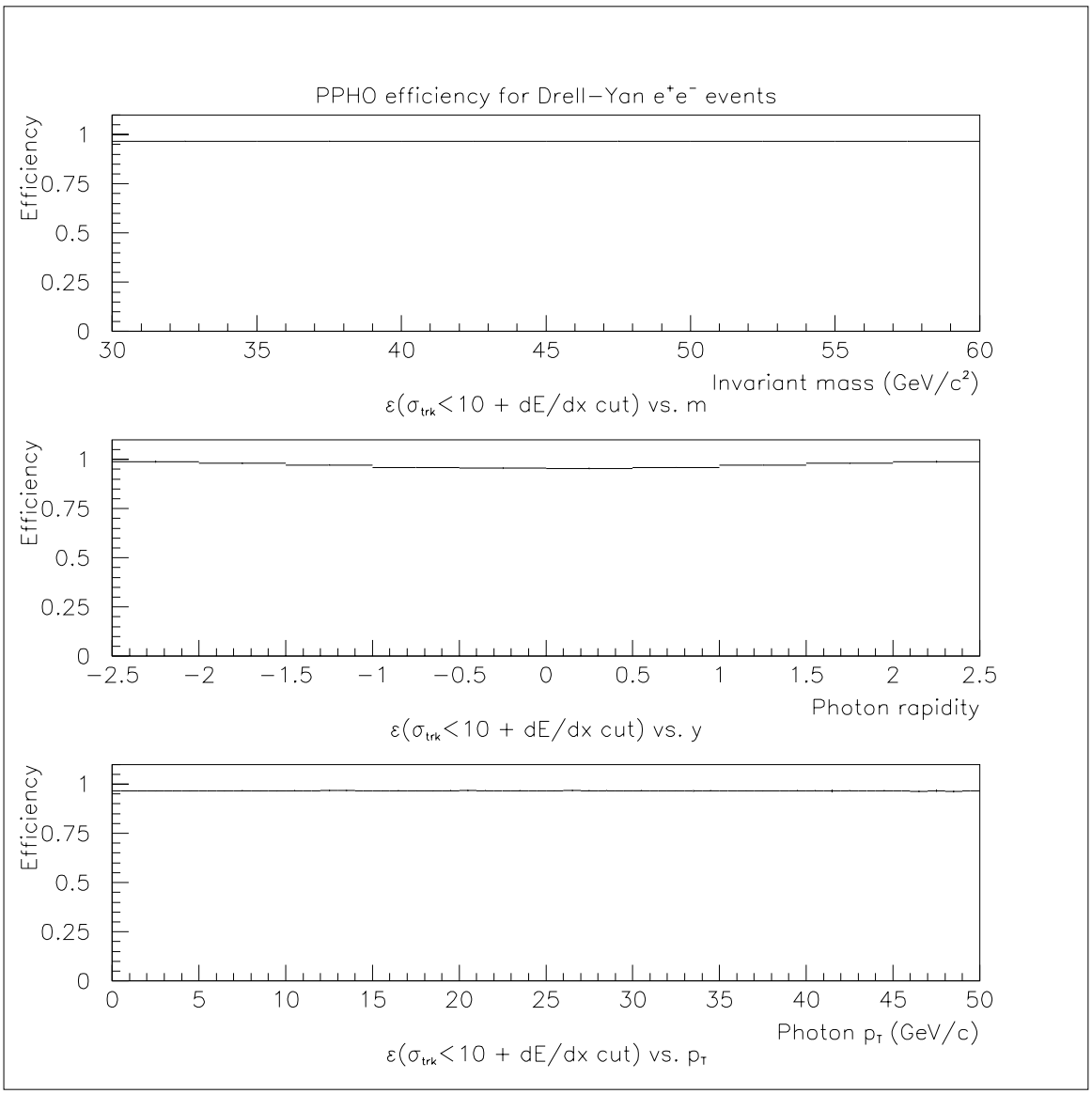

Figure 5.13: PPHO efficiency for Drell-Yan e^+e^- events.

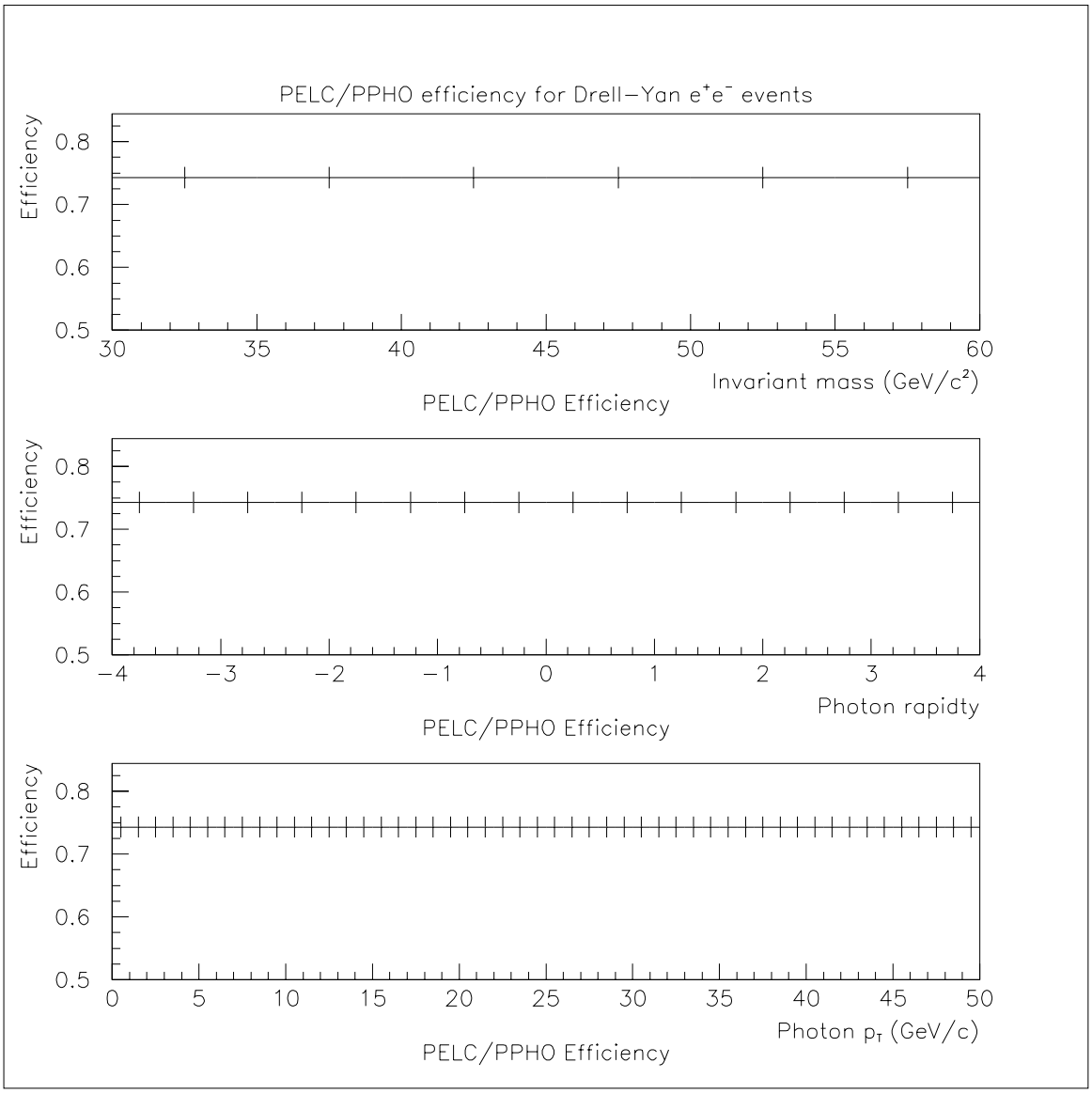

Figure 5.14: PELC/PPHO efficiency for Drell-Yan e^+e^- events.

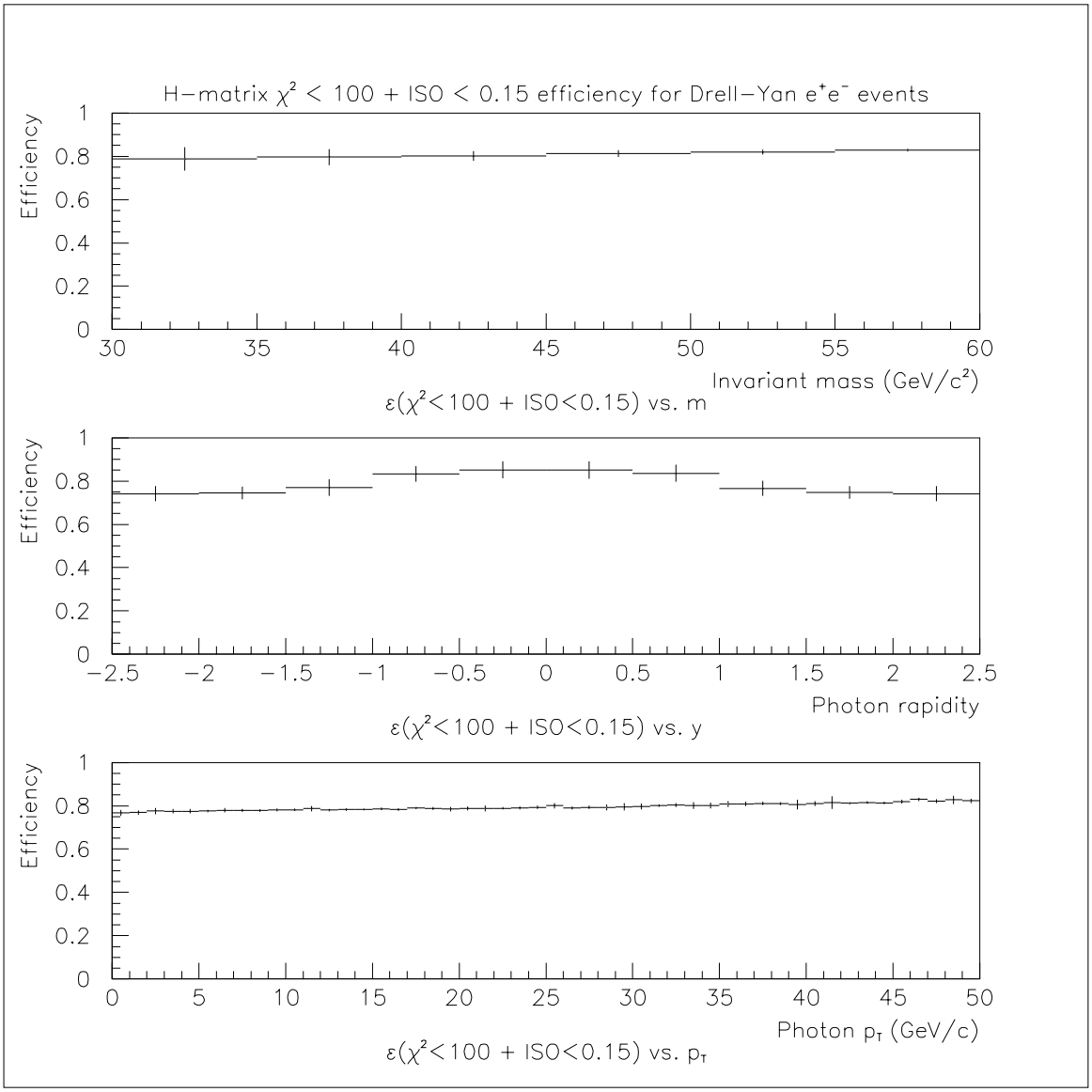

Figure 5.15: H-matrix $\chi^2 < 100 + \mathrm{ISO} < 0.15$ efficiency for Drell-Yan e^+e^- events.

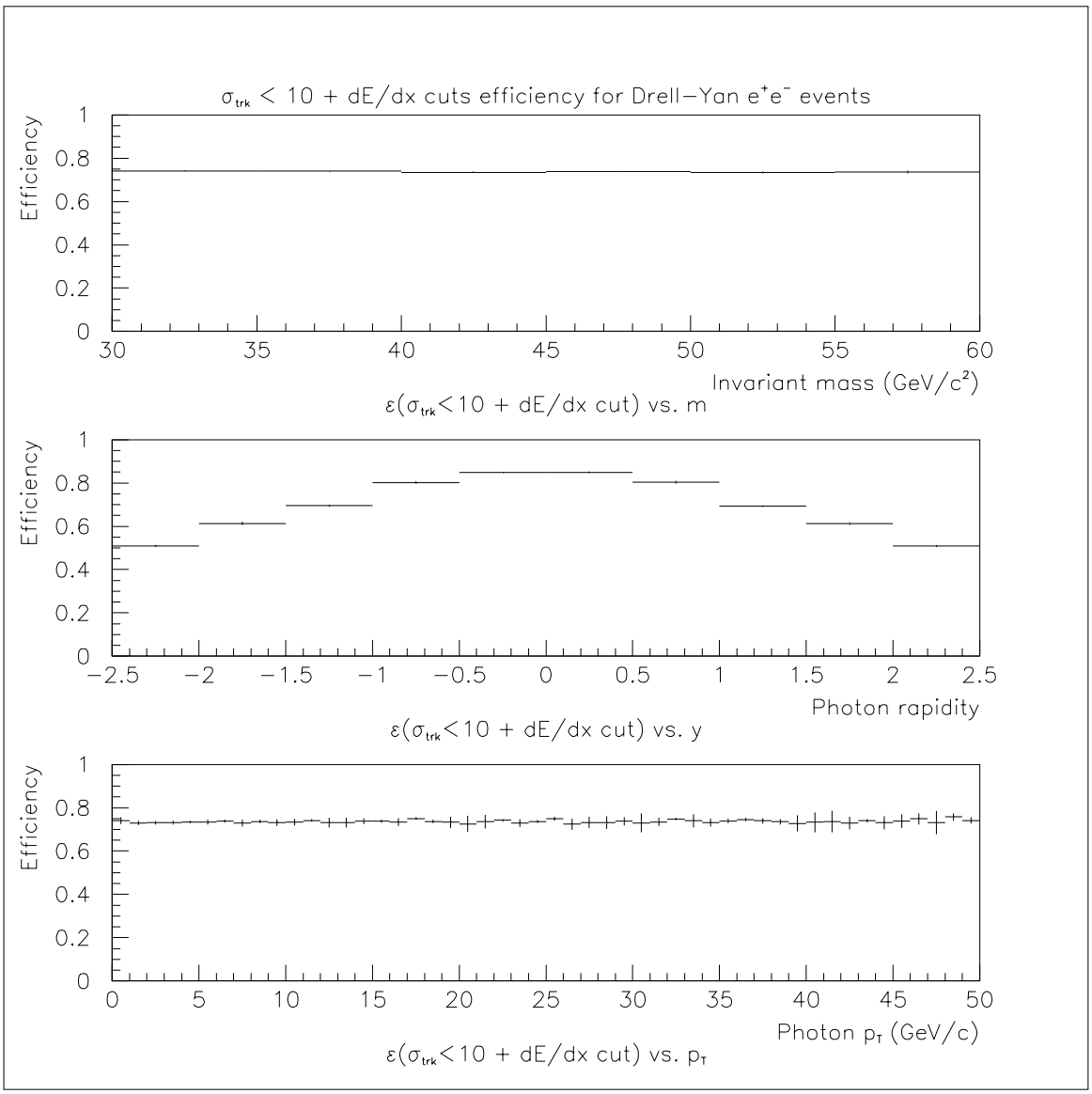

Figure 5.16: Track match significance + dE/dx cuts efficiency for Drell-Yan e^+e^- events.

Table 5.15: Efficiency corrections for Drell-Yan e^+e^- events per photon p_T bin.

p_T Bin	ϵ_{L1}	ϵ_{L1}	$\epsilon_{\chi^2_{HM}+ISO}$	ϵ_{PPHO}	$\epsilon_{PELC/PPHO}$	$\epsilon_{\sigma_{trk}+dE/dx}$	Total
0.0 - 1.0	0.986	0.999	0.767	0.965	0.743	0.741	0.401
1.0 - 2.0	0.985	0.999	0.769	0.966	0.743	0.730	0.397
2.0 - 3.0	0.989	0.999	0.776	0.966	0.743	0.731	0.402
3.0 - 4.0	0.988	0.999	0.775	0.966	0.743	0.732	0.402
4.0 - 5.0	0.988	0.999	0.775	0.966	0.743	0.735	0.404
5.0 - 6.0	0.988	0.999	0.776	0.966	0.743	0.734	0.404
6.0 - 8.0	0.987	0.998	0.779	0.966	0.743	0.733	0.404
8.0 - 10.0	0.987	0.998	0.779	0.966	0.743	0.734	0.404
10.0 - 12.0	0.988	0.999	0.784	0.966	0.743	0.738	0.410
12.0 - 16.0	0.987	0.998	0.783	0.966	0.743	0.735	0.407
16.0 - 24.0	0.986	0.998	0.787	0.966	0.743	0.736	0.409
24.0 - 32.0	0.987	0.998	0.795	0.966	0.743	0.734	0.413
32.0 - 40.0	0.989	0.998	0.806	0.966	0.743	0.738	0.421
40.0 - 50.0	0.991	0.999	0.819	0.966	0.743	0.739	0.430

no tracking exists beyond $|\text{IETA}| = 25$. In order to simplify the analysis, fiducial cuts were made to exclude the inter-cryostat region of $11 \leq |\text{IETA}| \leq 16$ (as well as remove IETA=15 which has some peculiarities in some of the electron id variables) and regions beyond which there is no tracking ($|\text{IETA}| > 25$). In order to easily compare the results of this experiment with theory, it is necessary to correct for the kinematic inefficiencies induced by the E_T thresholds and the excluded rapidity regions imposed by the fiducial cuts. Another fact of experimental life is that no measurement is exact; even a perfect experimental apparatus is limited to some quantum mechanically imposed resolution. The energy and position resolution of the DØ detector, while very good (although nowhere near the quantum limit!), results in a "feed-down" or "smearing" of most kinematic quantities one would like to measure. This smearing cannot be removed on an event-by-event basis, but can be corrected for statistically given some number of events.

The method used to make these kinematic, fiducial, and smearing corrections is straight forward, provided one can model one's apparatus accurately using computers.

It turns out that very detailed simulation of a large complicated detector such as DØ is very difficult and CPU intensive, however it can be done provided enough CPU cycles are available. This is exactly what the DØGEANT simulation attempts to do. It tracks each input particle through a precision computer representation of DØ using the physics of particle interactions with matter to determine the tracks, scattering angles, calorimeter shower shapes, etc...using a Monte Carlo method to simulate what that particle will look like in DØ. If enough CPU cycles were available, a full plate-level DØGEANT simulation could produce a very accurate representation of how events look in DØ. Unfortunately, even with today's high-speed computers, it still takes far too long to do a plate-level simulation of more than a few particles in DØ so further approximation of the DØ geometry is necessary. This is done by replacing the full description of all the uranium plates, readout boards, etc...by a homogeneous mixture of the various materials in DØ that presents the same number of radiation lengths to an incoming particle. This approximation works fairly well for broad quantities such as cluster energy, but not so well for quantities such as detailed shower shape information, since particles cannot fly off at large angles at the plate edges if there are no plate edges.

It is likely that for the kinematic, fiducial, and smearing corrections needed for this analysis, that a homogeneous mixture simulation is accurate enough, and so it is used. To calculate these corrections, we use the ISAJET Monte Carlo to generate Drell-Yan e^+e^- events which are fed into the homogeneous mixture DØGEANT simulation to provide the DØ raw data banks. The raw data is then reconstructed with DØRECO to provide all the typical kinematic quantities available in a DØ event. We then make histograms of the pair mass, rapidity, and p_T after making our kinematic and fiducial cuts. The DØGEANT simulation includes the inherent DØ energy and position resolution that causes the smearing. One then divides these histograms by histograms of

the same quantities of the input ISAJET events. So the correction for a given bin is

$$\epsilon_{Kinematic,Fiducial,Smearing} = \frac{N_{MCout}}{N_{MCin}}$$

This gives the bin-by-bin kinematic, fiducial, and smearing correction necessary to statistically correct for these effects. Since the event sample is rather small (≈2000 events), we fit the resulting histograms to produce a smoother correction. We then vary the fit parameters according to the errors on the fit to estimate the errors induced by the fit just as we did for the background, online efficiencies and offline efficiencies.

Since the energy and angular resolutions in DØ are known to some approximation ($\Delta E/E \approx 15\%/\sqrt{E}$ for example), it is possible to use an even simpler method to estimate the kinematic, fiducial and smearing corrections. One simply smears the Monte Carlo energies and angles of the Drell-Yan electrons according to Gaussian distributions with mean zero and width equal to the energy and angular resolutions and then recomputes the other kinematic variables using these smeared quantities. This method is likely less accurate than the detailed DØGEANT simulation (even using a homogeneous mixture) but it is also orders of magnitude faster. This method then can be used as check of the DØGEANT simulation and as a means to estimate the systematic error of using the ISAJET Monte Carlo as an input to the DØGEANT simulation by using a different input Monte Carlo. Figure 5.17 shows a comparison of this fast smearing method to the DØGEANT simulation. The RESBOS Monte Carlo was used as the input to the fast method. Figure 5.18 shows the combination of the kinematic, fiducial and smearing corrections vs. pair mass, rapidity, and p_T. The errors in Figure 5.18 include the difference between these two methods added in quadrature to the estimated fit error.

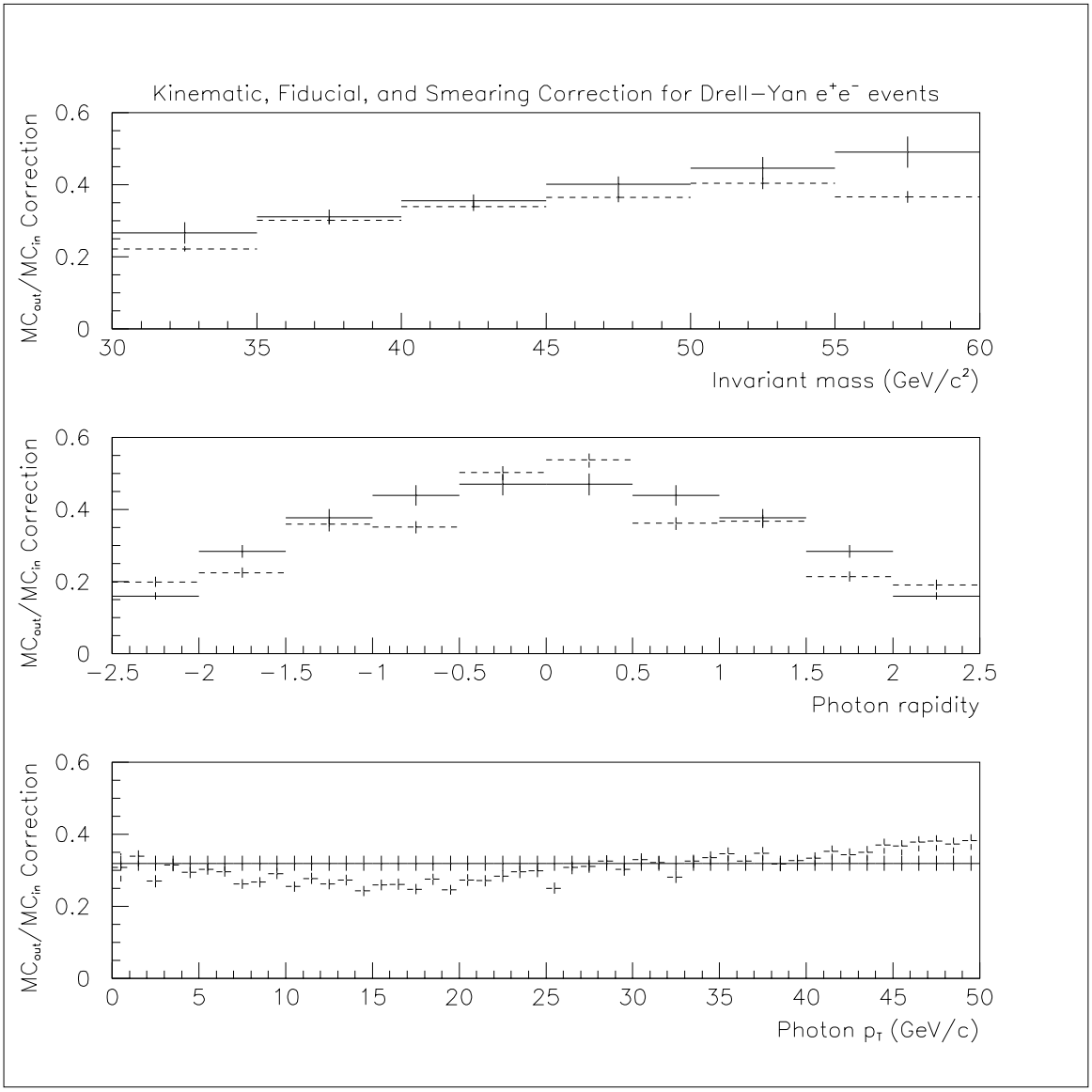

Figure 5.17: Comparison of RESBOS Monte Carlo fast kinematic, fiducial, and smearing correction (dashed) to the DØGEANT simulation (solid).

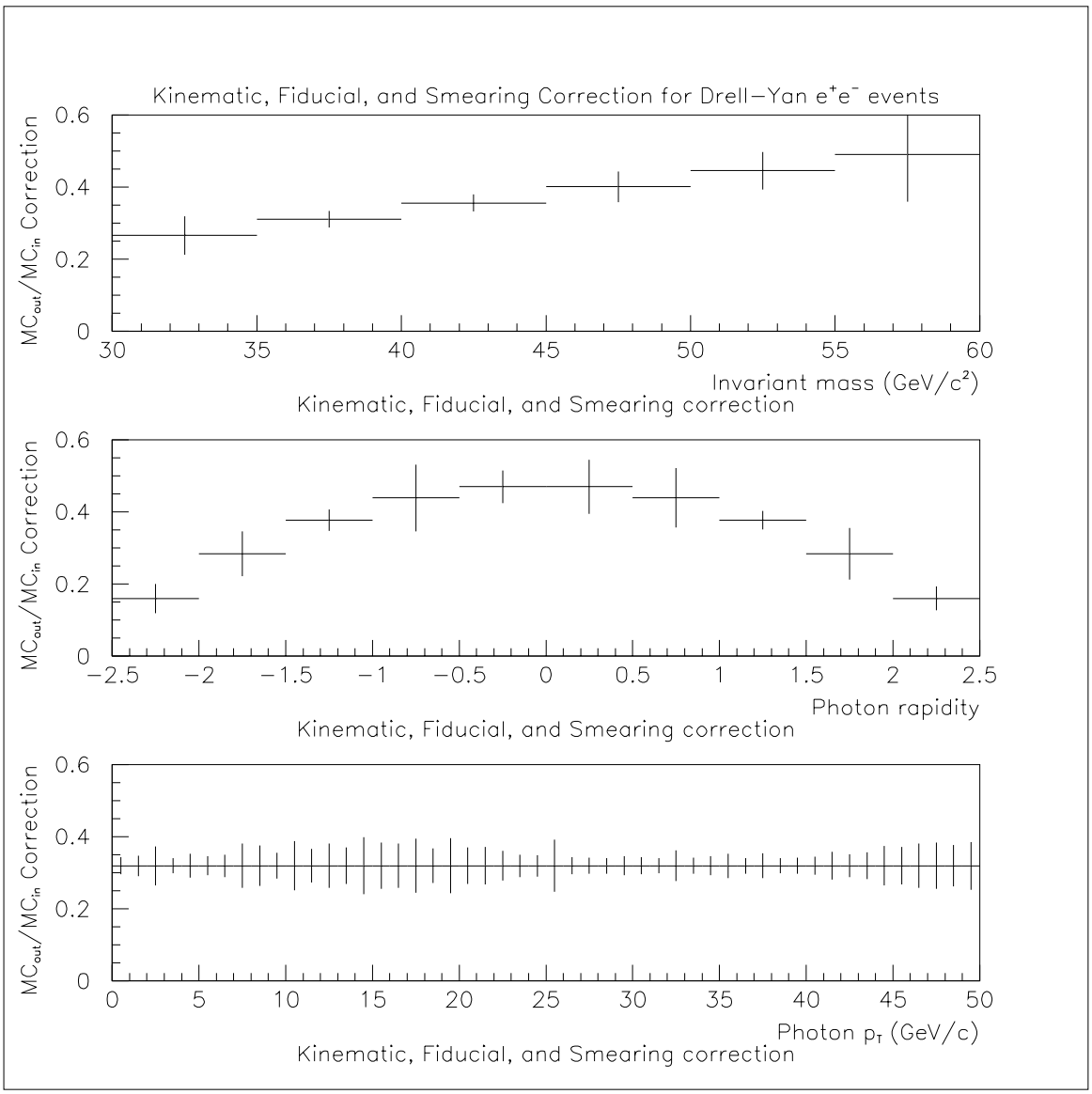

Figure 5.18: Kinematic, Fiducial Acceptance and Smearing correction for Drell-Yan e^+e^- events.

Table 5.16: Total Efficiency, Kinematic, Fiducial Acceptance and Smearing correction for Drell-Yan e^+e^- events per invariant mass bin.

Mass Bin (GeV/c^2)	Correction	Error
30.0 - 35.0	0.109	$\pm$0.023
35.0 - 40.0	0.130	$\pm$0.012
40.0 - 45.0	0.149	$\pm$0.012
45.0 - 50.0	0.171	$\pm$0.019
50.0 - 55.0	0.191	$\pm$0.023
55.0 - 60.0	0.214	$\pm$0.058
Average	0.161	$\pm$0.029

5.6 Cross Section

Figure 5.19 shows the combination of all efficiency, kinematic, fiducial, and smearing corrections to be applied to the Drell-Yan signal sample shown in 5.10. Tables 5.16, 5.17, and 5.18 give the bin-by-bin total correction vs. photon mass, rapidity, and p_T respectively. The efficiencies given in Tables 5.13, 5.14, and 5.15 were measured in such a way that they are all independent and also independent of the kinematic, fiducial, and smearing corrections (some cuts were made before the efficiency of the others were measured). Consequently, the total efficiency, kinematic, fiducial, and smearing correction is just the product of all these corrections given by

$$\begin{aligned}\epsilon_{total} &= \epsilon_{L1} \times \epsilon_{L2} \times \epsilon_{\chi^2+ISO} \times \epsilon_{PPHO} \times \epsilon_{PELC/PPHO} \times \epsilon_{\sigma_{trk}+dE/dx} \times \\ &\quad \epsilon_{Kinematic+Fiducial+Smearing}\end{aligned}$$

To produce a cross section we divide each bin by the integrated luminosity accumulated by the ELE_2_HIGH trigger and the total efficiency, kinematic, fiducial, and smearing correction according to the formula

$$\sigma_{bin} = \frac{N_{bin}}{\epsilon_{total}\mathcal{L}}$$

Table 5.17: Total Efficiency, Kinematic, Fiducial Acceptance and Smearing correction for Drell-Yan e^+e^- events per photon rapidity bin.

Rapidity Bin	Correction	Error
-2.5 - -2.0	0.044	± 0.012
-2.0 - -1.5	0.093	± 0.021
-1.5 - -1.0	0.144	± 0.014
-1.0 - -0.5	0.206	± 0.045
-0.5 - 0.0	0.238	± 0.026
0.0 - 0.5	0.238	± 0.040
0.5 - 1.0	0.207	± 0.041
1.0 - 1.5	0.142	± 0.013
1.5 - 2.0	0.093	± 0.024
2.0 - 2.5	0.044	± 0.009
Average	0.145	± 0.028

Table 5.18: Total Efficiency, Kinematic, Fiducial Acceptance and Smearing correction for Drell-Yan e^+e^- events per photon p_T bin.

p_T Bin (GeV/c)	Correction	Error
0.0 - 1.0	0.128	± 0.020
1.0 - 2.0	0.126	± 0.016
2.0 - 3.0	0.128	± 0.024
3.0 - 4.0	0.128	± 0.012
4.0 - 5.0	0.129	± 0.015
5.0 - 6.0	0.129	± 0.013
6.0 - 8.0	0.129	± 0.015
8.0 - 10.0	0.129	± 0.015
10.0 - 12.0	0.131	± 0.018
12.0 - 16.0	0.130	± 0.014
16.0 - 24.0	0.131	± 0.009
24.0 - 32.0	0.132	± 0.006
32.0 - 40.0	0.135	± 0.006
40.0 - 50.0	0.137	± 0.008
Average	0.130	± 0.014

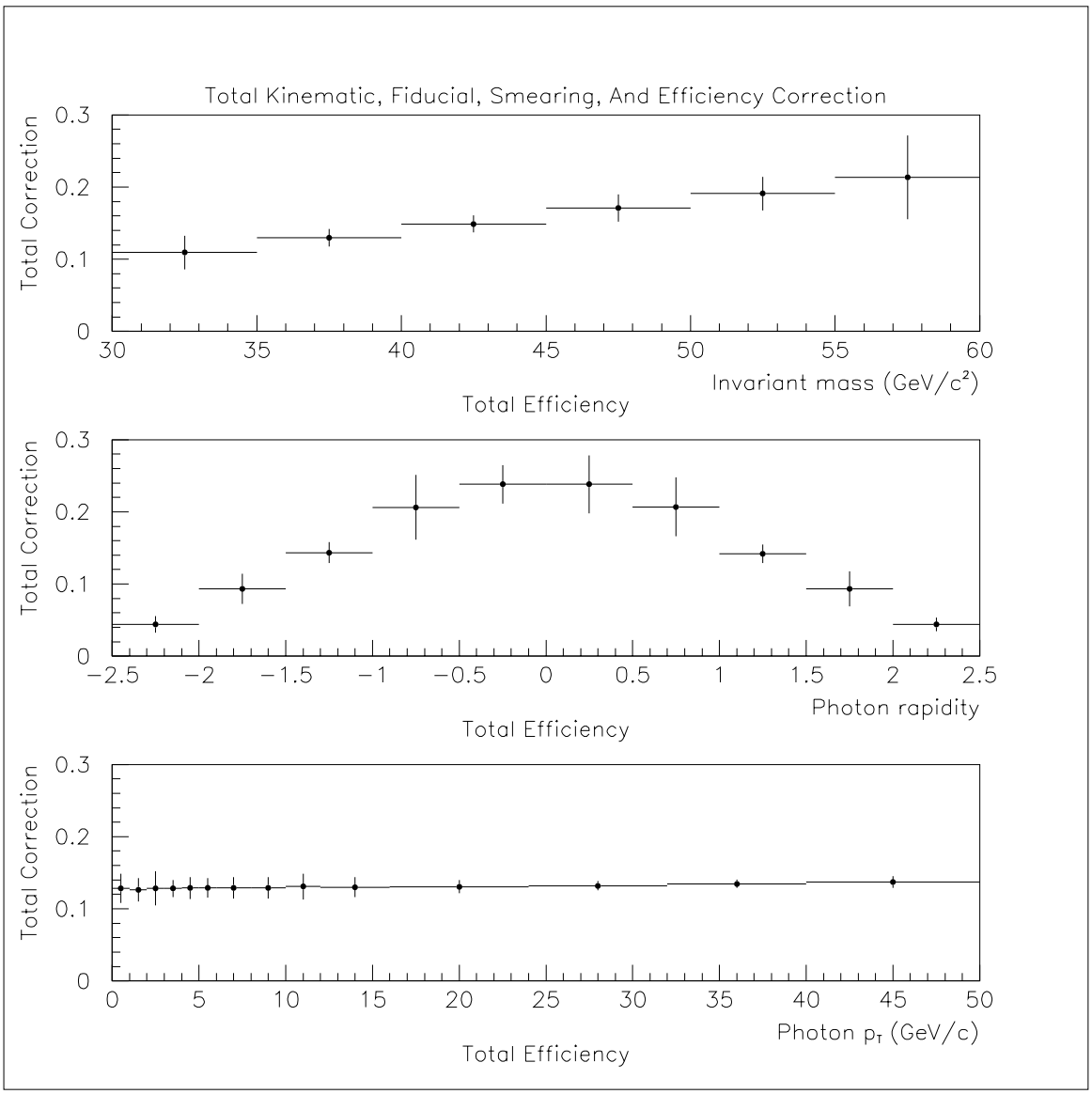

Figure 5.19: Total Efficiency, Kinematic, Fiducial Acceptance and Smearing correction for Drell-Yan e^+e^- events.

Table 5.19: Integrated Drell-Yan cross section per invariant mass bin.

Mass Bin (GeV/c^2)	Integrated Cross Section (pb)	Error (pb)
30.0 - 35.0	15.89	$\pm$ 5.10
35.0 - 40.0	11.96	$\pm$ 3.22
40.0 - 45.0	6.31	$\pm$ 2.26
45.0 - 50.0	5.28	$\pm$ 1.93
50.0 - 55.0	3.33	$\pm$ 1.49
55.0 - 60.0	2.33	$\pm$ 1.32
Total	45.07	$\pm$ 7.01

The bin contents are also divided by the bin width to give the correct units.

$$d\sigma_{bin}/dx_{bin} = \sigma_{bin}/\Delta_{bin}$$

Figures 5.20, 5.21, 5.22 show the measured inclusive Drell-Yan e^+e^- cross section vs. invariant mass, photon rapidity, and photon p_T respectively. The inner error bars are the statistical errors only, the outer error bars are the total statistical + systematic errors. Tables 5.19, 5.20, 5.21 list the actual integrated cross section per bin vs. photon mass, rapidity, and p_T along with the associated total error.

5.7 Systematic Errors

We have attempted to estimate some of the systematic errors associated with our cross section (which we described earlier) and have included those estimates in our error bars. However, since DØ is a relatively new experiment and this data was taken during its first data run, some systematic errors have been neglected since we are still learning about our apparatus. Others such as the smearing induced by the energy and position resolutions described in Section 5.5 are being meticulously studied by groups

Table 5.20: Integrated Drell-Yan cross section per photon rapidity bin.

Rapidity Bin	Integrated Cross Section (pb)	Error (pb)
-2.5 - -2.0	1.83	± 3.20
-2.0 - -1.5	2.20	± 2.15
-1.5 - -1.0	3.67	± 1.80
-1.0 - -0.5	5.32	± 1.99
-0.5 - 0.0	3.22	± 1.25
0.0 - 0.5	4.54	± 1.60
0.5 - 1.0	5.13	± 1.90
1.0 - 1.5	6.27	± 2.33
1.5 - 2.0	4.96	± 2.99
2.0 - 2.5	2.81	± 3.92
Total	39.93	± 7.71

Table 5.21: Integrated Drell-Yan cross section per photon p_T bin.

p_T Bin (GeV/c)	Integrated Cross Section (pb)	Error (pb)
0.0 - 1.0	1.64	± 1.10
1.0 - 2.0	6.07	± 2.19
2.0 - 3.0	6.01	± 2.36
3.0 - 4.0	5.77	± 2.15
4.0 - 5.0	4.14	± 1.92
5.0 - 6.0	2.61	± 1.62
6.0 - 8.0	3.81	± 2.04
8.0 - 10.0	4.14	± 1.98
10.0 - 12.0	4.03	± 1.91
12.0 - 16.0	3.30	± 1.86
16.0 - 24.0	3.47	± 1.84
24.0 - 32.0	1.48	± 1.16
32.0 - 40.0	0.50	± 0.72
40.0 - 50.0	1.24	± 0.87
Total	48.20	± 6.61

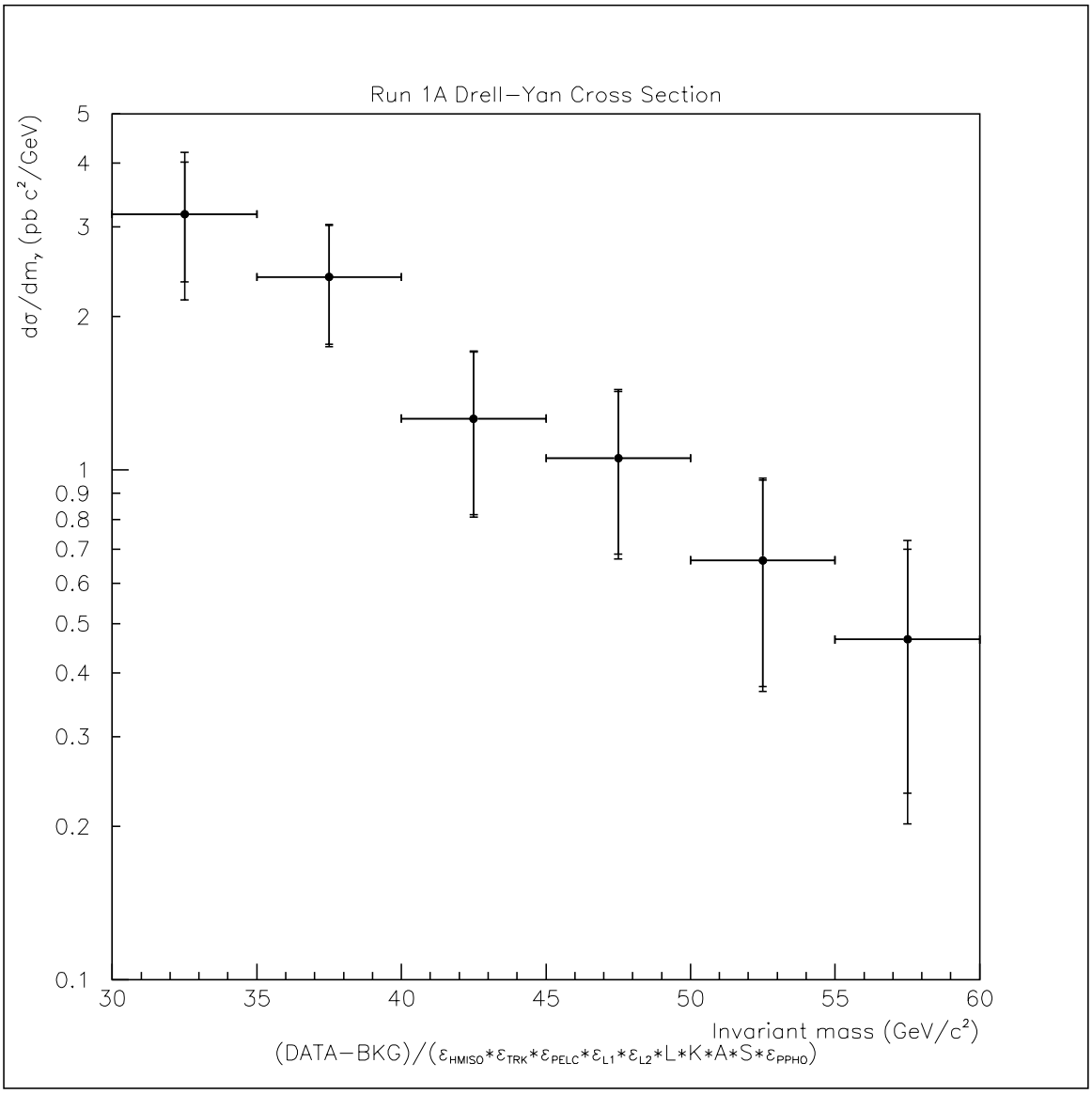

Figure 5.20: Drell-Yan e^+e^- differential cross section $d\sigma/dm$ vs. invariant mass. Inner error bars are statistical error only, outer error bars are statistical + systematic errors.

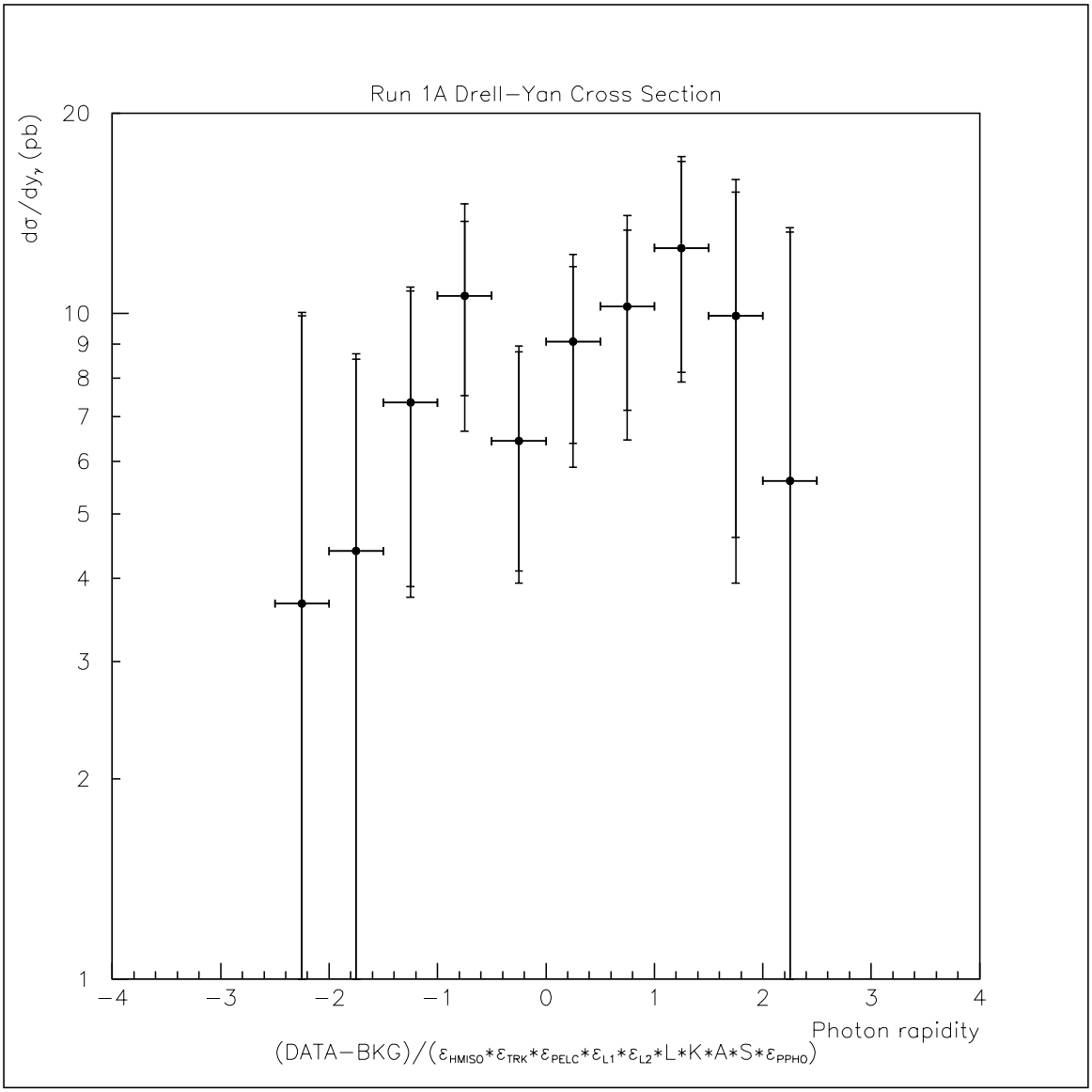

Figure 5.21: Drell-Yan e^+e^- differential cross section $d\sigma/dy$ vs. photon rapidity. Inner error bars are statistical error only, outer error bars are statistical + systematic errors.

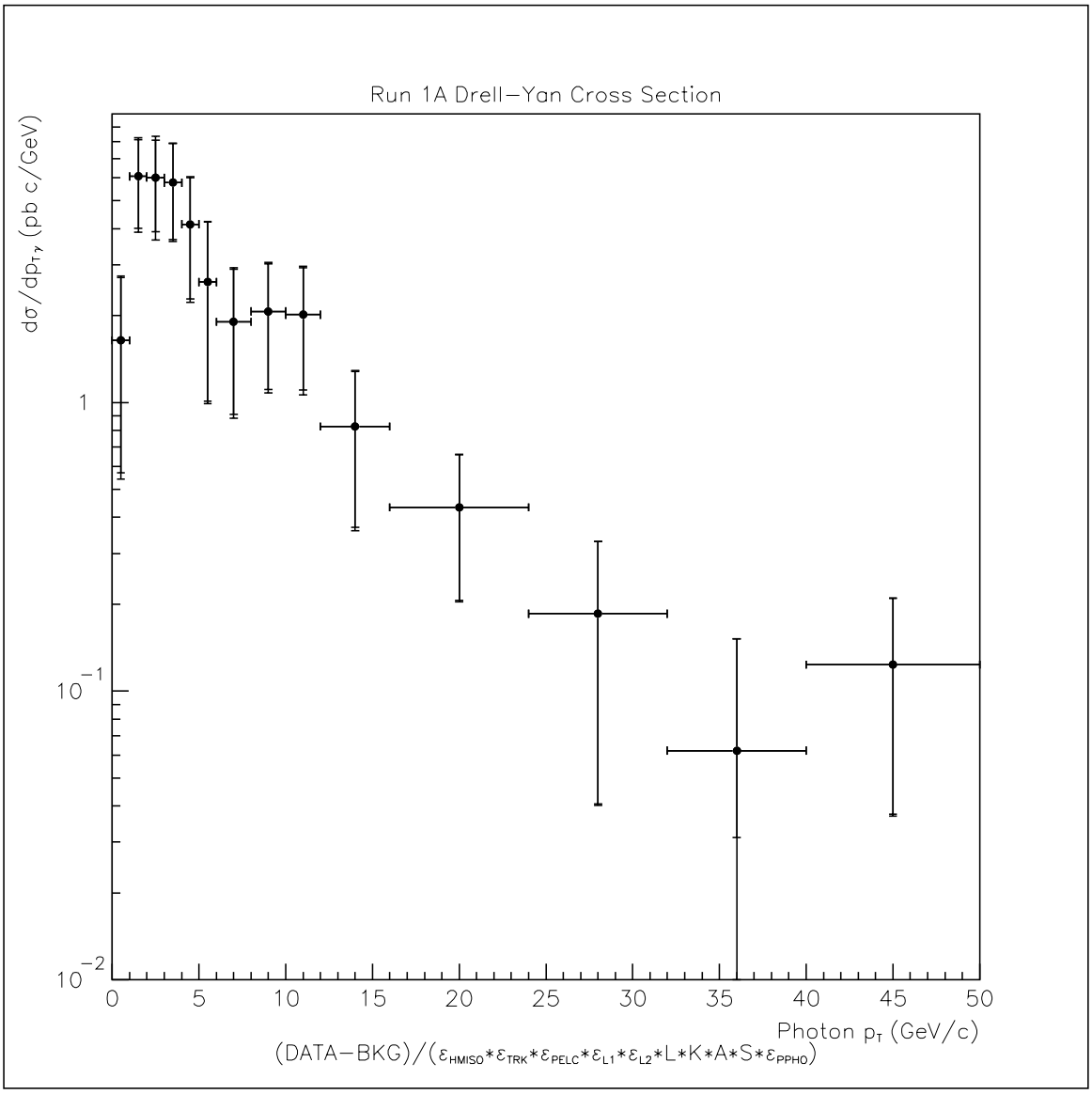

Figure 5.22: Drell-Yan e^+e^- differential cross section $d\sigma/dp_T$ vs. photon p_T. Inner error bars are statistical error only, outer error bars are statistical + systematic errors.

in DØ, most notably by the W mass group.

One area in which the energy and position resolutions can have a large effect is in the background subtraction. Fortunately we were able to devise a background estimation method that used our data sample for our dijet background which is by far our largest background. Since data was used to estimate the dijet background, the only systematic error we should incur by using it is due to the rejection fits which we varied in an attempt to quantify this error. The Z$\rightarrow \tau^+\tau^- \rightarrow e^+e^-$ background, on the other hand will induce systematic errors since these events were only smeared using an estimate of the energy and position resolutions, but this background is small and thus cannot have a very large systematic effect.

Another area in which we incur systematic errors are the various efficiency corrections for the trigger and calorimeter based electron identification cuts. In an attempt to minimize these systematic errors we used the full plate level DØGEANT simulation in our generation the single Monte Carlo electrons used to measure these efficiencies. In addition these events were overlapped with real DØ minimum bias events before reconstruction as described in Chapter 4. The addition of the minimum bias events adds uranium and electronics noise to the events which is absent from the DØGEANT simulation. It also adds some small hadronic activity such as may be due to the underlying event in a typical Drell-Yan event. Many groups in DØ are currently using this method since it has been shown to mimic real DØ electrons well. It would be preferable to use real electron data to measure these efficiencies, but no source of low energy electrons exists without removing the substantial dijet background by using the very cuts one wishes to analyze, so we must rely on Monte Carlo data. Real Z $\rightarrow ee$ data was used for the tracking cut efficiencies since they should be energy independent, so the systematic error incurred here should be mostly due to background contamination (which should be small since we can cut hard on one of the electrons,

and use the calorimeter cuts on the other).

Finally, all of these systematic errors are small compared to the statistical errors on this measurement as can be seen by the difference in size of the statistical and statistical + systematic errors shown in Figures 5.20, 5.21, and 5.22. Consequently, it is probably not worthwhile to work on most of the systematic errors any further for this measurement. Even with the factor of two reduction in the statistical error that may be possible by combining the Run 1B data sample with this data, the statistical error would still be significantly larger than the systematic error. The one area of systematic error that would likely benefit from further work is the kinematic, fiducial, and smearing correction.

Chapter 6

Results And Comparison To Theory

6.1 Statistical Compatibility Tests

The two most important properties of any statistical test are the power of the test and the confidence level of the test. The purpose of a statistical test is to distinguish between a null hypothesis H_0 (in our case H_0 is the the statement that the experimental and theoretical distributions are compatible) and the alternative hypothesis H_1 (the distributions are not compatible). The power of the test is the probability of rejecting the null hypothesis when the alternative is true. In our case the alternative H_1 is not well-defined since it is the ensemble of all hypotheses except the null hypothesis H_0. Thus it is not possible to determine whether one test is more powerful than another in general, but only with respect to certain particular deviations from the null hypothesis. The confidence level of a test is the probability of rejecting H_0 when it is in fact true. That is to say, if one accepts the null hypothesis whenever the confidence level is greater than 0.05, then truly compatible distributions will fail the test 5% of the time if the experiment were performed many times. Thus the confidence level is the probability that the distributions are compatible. A confidence level near 1.0 indicates that that the two distributions are very similar, values near 0.0 indicate that it is very unlikely that the two distributions came from the same parent distribution.

Several goodness-of-fit tests exist to help determine if our measured cross section agrees with the theoretical prediction. The tests we will use are the Pearson χ^2 test [64] and the Smirnov-Cramèr-Von Mises test [64]. The Pearson χ^2 test is the easiest to perform but does not take into account the sign of the deviations so it is less powerful in determining whether the shapes of two distributions are compatible, especially if the data has large errors associated with it. The Smirnov-Cramèr-Von Mises test uses the average squared difference of the cumulative distribution functions (integrated probability distributions) to calculate the test statistic and thus is a powerful test of whether the shapes of distributions are compatible. However, it is intended for unbinned data, so some of its power is lost when it is used on binned data since the information about the events' position within the bins is lost. The Smirnov-Cramèr-Von Mises test is not sensitive to any difference in the relative normalizations between two distributions since it acts on the cumulative distribution functions which are normalized to 1.0 by definition. However, it can be combined with a χ^2 test on the normalizations using the formula

$$P(shape + normalization) =$$
$$P(shape)P(normalization)(1 - \ln(P(shape)P(normalization)))$$

The reader should refer to [64] for a detailed descriptions of these tests; we simply define the tests here.

6.1.1 Pearson χ^2 Test

The χ^2 test uses the sum of the squared bin-by-bin deviation between the two distributions being compared divided by the probability content of the each bin under the null hypothesis H_0 as its test statistic T

$$T = \frac{1}{N} \sum_{i=1}^{k=bins} \frac{(t_i - Np_i)^2}{p_i}$$

where N is the integrated contents of the measured distribution, p_i is the probability content of bin i of the measured distribution $p_i = d_i/N$ (where d_i is the content of bin i of the measured distribution, $d_i = Np_i$), and t_i is the content of bin i of the theoretical distribution which we want to compare. Given these definitions we can rewrite this test statistic as

$$T = \sum_{i=1}^{k=bins} \frac{(t_i - d_i)^2}{\sigma_i^2}$$

where we have used the Poisson definition of the variance $\sigma_i^2 = d_i$. Thus, if H_0 is true, T is distributed as a χ^2, since it is the sum of the squares of standard scores $Z = x/\sigma$. The confidence level $P(T)$ of this test is then given by the upper tail integral of a χ^2 distribution with k degrees of freedom where k is the number of bins being compared between the two distributions

$$P(T) = P(\chi^2|k) = \frac{1}{\sqrt{2^k},\ (k/2)} \int_{\chi^2}^{\infty} e^{\frac{x}{2}} x^{\frac{k-1}{2}} dx$$

6.1.2 Smirnov-Cramèr-Von Mises Test

The Smirnov-Cramèr-Von Mises test uses the test statistic $n_{eff}\omega^2$ where

$$\omega^2 = \int_{-\infty}^{\infty} (F(x) - F^*(x))^2 dF(x)$$

and n_{eff} is the number of effective events since we are using weighted data. $F^*(x)$ is the cumulative probability distribution function of the measured distribution and $F(x)$ is the cumulative probability distribution function of the theoretical distribution we wish to compare. For binned data we replace the integral by a sum

$$\omega^2 = \sum_{i=1}^{bins} (F_i - F_i^*)^2 \Delta F_i$$

$$n_{eff} = \frac{\left(\sum_{i=1}^{N} w_i\right)^2}{\sum_{i=1}^{N} w_i^2}$$

The asymptotic characteristic function of this test is given by

$$\lim_{n_{eff}\to\infty} E(e^{it n_{eff}\omega^2}) = \sqrt{\frac{\sqrt{2it}}{\sin\sqrt{2it}}}$$

By inversion of this equation one can compute the confidence level associated with the test statistic $n_{eff}\omega^2$.

6.2 Mass Distribution

The integrated Drell-Yan e^+e^- cross section in the 30-60 GeV/c^2 mass range computed from the $d\sigma/dm$ distribution is $45.1 \pm 7.0(stat. + sys.)$ pb. The integrated RESBOS cross section is 52.4 ± 0.4 pb and the integrated ISAJET cross section is 52.2 ± 0.2 pb. These measurements are consistent within the errors. Figures 6.1 and 6.2 show a comparison between our experimental $d\sigma/dm$ distribution and the RESBOS and ISAJET Monte Carlo distributions respectively. The RESBOS Monte Carlo was

Table 6.1: Cumulative distribution functions from the $d\sigma/dm$ distribution used in the Smirnov-Cramèr-Von Mises test.

Bin	$F_{DATA}(m)$	$F_{RESBOS}(m)$	$F_{ISAJET}(m)$
1	0.352	0.398	0.383
2	0.618	0.638	0.618
3	0.758	0.788	0.768
4	0.875	0.887	0.869
5	0.948	0.954	0.943
6	1.000	1.000	1.000

run using the CTEQ3M parton distributions, whereas the ISAJET Monte Carlo was run using the CTEQ2L parton distributions. Figure 6.3 shows a comparison of the $m^3 d^2\sigma/dmdy|_{y=0}$ distribution between the data and the RESBOS Monte Carlo. The bin centers were used for the mass values. Figure 6.4 shows a comparison of our measured cross section to the CDF cross section from the 1988-1989 Fermilab collider run [68]. The x-coordinates of the points are the CDF mass centroid. The CDF integrated luminosity for this run was 4.13 pb^{-1}.

Table 6.1 shows the cumulative distribution functions used in the Smirnov-Cramèr-Von Mises test on the $d\sigma/dm$ distributions. Table 6.2 shows the value of the test statistics for the Pearson χ^2 and Smirnov-Cramèr-Von Mises goodness-of-fit tests along with the respective confidence levels of these test statistics computed between the data and RESBOS Monte Carlo and ISAJET Monte Carlo. The test statistics for the χ^2 and Smirnov-Cramèr-Von Mises tests were computed as described in Section 6.1. The χ^2 test confidence levels were calculated using the CERN program library function PROB [67]. The Smirnov-Cramèr-Von Mises test confidence levels were gotten by looking up the value in a Smirnov-Cramèr-Von Mises test significance table [65].

The results of the Pearson χ^2 and Smirnov-Cramèr-Von Mises tests indicate that invariant mass distributions from both the RESBOS and ISAJET Monte Carlo

Table 6.2: Goodness-of-fit test results from comparing the experimental $d\sigma/dm$ distribution to the RESBOS and ISAJET Monte Carlo distributions.

Theory	Test	Test Value	Confidence
RESBOS	Pearson χ^2	$\chi^2 = 1.458, k = 6$	0.962
RESBOS	Smirnov-Cramèr-Von Mises	0.045	0.876
ISAJET	Pearson χ^2	$\chi^2 = 1.482, k = 6$	0.961
ISAJET	Smirnov-Cramèr-Von Mises	0.016	0.997

Table 6.3: Smirnov-Cramèr-Von Mises test on the $d\sigma/dm$ distribution combined with a χ^2 test on the integrated cross section (normalization).

Theory	Test	Confidence
RESBOS	Smirnov-Cramèr-Von Mises	0.611
ISAJET	Smirnov-Cramèr-Von Mises	0.668

generators are compatible with our experimental measurement. This is not very surprising since ISAJET and RESBOS agree well in terms of the overall event rate they predict.

Table 6.3 shows the result of combining the Smirnov-Cramèr-Von Mises test with a χ^2 test on the integrated cross-section (normalization test) according to

$$P(\text{shape}) + P(\chi^2(\text{normalization})) = P_{shape} P_{norm}(1 - \ln(P_{shape} P_{norm}))$$

where $P(\text{shape})$ is the confidence level of the Smirnov-Cramèr-Von Mises test. The resulting combined probability indicates good agreement (less than 1 standard deviation) between the distributions.

6.3 Photon p_T Distribution

The integrated Drell-Yan e^+e^- cross section in the 30-60 GeV/c^2 mass range using the $d\sigma/dp_T$ distribution is 48.2 ± 6.6 pb. The integrated RESBOS cross section is 51.8 ± 0.4 pb and the integrated ISAJET cross section is 52.0 ± 0.7 pb. These integral

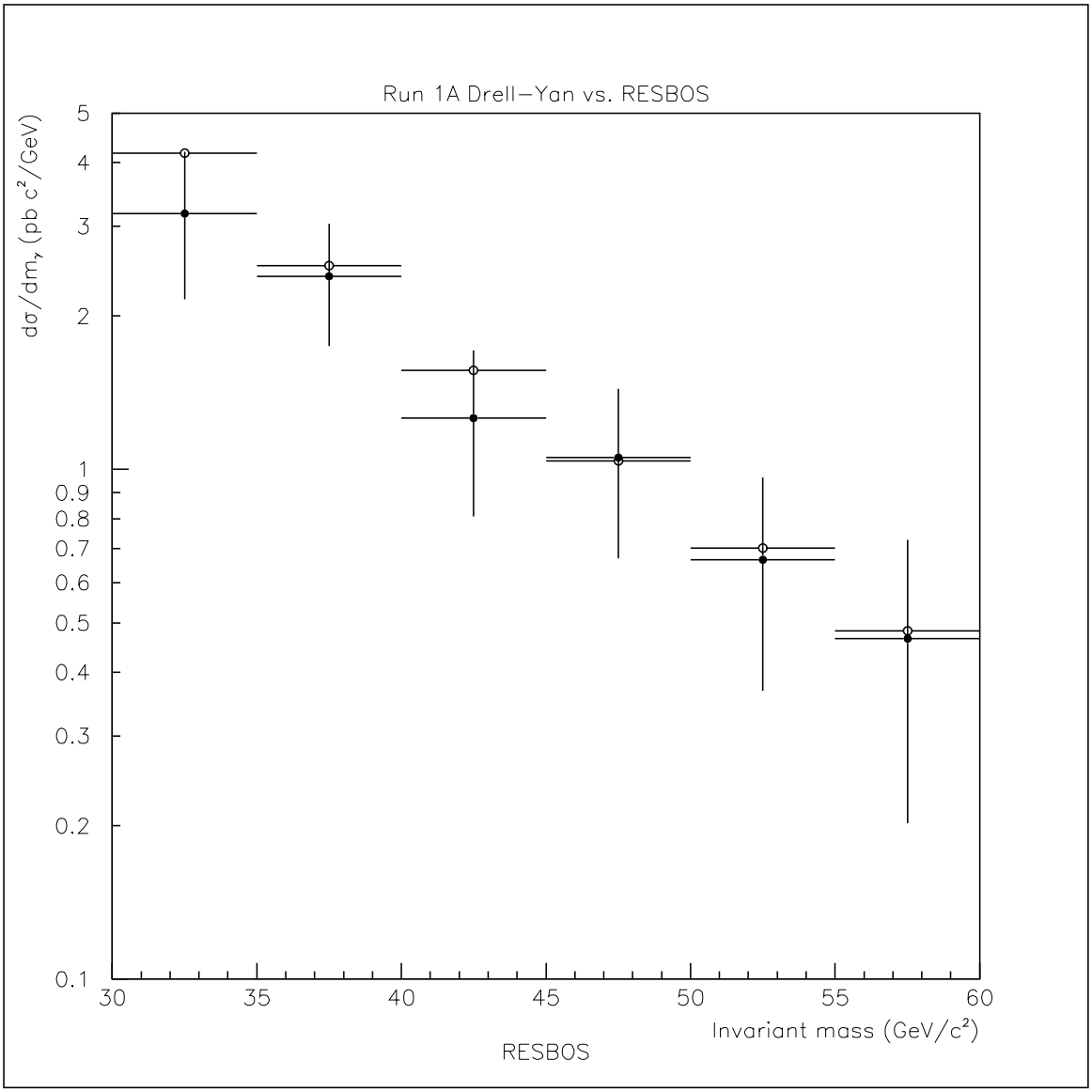

Figure 6.1: Drell-Yan e^+e^- differential cross section $d\sigma/dm$ vs. invariant mass (filled circles) compared to the resummed theoretical $d\sigma/dm$ distribution (open circles) from the RESBOS Monte Carlo.

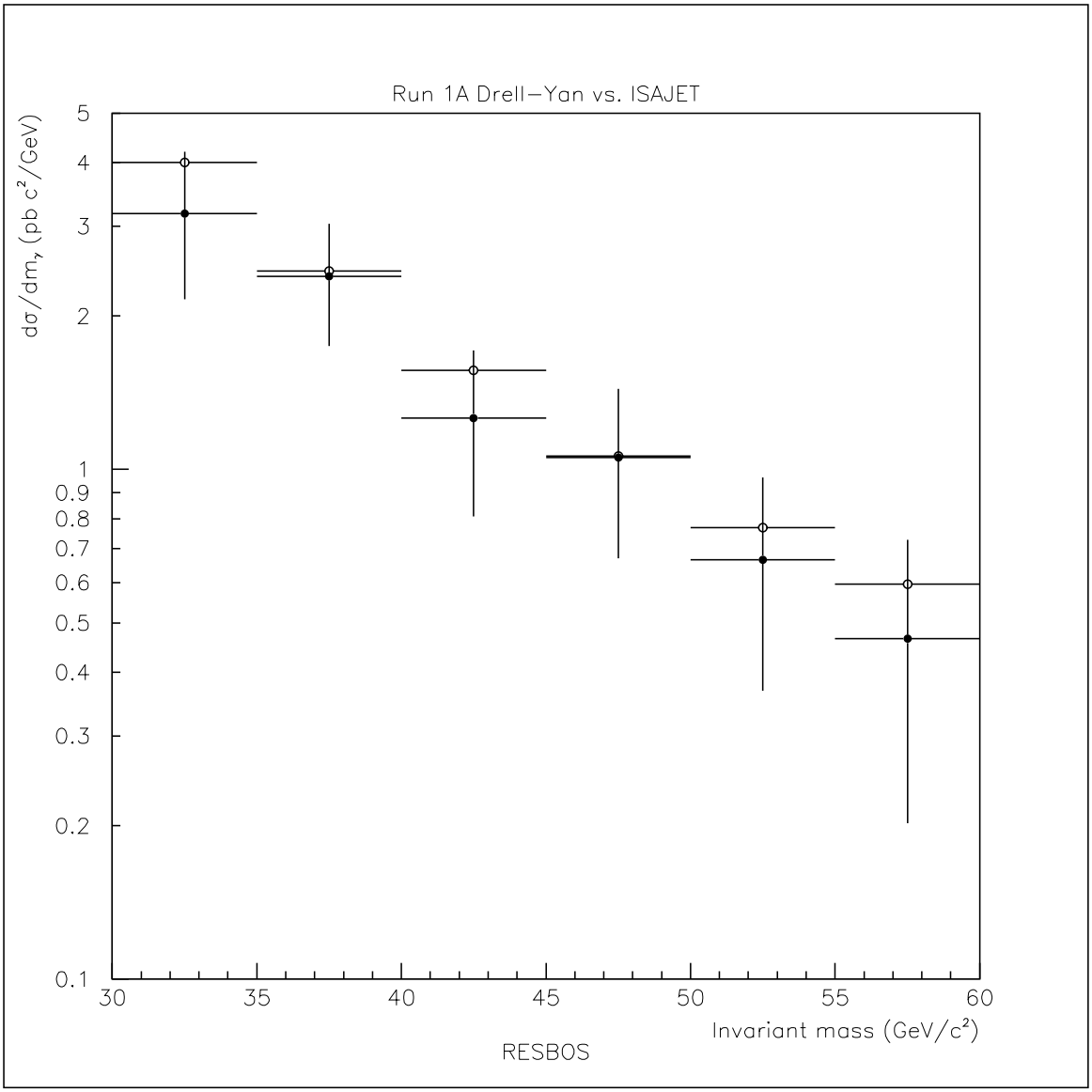

Figure 6.2: Drell-Yan e^+e^- differential cross section $d\sigma/dm$ vs. invariant mass (filled circles) compared to the theoretical $d\sigma/dm$ distribution (open circles) from the ISAJET Monte Carlo.

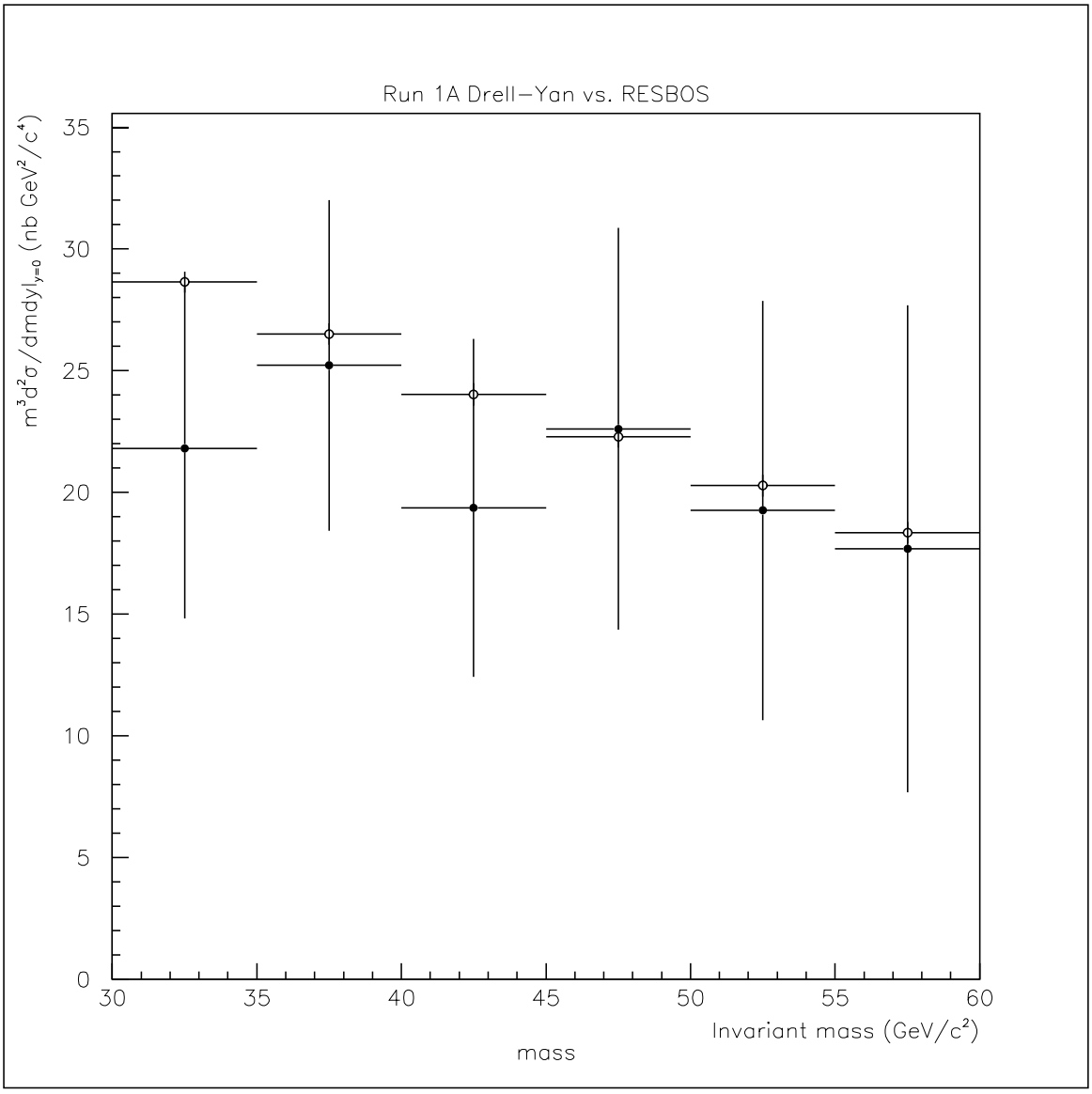

Figure 6.3: Drell-Yan e^+e^- differential cross section $m^3d^2\sigma/dmdy|_{y=0}$ vs. $m^3d^2\sigma/dmdy|_{y=0}$ invariant mass (filled circles) compared to the resummed theoretical distribution (open circles) from the RESBOS Monte Carlo.

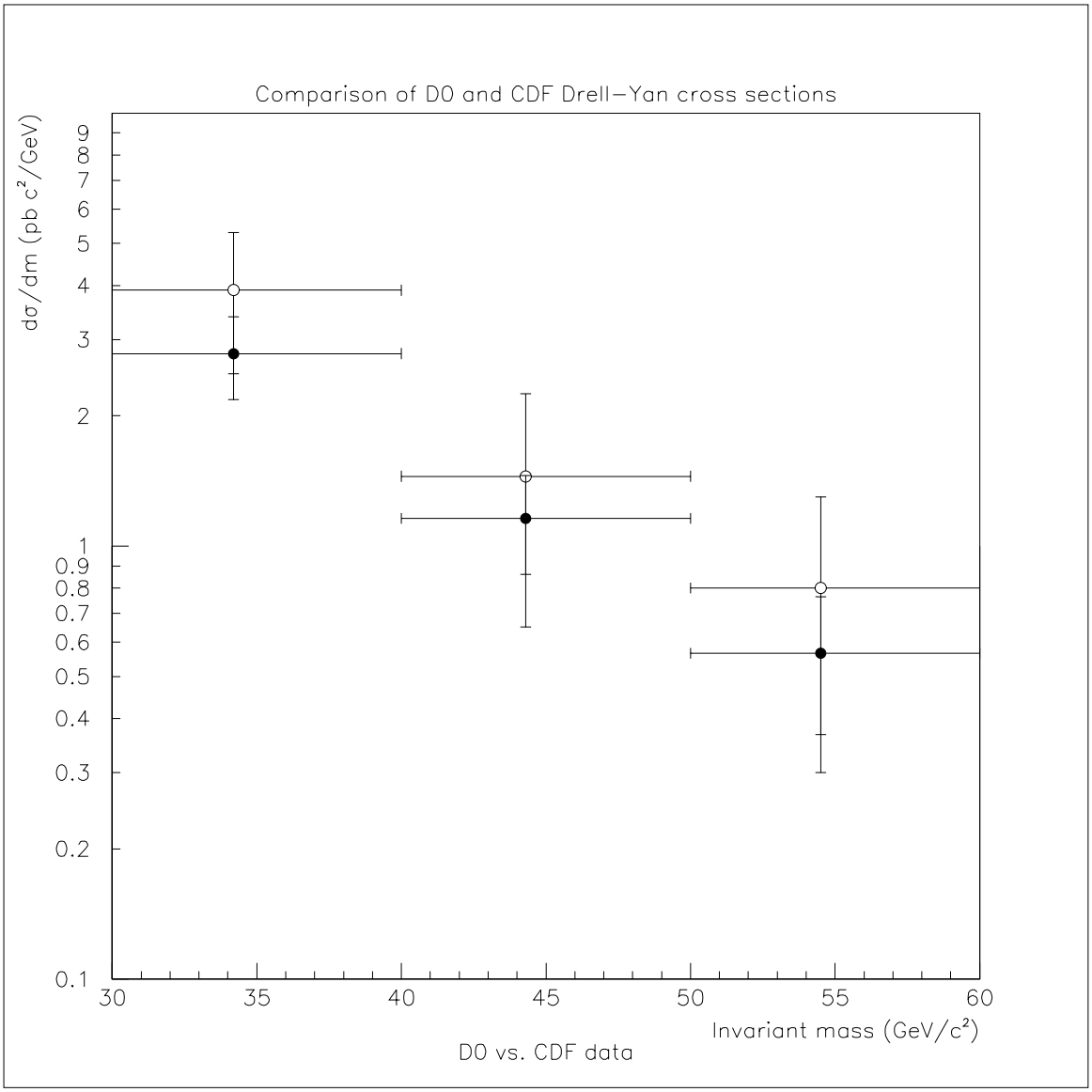

Figure 6.4: DØ Drell-Yan e^+e^- differential cross section $d\sigma/dm$ vs. invariant mass (filled circles) compared to the CDF $d\sigma/dm$ distribution (open circles) from the 1988-1989 collider run.

Table 6.4: Cumulative distribution functions from the $d\sigma/dp_T$ distribution used in the Smirnov-Cramèr-Von Mises test.

Bin	$F_{DATA}(p_T)$	$F_{RESBOS}(p_T)$	$F_{ISAJET}(p_T)$
1	0.034	0.042	0.049
2	0.160	0.140	0.207
3	0.285	0.257	0.392
4	0.404	0.364	0.527
5	0.490	0.454	0.617
6	0.544	0.525	0.681
7	0.623	0.640	0.769
8	0.709	0.723	0.828
9	0.793	0.784	0.870
10	0.861	0.870	0.921
11	0.933	0.945	0.968
12	0.964	0.975	0.987
13	0.974	0.991	0.995
14	1.000	1.000	1.000

cross section measurements also agree within one standard deviation. The differences between the Monte Carlo predictions is due to the difference in the shape of the photon p_T distributions and the integration limits of 0 to 50 GeV/c.

One may (correctly) wonder why the experimental integral cross section measured using the p_T distribution differs at all from the mass distribution measurement since we start with the same events. This is due to the method used to perform the efficiency, kinematic, fiducial acceptance, smearing and background corrections. Since we use an *average* bin-by-bin correction in mass and p_T, it means that the average total correction will be different between these two variables.

Table 6.4 shows the cumulative distribution functions used in the Smirnov-Cramèr-Von Mises test on the $d\sigma/dp_T$ distributions. Table 6.5 shows the results of the statistical tests described in Section 6.1. We see that in this case the Smirnov-Cramèr-Von Mises test indicates a strong similarity between the experimental distribution and the RESBOS resummed p_T distribution, and a very low compatibility between the data

Table 6.5: Goodness-of-fit test results from comparing the experimental $d\sigma/dp_T$ distribution to the RESBOS and ISAJET Monte Carlo distributions.

Theory	Test	Test Value	Confidence
RESBOS	Pearson χ^2	$\chi^2 = 3.615, k = 14$	0.997
RESBOS	Smirnov-Cramèr-Von Mises	0.028	0.976
ISAJET	Pearson χ^2	$\chi^2 = 7.858, k = 14$	0.897
ISAJET	Smirnov-Cramèr-Von Mises	0.551	0.030

Table 6.6: Smirnov-Cramèr-Von Mises test on the $d\sigma/dp_T$ distribution combined with a χ^2 test on the integrated cross section (normalization).

Theory	Test	Confidence
RESBOS	Smirnov-Cramèr-Von Mises	0.894
ISAJET	Smirnov-Cramèr-Von Mises	0.086

and the ISAJET p_T distribution. The χ^2 test on the other hand, suggests compatibility with both RESBOS and ISAJET distributions, although with a greater probability that the RESBOS distribution is compatible.

We again combine the Smirnov-Cramèr-Von Mises test with a χ^2 test of the normalization. The results are shown in Table 6.6. Combining the shape and normalization tests does not significantly change the conclusion of the shape test alone, the combined test still strongly favors the RESBOS distribution and rejects the ISAJET distribution. This was one of the goals of this measurement, to be able to clearly distinguish between the resummed p_T distribution and the artificially produced ISAJET p_T distribution. The shape of the ISAJET p_T distribution can be changed by varying the QTW input parameter, but this also affects the total rate and so it is not clear that one can produce the correct p_T distribution *and* the correct integrated cross section simultaneously using ISAJET.

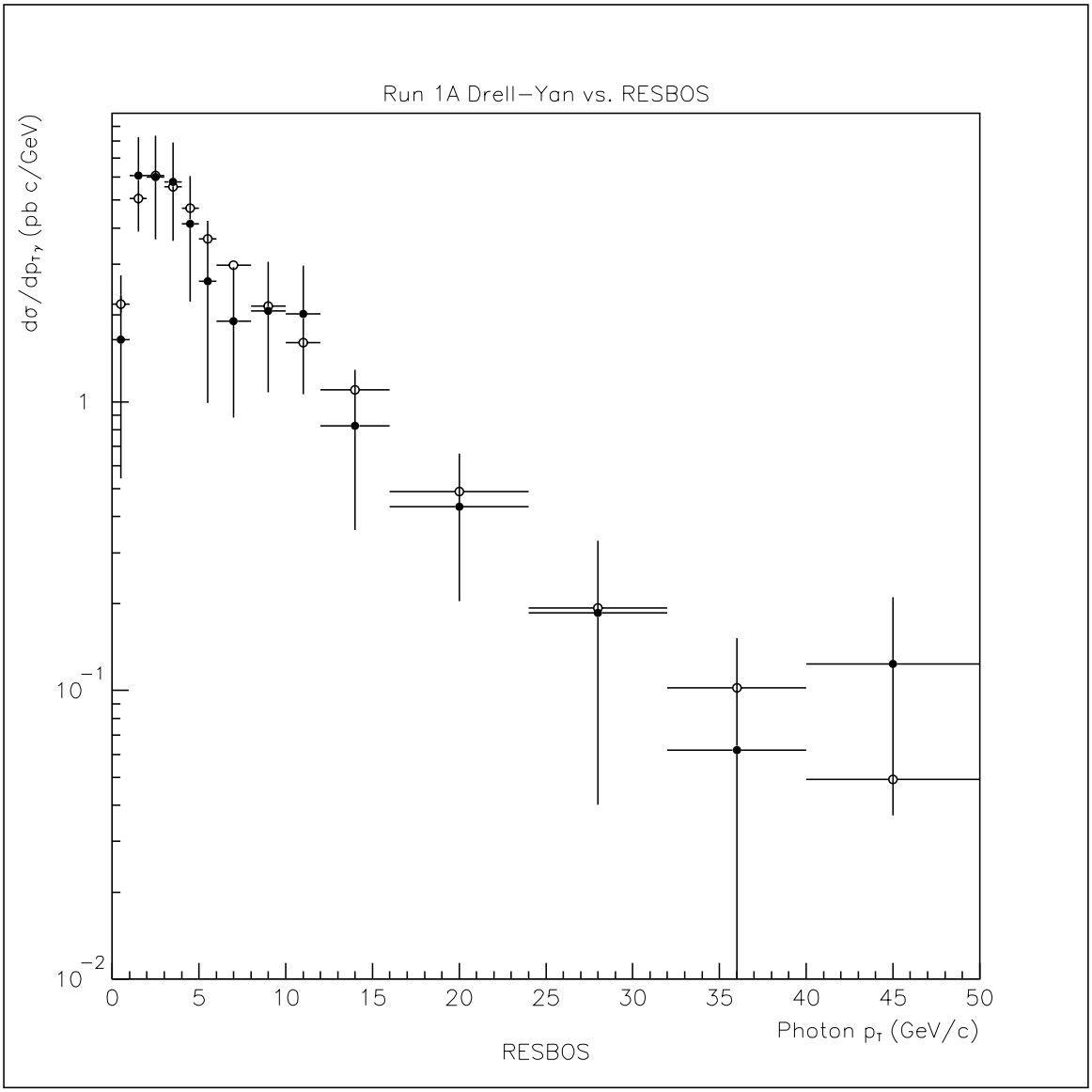

Figure 6.5: Drell-Yan e^+e- differential cross section $d\sigma/dp_T$ vs. photon p_T (filled circles) compared to the resummed theoretical $d\sigma/dp_T$ distribution (open circles) from the RESBOS Monte Carlo.

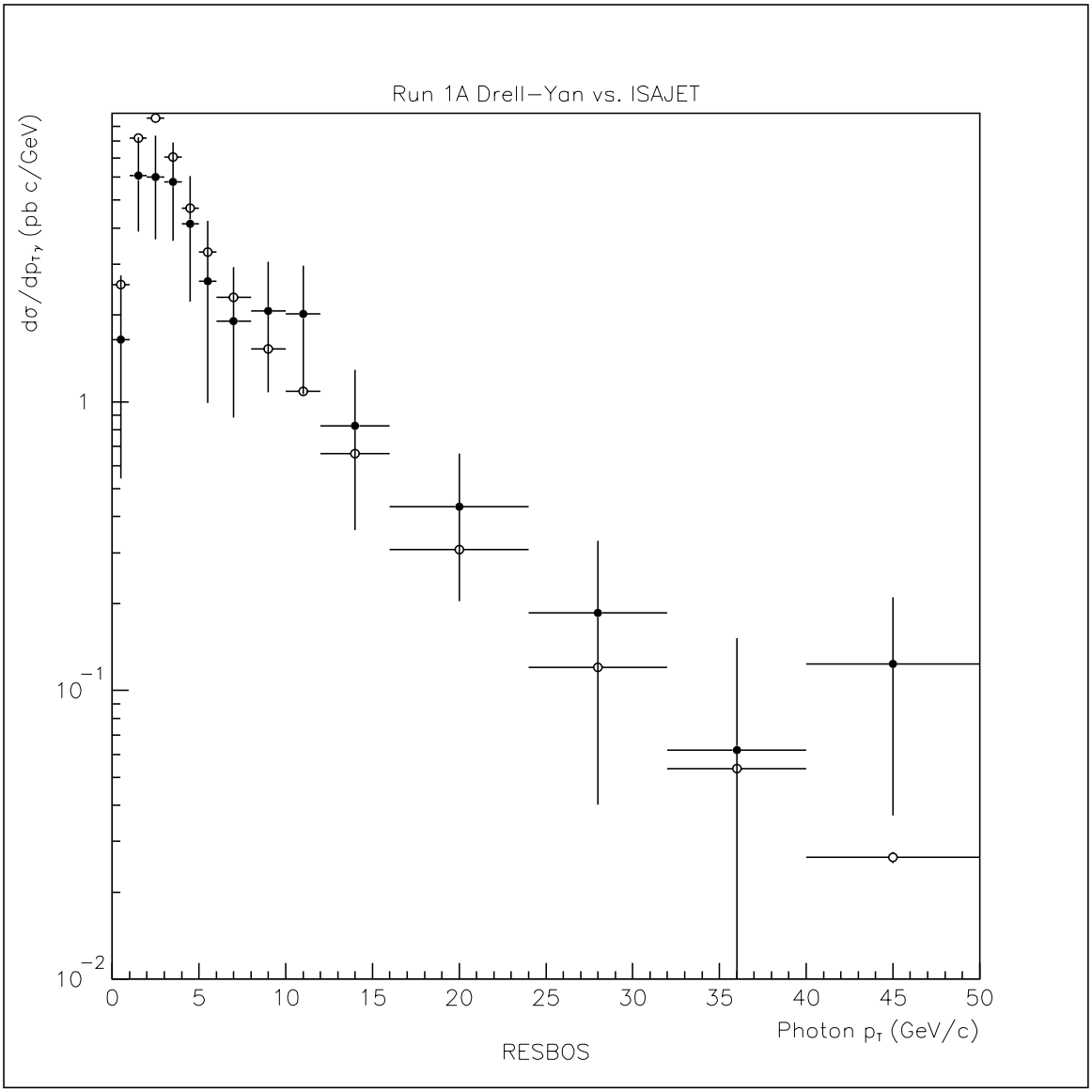

Figure 6.6: Drell-Yan e^+e- differential cross section $d\sigma/dp_T$ vs. photon p_T (filled circles) compared to the theoretical $d\sigma/dp_T$ distribution (open circles) from the ISAJET Monte Carlo.

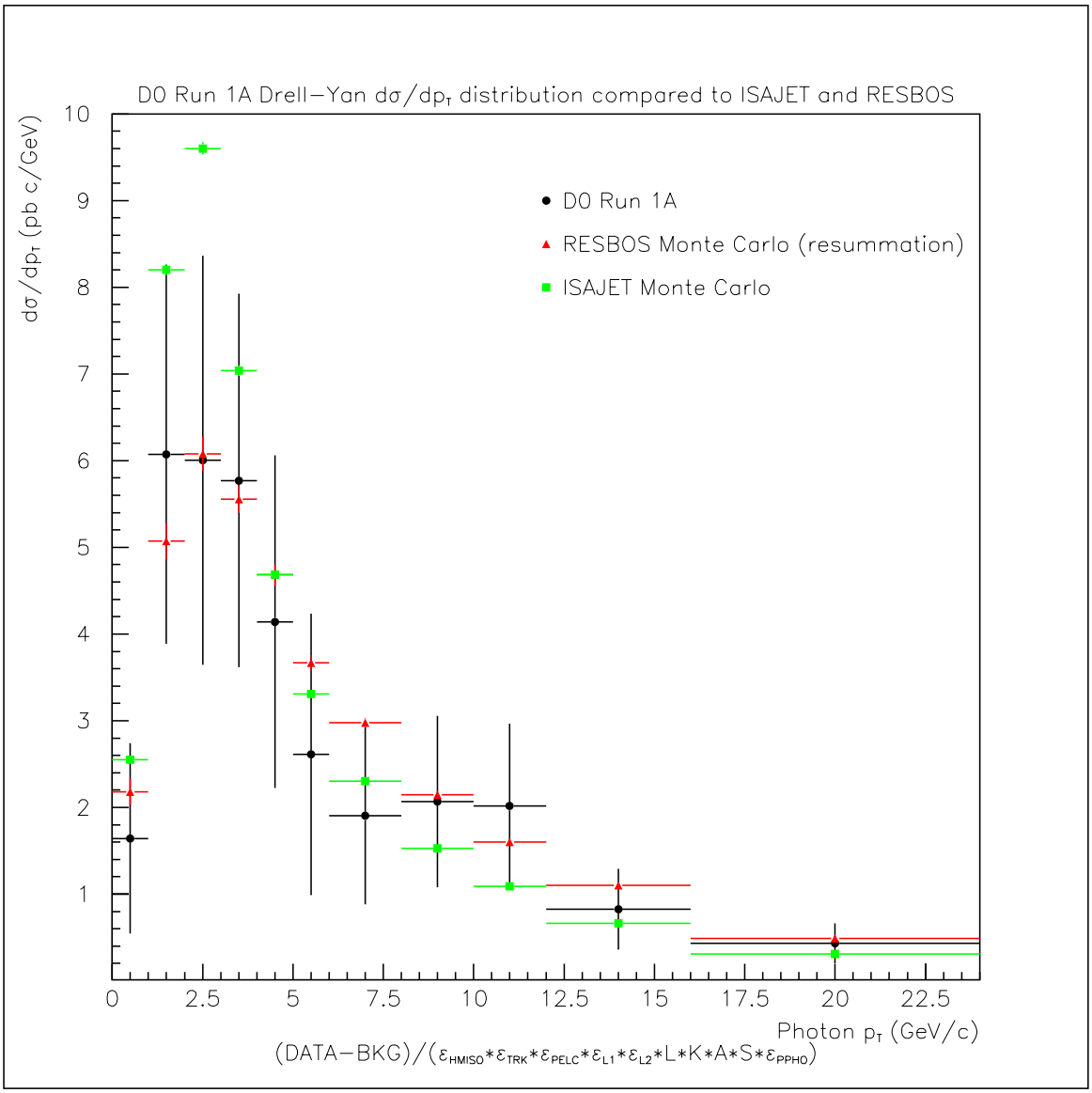

Figure 6.7: Drell-Yan e^+e- differential cross section $d\sigma/dp_T$ vs. photon p_T (circles) compared to the resummed theoretical $d\sigma/dp_T$ distribution (triangles) from the RESBOS Monte Carlo and the theoretical $d\sigma/dp_T$ distribution (squares) from the ISAJET Monte Carlo.

Table 6.7: Cumulative distribution functions from the $d\sigma/dy$ distribution used in the Smirnov-Cramèr-Von Mises test.

Bin	$F_{DATA}(y)$	$F_{RESBOS}(y)$	$F_{ISAJET}(y)$
1	0.046	0.086	0.078
2	0.101	0.190	0.177
3	0.193	0.292	0.285
4	0.326	0.393	0.392
5	0.407	0.496	0.499
6	0.520	0.598	0.605
7	0.649	0.700	0.714
8	0.806	0.810	0.821
9	0.930	0.912	0.922
10	1.000	1.000	1.000

6.4 Photon Rapidity Distribution

The integrated Drell-Yan e^+e^- cross section in the 30-60 GeV/c^2 mass range using the $d\sigma/dy$ distribution is 39.9 ± 7.7 pb. The integrated RESBOS cross section is 45.6 ± 0.4 pb and the integrated ISAJET cross section is 47.4 ± 0.7 pb. The experimental cross section agrees with both Monte Carlo estimates within the quoted error. The two Monte Carlo predictions now differ by 2.4 standard deviations. This is due to the difference in shape of the photon rapidity distributions and the fact that we are only integrating the region from -2.5 to 2.5 rapidity units. Also the reason the Monte Carlo integrated $d\sigma/dy$ cross section is lower than the integrated $d\sigma/dm$ cross section is that the integration limits were only -2.5 - 2.5 as imposed by the histogram bounds. There were no Drell-Yan events which passed our cuts with a photon rapidity outside of the $y = \pm 2.5$ window.

The experimental integrated cross section from the rapidity distribution is lower than the measured value from the mass distribution. The origin of this difference was explained in Section 6.3.

Table 6.7 shows the cumulative distribution functions used in the

Table 6.8: Goodness-of-fit test results from comparing the experimental $d\sigma/dy$ distribution to the RESBOS and ISAJET Monte Carlo distributions.

Theory	Test	Test Value	Confidence
RESBOS	Pearson χ^2	$\chi^2 = 4.816, k = 10$	0.939
RESBOS	Smirnov-Cramèr-Von Mises	0.110	0.538
ISAJET	Pearson χ^2	$\chi^2 = 5.020, k = 10$	0.890
ISAJET	Smirnov-Cramèr-Von Mises	0.112	0.538

Table 6.9: Smirnov-Cramèr-Von Mises test on the $d\sigma/dy$ distribution combined with a χ^2 test on the integrated cross section (normalization).

Theory	Test	Confidence
RESBOS	Smirnov-Cramèr-Von Mises	0.597
ISAJET	Smirnov-Cramèr-Von Mises	0.486

Smirnov-Cramèr-Von Mises test on the $d\sigma/dy$ distributions. The results of the statistical compatibility tests between the experimental and theoretical photon rapidity distributions are shown in Table 6.8. Both tests indicate good agreement between the data and both theoretical rapidity distributions. The ISAJET and RESBOS photon rapidity distributions are very similar, being very flat in the rapidity range -2.0 to 2.0. Consequently, it is unlikely that given the large errors on this measurement, we can make a significant distinction between the two.

The Smirnov-Cramèr-Von Mises test is once again combined with the normalization test. Table 6.9 shows the results of the combined tests. Again, we are unable to make a significant distinction between the ISAJET and RESBOS compatibility with data.

6.5 Effect Of Parton Distributions

The experimental parton distribution functions used in the factorization theorem can effect the rate and shape of the theoretical Drell-Yan distributions since they specify

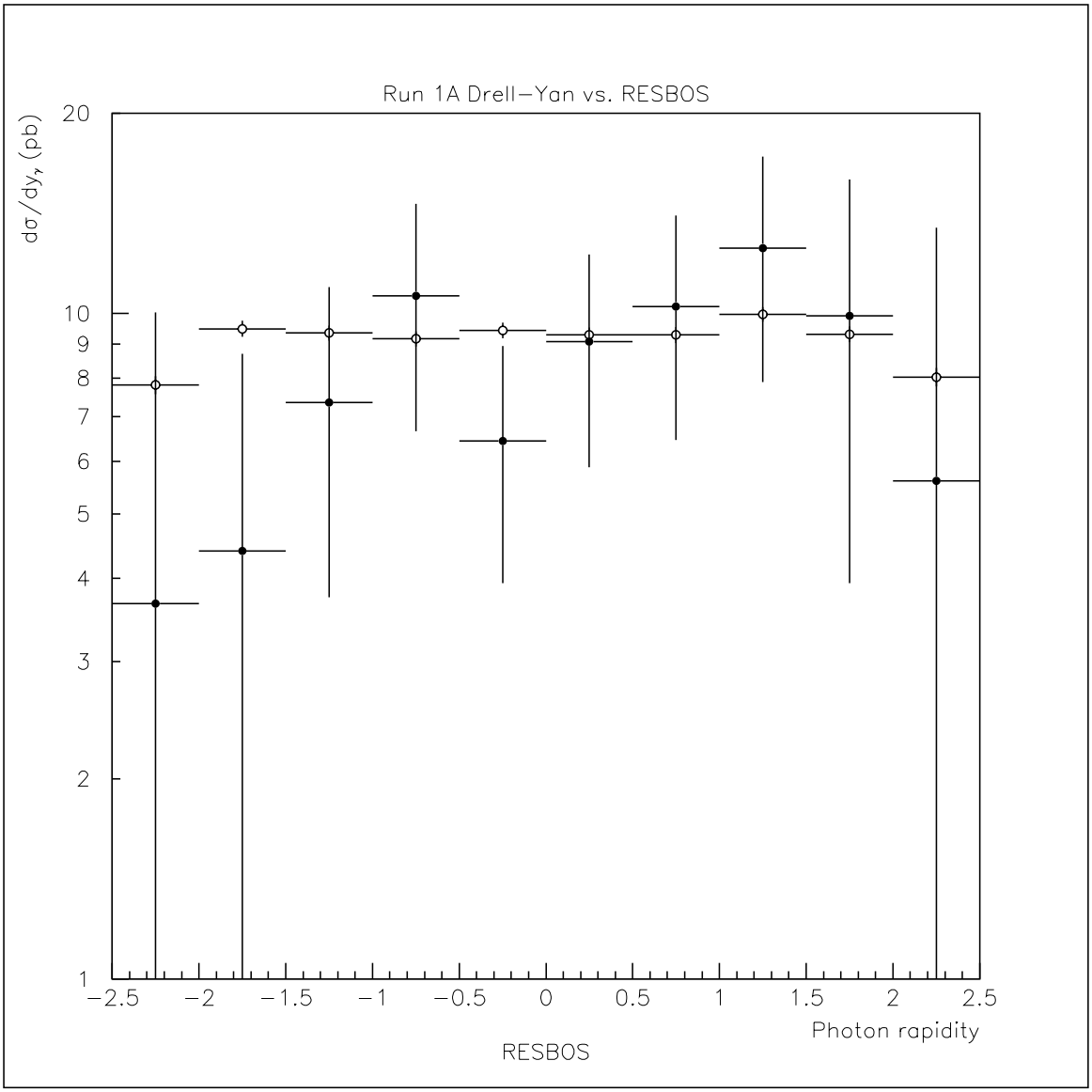

Figure 6.8: Drell-Yan e^+e- differential cross section $d\sigma/dy$ vs. photon rapidity (filled circles) compared to the resummed theoretical $d\sigma/dy$ distribution (open circles) from the RESBOS Monte Carlo.

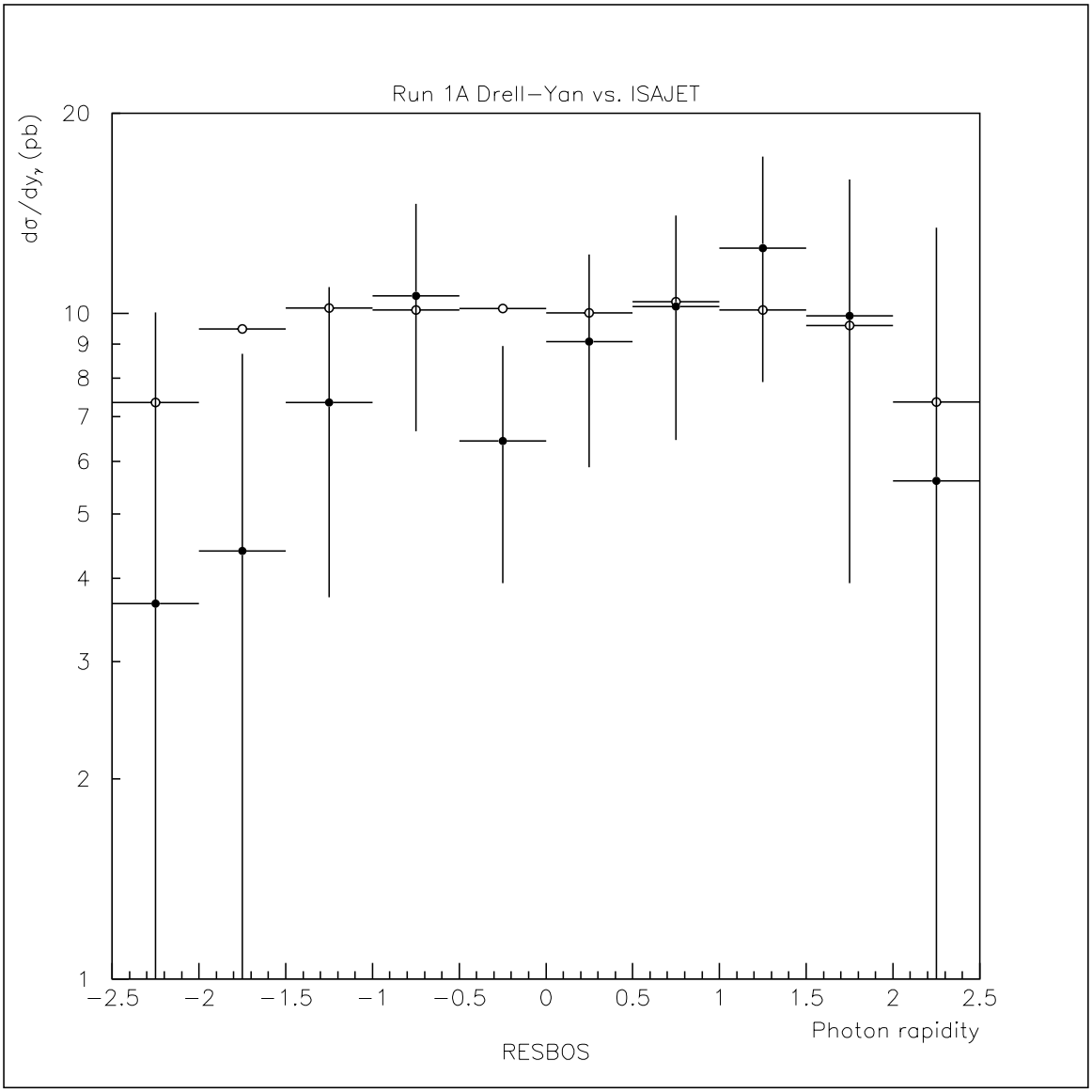

Figure 6.9: Drell-Yan e^+e- differential cross section $d\sigma/dy$ vs. photon rapidity (filled circles) compared to the resummed theoretical $d\sigma/dy$ distribution (open circles) from the ISAJET Monte Carlo.

Table 6.10: Difference in integrated cross sections due to input parton distribution functions.

Distribution	Data	RESBOS(CTEQ3M)	RESBOS(MRSD0′)
$\int d\sigma/dm$	45.1 ± 7.0 pb	52.4 ± 0.4 pb	52.6 ± 0.4 pb
$\int d\sigma/dp_T$	48.2 ± 6.6 pb	51.8 ± 0.4 pb	52.1 ± 0.8 pb
$\int d\sigma/dy$	39.9 ± 7.7 pb	45.6 ± 0.4 pb	46.9 ± 0.8 pb

the longitudinal momentum fractions of the partons in the parent hadrons (proton and antiproton in our case). In particular, the gluon distributions tend to vary quite a bit in the low $x = Q/\sqrt{S}$ region between different parton distribution function sets. Usually this causes only slight variations between the cross sections at higher x values since most recent parton distribution functions agree in this range. However, in the case of resummation, we have a two scale problem, namely the Q of the hard scattering and the Q_T of the multiple soft gluon radiation. Thus, even though our $x = Q/\sqrt{S}$ is generally in a region where different parton distributions agree well, we also are resumming the soft gluon emission. The resummation prescription convolutes the parton distributions with the Wilson coefficients which integrates over the whole x range (0-1) which may still cause large cross section differences, so we should compare the effect of using different parton distributions in the resummation results.

Table 6.10 shows a comparison of the integrated RESBOS cross sections using these two different parton distributions. Figure 6.10 shows the fractional change in the invariant mass, photon rapidity, and photon p_T distributions between the RESBOS Monte Carlo evaluated using the CTEQ3M and MRSD0′ parton distribution functions. We see that both the shape and overall rate *is* affected by changing the input parton distribution functions. The change in the integrated cross section is small, but Figure 6.10 shows that the shape can be significantly affected, especially the p_T distribution. The shape of the change in the $p_T < 20$ part of the p_T distribution is due to two effects. One effect is the convolution of the parton distributions

with the Wilson coefficients. The other effect is due to the fact that one should re-fit the non-perturbative function F^{NP} (that accounts for the non-perturbative $p_T < 0.5$ GeV/c cutoff in the resummation) using the new parton distributions which was not done. So we have two combined effects that change the shape of the low p_T part of the p_T distribution. It is possible that this variation would be reduced (or even go away altogether) if F^{NP}(MRSD0′) were available, but it is not. So the change in the shape of the low p_T part of the p_T distribution can be thought of as an upper limit on this effect [69]. We also see that the change in the high p_T portion of the p_T distribution is very small. This is what we would expect since RESBOS matches the low p_T portion (resummation) and high p_T portion (NLO result or "Y" piece) at 20 GeV/c and we do not expect the NLO result to change much in our $x = Q/\sqrt{S}$ range with the input parton distributions. As a comparison, Figure 6.11 shows the same fractional difference plot between RESBOS(CTEQ3M) and ISAJET(CTEQ2L). Here we see a much larger difference in the shape of the p_T distribution which we claim is due to the difference between the resummation calculation and the empirical method used by ISAJET.

Consequently, we need to perform the goodness-of-fit tests against the RESBOS Monte Carlo $d\sigma/dp_T$ distribution using the MRSD0′ parton distribution functions to check that the large compatibility difference we see between the ISAJET and RESBOS Monte Carlo $d\sigma/dp_T$ distributions and the data is not simply due to the input parton distributions. Table 6.11 shows a comparison of the goodness-of-fit tests between the data and RESBOS Monte Carlo using the CTEQ3M and MRSD0′ parton distributions. We see that the data is very compatible with the RESBOS $d\sigma/dp_T$ distribution using the MRSD0′ parton distribution functions as well as the CTEQ3M parton distribution functions, with MRSD0′ being slightly more favored.

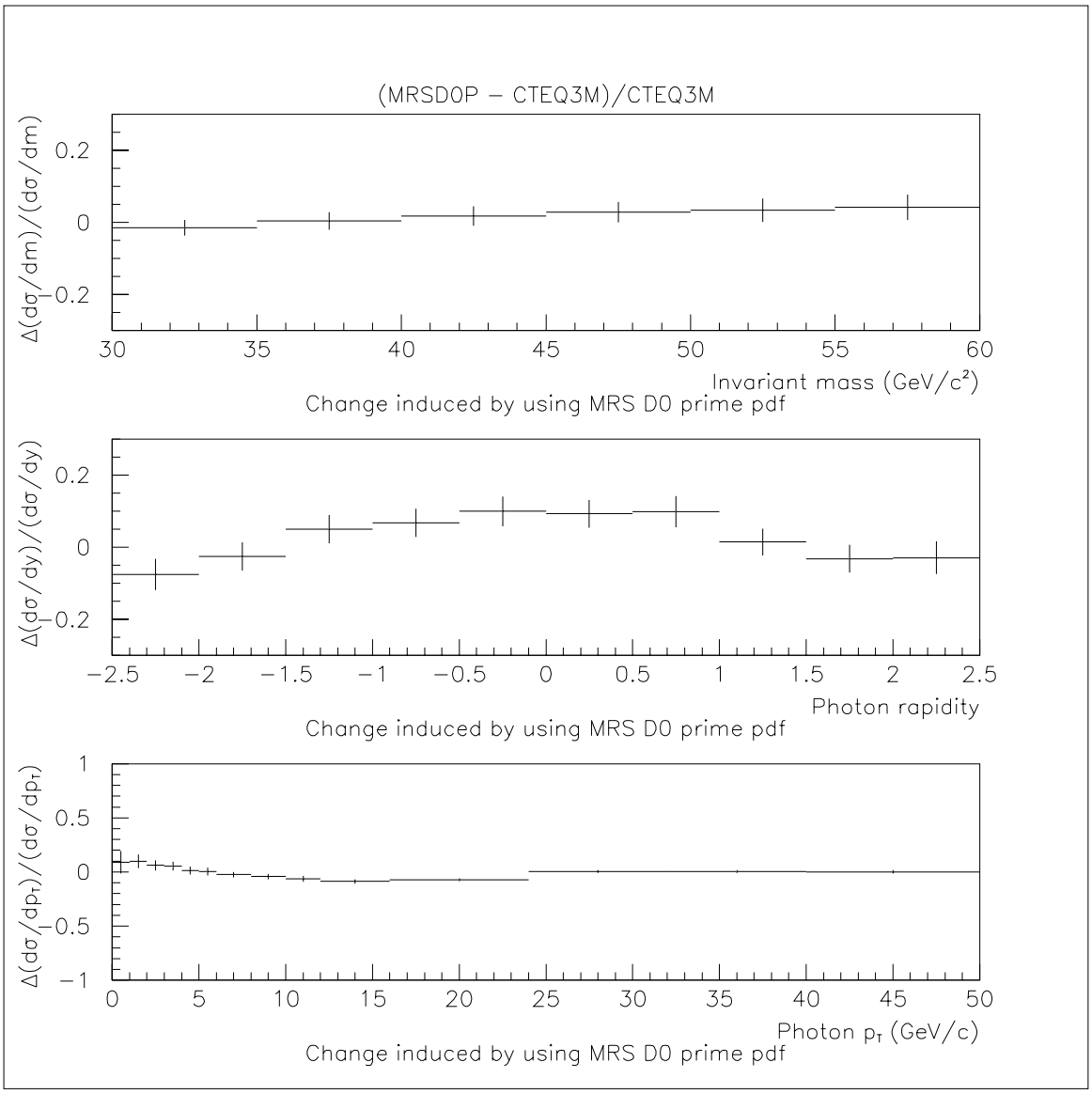

Figure 6.10: The change in the Drell-Yan e^+e- differential cross sections induced by using the MRSD0′ and CTEQ3M parton distributions as inputs to the RESBOS Monte Carlo.

Table 6.11: Goodness-of-fit test results from comparing the experimental $d\sigma/dp_T$ distribution to the RESBOS Monte Carlo distributions using the CTEQ3M and MRSD0′ input parton distribution functions.

Theory	Test	Test Value	Confidence
CTEQ3M	Pearson χ^2	$\chi^2 = 3.615, k = 14$	0.997
CTEQ3M	Smirnov-Cramèr-Von Mises	0.028	0.976
MRSD0′	Pearson χ^2	$\chi^2 = 3.419, k = 14$	0.998
MRSD0′	Smirnov-Cramèr-Von Mises	0.018	0.997

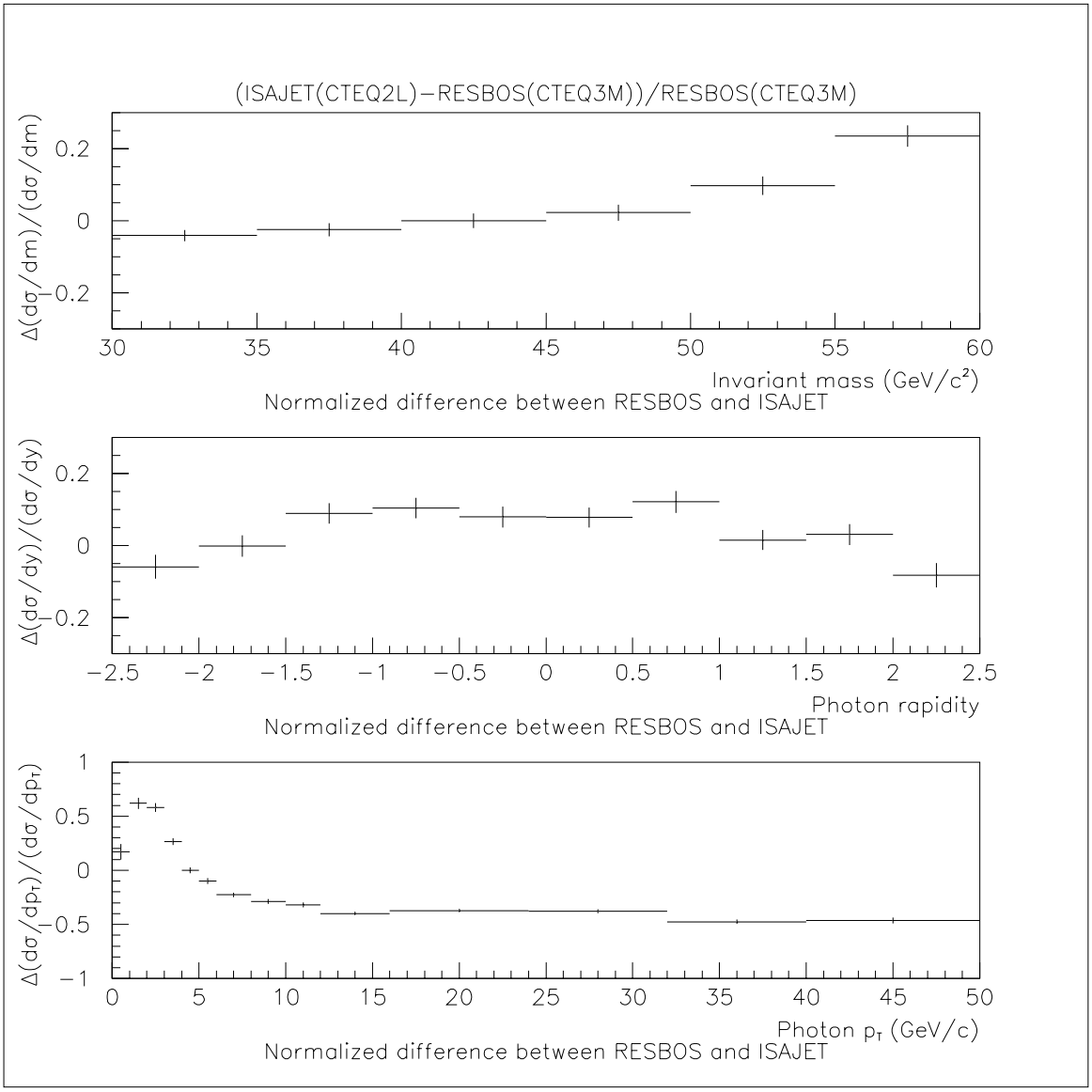

Figure 6.11: The change in the Drell-Yan e^+e- differential cross sections between the ISAJET(CTEQ2L) and RESBOS(CTEQ3M) Monte Carlos.

Table 6.12: Integrated cross section summary.

Distribution	Data	RESBOS	ISAJET
$\int d\sigma/dm$	45.1 ± 7.0 pb	52.4 ± 0.4 pb	52.2 ± 0.2 pb
$\int d\sigma/dp_T$	48.2 ± 6.6 pb	51.8 ± 0.4 pb	52.0 ± 0.7 pb
$\int d\sigma/dy$	39.9 ± 7.7 pb	45.6 ± 0.4 pb	47.4 ± 0.7 pb

6.6 Conclusions

We have calculated the integrated cross sections using the experimental $d\sigma/dm$, $d\sigma/dp_T$, and $d\sigma/dy$ distributions and compared these integral cross sections to the integrated cross sections from the RESBOS and ISAJET Monte Carlo distributions. All of our experimental measurements agree with the theoretical cross sections within one standard deviation. Table 6.12 shows a summary of the integrated cross sections.

We also have performed goodness-of-fit tests between the experimental $d\sigma/dm$, $d\sigma/dp_T$, and $d\sigma/dy$ distributions and the RESBOS and ISAJET Monte Carlo distributions. One of the goals of this experiment was to be able to differentiate between the resummed theoretical $d\sigma/dp_T$ distribution calculated in the RESBOS Monte Carlo and the more empirical distribution used in the popular ISAJET Monte Carlo. The Smirnov-Cramèr-Von Mises test very strongly favors the resummed p_T distribution over the ISAJET distribution. Thus we believe that we have succeeded in this goal, even though our statistical errors are large. The significance of the difference in compatibility between the shape of the data and RESBOS Monte Carlo and data and ISAJET Monte Carlo is greater than two standard deviations.

The effect of changing the input parton distributions to the RESBOS Monte Carlo from CTEQ3M to MRSD0′ was also evaluated. Although the shapes of the distributions and the total rate are affected by the input parton distributions, the goodness-of-fit tests still indicate very good agreement between the $d\sigma/dp_T$ distributions regardless

of the input parton distribution functions, with the MRSD0′ parton distributions being slightly favored.

The shape and shape plus normalization tests also indicate good agreement between the experimental mass and rapidity distributions and both ISAJET and RESBOS Monte Carlo distributions. This is not surprising since ISAJET and RESBOS agree within a few percent and the errors on the experimental data are large.

6.7 Possible Future Improvements

The best possible improvement one could make in this measurement would be to increase the statistics since our large errors allow us to make only rather weak comparisons with theory. Fortunately, this should be achievable relatively easily since the second run of DØ (Run 1B) has already been completed with an accumulated luminosity 6 times larger than the integrated luminosity from Run 1A (on which this analysis is based), waiting to be analyzed. It is possible that another DØ graduate student will analyze this data, and it is our hope that the progress made in this analysis will serve her/him well.

If it is possible to reduce the statistical error enough that the systematic errors become more significant, the most important improvement to the analysis would be a better kinematic, fiducial acceptance, and smearing correction. This is the single largest correction made in this analysis, and the difference between the correction from ISAJET events run through the DØGEANT simulation compared to the smeared RESBOS events is fairly large. A comparison of smearing both ISAJET and RESBOS events with our energy and position resolutions shows a difference of 5-10% due to the input kinematics alone, but the shapes of the corrections are similar. Thus, a full plate level DØGEANT simulation using RESBOS Monte Carlo Drell-Yan events as

the input would be preferable.

No correction was made for electrons lost in the recoil jets that are present in most Drell-Yan events. This was studied using Monte Carlo by failing an event if one of the electrons fell within a cone of $\Delta R = 0.5$ of the recoil direction of the jet (the opposite of the momentum vector of the photon) but was found to have a negligible effect. Since these recoil jets are usually soft, the electrons would not necessarily fail even if they were within $\Delta R = 0.5$ of the jet center, and since failing them if they fell this close had almost no effect, this correction was ignored. Also since we added minimum bias data to our single Monte Carlo electrons when we measured our trigger and electron id cut efficiencies, if there is any systematic error associated with ignoring the recoil jets in the event, it is probably at least somewhat compensated for in our other efficiency measurements.

An upgrade to the DØ detector is currently underway, and is slated to be completed in 1998. This upgrade includes adding a central magnetic field to DØ to allow determination of the sign of charged particles. This will be a great addition to DØ from the point of view of electron final states. It will not only allow one to perform measurements such as the forward-backward asymmetry in Z decays which cannot currently be done with DØ but can aid in analyses such as the Drell-Yan e^+e^- analysis, by allowing one to compare same sign pair vs. opposite sign pair distributions, thus aiding in the background determination.

Of course better understanding of the DØ detector will greatly improve the quality of any DØ analysis. Much progress has been made since the data sample for this analysis was frozen due to time constraints. New versions of the reconstruction program promise to provide better energy and position measurements and several versions of the reconstruction program have passed during the preparation of this dissertation.

The error induced by the corrections used in this analysis (evidenced by the differences in the integrated cross sections from the mass, rapidity, and p_T distributions) is unfortunate, but it is due to the large kinematic corrections that are necessary. The only way to improve this would be to use a more efficient Drell-Yan e^+e^- trigger, which was not possible.

Finally, there are some sources of systematic errors not thoroughly studied in this dissertation. These include a more detailed understanding of the energy scale. However, the effect of the energy scale variation is rather small for this analysis.

Appendix A

The Level 2 Electromagnetic Filter

This appendix describes the L2_EM Level 2 Electromagnetic Filter algorithm, event selection cuts, cut tuning, and call tree as well as other details that are necessary to fully understand the filter. The cuts are described functionally and the tuning methods are briefly described. The sections below include:

Filter Script What the parameters are and what they mean.

Algorithm What is being done.

- Longitudinal algorithm
- Transverse algorithm
- Cone algorithm

Energy And η Dependence Of Cuts

Cut Tuning Brief description.

- CC cut tuning
- EC cut tuning

Code Organization

Calorimeter Geometry

L2_EM Selection Cuts

Input parameters for the L2_EM filter come from 2 sources: the filter script, which supplies the typical user input, and the RCP (Run Control Parameters) file, which contains the tuned selection cuts as well as other control parameters.

A.1 Filter Scripts

As an example, here is the filter script for the ELE_2_HIGH filter used in Run 1A to trigger on 2 isolated EM candidates both with $E_T > 10$ GeV and which passed the primary electron shape cuts.

```
! ele_2_high.filt
! Generated from `ofln_v73.glb-triglist;1´ by trigparse 1.19.
!
filter_bit ele_2_high pass_1_of 0 speed 1.0 must_try
l2_em
    num_em  2
    etmin_cc  10.0
    etmin_ec  10.0
    track_match  ´IGNORE´
    del_eta_track  0.03
    del_phi_track  0.03
    shape_cuts  ´ELECTRON´
    do_isolation  true
    cone_delta_r  0.4
```

```
    cone_fract_max  0.15
script_end
```

Description of script parameters:

num_em For the filter to pass, this many candidates must pass all other cuts

etmin_cc E_T threshold if the candidate is in the CC

etmin_ec E_T threshold if the candidate is in the EC

track_match string describing type of tracking to do:

'IGNORE' = do not require a matching track

'REQUIRE' = require a track to calorimeter cluster match (CDC or FDC)

'CDC_ONLY' = require a track match IF in |IETA| < 13 (CC)

'FDC_ONLY' = require a track match IF in |IETA| > 13 (EC)

'VETO' = Fail if a track points to EM candidate cluster (CDC or FDC)

'VETO_CDC' = veto if find a track match and in |IETA| < 13 (CC)

'VETO_FDC' = veto if find a track match and in |IETA| > 13 (EC)

del_eta_track η road size in which to look for matching track

del_phi_track ϕ road size in which to look for matching track

shape_cuts string describing what shower shape cuts to do:

'ELECTRON' = uses primary longitudinal and transverse cuts only

'PHOTON' = drops cuts on EM1 and EM2

'E_LONG' = does longitudinal only for electron

'E_TRANS' = does transverse only for electron

'E_IGNORE' = or anything else not among the above does no shape cuts but calls it an electron

'G_LONG' = does longitudinal only for photon

'G_TRANS' = does transverse only for photon

'G_IGNORE' = or anything else not among the above does no shape cuts but calls it a photon

'P_...' = also works same as 'G_...'

'xx_TIGHT' = use ALL variables; default is only 4 main variables: FH1, EM3, $\sigma_5 - \sigma_3$ or $\Delta E_{5X5}/E_{3X3}$. All variables means all variables which are turned on in the RCP file, some are turned off. [This option no longer includes EM1 or EM2 cuts]

do_isolation If true pass only candidates whose fractional energy difference between a cone of radius 0.15 and a cone of radius cone_delta_r is less than cone_fract_max.

cone_delta_r radius of isolation cone in $\sqrt{\Delta\eta^2 + \Delta\phi^2}$ units

cone_fract_max actual cut on fractional energy in isolation

(cone-core)/core < cone_fract_max

A.2 The L2_EM Algorithm

This algorithm description explains ALL the possible cuts. All the cuts are done if the E_TIGHT parameter option is selected. But generally all cuts have not been used in the past, neither for electrons nor for photons. Cut values not specified directly as tool parameters come from D0$LEVEL2$L2SIM:L2_EM.RCP, which is downloaded as an STP (Static Parameters) file to Level 2.

1. Find candidate(s) from Level 1

2. Find peak EM3 cell in a trigger tower which triggers at Level 1

3. Unpack EM + FH1 energy in 3X3 readout towers around peak EM3 cell
4. Find centroid of shower
5. Get vertex z position
6. Correct Et for vertex position and leakage out of nominal cluster size.
7. Cut on Level 2 EM Et
8. Cut on longitudinal shape
9. Cut on transverse shape
10. Cut on track match
11. Cut on isolation of candidate

The peak EM3 cell is the one with the largest single EM3 energy deposit inside the original candidate trigger tower.

A.2.1 Longitudinal Algorithm

The cuts are divided into two groups: primary and secondary. The primary cuts are FH1/SUMEM and EM3/SUMEM (f_5 and f_3 below) and are used unless the SHAPE_CUTS field in the filter script is set to IGNORE. The secondary cuts are not used unless the E_TIGHT option is selected in the filter script SHAPE_CUTS field. For the P_TIGHT or PHOTON options, f_1 and f_2 below are not done.

The tested region for the longitudinal algorithm is 3X3 readout towers around the readout tower containing the peak EM3 cell. This size is independent of eta. This 3X3 region is also the core region used in the cone isolation algorithm.

Floor fractions, $f_i = E_i/\text{SUMEM}$, $i = 1-5$, are calculated. SUMEM is the sum of the energy in the 4 EM floors. Only FH1 participates in floor 5. The cuts are made on $f_5, f_3, f_1, (f_1+f_2), f_4$ (in that order) **[NOTE: because of the offset introduced in the energy scale, the f_1 and $f_1 + f_2$ cuts are no longer performed even for E_TIGHT]**

There are lower and upper cuts on f_1 through f_4; f_5 has only an upper side cut performed on it. However, the low side cuts on $f_1, (f_1 + f_2), f_4$ are turned off in the RCP file at this writing. All longitudinal cuts depend on both energy and η. Presently the f_3 cuts are quite loose, so that they effectively only serve to eliminate 'hot' single cells in the EM layers which trigger.

A.2.2 Transverse Algorithm

The primary cuts are:

- CC: $\sigma_5 - \sigma_3$ (99% efficient value)
- EC(IETA < 31): $\Delta E_{5X5}/E_{3X3}$ (99% efficient value)
- EC(IETA = 31,32): $\Delta E_{7X7}/E_{5X5}$ (100% efficient value)

The other cuts are used only in the E_TIGHT option of the shape_cuts filter script parameter. Some of the cuts described below are turned off even if the E_TIGHT option is selected.

IETA	MAX/3X3	σ_3	$\Delta E_{5X5}/E_{3X3}$	σ_5	$\sigma_5 - \sigma_3$	$\Delta E_{4X4}/E_{2X2}$	$\Delta E_{7X7}/E_{5X5}$
1-12	x	x	x	x	x	x	
13							
14-25			x	x			
26-30			x	x			
31-32							x
x 33-37							

There is no EM calorimeter at IETA=13, so there are no EM triggers there. The candidate automatically fails at IETA =33-37 (no trigger here now).

The above diagram shows what cuts the L2_EM filter tool will attempt under the E_TIGHT option, however if the cut values are set very large in the RCP file which contains the cut values, it is as if no cut was made. The descriptions below note those cuts which are turned off in the RCP file at this writing.

Transverse Cut Variable Definitions:

σ_3 and σ_5 are defined as energy-weighted $< r >$ (NOT rms) in units of EM3 cells computed using a 3X3 or 5X5 grid respectively around the peak EM3 cell.

- MAX/3X3 $\geq$ cut

  Peak EM3 cell energy divided by the sum in a 3X3 EM3 region around the peak cell (no E, η dependence), turned off in RCP file.

- cut $< \sigma_3 <$ cut

  cut $= -(A_2(\text{peak})^2 + B_1(\text{peak}) + C_0) \pm \Delta$

  (peak) is the energy in the peak EM3 cell, turned off in the RCP file.

- $\Delta E_{5X5}/E_{3X3} <$ cut

  cut on $(E_{5X5} - E_{3X3})/E_{3X3}$, primary in EC, secondary in CC, SUMEM and IETA dependent. E_{5X5}, E_{3X3} are energy sums in 5X5 and 3X3 EM3 cell regions around the peak EM3 cell respectively.

- $\sigma_5 <$ cut, (independent of E, η)

- $\sigma_5 - \sigma_3 <$ cut depending on SUMEM, IETA, primary in CC, secondary in EC (turned off in the RCP file above IETA=25).

- min $< \Delta E_{4X4}/E_{2X2} <$ max

  From peak EM3 cell, find η, ϕ neighbors with highest energies. Build a 2X2 EM3 array including these 3 cells and the cell which fills out the 2X2 square. Then make a surrounding 4X4 cell square. Call the energies in these two E_{2X2} and E_{4X4}. Seconary only in CC. Not done in EC, turned off in the RCP file. No energy or η dependence.

- $\Delta E_{7X7}/E_{5X5} <$ cut

  cut on $(E_{7X7} - E_{5X5})/E_{5X5}$, independent of energy and η.

  Since candidate is far forward, it will always be high energy if it passes the E_T threshold. Done only for IETA=31,32.

A.2.3 Cone Algorithm

The core is a sum over the layers selected in D0$LEVEL2$L2SIM:L2_EM.RCP: Core sums from LO_GAMMA_FLOOR to HI_GAMMA_FLOOR (as of Run 1A, EM 1-4), over the 3X3 Readout Towers centered about the highest EM3 cell.

The cone is a sum over LO_CONE_LAYER to HI_CONE_LAYER, with possibly the ICD/MG turned off by CONE_USE_ICD (as of Run 1A, the sum is over all layers except the ICD/MG). The lateral extent is chosen by the CONE_DELTA_R parameter for the script: cells with centers within this radius of the central readout tower are included.

A.3 Energy And η Dependence Of Cuts

Energies are broken up into 4 ranges:

$$
\begin{aligned}
0 &< L(1) < ETH1 \\
ETH1 &< M(2) < ETH2 \\
ETH2 &< H(3) < ETH3 \\
ETH3 &< X(4) < \infty
\end{aligned}
$$

The L,M,H,X notation is used below in the description of the RCP file contents. The actual energy boundaries ETH1,ETH2,ETH3 are different for CC and EC:

	CC	EC
ETH1	14.0 GeV	29.0 GeV
ETH2	35.0 GeV	70.0 GeV
ETH3	65.0 GeV	150.0 GeV

There are 8 eta regions:

|IETA|	L2_EM eta region
1-2	CC index 1
3-6	CC index 2
7-12	CC index 3
13	no EM, index 4
14-15	EC index 5
16-18	EC index 6
19-24	EC index 7
25-31	EC index 8
32-37	no trigger

These indices are used below in the description of input bank contents.

A.4 Cut Tuning

The 99% efficient point is defined as that cut value which passes 99% of the test sample (TB for test beam data, MC for Monte Carlo). The '100%' point is defined a little differently, its precise meaning varies and is described below.

PRIMARY CUTS:

- $0.1 < f_3 < 0.9$
- $f_5 < 1.5 \times 99\%$ value
- $\sigma_5 - \sigma_3 <$ cut (CC) or $\Delta E_{5X5}/E_{3X3} <$ cut (EC). Main cuts set to 99% value (after TB selection cuts!) For very low energy electrons ($E_T < 10$ GeV) the efficiency of these cuts is reduced due to changes in longitudinal shower profile. At 5 GeV these cuts are approximately 95% efficient, decreasing with decreasing energy. At IETA=31,32 the $\Delta E_{7X7}/E_{5X5} <$ cut selection is used.

SECONDARY CUTS:

chosen at '100%' efficiency point defined as follows

- EC: '100%' = 99%(actual) $\times$ 1.25 cuts used
  - added cuts for the EC:
    - $f_1 <$ cut
    - $(f_1 + f_2) <$ cut
    - cut $< f_4<$ cut
    - $\sigma_5 - \sigma_3 <$ cut (for ieta<26)
- CC: 100% = 99% + (99%-90%) cuts used
  - added cuts for the CC:

* $f_1 <$ cut
* $(f_1 + f_2) <$ cut
* cut $< f_4<$ cut
* $\Delta E_{4X4}/E_{2X2} <$ cut
* $\Delta E_{5X5}/E_{3X3} <$ cut

All other cuts are turned off by setting cuts to ± 10000

A.4.1 Tuning Of EC Shower Shape Cuts

Data Used:

Ntuples of the L2_EM cut variables were made (old calorimeter reconstruction, but the sampling fractions used were changed to match the new software) from test beam Load 1 ECEM data. One η scan and two energy scans were used. Zero suppression was applied in software at the $\pm 2\sigma$ level.

η **scan:** (ECEM η scan 2)

- Energy = 100 GeV
- η = 1.55, 1.65, 1.75, 1.85, 1.95, 2.05, 2.25, 2.55, 2.65, 2.86, 3.05
- ϕ = 61

Energy scan 1: (ECEM E scan 5)

- Energy = 25, 50, 75, 100, 125, 150 GeV
- η = 1.95
- ϕ = 61

Energy scan 2 (ECEM E scan 7)

- Energy = 25, 50, 100, 150
- $\eta = 2.55$
- $\phi = 61$

Note: For one run, the new version of the ntuple package was used (new CAHITS), and the results were the same as for the old package with correct sampling fractions.

Analysis:

Tables of efficiency vs cut value for all L2_EM variables were made from the ntuples using PAW (CERN Physics Analysis Workstation program) macros. Several tables for each variable/ntuple combination were made, in order to study the effects of several technical cuts and try to get a clean electron sample. The technical test beam electron id cuts tried were:

TRK at least 1 MWPC track in all views

CRY $1 \leq$ ncryox ≤ 4 and $1 \leq$ ncryoy ≤ 4 (ie, require not too many hits in cryostat MWPCs)

ETA Require IETA of max EM3 tower (L2_ETA) equal to selected IETA (some runs cover more than one ieta tower, depending on pad size)

PHI Require IPHI of max EM3 tower (L2_PHI) equal to 31 (benchmark phi)

TAG BIT 5,6 and 8 in TAG_WORD set (cerenkov bits)

The combinations tried were:

- NOCUTS

- CRY+ETA
- TRK+CRY+ETA
- CRY+ETA+TAG
- CRY+ETA+PHI
- CRY+ETA+PHI+TAG

The combination used was CRY+ETA+PHI, which seemed to give the best signal/noise (further cuts seemed to just reduce the statistics without significant cleaning of the signal). For one run (E=125, ETA=1.95), CRY+ETA+TAG+PHI was used, as there seemed to be unusually large pion contamination.

The energy and η dependence of the four primary cuts was parameterized for each efficiency value using simple functions based on the data in the efficiency tables. The cut values for $f_5 <$ cut and $\Delta E_{5X5}/E_{3X3} <$ cut were obtained using these parameterizations. For each bin in (E,η), the least restrictive point of the parameterization was used. For $f_5 <$ cut, the cuts are 1.5 times the 99% parameterization value; for the $\Delta E_{5X5}/E_{3X3} <$ cut, an additional safety factor was added (ie, the cuts are 99%+0.25(99%-98%)).

A.4.2 Tuning Of CC Shower Shape Cuts

Data Used:

Ntuples of the L2_EM cut variables were made from test beam Load 2 CCEM data. One η scan and two energy scans were used.

- Three fine energy scans in the 7.5-100 GeV energy range. $\eta = 0.05, 0.45, 1.05$ $\phi = 31.6$ (corresponding to the benchmark point. approx. 4.5 cm from the CCEM crack)

- Energy dependence of cut limits obtained at three η values on the basis of these three energy scans. Simple functional fits to energy dependence were obtained at each η. Linear interpolation of fit parameters was used to set limits in prescribed $(\eta \times E)$ bins.

Test Beam Selection Cuts Used:

1. Require a good track (one MWPC track upstream of the bending magnet, one MWPC track downstream of the bending magnet).

2. Require that the calculated beam momentum is within 20% of the nominal value.

3. Require at least one upstream cerenkov.

4. No hits closer than (approx.) 2 cm from the CCEM crack.

Additional tests performed:

- Require one and only one cluster in each plane of the cryostat MWPC.
  NO EFFECT ON RESULTS

- Veto on MIP and muon counters.
  NO EFFECT ON RESULTS

Systematic Error:

- The typical test beam run does not illuminate the calorimeter surface uniformly. Potentially, this can cause an error in the determination of transverse cuts (based on transverse energy sharing). To assess this error we analyzed two sets of runs which were taken to study the position resolution in the CC. In these sets, one readout tower (η=0.05, η=0.55) was carefully scanned with the beam (both in η and ϕ) to effectively create a uniform illumination of a single readout tower. We analyzed these runs in the same manner as the three energy scans used to establish cut values. We then compared all results, searching for significant deviations due to the change in the position of the beam. Based on this analysis, we believe that the error on $\sigma_5 - \sigma_3$ is no larger than 2% off the nominal efficiency value. A similar argument can be made concerning the influence of vertex smearing on longitudinal cuts. We analyzed a set of test beam runs which were dedicated to the scanning of the vertex position. Using the same principle, we conclude that the vertex smearing does not introduce significant errors in our cuts. In addition, all longitudinal cuts were opened beyond their 99% values to increase the safety margin. We found that most of these cuts can be opened without damaging the background rejection in a significant way.

- The cuts are based on test beam data. No effect of an underlying event, pile-up, etc. were taken into account.

A.5 Internal Organization Of The L2_EM Filter

L2_EM Call Tree

```
L2_EM-+-(ERRMSG)
      |
      +-L2_EM_PARSE_CUTS-+-(TRULEN)
```

```
+-(L2J_L1_LIST_FORCE)
+-(L2JETS_HOTFL)
+-L2_EM_GET_CAND-+-(IHOT_MSK_EM)
|                +-(IHOT_ADR_EM)
|                +-L2_EM3_MAX-+-(CL2_RING12)
|                |            +-(CL2_ROTOW_ETNOM)
|                |            +-(CL2_ROTOW_ETNOM)
|                |            +-(CL2_RING12)
|                |            +-(GZCAEP)
|                +-L2_EM_UNPACK-+-(CL2_RING22)
|                               +-(VZERO)
|                               +-(GZCAEP)
|                               +-(CL2_RING22)
|                               +-(CL2_ROTOW_ETNOM)
|                               +-(CL2_SNTH)
+-L2_EM_XYZ_POSITION-+-L2_EM_LOGW_CONSTS
|                    +-(CL2_SNTH)
|                    +-(CL2_RING22)
|                    +-(GZCAEP)
|                    +-(CELXYZ)
+-(L2_VERT)
+-(ETA_ZCORR)
+-(CL2_ET_CORR_FINE)
+-L2_EM_LEAK_FIX (1)--(ERRMSG)
+-L2_EM_CUT_BINS
+-L2_EM_LONG_CUT
```

```
+-L2_EM_TRANS_CUT

+-L2_EM_TRACK_ROADS

+-(L2_CD_MATCH)

+-L2_EM_ISOL-+-(CL2_RING22)

|            +-(CL2_ROTOW_ETNOM)

|            +-(GZCAEP)

|            +-L2_EM_LEAK_FIX see 1

+-(ESUMFL)

+-(L2EMFL)
```

A.5.1 Correspondence Between RCP And Internal Variables

Energy and η bin indices are described above.

L2_EM variable name to RCP file name mapping:

RCP name	internal name
EBOUNDS	J_ENRG_BIN
ETABOUNDS	J_ETA_BIN
S3A2	A2
S3B1	B1
S3C0	C0
SSIG3	SS3
EP3	EM3L
ELECT3	ESIZE

Energy and η independent L2_EM RCP variable definitions:

J_ENRG_BIN index to cut array based on energies in EBOUNDS (CC $\rightarrow$ 1-3, EC $\rightarrow$ 4-6).

J_ETA_BIN index to cut array based on η in ETABOUNDS.

A2 parameters for central value of σ_3 cut.

B1 parameters for central value of σ_3 cut.

C0 parameters for central value of σ_3 cut.

SS3 difference between min and max of σ_3 cut.

EM3L min size of MAX/E3X3.

ESIZE various transverse cuts:

- 1,2 - not used
- 3,4 - not used
- 5,6 - $\Delta E_{7X7}/E_{5X5}$
- 7 - not used
- 8 - max σ_5 (CC)
- 9,10 - not used

All the energy and η dependent RCP cut arrays below get mapped into the L2_EM internal array EMCUTS(j,i,x), where x=1,2,3,4=L,M,H,X below and the IETA index is as described in the energy and η binning description section.

RCP cut arrays:

ELCxi(j) x = L,M,H,X energy index

i = η index for CC: 1,2,3 table above gives ranges.

j = cut number:

- 1,2 min,max for floor fraction f_1
- 3,4 min,max for floor fraction $(f_1 + f_2)$
- 5,6 min,max for floor fraction f_3

- 7,8 min,max for floor fraction f_4
- 9 max for floor fraction f_5
- 10 max for $\sigma_5 - \sigma_3$
- 11 max for $\Delta E_{5X5}/E_{3X3}$
- 12 max for $\Delta E_{4X4}/E_{2X2}$

ELExi(j) x = L,M,H energy index

i = η index for EC: 1,2,3,4 see table (5,6,7,8 in L2_EM)

j = cut number: see above for CC

E15xCT(j) as above, for IETA=15 in EC

EL12xCT(j) as above, for IETA=13, never used since no EM

A.6 Calorimeter Geometry

Summary Of EM Signal Availability in D0:

IETA	Comments	IETA_TT
1-11	All EM signals present	1-5, $\frac{1}{2}$ of TT 6
12	Lose some EM signals	$\frac{1}{2}$ of TT 6
13	No EM signals	$\frac{1}{2}$ of TT 7
14	Lose some EM signals	$\frac{1}{2}$ of TT 7
15-26	All EM signals present	8-13
27-32	No EM3 subdivision	14-16
33-35	Cells coarsen Only odd IPHI exist No EM3 subdivision	17-19
36-37	No EM signals	20, (21 does not exist)

The signal naming convention is as follows:

Layer Number	Layer Name	L2_EM limit parameter
1	EM1	(MNLYEM = 1)
2	EM2	
3	EM3a	
4	EM3b	
5	EM3c	
6	EM3d	
7	EM4	(MXLYEM = 7)
8	CC Massless gap	(MNLYMG = 8)
9	ICD	
10	EC Massless gap	(MXLYMG = 10)
11	FH1 (Fine Hadronic)	(MNLYFH = 11)
12	FH2	
14	FH4	(MXLYFH = 14)
15	CH1 (Coarse Hadronic)	(MNLYCH = 15)
16	CH2	
17	CH3	(MXLYCH = 17)

The definition of the EM3 sub-layer order is:

$\uparrow$	EM3b 4	EM3d 6
ϕ	EM3a 3	EM3c 5
	z	$\rightarrow$

The same orientation is used in all parts of the calorimeter, with respect to the ϕ and $+z$ directions. The EM3 layer is indexed effectively with sub-indices in the ϕ and η directions, with ϕ running fastest.

An auxiliary system is also sometimes used, substituting a different coordinate, floor, for the depth dimension, and summing all the EM3 signals into a single floor:

Floor Definitions:

Floor	Layers	Floor Name
1	1	EM1
2	2	EM2
3	3,4,5,6	EM3
4	7	EM4
5	8-14	FH+MG+ICD
6	15-17	CH

The layers in each η bin in the offline system are listed below: An x indicates that these regions are instrumented, a g indicates two or more layers which are ganged together.

CAL Type	→ →	EM							CCMG	ICD	ECMG	FH				CH		
Layer Number	→ →	1	2	3	4	5	6	7	8	9	10	11	12	13	14	15	16	17
η range	IETA																	
0.0 0.1	1	x	x	x	x	x	x	x				x	x	x		x		
0.1 0.2	2	x	x	x	x	x	x	x				x	x	x		x		
0.2 0.3	3	x	x	x	x	x	x	x				x	x	x		x		
0.3 0.4	4	x	x	x	x	x	x	x				x	x	x		x		
0.4 0.5	5	x	x	x	x	x	x	x				x	x	x		x		
0.5 0.6	6	x	x	x	x	x	x	x				x	x	x		x		
0.6 0.7	7	x	x	x	x	x	x	x				x	x	x		x		
0.7 0.8	8	x	x	x	x	x	x	x	x		x	x	x	x		x		
0.8 0.9	9	x	x	x	x	x	x	x	x	x	x	x	x			x	x	
0.9 1.0	10	x	x	x	x	x	x	x	x	x	x	x				x	x	
1.0 1.1	11	x	x	x	x	x	x	x	x	x	x	x				x	x	x
1.1 1.2	+12*	x	x	x	x				x	x	x	x	x			x	x	x
-1.1 -1.2	-12*	x	x			x	x		x	x	x	x	x			x	x	x
1.2 1.3	13									x	x	x	x	x	x		x	x
1.3 1.4	+14*					x	x	x		x		x	x	x	x	x		x
-1.3 -1.4	-14*			x	x			x		x		x	x	x	x	x		x
1.4 1.5	15	x	x	x	x	x	x	x				x	x	x	x	g		g
1.5 1.6	16	x	x	x	x	x	x	x				x	x	x	x	x		
1.6 1.7	17	x	x	x	x	x	x	x				x	x	x	x	x		
1.7 1.8	18	x	x	x	x	x	x	x				x	x		x	x		
1.8 1.9	19	x	x	x	x	x	x	x				x	x	x		x		
1.9 2.0	20	x	x	x	x	x	x	x				x	x	x	x	x		
2.0 2.1	21	x	x	x	x	x	x	x				x	x	x	x	x		
2.1 2.2	22	x	x	x	x	x	x	x				x	x	x	x	x		
2.2 2.3	23	x	x	x	x	x	x	x				x	x	x	x	x		
2.3 2.4	24	x	x	x	x	x	x	x				x	x	x	x	x		
2.4 2.5	25	x	x	x	x	x	x	x				x	x	x	x	x		
2.5 2.6	26	x	x	x	x	x	x	x				x	x	x	x	x		
2.6 2.7	27	x	x	x				x				x	x	x	x	x		
2.7 2.8	28	x	x	x				x				x	x	x	x	x		
2.8 2.9	29	x	x	x				x				x	x	x	x	x		
2.9 3.0	30	x	x	x				x				x	x	x	x	x		
3.0 3.1	31	x	x	x				x				x	x	x	x	x		
3.1 3.2	32	x	x	x				x				x	x	x	x	x		
3.2 3.42	33	x	x	x				x				x	x	x	x	x		
3.42 3.7	34	x	x	x				x				x	x	x	x	x		
3.7 4.1	35	x	x	x				x				x	x	x	x	x		
4.1 4.45	36											x	x	x	x	x		
4.45 **	37													x	x	x		

A.7 L2_EM filter cut values

Below are the actual RCP files used with the L2_EM filter. The first is D0$LEVEL2$L2SIM:L2_EM_TB05.RCP which contains the cuts used for normal data taking in DØ. The second is D0$LEVEL2$L2SIM:L2_EM_MC05.RCP which contains cuts intended for use with the Level 2 simulator (L2SIM) when analyzing homogeneous mixture Monte Carlo (instead of plate level DØGEANT). The efficiency of these MC tuned cuts on mixture MC should compare closely to the efficiency of the test beam tuned cuts on real DØ data. The test beam cuts should be used for plate level MC since the shower shapes agree well between plate MC and real data.

Test Beam Cuts Used Online:

```
\START        L2_EM_RCP
\SIZE        534       161
!-----------------------------------------------------------------
!    ELECTRON SRCP bank for ELECTRON analysis.
!    Created 28-NOV-1991 by Yi Xia
!    Updated 12-OCT-1992 by James T. McKinley, Mirek Fatyga,
!                           Peter Grudberg, & James T. Linnemann
!    Updated 14-NOV-1993 by James T. Linnemann   add ETMIN_CELL
!
! THIS IS L2_EM_TB05.RCP
!
! Order of binned cuts in EXXXXX arrays
! (except ELECT3 which uses UN-binned cuts)
!
! EM1(min) EM1(max) EM12(min) EM12(max) EM3(min) EM3(max)
! EM4(min) EM4(max) FH1(max) SIG5M3(max) 5X5-3X3/3X3(max) 4X4-2X2/2X2(max)
!-----------------------------------------------------------------
!
!Format version (old format is implicitly version 0)
L2EM_VERSION    3   ! (add ETMIN_CELL)
!
!   For unpacking
ETMIN_CELL  0.0     !if ETnominal < this, exclude from ALL sums and cone
ET_IN_CAEP .TRUE.
!
!   Divider of eta bins
\ARRAY       ETA_BOUNDS     8
     2     6    12    13    15    19    25    32
\END
!
!   Divider of energy bins
\ARRAY       E_BOUNDS     6
      14.000      35.000      65.000      29.000      70.000      150.000
\END
!
!    SIGMA3 cut
S3A2                    2.1408
S3B1                   -2.07643
```

```
S3C0                  -0.01391
SSIG3              10000.000
!
!    EM3MAX cut
EP3               -10000.000
!
LO_GAMMA_FLOOR    1
HI_GAMMA_FLOOR    4       !4 for EM4; 5 for FH1; 6 for all FH; 7for CH; 8 for
ICDMG
!
LO_CONE_LAYER     1
HI_CONE_LAYER     17      !7 for EM4  11 for FH1  14 for FH 17 fo  CH
CONE_USE_ICD    .FALSE.     !include ICD/MG in CONE ?
!
!   WARNING: CONE_USE_ICD is not fully implemented
!
! BINNED SHAPE CUTS START HERE
!
! CCEM E < ETH1  GEV    0.0 - 0.2
\ARRAY       ELCCL1     12
  -10000.000  0.420  -10000.000  0.76  0.100  0.900
  -10000.000  0.590       0.104  0.15  0.100  0.15
\END
!
! CCEM E < ETH1  GEV    0.3 - 0.6
\ARRAY       ELCCL2     12
  -10000.000  0.560  -10000.000  0.89  0.100  0.900
  -10000.000  0.510       0.113  0.17  0.12   0.22
\END
!
! CCEM E < ETH1  GEV    0.7 - 1.2
\ARRAY       ELCCL3     12
  -10000.000  0.850  -10000.000  1.000  0.100  0.900
  -10000.000  0.330       0.110  0.210  0.180  0.38
\END
!
! CCEM E < ETH1  GEV    1.3
\ARRAY       E12LCT     12
  -10000.000   10000.000  -10000.000   10000.000  -10000.000   10000.000
  -10000.000   10000.000   10000.000   10000.000   10000.000   10000.000
\END
!
! CCEM ETH1 < E < ETH2 GEV  0.0 - 0.2
\ARRAY       ELCCM1     12
  -10000.000  0.240  -10000.000  0.510  0.100  0.900
  -10000.000  0.660       0.062  0.084  0.052  0.09
\END
!
! CCEM ETH1 < E < ETH2 GEV  0.3 - 0.6
\ARRAY       ELCCM2     12
  -10000.000  0.340  -10000.000  0.630  0.100  0.900
  -10000.000  0.570       0.056  0.094  0.074  0.12
\END
!
! CCEM ETH1 < E < ETH2 GEV  0.7 - 1.2
\ARRAY       ELCCM3     12
  -10000.000  0.600  -10000.000  1.000  0.100  0.900
  -10000.000  0.380       0.044  0.110  0.110  0.22
\END
!
! CCEM ETH1 < E < ETH2 GEV  1.3
\ARRAY       E12MCT     12
  -10000.000   10000.000  -10000.000   10000.000  -10000.000   10000.000
  -10000.000   10000.000   10000.000   10000.000   10000.000   10000.000
\END
!
! CCEM ETH2 < E < ETH3 GEV    0.0 - 0.2
\ARRAY       ELCCH1     12
```

```
  -10000.000  0.160  -10000.000  0.390  0.100  0.900
  -10000.000  0.720       0.069  0.063  0.042  0.07
\END
!
! CCEM ETH2 < E < ETH3 GEV    0.3 - 0.6
\ARRAY       ELCCH2     12
  -10000.000  0.240  -10000.000  0.510  0.100  0.900
  -10000.000  0.620       0.050  0.068  0.058  0.09
\END
!
! CCEM ETH2 < E < ETH3 GEV    0.7 - 1.2
\ARRAY       ELCCH3     12
  -10000.000  0.440  -10000.000   0.800  0.100  0.900
  -10000.000  0.410       0.0225  0.075  0.092  0.17
\END
!
! CCEM ETH2 < E < ETH3  GEV    1.3
\ARRAY       E12HCT     12
  -10000.000   10000.000  -10000.000   10000.000  -10000.000   10000.000
  -10000.000   10000.000   10000.000   10000.000   10000.000   10000.000
\END
!
! CCEM E > ETH3  GEV    0.0 - 0.2
\ARRAY       ELCCX1     12
  -10000.000  0.11  -10000.00  0.33   0.100   0.900
  -10000.000  0.79       0.11  0.057  0.034   0.06
\END
!
! CCEM E > ETH3  GEV    0.3 - 0.6
\ARRAY       ELCCX2     12
  -10000.000  0.185  -10000.000  0.45   0.100  0.900
  -10000.000  0.68        0.072  0.061  0.054  0.08
\END
!
! CCEM E > ETH3  GEV    0.7 - 1.2
\ARRAY       ELCCX3     12
  -10000.000  0.38  -10000.00   0.75   0.100  0.900
  -10000.000  0.45       0.015  0.065  0.088  0.15
\END
!
! CCEM E > ETH3  GEV    1.3
\ARRAY       E12XCT     12
  -10000.000   10000.000  -10000.000   10000.000  -10000.000   10000.000
  -10000.000   10000.000   10000.000   10000.000   10000.000   10000.000
\END
!
! ECEM E < ETH1  GEV    1.4 - 1.5
\ARRAY       E15LCT     12
  -10000.000   0.345      -10000.000   0.715           0.100       0.900
   0.000       0.315           0.037   0.240           0.116   10000.000
\END
!
! ECEM E < ETH1  GEV    1.6 - 1.9
\ARRAY       ELECL1     12
  -10000.000   0.345      -10000.000   0.715           0.100       0.900
   0.005       0.365           0.037   0.240           0.115   10000.000
\END
!
! ECEM E < ETH1  GEV    2.0 - 2.5
\ARRAY       ELECL2     12
  -10000.000   0.345      -10000.000   0.715           0.100       0.900
   0.025       0.440           0.037   0.315           0.402   10000.000
\END
!
! ECEM E < ETH1  GEV    2.6 - 3.2
\ARRAY       ELECL3     12
  -10000.000   0.345      -10000.000   0.715           0.100       0.900
   0.045       0.365           0.037   10000.000       0.205   10000.000
```

```
\END
!
! ECEM ETH1 < E < ETH2 GEV  1.4 - 1.5
\ARRAY       E15MCT     12
  -10000.000   0.295      -10000.000   0.625          0.100       0.900
   0.005       0.415           0.041   0.200          0.072   10000.000
\END
!
! ECEM ETH1 < E < ETH2 GEV  1.6 - 1.9
\ARRAY       ELECM1     12
  -10000.000   0.295      -10000.000   0.625          0.100       0.900
   0.020       0.465           0.041   0.200          0.072   10000.000
\END
!
! ECEM ETH1 < E < ETH2 GEV  2.0 - 2.5
\ARRAY       ELECM2     12
  -10000.000   0.295      -10000.000   0.625          0.100       0.900
   0.040       0.540           0.041   0.275          0.189   10000.000
\END
!
! ECEM ETH1 < E < ETH2 GEV  2.6 - 3.2
\ARRAY       ELECM3     12
  -10000.000   0.295      -10000.000   0.625          0.100       0.900
   0.060       0.465           0.041   10000.000      0.125   10000.000
\END
!
! ECEM ETH2 < E < ETH3 GEV    1.4 - 1.5
\ARRAY       E15HCT     12
  -10000.000   0.210      -10000.000   0.490          0.100       0.900
   0.005       0.525           0.073   0.150          0.061   10000.000
\END
!
! ECEM ETH2 < E < ETH3 GEV    1.6 - 1.9
\ARRAY       ELECH1     12
  -10000.000   0.210      -10000.000   0.490          0.100       0.900
   0.020       0.575           0.073   0.150          0.061   10000.000
\END
!
! ECEM ETH2 < E < ETH3 GEV    2.0 - 2.5
\ARRAY       ELECH2     12
  -10000.000   0.210      -10000.000   0.490          0.100       0.900
   0.040       0.650           0.073   0.225          0.136   10000.000
\END
!
! ECEM ETH2 < E < ETH3 GEV    2.6 - 3.2
\ARRAY       ELECH3     12
  -10000.000   0.210      -10000.000   0.490          0.100       0.900
   0.060       0.575           0.073   10000.000      0.118   10000.000
\END
!
! ECEM E > ETH3  GEV   1.4 - 1.5
\ARRAY       E15XCT     12
  -10000.000   0.135      -10000.000   0.390          0.100       0.900
   0.000       0.575           0.093   0.075          0.063   10000.000
\END
!
! ECEM E > ETH3  GEV   1.6 - 1.9
\ARRAY       ELECX1     12
  -10000.000   0.135      -10000.000   0.390          0.100       0.900
   0.015       0.625           0.093   0.075          0.063   10000.000
\END
!
! ECEM E > ETH3  GEV   2.0 - 2.5
\ARRAY       ELECX2     12
  -10000.000   0.135      -10000.000   0.390          0.100       0.900
   0.030       0.700           0.093   0.150          0.148   10000.000
\END
!
```

```
! ECEM E > ETH3  GEV   2.6 - 3.2
\ARRAY       ELECX3     12
  -10000.000   0.135      -10000.000   0.390          0.100       0.900
   0.050       0.625           0.093   10000.000      0.126   10000.000
\END
!
!
!    SPARE (EM3CUT)
\ARRAY       ELECT3     10
  -10000.000   10000.000  -10000.000   10000.000  -10000.000   0.08
   10000.000   10000.000  -10000.000   10000.000
\END
!CC5L--CC5H--EC5L--E35--EC7L--EC7H--S3--S5--4L--4H---------
!the .08 cut on 7x7-5x5 HI is from Yi Xia´s tuning
\STOP
```

Monte Carlo Cuts:

```
\START        L2_EM_RCP
\SIZE        564       191
!-----------------------------------------------------------------
!    ELECTRON SRCP bank for ELECTRON analysis.
!    Created 28-NOV-1991 by Yi Xia
!
!    Updated 28-SEP-1992 using DAT_RCP program written by James T. McKinley
!    Updated 14-NOV-1993 James T. Linnemann  add ETMIN_CELL
!
! THIS IS L2_EM_MC05.RCP
!
!   Cuts used:
!
! PRIMARY CUTS:
!
!   EM3       cuts set to .1 .9 (lo, hi)
!   FH1       cuts set to 1.5*99% value
!   SIGMA5-SIGMA3 or 5x5-3x3 as main cuts set to 99% value
!       (after MC selection cuts!!)
!       for IETAC=31,32 use Yi Xia´s value of cut on 7x7-5x5
!
! SECONDARY CUTS:
!   set at "100% values" where 100% is defined differently for CC and EC
!
!       EC: 100% = 99% * 1.25
!       added cuts for the EC:
!           EM1(high), EM12(high),EM4(low, high),(4x4-2x2)/2x2(high)
!       also SIG5M3 as secondary transverse variable (for ieta<26)
!
!       CC: 100% = 99% + (99%-90%)
!       EM1(high), EM1+2(high), EM4(low, high)
!       also 5x5-3x3 as secondary transverse variable
!
! All other cuts turned off by setting cuts to +-10000
!
! Cuts tuned and tested by M. Tartaglia and J. McKinley,
! using single track electrons generated by N. Graf with GEANT  3.11,
! version N, full showering, low cutoff, homogeneous mixture Monte Carlo;
! events are distributed with Zvertex smeared (sigma=+-30cm), uniformly
! illuminating each eta bin from ieta=2 to 32, (eta=1 events were bad),
! and uniformly spread in phi across (half of) two modules and a phi crack.
! No noise or underlying event was included.
!
! CC efficiency was determined using a FH1 / EMTOT < 0.1 cut
! to eliminate electrons in phi cracks (no ISAJET info kept in this version
! of cut-tuning ntuple); no selection cuts were imposed on EC  electrons.
!
! CUTS ARE IN THE FOLLOWING ORDER IN THE EXXXXX ARRAYS:
! EM1(min) EM1(max) EM12(min) EM12(max) EM3(min) EM3(max)
! EM4(min) EM4(max) FH1(max) SIG5M3(max) 5X5-3X3/3X3(max)
!
!-----------------------------------------------------------------
!Format version (old format is implicitly version 0)
L2EM_VERSION    3   !   (add ETMIN_CELL)
!
!   For unpacking
ETMIN_CELL  0.0     !if ETnominal < this, exclude from ALL sums and cone
ET_IN_CAEP .TRUE.
!
!   Divider of eta bins
\ARRAY       ETA_BOUNDS     8
     2     6    12    13    15    19    25    32
\END
!
!   Divider of energy bins
```

```
\ARRAY       E_BOUNDS     6
      14.000      35.000      65.000      29.000      70.000     150.000
\END
!
!    SIGMA3 cut
S3A2                    2.1408
S3B1                   -2.07643
S3C0                   -0.01391
SSIG3               10000.000
!
!    EM3MAX cut
!
EP3                -10000.000
!
LO_GAMMA_FLOOR    1
HI_GAMMA_FLOOR    4       !4 for EM4; 5 for FH1; 6 for all FH; 7for CH; 8 for
ICDMG
!
LO_CONE_LAYER     1
HI_CONE_LAYER     17      !7 for EM4  11 for FH1  14 for FH 17 fo  CH
CONE_USE_ICD    .FALSE.     !include ICD/MG in CONE ?
!   warning: CONE_USE_ICD is not fully implemented
!
! CCEM E < ETH1  GEV    0.0 - 0.2
\ARRAY       ELCCL1     12
  -10000.000       0.264  -10000.000       0.676       0.100       0.900
      -0.012       0.630       0.113       0.099       0.082       0.155
\END
!
! CCEM E < ETH1  GEV    0.3 - 0.6
\ARRAY       ELCCL2     12
  -10000.000       0.340  -10000.000       0.728       0.100       0.900
      -0.004       0.653       0.108       0.127       0.097       0.188
\END
!
! CCEM E < ETH1  GEV    0.7 - 1.2
\ARRAY       ELCCL3     12
  -10000.000       0.476  -10000.000       0.902       0.100       0.900
      -0.008       0.625       0.093       0.182       0.151       0.249
\END
!
! CCEM E < ETH1  GEV    1.3
\ARRAY       E12LCT     12
  -10000.000   10000.000  -10000.000   10000.000  -10000.000   10000.000
  -10000.000   10000.000   10000.000   10000.000   10000.000   10000.000
\END
!
! CCEM ETH1 < E < ETH2 GEV  0.0 - 0.2
\ARRAY       ELCCM1     12
  -10000.000       0.151  -10000.000       0.510       0.100       0.900
      -0.007       0.750       0.127       0.058       0.041       0.146
\END
!
! CCEM ETH1 < E < ETH2 GEV  0.3 - 0.6
\ARRAY       ELCCM2     12
  -10000.000       0.184  -10000.000       0.593       0.100       0.900
      -0.014       0.726       0.097       0.073       0.062       0.201
\END
!
! CCEM ETH1 < E < ETH2 GEV  0.7 - 1.2
\ARRAY       ELCCM3     12
  -10000.000       0.361  -10000.000       0.843       0.100       0.900
      -0.008       0.776       0.123       0.096       0.109       0.210
\END
!
! CCEM ETH1 < E < ETH2 GEV  1.3
\ARRAY       E12MCT     12
  -10000.000   10000.000  -10000.000   10000.000  -10000.000   10000.000
```

```
  -10000.000   10000.000   10000.000   10000.000   10000.000   10000.000
\END
!
! CCEM ETH2 < E < ETH3 GEV    0.0 - 0.2
\ARRAY       ELCCH1     12
  -10000.000       0.079  -10000.000       0.378       0.100       0.900
      0.008       0.679       0.086       0.038       0.031       0.147
\END
!
! CCEM ETH2 < E < ETH3 GEV    0.3 - 0.6
\ARRAY       ELCCH2     12
  -10000.000       0.119  -10000.000       0.480       0.100       0.900
     -0.004       0.656       0.107       0.048       0.045       0.202
\END
!
! CCEM ETH2 < E < ETH3 GEV    0.7 - 1.2
\ARRAY       ELCCH3     12
  -10000.000       0.217  -10000.000       0.683       0.100       0.900
      0.003       0.751       0.120       0.072       0.074       0.213
\END
!
! CCEM ETH2 < E < ETH3 GEV    1.3
\ARRAY       E12HCT     12
  -10000.000   10000.000  -10000.000   10000.000  -10000.000   10000.000
  -10000.000   10000.000   10000.000   10000.000   10000.000   10000.000
\END
!
! CCEM E > ETH3  GEV    0.0 - 0.2
\ARRAY       ELCCX1     12
  -10000.000       0.060  -10000.000       0.321       0.100       0.900
     -0.011       0.753       0.114       0.031       0.024       0.124
\END
!
! CCEM E > ETH3  GEV    0.3 - 0.6
\ARRAY       ELCCX2     12
  -10000.000       0.093  -10000.000       0.482       0.100       0.900
     -0.028       0.665       0.097       0.036       0.043       0.202
\END
!
! CCEM E > ETH3  GEV    0.7 - 1.2
\ARRAY       ELCCX3     12
  -10000.000       0.166  -10000.000       0.643       0.100       0.900
      0.005       0.738       0.120       0.068       0.072       0.217
\END
!
! CCEM E > ETH3  GEV    1.3
\ARRAY       E12XCT     12
  -10000.000   10000.000  -10000.000   10000.000  -10000.000   10000.000
  -10000.000   10000.000   10000.000   10000.000   10000.000   10000.000
\END
!
! ECEM E < ETH1  GEV    1.4 - 1.5
\ARRAY       E15LCT     12
  -10000.000       0.080  -10000.000       0.574       0.100       0.900
      0.030       0.419       0.034       0.134       0.051   10000.000
\END
!
! ECEM E < ETH1  GEV    1.6 - 1.9
\ARRAY       ELECL1     12
  -10000.000       0.084  -10000.000       0.553       0.100       0.900
      0.040       0.500       0.053       0.161       0.076   10000.000
\END
!
! ECEM E < ETH1  GEV    2.0 - 2.5
\ARRAY       ELECL2     12
  -10000.000       0.059  -10000.000       0.489       0.100       0.900
      0.047       0.576       0.066       0.345       0.132   10000.000
\END
```

```
!
! ECEM E < ETH1  GEV    2.6 - 3.2
\ARRAY       ELECL3     12
  -10000.000       0.044  -10000.000       0.415       0.100       0.900
       0.055       0.896       0.072       1.244       0.107   10000.000
\END
!
! ECEM ETH1 < E < ETH2 GEV  1.4 - 1.5
\ARRAY       E15MCT     12
  -10000.000       0.030  -10000.000       0.360       0.100       0.900
       0.074       0.415       0.038       0.055       0.022   10000.000
\END
!
! ECEM ETH1 < E < ETH2 GEV  1.6 - 1.9
\ARRAY       ELECM1     12
  -10000.000       0.040  -10000.000       0.355       0.100       0.900
       0.091       0.529       0.054       0.095       0.044   10000.000
\END
!
! ECEM ETH1 < E < ETH2 GEV  2.0 - 2.5
\ARRAY       ELECM2     12
  -10000.000       0.030  -10000.000       0.301       0.100       0.900
       0.116       0.589       0.089       0.349       0.091   10000.000
\END
!
! ECEM ETH1 < E < ETH2 GEV  2.6 - 3.2
\ARRAY       ELECM3     12
  -10000.000       0.036  -10000.000       0.390       0.100       0.900
       0.075       0.519       0.059       1.245       0.145   10000.000
\END
!
! ECEM ETH2 < E < ETH3 GEV    1.4 - 1.5
\ARRAY       E15HCT     12
  -10000.000       0.020  -10000.000       0.291       0.100       0.900
       0.108       0.519       0.048       0.045       0.027   10000.000
\END
!
! ECEM ETH2 < E < ETH3 GEV    1.6 - 1.9
\ARRAY       ELECH1     12
  -10000.000       0.026  -10000.000       0.304       0.100       0.900
       0.101       0.554       0.076       0.086       0.065   10000.000
\END
!
! ECEM ETH2 < E < ETH3 GEV    2.0 - 2.5
\ARRAY       ELECH2     12
  -10000.000       0.020  -10000.000       0.246       0.100       0.900
       0.146       0.611       0.079       0.106       0.091   10000.000
\END
!
! ECEM ETH2 < E < ETH3 GEV    2.6 - 3.2
\ARRAY       ELECH3     12
  -10000.000       0.020  -10000.000       0.271       0.100       0.900
       0.121       0.613       0.138       1.246       0.077   10000.000
\END
!
! ECEM E > ETH3  GEV   1.4 - 1.5
\ARRAY       E15XCT     12
  -10000.000       0.018  -10000.000       0.256       0.100       0.900
       0.111       0.533       0.049       0.050       0.034   10000.000
\END
!
! ECEM E > ETH3  GEV   1.6 - 1.9
\ARRAY       ELECX1     12
  -10000.000       0.024  -10000.000       0.278       0.100       0.900
       0.109       0.615       0.083       0.129       0.091   10000.000
\END
!
! ECEM E > ETH3  GEV   2.0 - 2.5
```

```
\ARRAY       ELECX2     12
  -10000.000       0.016  -10000.000       0.207       0.100       0.900
       0.164       0.648       0.102       0.446       0.147   10000.000
\END
!
! ECEM E > ETH3  GEV   2.6 - 3.2
\ARRAY       ELECX3     12
  -10000.000       0.020  -10000.000       0.271       0.100       0.900
       0.121       0.613       0.138       1.246       0.077   10000.000
\END
!
!    SPARE (EM3CUT)
\ARRAY       ELECT3     10
  -10000.000   10000.000  -10000.000   10000.000  -10000.000       0.004
   10000.000   10000.000  -10000.000   10000.000
\END
!CC5L--CC5H--EC5L--E35--EC7L--EC7H--S3--S5--4L--4H---------
\STOP
```

Bibliography

[1] Sidney D. Drell and Tung-Mow Yan, Phys. Rev. Lett. 25, 5 (1970).

[2] John C. Collins and Davison E. Soper, Phys. Rev. D 16, 7 (1977).

[3] George Sterman, An Introduction To Quantum Field Theory, Cambridge University Press, 252 (1993).

[4] John C. Collins, Davison E. Soper, and George Sterman, Phys. Lett. B 263, 134 (1984).

[5] G. 't Hooft and M. Veltman, Nucl. Phys. B 246, 189 (1972); P. Breitenlohner and D. Maison, Comm. Math Phys. 52, 11 (1977).

[6] J.G. Körner, G. Schuler, G. Kramer, and B. Lampe, Z. Phys. C 32, 181 (1986).

[7] J.G. Körner, E. Mirkes, G. Schuler, Internat. Jour. Of Modern Phys. A 4, 7 (1989) 1781.

[8] J. Collins and D. Soper, Nucl. Phys. B 193, 381 (1981); Nucl. Phys. B 197, 446 (1982); Nucl. Phys. B 213, 545 (1983) (E).

[9] J. Collins, D. Soper, and G. Sterman, Nucl. Phys. B 250, 199 (1985).

[10] C. Balázs, J. Qiu, C.-P. Yuan, Phys. Lett. B 355, 548 (1995).

[11] R.P. Feynman, Phys. Rev. Lett. 23, 1415 (1969).

[12] R.P. Feynman, High energy Collisions, ed. C.N. Yang, J.A. Cole, M. Good, R. Hwa, and J. Lee-Franzini, Gordon and Breach, New York (1969).

[13] Peter B. Arnold and Russel P. Kauffmann, Nucl. Phys. B 349, 381 (1991).

[14] Frank E. Paige and Serban D. Protopopescu, ISAJET 7.13, A Monte Carlo event generator for pp and $p\bar{p}$ reactions.

[15] C.-P. Yuan, C. Balàzs, RESBOS Version 3.1, Department of Physics and Astronomy, Michigan State University, RESBOS computes the resummed portion of $d\sigma/dQ_T dy dQ^2 d\Omega$.

[16] S. Abachi *et al.*, Nucl. Inst. and Meth. **A338** (1994) 185.

[17] A. R. Clark *et al.*, Nucl. Inst. and Meth. **A261** (1987) 420.

[18] A. R. Clark *et al.*, Nucl. Inst. and Meth. **A315** (1992) 193.

[19] A. R. Clark *et al.*, Nucl. Inst. and Meth. **A279** (1989) 243.

[20] E. Oltman, DØ internal note #1169 (unpublished).

[21] NiCoTin is an alloy of 38.5% Co, 19.3% Cr, 15.6% Ni, 13.3% Fe, and 11.4% Mo manufactured by Microfil Industries SA, Switzerland.

[22] J. D. Jackson, Classical Electrodynamics 2nd Ed., John Wiley & Sons 1975, pp. 685-693.

[23] F. Feinstein, Ph. D. Thesis, A l'Universite de Paris-Sud, Centre d'Orsay, December 1987 (unpublished).

[24] R. Yarema, IEEE Trans. Nucl. Sci. **NS-33** (1986) 933.

[25] B. Chase, DØ internal note #953 (unpublished).

[26] B. Chase and G. Saewert, DØ internal note #630 (unpublished).

[27] M.I. Martin, M.E. Johnson, M.J. Mayberry, and D.C. DeGroot, IEEE Trans. Nucl. Sci. **NS-34** (1987) 258.

[28] D.C. DeGroot, DØ internal note #1013 (unpublished).

[29] Manufacturing Sciences Corp., Oak Ridge, TN.

[30] NVF Company, P.O. Box 6096, Broadview, IL 60153.

[31] Abatron Inc., 33 Center Dr., Gilberts, IL 60136.

[32] The small-$|\eta|$ tubes are Russian built PM60 phototubes, the large-$|\eta|$ tubes are Hammamatsu R647 phototubes.

[33] E.I. DuPont de Nemours Inc., Wilmington, DE

[34] P. Franzini, Proc. First Int. Conf. on Calorimetry in High Energy Physics, Batavia, IL Oct 29-Nov 1, 1990, C. Sazama, p. 101.

[35] R.D. Schamberger, Proc. Second Int. Conf. on Advanced Technology and Particle Physics, Como, Italy, 11-15 June, 1990.

[36] M. DeMarteau, Proc. First Int. Conf. on Calorimetry in High Energy Physics, Batavia, IL, Oct 29-Nov 1, 1990, eds. D. Anderson, M. Derrick, H.E. Fisk, A. Para and C. Sazama, p. 91.

[37] P.M. Tuts, Proc. on Instrumentation for Colliding Beam Physics, Novosibirsk (1985), p. 183.

[38] D.L. Huffman, Proc. IEEE Meeting, Nov. 1991 (Santa Fe, NM)

[39] C. Brown *et. al.*, Nucl. Instr. and Meth. A 279 (1989) 331.

[40] Polyester and epoxy copolymer sheets with chopped glass fibers. Galsteel Inc., 1727 Buena Vista Ave., Duarte, CA.

[41] J.M. Butler *et. al.*, Nucl. Instr. and Meth. A 290 (1990) 122.

[42] Y.M. Antipov *et. al.*, Nucl. Instr. and Meth. A 297 (1990) 121.

[43] Antipov *et. al.* DØ internal note #1278 (unpublished).

[44] G.S. Gao and R. Partridge, IEEE Trans. Nucl. Sci. NS-38 (1991) 286.

[45] D. Cutts, R. Zeller, R.D. Schamberger and R. Van Berg, Proc. 1984 Conf. on Recent Developments in Computing, Processor and Software Research For High-energy Physics, Guanajuato, Mexico, p. 403.

[46] D. Cutts et. al., Proc. Conf. on Computing in High Energy Physics, Amsterdam (1985) p. 287.

[47] D. Cutts et. al., Proc. IEEE 1988 Nuclear Science Symposium, Orlando, FA, Nov. 9-11, 1988.

[48] D. Cutts et. al., Proc. Int. Conf. on Computing in High Energy Physics, Oxford, England, Apr. 10-14, 1989.

[49] D. Cullen-Vidal et. al., Proc. Conf. on Computing in High Energy Physics, Tsukuba, Japan (March 1991).

[50] D. Cutts et. al., Proc. Conf. on Computing in High Energy Physics, Annecy, France, CERN Preprint 92-01, p. 262 (1992).

[51] ZRL Inc., Bristol, RI.

[52] R. Angstadt et. al., Proc. IEEE Meeting, Nov. 1991 (Santa Fe, NM).

[53] J. Hoftun, DØ internal note #909 (unpublished).

[54] J. Bantly et. al., D0 Luminosity Working Group, DØ internal note #2544

[55] Saul Youssef, Comp. Phys. Comm. 45, 423–426 (1987).

[56] Particle Data Group. Phys. Rev. D50 (3), 1173–1876 (August 1994).

[57] Meena Narain, Electron identification in the D detector, The Fermilab Meeting: DPF 92, eds. Carl H. Albright et al., volume 2, p. 1678, World Scientific, (November 1992).

[58] Ulrich Heintz, DØ internal note #2267 (unpublished).

[59] Ulrich Heintz private communication.

[60] Particle Properties Data Booklet, Particle Data Group, p. 116, (June 1992).

[61] L. Sawyer, M. Sosebee, A. White, J. White, DØ internal note #2520 (unpublished).

[62] M. Kelly, DØ internal note #2215 (unpublished).

[63] D. Chakraborty, M. Fatyga DØ internal note #1753 (unpublished).

[64] W. T. Eadie, F. Drijard, F. James, M. Roos, B. Sadoulet, Statistical Methods In Experimental Physics, North-Holland, 1971, ch. 11, p. 255–284.

[65] Byron P. Roe, Probability and Statistics In Experimental Physics, Springer-Verlag, 1992, ch. 17, p. 192–193

[66] CERN Applications Software Group, HBOOK Reference Manual version 4.22, p. 97–99.

[67] CERN Applications Software Group, CERN Program Library Short Writeups, G100, Upper Tail Probability Of Chi-Squared Distribution.

[68] F. Abe, et. al., CDF collaboration, Phys. Rev. D, Vol. 49, 1, p. 49, 1994

[69] C. Balàzs, private communication.